

UNIVERSITY OF BIRMINGHAM

Rational design of supported catalysts based on layered transition metal oxides towards electrochemical water splitting

by

Yayun Pu

A thesis submitted to the University of Birmingham for the degree of

DOCTOR OF PHILOSOPHY

School of Chemistry

College of Engineering and Physical Sciences

University of Birmingham

June 2021

UNIVERSITY OF
BIRMINGHAM

University of Birmingham Research Archive

e-theses repository

This unpublished thesis/dissertation is copyright of the author and/or third parties. The intellectual property rights of the author or third parties in respect of this work are as defined by The Copyright Designs and Patents Act 1988 or as modified by any successor legislation.

Any use made of information contained in this thesis/dissertation must be in accordance with that legislation and must be properly acknowledged. Further distribution or reproduction in any format is prohibited without the permission of the copyright holder.

Abstract

Under the circumstance of urgent demand for clean, renewable hydrogen fuel on a global scale, large-scale pure hydrogen production has drawn extensive attention from both industrial and science communities. To date, most commercial hydrogen is produced by steam methane reforming, which operated under harsh conditions with high energy-cost.[1] Alternatively, electrolysis of water is an effective strategy that can produce high purity H_2 under mild conditions. In this context, high active, low-cost electrocatalysts tend to be the specific target to realize the industrial application. To design and develop prospective catalysts, insight into the correlation between composition, coordination environment and electronic structure of electrocatalysts is undoubtedly important. With this in mind, this thesis reports various kinds of electrocatalysts that can effectively catalyze the hydrogen/oxygen evolution reaction (HER/OER), with tailored coordination structure/electronic structure. Through a variety of characterizations, the correlation between chemical environments of actives species and corresponding electrochemical activity towards HER/OER is elucidated.

***Chapter* 4** presents the phase transformations from lepidocrocite titania nanosheets (L-TiO_2) to rutile (R-TiO_2) and anatase (A-TiO_2).[2] We report that temperature determined the final phase-structure in the transition phase of the L-TiO_2 nanosheets into TiO_2 nanoparticles, while the pH determined the final morphology and particle size. Based on the experimental results, two different transition pathways of dissolution-recrystallization (pH=3) and topologically rolling transition (pH=9) have been proposed. Atomic dispersed Pt species were deposited on the pre-synthesized A-TiO_2 surface via photochemical reduction reaction. Due to the strong interaction of deposited Pt species and TiO_2 supports, a lower oxidation state of Pt was found on Pt@TiO_2-pH9. In 0.5 M H_2SO_4, Pt@TiO_2-pH9 delivered the best HER activity than other Pt decorated TiO_2 supports. It only requires an overpotential of 30 mV to reach 10 mA cm^{-2}_{geo}. In addition, with regard to the mass activity, all the Pt decorated TiO_2 samples show

excellent HER performance superior to commercial Pt/C due to ultralow loading of Pt on the catalyst.

***Chapter* 5** describes that low-loading (< 20 wt.%) Ni-confined in layered metal oxides anode catalysts have been synthesized by facile ion exchange methodology and subjected to systematic electrochemical studies.[3] It was found that Ni-intercalated on K-rich birnessite (Ni-KMO) presents an onset overpotential (η_{onset}) as low as 100 mV and overpotential at 10 mA cm^{-2} (η_{10}) of 206 mV in pH=14 electrolyte. By combining electrochemical methods XAS and XES, we demonstrate that Ni sites are the active sites for OER catalysis and that the Mn^{3+} sites facilitate Ni intercalation during the ion-exchange process. Different coordination structures of Ni species were confirmed on Ni-KMO and Ni-HMO, which are strongly correlated to the electrochemical behavior and corresponding OER activity. The effect of the pH and the nature of the supporting electrolyte on the electrochemical performance were also evaluated to reveal the electrochemical features of Ni intercalated KMO.

***Chapter* 6** shows the surface galvanic formation of Co-OH on KMO was achieved via the redox reaction of hydrated Co^{2+} with crystalline Mn^{4+}.[4] The synthesis method takes place at ambient temperature without using any surfactant agent or organic solvent, providing a clean, green route for the design of highly efficient catalysts. The redox reaction resulted in the formation of ultrathin Co-OH nanoflakes. XAS and XPS analysis confirmed the changes in the oxidation state of the bulk and surface species on the Co-OH nanoflakes supported on the KMO. XPS and Time of flight secondary ion mass spectrometry (ToF-SIMS) analysis demonstrated that the layer of CoO_xH_y deposited on the KMO and its electronic structure strongly depends on the anion of the precursor used. In particular, it was found that Cl^- favors the formation of Co-OH, changing the rate-determining step of the reaction, which enhances the catalytic activity towards the OER, producing the most active OER catalyst in alkaline media.

Acknowledgement

I would like to express my sincere appreciation to all the people who help and support my Ph.D. study. I really miss the past three years in Birmingham and Shenzhen, where I enjoyed lives so much.

As a student of the Joint PhD Training Program offered by the University of Birmingham (UoB) and Southern University of Science and Technology (SUSTech), I would like to express my heartfelt gratitude to my supervisors, Paramaconi Rodriguez in UoB and Limin Huang in SUSTech, for their supervision as well as to UoB and SUSTech for their support for my studies in both universities. Their professional background knowledge, attitude towards research work and useful suggestions help me a lot in theory learning, experiment operation and critical thinking. Group meeting and timely discussion guarantee my research project is proceeding on the right path.

I also wish to thank Dr. Veronica Celorrio for her expertise on XAS characterization and data analysis. Thanks to Prof. Meng Gu and Dr. Qi Wang for their work on TEM characterization. I am thankful to my colleagues in Paramaconi's and Huang's group, Dr. Matthew J Lawrence, Carlos Guillen-Posteguillo, Elizabeth Sargeant, Dr. Zongzhao Sun, Qianwen Chen et al for their help from all aspects, the experimental skills, questions discussion and the life in off-work.

This work is supported under the Southern University of Science and Technology Ph.D scholarship. I express my gratitude to the financial sponsors.

Last but not least I would like to thank my families for their love, support and encouragement whenever needed. Without them it would be very hard for me or even impossible to complete this work.

Table of content

ABSTRACT **1**

ACKNOWLEDGEMENT **3**

TABLE OF CONTENT **4**

LIST OF FIGURES **8**

LIST OF TABLES **16**

CHAPTER 1. INTRODUCTION **18**

1.1 Background and state-of-the-art progress 19

1.2 Fundamental mechanism of HER and OER 20

1.2.1 Fundamentals of Hydrogen Evolution Reaction *20*

1.2.2 Fundamentals of Oxygen Evolution Reaction *22*

1.3 Metal oxides/hydroxides for Hydrogen Evolution Reaction 25

1.3.1 Simple metal oxides *26*

1.3.2 Metal (hydro)oxides supported catalyst *27*

1.4 Metal oxides/hydroxides for Oxygen Evolution Reaction 29

1.4.1 Layered metal oxide *31*

1.4.2 Layered double hydroxides (LDHs) *33*

1.4.3 Cation modified metal oxide/hydroxide *36*

References 38

CHAPTER 2. AIM AND OBJECTIVES **44**

CHAPTER 3. THEORY AND TECHNIQUES **47**

3.1 Electrochemical theory 48

3.1.1 Overpotential *48*

3.1.2 Tafel slope *48*

3.1.3 Exchange current density (j^0) *49*

3.1.4 Turnover frequencies (TOF) *49*

3.1.5 Electrochemical active surface area (ECSA) *50*

3.2 ELECTROCHEMICAL TECHNIQUES 51

3.2.1 Cyclic Voltammetry (CV) and Linear Scanning Voltammetry (LSV) *51*

3.2.2 Chronoamperometry (CA) and Chronopotentiometry (CP) *53*

3.3 PHYSICAL CHARACTERIZATION TECHNIQUES 54

3.3.1 Electron microscopy *54*

3.3.2 X-ray based techniques *54*

3.3.3 Raman and Infrared Spectroscopy *58*

3.3.4 Thermal Gravimetric Analysis and Differential Thermal Analysis *59*

REFERENCES 60

CHAPTER 4. STUDY OF ANOMALOUS PHASE TRANSITION OF LAYERED LEPIDOCROCITE TITANIA NANOSHEETS TO ANATASE AND RUTILE, AND THEIR ELECTROCHEMICAL HER PERFORMANCE WITH PT DECORATION 62

4.1 INTRODUCTION 64

4.2 METHODS 66

4.2.1 Preparation of layered lepidocrocite-type TiO_2 nanosheets suspension *66*

4.2.2 Hydrothermal treatment of colloidal suspension *66*

4.2.3 Preparation of Pt@TiO_2 after phase transition by photochemical reduction reaction *67*

4.2.4 Physicochemical and structural characterization *67*

4.2.5 Electrochemical characterization *68*

4.3 RESULTS AND DISCUSSION 70

4.3.1 Phase transition of L-TiO_2 ..... *70*

4.3.2 Characterization of Pt decorated TiO_2 ..... *84*

4.3.3 Electrochemical study of Pt decorated TiO_2 ..... *98*

4.4 CONCLUSIONS 105

REFERENCES 107

CHAPTER 5. NICKEL CONFINED IN LAYERED METAL OXIDE LAYERS FOR HIGHLY

EFFICIENT AND DURABLE OXYGEN EVOLUTION CATALYSTS 109

5.1 INTRODUCTION 111

5.2 METHODS 113

5.2.1 Materials synthesis 113

5.2.2 Materials characterizations 114

5.2.3 Electrochemical characterization 115

5.3 RESULTS AND DISCUSSION 117

5.3.1 Characterization of Ni-confined KMO 117

5.3.2 XAS analysis of Ni intercalated metal oxides 120

5.3.3 Evaluation of the electrochemical activity and durability 131

5.3.4 Effect of the cations on the OER catalytic activity 143

5.3.5 Investigation of the coordination of active Ni on the catalytic activity 145

5.4 CONCLUSIONS 154

REFERENCES 156

CHAPTER 6. SURFACE GALVANIC FORMATION OF CO-OH ON LAYERED BIRNESSITE OXIDE AND ITS CATALYTIC ACTIVITY FOR THE OXYGEN EVOLUTION REACTION 158

6.1 INTRODUCTION 160

6.2 METHODS 162

6.2.1 Synthesis of the materials 162

6.2.2 Materials characterization 162

6.2.3 Electrochemical characterization: 165

6.3 RESULTS AND DISCUSSION 167

6.3.1 Synthesis and characterization of Co@KMO-Cl 167

6.3.2 Effect of the anions on morphology and electronic structure of Co@KMOs 177

6.3.3 Assessment of the oxygen evolution reaction on Co@KMOs 190

6.3.4 Long term stability of Co@KMOs during the oxygen evolution reaction 197

6.4 CONCLUSIONS 201

REFERENCES 202

CHAPTER 7 CONCLUSIONS AND FUTURE WORK 205

7.1 CONCLUSIONS 206

7.2 FURTHER WORK 209

REFERENCES 211

List of Figures

Figure 1. 1 Schematic graph of electrochemical water splitting. Reprinted from reference.[13] Copyright ©2020, American Chemical Society 20
Figure 1. 2 Mechanism of hydrogen evolution on catalyst surface in different media. Reprinted from reference.[13] Copyright ©2020, American Chemical Society 21
Figure 1. 3 (a) Traditional WNA-OER mechanism in acidic medium (blue) and alkaline medium (red).[24] Copyright © 2017, Royal Society of Chemistry. (b) Activity trends towards oxygen evolution of a wide variety of metal oxides.[19] Copyright © 2011, John Wiley and Sons 24
Figure 1. 4 Schematic illustration of the LOM-OER mechanism in alkaline condition.[26] Copyright © 2017, Springer Nature 25
Figure 1. 5 (a) Scheme for synthesis of Pt NWs/SL-Ni(OH)$_2$, (b) HER activity of Pt NWs/SL-Ni(OH)$_2$, Pt NPs/SL-Ni(OH)$_2$, pure Pt NWs and commercial Pt/C (20 wt%) in 1 M KOH at room temperature, (c) current-time chronoamperometric responses for HER at Pt NWs/SL-Ni(OH)$_2$, Pt NPs/SL-Ni(OH)$_2$ Pt NWs and commercial Pt/C (20 wt%) electrodes in 1 M KOH solution.[68] Copyright © 2015, Springer Nature 29
Figure 1. 6 Crystal structures of typical layered metal oxides. 33
Figure 1. 7 (a) Cyclic voltammetry (CV) curves of Au/NiFe LDH, pure NiFe LDH and bare Ti mesh in 1 M KOH. (b) Overpotential (η) at 10 mA cm^{-2} (left) and Tafel slope (right) for sAu/NiFe LDH and pure NiFe LDH. (c) Differential charge densities of NiFe LDH with and without Au atom.[131] Copyright © 2018, American Chemical Society 37

Figure 3. 1 Cyclic voltammetry of Pt nanoparticles at 20 mV s^{-1} in Ar-saturated 0.1 M NaOH, shaded regions are H adsorption/desorption area. 50
Figure 3. 2 (a) Repetitive triangular wave signal of potential variation during the cyclic voltammetry, (b) typical voltammogram of Ni^{2+}/Ni^{3+} redox in 1 M NaOH with scan rate υ = 20 mV s^{-1} 53
Figure 3. 3 Schematic graph of the diffraction occurs on a crystal surface.[15] Copyright ©2016, Elsevier 55
Figure 3. 4 Schematic graph of the principle on characteristic X-ray generation.[18] Copyright ©2015, Elsevier 56
Figure 3. 5 (a) Schematic graph of XAS excitation and energy diagram, (b) typical XAS spectrum.[19] Copyright © 2017, Royal Society of Chemistry 57

Figure 4. 1 Characterization of L-TiO$_2$ nanosheets by a) SEM image and b) TEM image. Photographs of colloidal solution of L-TiO$_2$ nanosheets at different pH (c) and their corresponding UV-Vis spectra (d) and Zeta-potentials (e). The inset in figure (d) corresponds to the plot of the intensity at 266 nm as a function of the pH. 71
Figure 4. 2 a) AFM image and b) height profile of the L-TiO$_2$ nanosheets supported on Si wafer, c) UV-Vis spectrum of a colloidal solution of as synthesized L-TiO$_2$ nanosheets at pH = 12. 72

Figure 4. 3 X-ray patterns of different exfoliated L-TiO_2 nanosheets (pH = 3, 6, 9) under different heat treatment as indicated in the figures. (f) freeze-drying with water, (g) freeze-drying without water. 74
Figure 4. 4 Observed, calculated, and difference profiles from the refinement XRD data of L-TO to A-TO/R-TO transition at 80 °C. 75
Figure 4. 5 a) XRD diffraction patterns and b) Raman scattering spectra of hydrothermally treated L-TiO_2 nanosheets at pH=3 and at different temperatures as indicated in the figure. 77
Figure 4. 6 (a-f) SEM images of stacked L-TiO_2 nanosheets and A-TiO_2 nanoparticles at different temperatures and pHs as indicated in the figure. (g-l) TEM images and HRTEM images of A-TiO_2 nanoparticles prepared at different pHs and after treatment at different temperatures as indicated in the figure. 79
Figure 4. 7 (a), (c) HRTEM image and (b) Inverse FFT image of A-TiO_2 at 180 ^oC of pH=3; (d), (f) HRTEM image and (e) Inverse FFT image of A-TiO_2 at 180 ^oC of pH=9. The insert in (c), (f) is FFT patterns. 80
Figure 4. 8 Schematic illustrations for the pH-dependence transition mechanism of L-TiO_2 to A-TiO_2 nanoparticles. 82
Figure 4. 9 SEM images of the L-TiO_2 samples prepared at pH=3 and annealed at 180 ^oC at different times (a) 6 h, (b) 12 h, (c) 18 h, and (d) 24 h. 82
Figure 4. 10 SEM images of hydrothermal treatment of L-TiO_2 (pH=3) and pH=9 at different annealing temperatures as indicated in the figure. 83
Figure 4. 11 (a) X-ray diffraction patterns of restacked L-TiO_2 nanosheets at different pH's, (b) Thermogravimetric analysis of L-TiO_2 nanosheets adjusted at different pH followed by freeze-drying protocol (ii). (c) Schematic graph of TBA intercalated in L-TiO_2 with different orientations under different pHs. 83
Figure 4. 12 Schematic graphs of photochemical reduction deposition of Pt on A-TiO_2. 85
Figure 4. 13 X-ray diffraction patterns of Pt decorated TiO_2 samples synthesized by a photochemical reduction reaction. 85
Figure 4. 14 X-ray diffraction patterns of as-synthesized HTO and L-TiO_2. 86
Figure 4. 15 X-ray diffraction patterns of Pt@HTO and Pt@L-TiO_2 after photochemical reduction reaction. 86
Figure 4. 16 SEM images of (a) Pt@TiO_2-pH3, (b) Pt@TiO_2-pH9, (c) Pt@TiO_2-pH3-N300, (d) Pt@TiO_2-pH9-N300. 87
Figure 4. 17 HAADF-STEM images of (a) Pt@TiO_2-pH3, (b) Pt@TiO_2-pH9 with EDS elemental mappings. 88
Figure 4. 18 SEM images of (a) Pt@TiO_2-pH12, (b) Pt@TiO_2-pH12-N300. 88
Figure 4. 19 SEM images of (a) Pt@TiO_2-pH9-N300, (b) Pt@TiO_2-C, (c) Pt@HTO, (d) Pt@L-TiO_2. 89
Figure 4. 20 (a) Raman spectrums of Pt@TiO_2 at different pHs, (b) enlarged area of E_g model at *ca.* 142 cm^{-1} of Pt@TiO_2-pH3 and Pt@TiO_2-pH9, (c) integration of each vibration models 90
Figure 4. 21 Vibration models of anatase TiO_2.[28] 91
Figure 4. 22 FTIR spectra of Pt@TiO_2-pH3 (blue) and Pt@TiO_2-pH9 (red). 92

Figure 4. 23 UV-Vis spectra of Pt decorated A-TiO_2 samples prepared at different pHs. Insert images are photographs of corresponding samples. 93
Figure 4. 24 UV-Vis spectra of (a) Pt@TiO_2-C and (b) Pt@TiO_2-pH3. Inset images are photographs of corresponding samples.....94
Figure 4. 25 High resolution XPS of Pt@TiO_2 at different pHs, (a) Pt 4f, (b) O 1s, (c) Ti 2p, (d) C 1s. 96
Figure 4. 26 Fit results of high-resolution XPS of Pt 4f, Ti 2p, O 1s on Pt@TiO_2-pH3 and Pt@TiO_2-pH9. All of the baselines are Shirley curve.....96
Figure 4. 27 High resolution XPS of Pt@TiO_2-pH3 and Pt@TiO_2-pH3-C, (a) Pt 4f, (b) O 1s, (c) Ti 2p, (d) C 1s. 97
Figure 4. 28 LSV curves of Pt@TiO_2 samples prepared in different pHs: (a) as-synthesized, (b) annealing at 300 °C in N_2 atmosphere. The samples were measured in 0.5 M H_2SO_4 solution with scan rates υ = 5 mV s^{-1}.....99
Figure 4. 29 Overpotentials at 10 mA cm^{-2} for Pt@TiO_2 samples prepared at different pHs, (a) as-synthesized, (b) after annealing at 300 °C in N_2 atmosphere.....100
Figure 4. 30 (a) LSV curves (b) Tafel slopes of Pt@TiO_2-pH9-N300, Pt@HTO, Pt@TiO_2-C and Pt@L-TiO_2 in 0.5 M H_2SO_4, with a scan rate of υ = 5 mV s^{-1}. (c) Chronoamperometry for 24 h, (d) LSV before/after chronoamperometry test of Pt@TiO_2-pH-N300. 101
Figure 4. 31 Overpotentials η_{10} (mV) for different Pt-decorated TiO_2 supports and the Pt/C reference.....102
Figure 4. 32 (a) LSV curves (b) Tafel slope of Pt@TiO_2-pH3 and Pt@TiO_2-C.....103
Figure 4. 33 Mass activity of Pt decorated samples, at the overpotential of 30 mV..104

Figure 5. 1 (a) Schematic illustration of the impact of Ni intercalation into layered K-birnessite manganese oxide. (b) X-ray diffraction patterns of Ni-KMO and pristine KMO. (c) SE-SEM image of Ni-KMO nanoplates. The particle size distribution histogram is inset. (f) SAD diffraction pattern (ZA= $[001]_{Ni\text{-}KMO}$) of particle in (e). (e) Bright field (BF) and (f) HAADF-STEM images of Ni-KMO nanoparticle seen along [001]. zone axis (ZA). HAADF-STEM images (g), and (h) enlarged Ni agglomeration at the edge of a Ni KMO nanoplate. (i) HAADF-STEM image of single Ni-KMO nanoplate with corresponding EDS elemental mapping.....118
Figure 5. 2 SEM image of $K_{0.45}MnO_2$ nanoparticles synthesized by solid state calcination.....119
Figure 5. 3 (a) STEM-EDS spectrum, (b) XRF spectrum of Ni-KMO. 119
Figure 5. 4 TGA curves of as-synthesized Ni exchanged layered metal oxides.....120
Figure 5. 5 Normalized XANES spectra measured at the (a) Mn K-edge and (b) Ni K-edge for KMO, HMO, Ni-KMO, Ni-HMO and Ni-HTO catalysts, in addition to relevant standard oxide compounds and metal foils. References, represented by dashed lines, are shown for comparison. 121
Figure 5. 6 Normalised absorption pre-edge features of X-KMO nanoplates (where M= H or Ni) and oxide reference compounds at (a) Mn K-edge and (b) Ni K-edge. The edge position of the metallic foils, in eV, has been subtracted from the measured spectra

presented. 123
Figure 5. 7 Measured experimental XES spectra of (a) KMO, (b) H(K)MO and (c) Ni-KMO with corresponding fitting contributions from MnO, Mn_2O_3 and MnO_2 standard oxide compounds. 124
Figure 5. 8 EXAFS FTs of $k^3\chi(k)$ functions for KMO, H(K)MO, Ni-KMO, Ni-HMO and Ni-HMO nanosheets and standard oxide reference compounds at (a) Mn K-edge and (b) Ni K-edge. References are shown for comparison. 126
Figure 5. 9 k^3 weighted χ data (a, c) and k^3 weighted Fourier transform EXAFS data (b, d) fits of H(K)MO and Ni-KMO. 127
Figure 5. 10 k^3 weighted χ data (left) and k^3 weighted Fourier transform EXAFS data (right) fits for the Ni-KMO catalysts measured at the Ni K-edge. 127
Figure 5. 11 k^3 weighted χ data (left) and k^3 weighted Fourier transform EXAFS data (right) fits for the Ni-HMO catalysts collected at the Ni K edge (a, b) and the Mn K edge (c, d) 128
Figure 5. 12 k^3 weighted χ data (left) and k^3 weighted Fourier transform EXAFS data (right) fits for the Ni-HTO catalysts collected at the Ni K edge. 128
Figure 5. 13 (a) Stable cyclic voltammograms of Ni-KMO at various pHs after 30 consecutive scans in NaOH electrolyte, with scan rate of 20 mV s^{-1}. The profile of the glassy carbon (GC) support is included for comparison. All the curves are iR-corrected. (b) The onset overpotential (η_{onset}) and overpotential at j = 10 mA cm^{-2} (η_{10}) obtained from (a). (c) Enlarged region showing the $Ni^{2+} \rightarrow Ni^{3+}$ redox peaks at various pHs. (d) Integrated charge of Ni^{2+}/Ni^{3+} oxidation peak as a function of pH at various scan rates. (e) OER onset potential, pre-OER oxidation peak potential and Ni^{2+}/Ni^{3+} ΔE variation with pH. (f) Chronoamperometry profiles of Ni-KMO at pH=14 at various applied potentials as indicated in the figure. 133
Figure 5. 14 Evolution of Ni-KMO voltammograms over 30 cycles at (a) pH=14, (c) pH=13, (e) pH=12. Corresponding enlarged redox peaks of Ni^{2+}/Ni^{3+} redox couple at (b) pH=14, (d) pH=13, (f) pH=12. 134
Figure 5. 15 Redox peak correlated NiOOH structure evolution of Ni-KMO at (a) pH=14. (b) pH=13. (c) pH=12, with scan rate v = 5 mV s^{-1}. 135
Figure 5. 16 Schematic graph of Ni based phase transition.[38] 136
Figure 5. 17 Cyclic voltammograms of Ni-KMO in NaOH, (a) Ni^{2+}/Ni^{3+} redox peaks of Ni-KMO with varying scan rates at pH=14, (b) corresponding linear fitting of peak value against scan rate. (c) Ni^{2+}/Ni^{3+} redox peaks against scan rate of Ni-KMO at pH=12, (d) corresponding linear fitting of peak current value against square root of scan rate, (e) asymptotic independence of peak currents against scan rate at pH=12. 137
Figure 5. 18 Graphic demonstration of the potential limits and base line for the integration of the charge associated to the Ni redox peaks of Ni-KMO at (a) pH=14, (b) pH=13, (c) pH=12 and different scan rates. 139
Figure 5. 19 Integration charge of scan1 and scan 30 at pH=14, pH=13 and pH=12 with the corresponding schematical crystal structures. 140
Figure 5. 20 (a) Tafel slopes of Ni-KMO, with corresponding slope fitting at (b) pH=14, (c) pH=13, (d) pH=12. 142
Figure 5. 21 (a) SEM and STEM-EDS images of Ni-KMO before electrochemical

evaluation, (b) chronoamperometry of Ni-KMO at 1.48 V over 10 h, (c) SEM and STEM-EDS images of Ni-KMO after electrochemical evaluation. 143
Figure 5. 22 Voltammetric profiles of Ni-KMO in 1 M KOH and NaOH electrolyte, as indicated in the figure, inset is the enlarged redox features. Glassy carbon shown for comparison. Scan rate υ = 20 mV s^{-1}. 144
Figure 5. 23 XRD patterns of pristine (a) HTO and (c) HMO, and after Ni-exchange intercalation. SEM images of (b) Ni-HTO, (d) Ni-HMO. 146
Figure 5. 24 (a) iR-corrected voltammetric profiles of Ni-KMO, Ni-HMO and Ni-HTO after 30 consecutive scans at pH=14, in 1 M NaOH at 20 mV s^{-1}. The evolution of the voltammograms as function of the number of scans can be found in Figure 5.25. (b) Enlarged region showing the $Ni^{2+} \rightarrow Ni^{3+}$ redox peaks and OER onset. (c) η_{50} and η_{10} obtained from (a). (d) TOF as a function of potential calculated using the content of Ni content on Ni-KMO, Ni-HMO and Ni-HTO determined by the Ni^{+2}/Ni^{+3} redox charge and the XRF. 147
Figure 5. 25 Voltammetric profiles of (a) Ni-HTO and (b) Ni-HMO evolved in 30 cycles in 1 M NaOH. 148
Figure 5. 26 CV of (a) GC electrode and pristine (b) KMO, (c) HTO and (d) HMO, (e) Ni-HTO and HTO for comparison, (f) Ni-HMO and HMO for comparison at pH=14. 148
Figure 5. 27 (a) Tafel plots of Ni-exchanged layered metal oxides, corresponding fitting of (b) Ni-KMO, (c) Ni-HMO, (d) Ni-HTO at pH=14. 149
Figure 5. 28 Calculated TOFs normalized by the integrated charge of Ni-exchanged samples at η_{10} = 240 mV. 150
Figure 5. 29 (a) Voltammetric mass activity of Ni-KMO, Ni-HMO, and Ni-HTO measured in 1 M NaOH. Scan rate of 20 mV s^{-1}, (b) corresponding activity at 1.53 V vs RHE. 152
Figure 5. 30 Chronoamperometry of (a) Ni-KMO at 1.48 V and (b) Ni-HTO at 1.51 V in 1 M NaOH at least 20 h. 152
Figure 5. 31 (a) Cyclic voltammetry of Ni-KMO with different exchange time in 1 M KOH, scan rate of 20 mV s^{-1}. Inset show the potential range between 0.8 and 1.5V showing the Ni^{2+}/Ni^{3+} redox peaks (b) Ni content of Ni-KMO determined by XRF analysis as a function of the Ni-exchange time. 153

Figure 6. 1 Schematic graph of hydrated Co^{2+} reacting with crystalline Mn^{4+} at room temperature. 161
Figure 6. 2 (a-b) SEM images, (c) EDS, (d-e) TEM images of Co@KMO-Cl nanoplates. (f) enlarged area of COOH on the surface of Co@KMO-Cl, (g) HAADF-STEM image of a Co@KMO-Cl nanoplate with corresponding EDS elemental mapping. 168
Figure 6. 3 (a-b) SEM images of as synthesized KMO nanoparticles prepared by solid-state calcination, (c) TEM image, (d) high resolution TEM, (e) reversed FFT image of single KMO nanoparticle. 169
Figure 6. 4 HRTEM images of Co@KMO-Cl exposed on TEM beam for consecutive 50 s, dose rate: ~500 e/$Å^2$/s. 169

Figure 6. 5 (a) XRD patterns, (b) Raman spectra of pristine KMO and Co@KMO-Cl, (c) XPS of Co@KMO-Cl with fit, left Co 2p3/2, right Cl 2p. Shirley baseline was adopted for the fit in (c). 170
Figure 6. 6 Raman spectra of (a) KMO and (b) Co@KMO-Cl at different laser power intensities. 171
Figure 6. 7 Normalized XANES spectra at the (a) Co K-edge, (b) Mn K-edge of the synthetized electrocatalysts. Spectra for reference compounds have been included as a comparison. Insets show the pre-edge region. Structure in Figure 6.6b represents the structure of edge shared M-O octahedra from KMO where the red atoms are O, the dark blue atoms are Mn. EXAFS FTs of k^3 χ(k) functions for the materials from Figure 6.6a at the (c) Co K-edge, and (d) Mn K-edge. 173
Figure 6. 8 Mean Co oxidation state as a function of the Co K-edge position for the prepared Co@KMO catalysts. 174
Figure 6. 9 Measured experimental XES spectra of (a) Co@KMO-Cl, (b) KMO with corresponding fitting contributions from MnO, Mn_2O_3 and MnO_2 standard oxide compounds. 174
Figure 6. 10 k^3 weighted Fourier transform EXAFS data fits and k^3 weighted χ data of Co@KMnO-Cl at the Co K-edge..... 175
Figure 6. 11 k^3 weighted Fourier transform EXAFS data fits and k^3 weighted χ data of Co@KMnO-Cl at Mn K-edge. 175
Figure 6. 12 k^3 weighted Fourier transform EXAFS data fits and k^3 weighted χ data of KMO at Mn K-edge. 176
Figure 6. 13 (a-c) SEM, (d-f) TEM and (g-i) EDS spectra of Co@KMO-Cl, Co@KMO-NO and Co@KMO-SO as indicated left of the figure. 178
Figure 6. 14 XRF spectra of (a) Co@KMO-Cl, (b) Co@ KMO-NO and (c) Co@ KMO-SO, with corresponding elemental atomic fractions summarized in table. 179
Figure 6. 15 XPS spectra of KMO before/after reaction with different Co salts..... 179
Figure 6. 16 High resolution XPS of pristine KMO and the relative Co reacted samples, (a) K 2p, (b) Mn 2p, (c) Co 2p, (d) O1s, (e) C 1s, (f) Cl 2p of Co@KMO-Cl, N1s of Co@KMO-NO, S 2p of Co@KMO-SO. KMO, Co@KMO-Cl, Co@KMO-NO, Co@KMO-SO. 180
Figure 6. 17 (A) ToF-SIMS positive ions 3D data reconstruction on the Co@KMO-Cl, Co@KMO-NO and Co@KMO-SO catalysts supported on glassy carbon. ToF-SIMS data were acquired using collimated, burst, alignment mode.[45, 46] The 3D overlay images are reconstructed with the Co^+ fragments (m/z= 59) in green and the anion (Cl, NO_3 and SO_4) fragments in red respectively. Each system was acquired with a different field-of-view (FoV); 50 × 50 μm^2 for the Co@KMO-Cl and Co@KMO-SO systems and 20 × 20 μm^2 for the Co@KMO-NO system. (B) ToF-SIMS negative ions depth profiles using the spectrometry mode (high-current bunched mode) on the Co@KMO-Cl, Co@KMO-NO and Co@KMO-SO catalysts. Information about the acquisition and sputtering is given in the experimental section. 181
Figure 6. 18 High resolution XPS spectra of different Co-modified KMOs: (a) Co 2p, (b) O 1s. 183
Figure 6. 19 High resolution Mn $2p_{3/2}$ spectra of KMO, Co@KMO-Cl, Co@KMO-NO,

and Co@KMO-SO. correspond to the original data, correspond to the convoluted curves of Mn^{+3}, correspond to the convoluted curves of Mn^{+4} and correspond to the fit. 184
Figure 6. 20 SEM (a-d) and TEM (e-h) images of Co@KMO-Cl prepared by different concentrations of $CoCl_2$ as indicated in the figure..... 185
Figure 6. 21 STEM-EDS mapping of Co@KMO-$Cl_{0.5}$ and Co@KMO-$Cl_{0.01.}$ 186
Figure 6. 22 Difference of the anodic and cathodic current densities (Δj) at 1.15 V vs RHE as a function of the scan rate. 186
Figure 6. 23 Survey and high resolution XP-spectra of Co@KMO-$Cl_{0.5}$ and Co@KMO-$Cl_{0.01.}$ 188
Figure 6. 24 (a) Co $2p_{3/2}$ and (b) O 1s fit results of Co@KMO-$Cl_{0.5}$ and Co@KMO-$Cl_{0.01.}$ 189
Figure 6. 25 XPS spectra and elements ratio of (a) Co@KMO-$Cl_{0.5}$ and (b) Co@KMO-$Cl_{0.01.}$ 189
Figure 6. 26 (a) Stable cyclic voltammograms of Co salts reacted Co@KMO at pH=14 after 10 consecutive scans in NaOH electrolyte, with scan rate of 20 mV s^{-1}. The profile of the glassy carbon (GC) support is included for comparison. All the curves are iR-corrected. (b) Enlarged region showing the double layer region of various Co@KMO. (c) The onset overpotential (η_{onset}) and overpotential at j = 10 mA cm^{-2} (η_{10}) obtained from (a). (d) Tafel slopes for the OER on the Co@KMO catalyst prepared with different anions. 191
Figure 6. 27 Cyclic voltammetries in the double-layer capacitive potential window a at different scan rates (a) Co@KMO-Cl, (b) Co@KMO-NO, (c) Co@KMO-Cl, (d) KMO. (e) difference of the anodic and cathodic current densities (Δj) at 1.15 V vs RHE taken from (a-d) as a function of the scan rates. 192
Figure 6. 28 Mass activity normalized by loaded Co mass of Co@KMOs (solid line); ECSA-normalized curves of Co@KMOs (dot line) measured in 1M NaOH electrolyte. 193
Figure 6. 29 (a) Stable cyclic voltammograms in 1 M NaOH solution of Co@KMO-Cl samples synthesized with different concentration of $CoCl_2$ as indicated in different color, solid lines (left Y axis): geometrical activity; (◦) symbols (right Y axis): mass activity. The stable voltammogram was recorded after 10 consecutive scans. The voltammogram of the glassy carbon (GC) support is included for comparison. All the curves are iR-corrected. Scan rate υ= 20 mV s^{-1}. (b) corresponding Tafel plots in the potential range between 1.4 and 1.7 V vs RHE. 196
Figure 6. 30 (a) 24 h chronoamperometry profile of Co@KMO-$Cl_{0.5}$ at 1.48 V vs. RHE in 1 M NaOH solution. HR-TEM images of Co@KMO-Cl (b) before, and (c) after electrolysis. 198
Figure 6. 31 Cyclic voltammograms of Co@KMO-Cl before and after long term durability test. 199
Figure 6. 32 SEM images of Co@KMO-Cl after 10 cycles of OER. 199
Figure 6. 33 Raman spectra of Co@KMO-Cl before/after chronoamperometry. 200
Figure 6. 34 SEM-EDS mapping of Co@KMO-Cl after chronoamperometry at 1.48 V vs. RHE in 1 M NaOH. 200

List of Tables

Table 4. 1 Refined cell parameters of Rutile. 75
Table 4. 2 Refined structural parameters for rutile using XRD data. 76
Table 4. 3 Refined cell parameters of Anatase. 76
Table 4. 4 Refined structural parameters for rutile using XRD data. 76
Table 4. 5 Integral areas of different vibration models of Pt@TiO_2 at different pHs. 91
Table 4. 6 Binding energies, FWHM and area percentage of each component of Pt(4f) fit spectra on Pt decorated A-TiO_2 samples from Figure 4.25. 97
Table 4. 7 ICP-MS results of selected Pt decorated samples. 104

Table 5. 1 XRF results of Ni-KMO, Ni-H(K)MO and Ni-HTO 120
Table 5. 2 Ratio of Mn^{n+} species and corresponding mean Mn oxidation state of prepared KMO derivatives determined by XES. 125
Table 5. 3 EXAFS distances and fitting parameters for the HMO catalyst. Fitting parameters: $S_0^2 = 0.8$ calculated using a Mn foil standard; fit range $3.0 < k < 13.8$, $1.2 < R < 3.5$. $\Delta E_0 = 0.2 \pm 0.7$ eV; $R_{factor} = 0.008$ 128
Table 5. 4 EXAFS distances and fitting parameters for the Ni-KMO catalyst at the Mn K-edge. Fitting parameters: $S_0^2 = 0.8$ calculated using a Mn foil standard; fit range $3.0 < k < 13.9$, $1.2 < R < 3.5$. $\Delta E_0 = 0.5 \pm 0.7$ eV; $R_{factor} = 0.006$ 129
Table 5. 5 EXAFS distances and fitting parameters for the Ni-KMO catalyst at the Ni K-edge. Fitting parameters: $S_0^2 = 0.8$ calculated using a Ni foil standard; fit range $3.0 < k < 12.1$, $1.0 < R < 3.2$. $\Delta E_0 = -0.4 \pm 1.0$ eV; $R_{factor} = 0.022$ 129
Table 5. 6 EXAFS distances and fitting parameters for the Ni-HMO catalyst at the Ni edge. Fitting parameters: $S_0^2 = 0.8$ calculated using a Ni foil standard; fit range $3.2 < k < 12.9$, $1.0 < R < 3.2$. $\Delta E_0 = -4.0 \pm 1.7$ eV; $R_{factor} = 0.027$ 129
Table 5. 7 EXAFS distances and fitting parameters for the Ni-HMO catalyst at the Mn edge. Fitting parameters: $S_0^2 = 0.8$ calculated using a Mn foil standard; fit range $3.0 < k < 13.9$, $1.2 < R < 3.5$. $\Delta E_0 = -0.1 \pm 0.7$ eV; $R_{factor} = 0.008$ 130
Table 5. 8 EXAFS distances and fitting parameters for the Ni-HTO catalyst at the Ni edge. Fitting parameters: $S_0^2 = 0.8$ calculated using a Ni foil standard; fit range $3.2 < k < 11.1$, $1.0 < R < 3.2$. $\Delta E_0 = -6.4 \pm 0.7$ eV; $R_{factor} = 0.004$ 130
Table 5. 9 Summary of electrochemical data of Ni-KMO, Ni-HMO, Ni-HTO. 151

Table 6. 1 Ratio of Mn^{n+} fractions and corresponding mean Mn oxidation state of prepared CoKMO-Cl determined by XES. 175
Table 6. 2 EXAFS distances and fitting parameters for the Co@KMO-Cl catalyst. Fitting parameters: $S_0^2 = 0.8$ calculated using a Co foil standard; fit range $2.7 < k < 11.3$, $1.0 < R < 3.0$. $\Delta E_0 = -3.1 \pm 1.7$ eV; $R_{factor} = 0.016$ 176
Table 6. 3 EXAFS distances and fitting parameters for the CoKMnO-Cl catalyst. Fitting parameters: $S_0^2 = 0.8$ calculated using a Mn foil standard; fit range $3.0 < k < 13.8$, $1.2 < R < 3.5$. $\Delta E_0 = 0.2 \pm 1.0$ eV; $R_{factor} = 0.011$ 176

Table 6. 4 EXAFS distances and fitting parameters for the KMO catalyst. Fitting parameters: S_0^2 = 0.8 calculated using a Mn foil standard; fit range 3.0 < k < 12.2, 1.2 < R < 3.2. ΔE_0 = -2.3 ± 1.7 eV; R_{factor} = 0.010 176
Table 6. 5 Comparative values of state-of-the-art catalyst for the oxygen evolution reaction in alkaline media. 194

Chapter 1. Introduction

This chapter is the collection of the basic background of the Ph.D course, including the physical/electrochemical theory and motivating factors behind the course and literature works.

1.1 Background and state-of-the-art progress

Sustainable, green and renewable energy supply is of paramount importance in powering a prosperous civilization. According to the International Energy Agency, global energy demand will reach 24-26 TW in 2040.[5] Such a huge increase accomplished with the transformation from traditional fossil (coal, oil, gas) to renewable energy has raised substantial concerns and need for new technologies, such as fuel cells, metal-air batteries and water splitting electrolyzers.[6-8] Among these energy generation/conversion solutions, electrochemical water splitting is an efficient and clean technology to convert H_2O into molecular H_2 and O_2, where the hydrogen evolution reaction (HER) takes place on cathode and oxygen evolution reaction (OER) on the anode.[9] By making use of water as feedstock, the most universal on earth, electrolyzer can produce sustainable hydrogen resource without other by-products. The produced H_2 as an energy carrier can be used in fuel cells converting chemical energy to electricity.[10] To realize these electrochemical conversion processes, electrocatalysts are indispensable and pivotal. They not only reduce the reaction energy barrier that drive catalysis reactions with low overpotential, but also determine the rate, efficiency and selectivity of chemical transformation involved. However, commercialized catalysts are still far from satisfied for their cost, efficiency and stability. The pursuit of advanced catalysts remains a great challenge, motivating both the scientific community and technology companies to make progress unremittingly.[7, 11, 12]

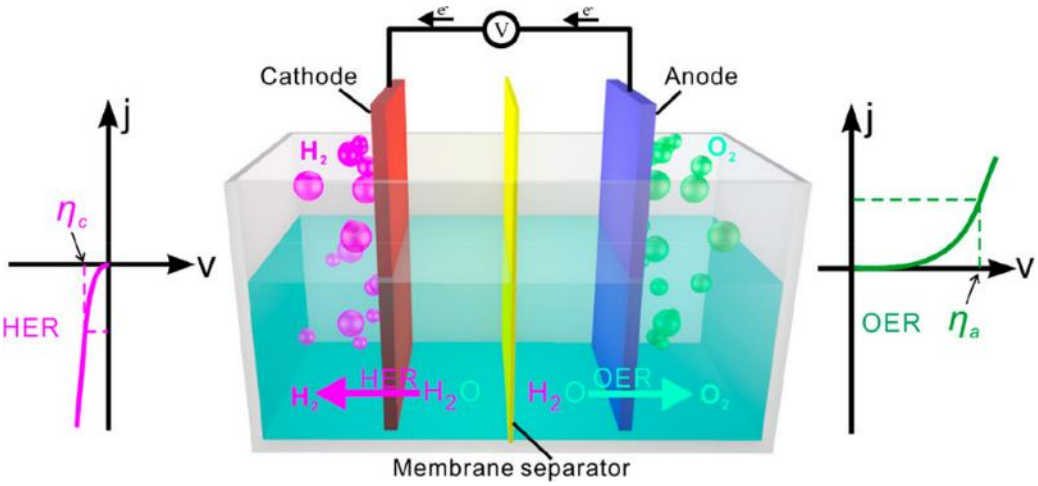


Figure 1. 1 Schematic graph of electrochemical water splitting. Reprinted from reference.[13] Copyright ©2020, American Chemical Society

1.2 Fundamental mechanism of HER and OER

1.2.1 Fundamentals of Hydrogen Evolution Reaction

It is well known that water splitting is composed of two half reactions, e.g. hydrogen evolution reaction (HER) and oxygen evolution reaction (OER). At the cathodic part, the H^+ is being reduced to H_2 at the catalyst surface via a two-step electron transfer process. Based on the different combination pathway of H_2, this has Volmer-Heyrovsky and Volmer-Tafel mechanism.[13, 14] More specifically, Volmer step as the first step denote the adsorption of H on active site M*, to obtain intermediate M*H; the second step can proceed either by the Heyrovsky step where *H is attacked by H^+ or H_2O to get H_2 evolution or by Tafel step where two adjacent *H recombined directly. The Heyrovsky step is electrochemical desorption process, while the Tafel step is chemical desorption. Considering different pH conditions, the equation can be written as follow (see Figure 1. 2).

Acidic medium:

$M^* + H_3O^+ + e^- \rightarrow M^*H + H_2O$ (Volmer step) [1.1]

$M^*H + H_3O^+ + e^- \rightarrow M^* + H_2 + H_2O$ (Heyrovsky step) [1.2]

$M^*H + M^*H \rightarrow M^* + M^* + H_2$ (Tafel step) [1.3]

Alkaline medium:

$M^* + H_2O + e^- \rightarrow M^*H + OH^-$ (Volmer step) [1.4]

$M^*H + H_2O + e^- \rightarrow M^* + H_2 + OH^-$ (Heyrovsky step) [1.5]

$M^*H + M^*H \rightarrow M^* + M^* + H_2$ (Tafel step) [1.6]

Notably, owing to the deficient H^+ in the alkaline medium, dissociation of H_2O molecule at the catalyst surface should be prior to adsorption of H. Comparative slower kinetic is always found in alkaline solution in contrast to acidic condition, where sufficient proton can be easily accessed by the active site.

The rate determining step (RDS) controls the overall reaction kinetics in the multistep catalytic process.[15] Better understanding of the RDS of the certain catalyst is regarded as the key in catalyst design. Tafel slope analysis, a traditional but effective method, therefore is widely adopted and performed. The value of Tafel slope indicates the rate of current density change in a small range of potential window. The smaller the better. As for the HER process, the Tafel slope of 29 mV dec^{-1} implies Tafel step is the RDS, i.e. Volmer or Heyrovsky step is fast and *H combination reaction control the reaction. If the Tafel value is 39 mV dec^{-1}, The Heyrovsky step becomes the RDS. While if the adsorption of proton is most difficult, the Tafel slope should be 116 mV dec^{-1}.[16]

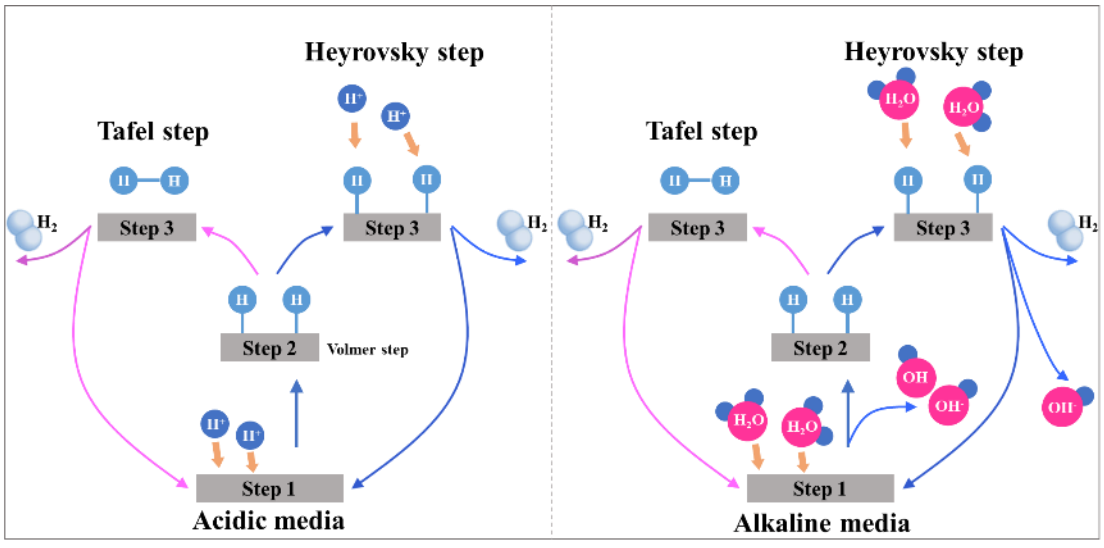


Figure 1. 2 Mechanism of hydrogen evolution on catalyst surface in different media. Reprinted from reference.[13] Copyright ©2020, American Chemical Society

1.2.2 Fundamentals of Oxygen Evolution Reaction

The oxygen evolution reaction take place at the anode with four proton coupled electron transfer (PCET) steps.[17] It is considered to be more complicated and requires high overpotential. Sluggish kinetic and multiple intermediates such as M*OH, M*O, M*OOH bring substantial challenge to the OER study.[18] Therefore fundamental understanding of basic thermodynamics and reaction mechanism is necessarily needed. The standard equilibrium potential for $H_2O \rightarrow O_2$ is +1.229 V vs. SHE (standard hydrogen electrode).[19] By consideration of acidic/alkaline condition, it is usually transformed to reverse hydrogen electrode (RHE), with 59.2 mV/pH increase on the dependence of pH. At acidic and alkaline conditions, the reaction pathways would be different for each other.

Acidic medium:

$$M^* + H_2O \rightarrow M^*OH + H^+ + e^- \quad [1.7]$$

$$M^*OH + HO\text{-}H \rightarrow M^*O + H_2O + H^+ + e^- \quad [1.8]$$

$$M^*O + H_2O \rightarrow M^*OOH + H^+ + e^- \quad [1.9]$$

$$M^*OOH \rightarrow M^* + O_2 + H^+ + e^- \quad [1.10]$$

Alkaline medium:

$$M^* + OH^- \rightarrow M^*OH + e^- \quad [1.11]$$

$$M^*OH + OH^- \rightarrow M^*O + H_2O + e^- \quad [1.12]$$

$$M^*O + OH^- \rightarrow M^*OOH + e^- \quad [1.13]$$

$$M^*OOH + OH^- \rightarrow M^* + O_2 ++ H_2O + e^- \quad [1.14]$$

Intermediates M*OH, M*O, M*OOH play the key role in traditional water nucleophilic attack (WNA) mechanism analysis of OER. On the one hand, each intermediate formation can be correlated to the anodic reaction kinetics. Similar to the HER, Tafel slope is used to determine which step limit the oxygen evolution. Take the alkaline condition as an example, the following equation is used for the determination of the

rate-determining step (RDS) by Tafel slope[20]:

$$b = \frac{2.3RT}{a\,F} \quad [1.15]$$

$$a = \frac{n_f}{v} + n_r\beta \quad [1.16]$$

R is the gas constant, T is temperature, F is faraday's constant, n_f is the number of electrons transferred before the RDS, v is the stoichiometric number with a typical value of 1, n_r is the number of electrons transfer in a single RDS, β is the symmetry factor with a typical value of 0.5. when the value is 24 mV dec^{-1}, it is the third step (Eqn. 1.13) where M*OOH formation is the RDS; if the value is 40 mV dec^{-1}, the second step of M*O formation (Eqn. 1.12) becomes the RDS; Tafel slope of 60 mV dec^{-1} implies the chemical deprotonation step after first electron transfer limits the control of the whole reaction; if the first step that adsorption of OH becomes most difficult (Eqn. 1.11), the value would be 120 mV dec^{-1}.[21, 22]

On the other hand, there is a correlation of the energy barrier for each intermediate formation, called scaling relation.[19, 23] Specifically, since both *OH and *OOH bind on active site and are in the same single bond form, a roughly constant difference was found between the binding energy of *OH and *OOH, with a value of 3.2 ± 0.2 eV. It applies either on metals or metal oxides, regardless of the binding site. In a certain catalyst, the lower barrier of *OH → *O would correspond to higher barrier of *O → *OOH. If taking the energy difference (ΔG) of *OH and *OOH as a single descriptor, the overpotential of different catalyst would present a volcano shape, *e.g.* the widely known volcano plot. Catalysts at/around the summit of the volcano possess the optimal oxygenates binding energy, which means the lowest theoretical overpotential for the OER.

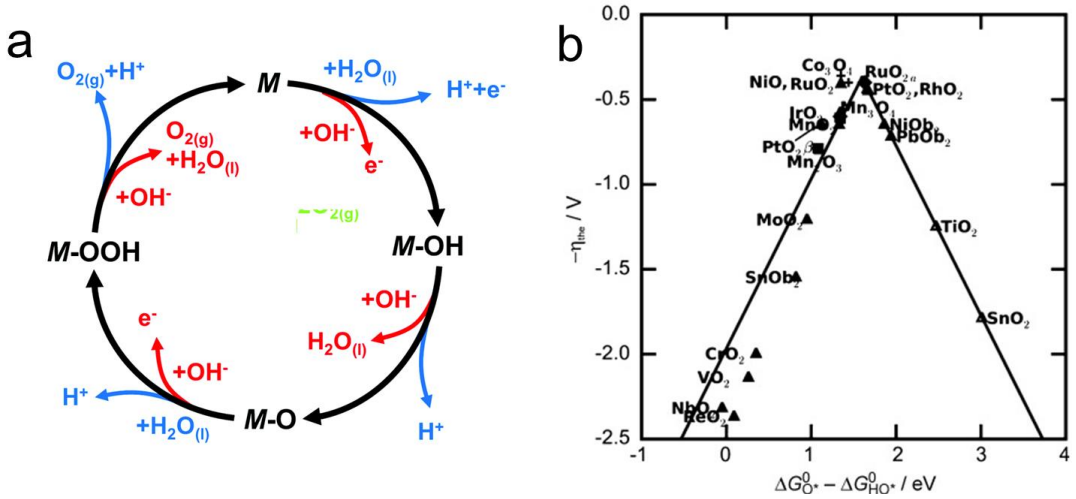


Figure 1. 3 (a) Traditional WNA-OER mechanism in acidic medium (blue) and alkaline medium (red).[24] Copyright © 2017, Royal Society of Chemistry. (b) Activity trends towards oxygen evolution of a wide variety of metal oxides.[19] Copyright © 2011, John Wiley and Sons

It should be noted that except for WNA mechanism, a certain number of catalysts operate through a lattice-oxygen-mediated mechanism (LOM).[25-29] During this process, two neighboring oxo species (*O) are formed after the protonation of *OH on the active site. One O locates on the outermost surface while another O bridges two neighboring metal sites. Then, instead of formation of *OOH through nucleophilic attack by the H_2O/OH^- species from the electrolyte, two oxo species couple directly and then O_2 is released. Exposed metal centers are filled by new OH^- immediately from the electrolyte. Single cycle of oxygen evolution is completed and new cycles starts to continue. Due to the lack of *OOH formation, the scaling relationship is no longer the dominant mechanism of OER. The binding energy of *OH and *O are possibly close to optimal. It should be noted that the prerequisite of oxo species tending to couple with each other is their considerable spin density, which is heavily sensitive to ligand environment.[29]

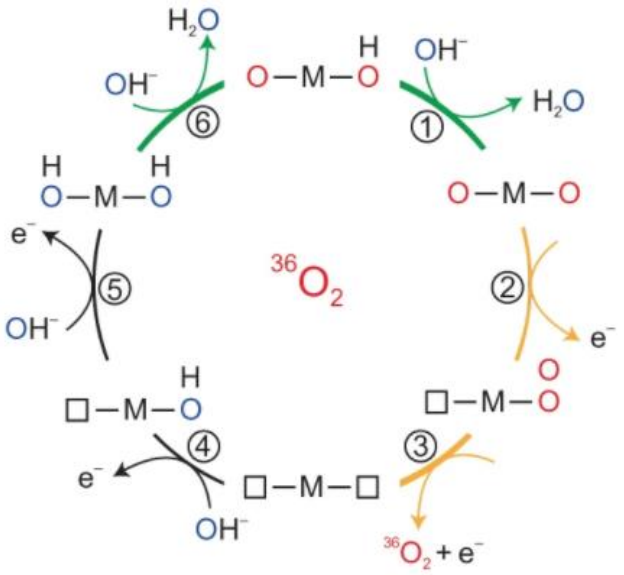


Figure 1. 4 Schematic illustration of the LOM-OER mechanism in alkaline condition.[26] Copyright © 2017, Springer Nature

1.3 Metal oxides/hydroxides for Hydrogen Evolution Reaction

Currently, the benchmark of electrochemical hydrogen evolution is platinum.[30] Optimal H adsorption energy and desorption energy render it most close to the peak in the volcano plot, presenting the highest intrinsic activity towards HER. However, its scarcity and high cost impede the large-scale application, which is an expected solution to resolve global energy demand.[31] Developing electrocatalysts with both excellent performance and cost-efficiency is highly urgent. To this end, there has been two different routes. The first one is directly developing non noble alternatives with comparable activity to Pt such as transition metal oxides (TMOs),[32-34] dichalcogenides (TMDs),[35-37] phosphides (TMPs),[38, 39] carbides (TMCs),[40, 41] nitrides (TMNs)[42-44] and metal alloys[45, 46]. These kinds of materials are cheap but of inferior intrinsic activity that need electronic structure regulation or composite fabrication. Another approach is designing supported catalysts by significantly reducing noble metal loading as compared to the commercial Pt/C, which contains 20 wt% Pt loading. Ultrasmall nanoparticles, clusters and even single atoms have widely been investigated, which can maximize the atomic utilization to boost activity and lower the cost.

Metal oxides with diverse composition, structure and cation oxidation state are substantially applied in various fields, especially in the catalysis regime.[47-49] Reactions such as the oxygen evolution/reduction or CO_2 reduction commonly take place on the surface of metal oxide/hydroxides.[50, 51] Whereas TMOs are considered as poor active HER materials due to weak interaction with hydrogen. Difficult adsorption of protons on the active sites seriously prohibits the HER. To address this issue, numerous strategies have been developed, including defect-engineering, hierarchical structure and electronic structure optimization.[49]

1.3.1 Simple metal oxides

The HER activity of simple metal oxides is restricted by the pH, since different mechanism controls the reaction under acidic or alkaline medium. For the acidic condition, transition metal Ti, Mo, W oxide group is often used because of its good endurability under such harsh environment. In this context, oxygen-deficient $WO_{2.9}$ shows η_{10} (overpotential at 10 mA $cm^{-2}_{geo.}$) of 70 mV and Tafel slope of 50 mV dec^{-1}. Enhanced activity is originated from tailored electronic structure of exposed W due to local ordered defect structure.[52] Similar strategy was implemented by Zheng *et al.* to design the degenerate semiconductor, exfoliated WO_3, which show high conductivity and desirable hydrogen adsorption free energy. Liquid exfoliation created oxygen vacancies introduce gap states in WO_3, modulating its electronic structure and boosting the HER performance.[53] In addition to WO_3, P doped MoO_{3-x} nanosheets not only show η_{10} of 166 mV in acidic solution, it also exhibited good stability in a wide range of pH (0.5 M H_2SO_4, 0.5 M Na_2SO_4, 0.1M NaOH). Synergistic effect of doped P and oxygen vacancies contribute to the superior performance.[54] Lattice defect can also be created by incorporation of hetero S atoms into MoO_2, which enhance the charge transfer further enhancing HER activity.[55] Doping of Mo within $W_{18}O_{49}$ matrix can increase the number of active sites and optimize hydrogen adsorption energy. Combined with promoted electron transport, small onset potential and Tafel slope were obtained.[56]

Proper amount Mo atoms in MoO_2 replaced by Ni atoms can cause electron deficiency on neighboring O, which improves proton adsorption and increase surface hydrogen coverage.[57] Both metal cation doping methods increase active sites that accelerate HER.

The alkaline medium is more friendly to many groups of transition metal oxides in contrast to acidic medium, whereas slow kinetic due to H_2O dissociation and H adsorption remains a great challenge. To overcome this difficult, Qiao's group introduced tensile strain on the outermost surface of Co oxide nanorods that aim to facilitate water dissociation and optimize hydrogen adsorption. Large numbers of oxygen vacancies were generated and the electronic structure was modified.[58] Substitution of oxygen by other anion (fluorine or sulfur) can redistribute electron cloud of neighboring Co or result in disordered structure on Co oxides, facilitating water dissociation and improve HER activity.[59, 60] Apart from anion doping, cation incorporation plays a different role in improving HER activity in alkaline condition. For example, in Ni, Zn co-doped Co oxide, Ni dopants segregated at surface oxygen vacancy that act as hydrogen intermediate binding sites; meanwhile Zn dopants embedded into bulk Co oxide boost the electric conductivity. Synthesized Ni, Zn co-doping CoO nanorods only require 53 mV overpotential to reach 10 mA cm^{-2}.[61] Introducing Zr into spinel $CoFe_2O_4$ not only increase active sites by tuning morphology but also change the electronic structure around Co, Fe. Ternary ZrCoFe oxide exhibit unprecedented HER activity of η_{10} = 104 mV.[62] For those metal (oxy)hydroxide with intrinsic poor HER activity, the incorporated cation itself serve as active sites. Ru doped NiFe LDH and Ir doped NiCo LDH display excellent HER performance with η_{10} = 29 mV and 21 mV, respectively.[63, 64]

1.3.2 Metal (hydro)oxides supported catalyst

The basic principle of fabricating supported catalysts fabrication is to introduce HER active species such as noble metal or sulfides onto (hydro)oxide surface. For example, in acidic condition, Pt is the most frequently used active species. Metallic Pt^0 clusters

anchored on the surface of WO_3 act as active sites towards HER. In-situ electrochemical phase transition of WO_3 to H_xWO_3 give rise to fast electron/hydrogen transportation that contribute to excellent HER activity.[65] In Jiang's work, Pt nanoparticles were confined by MoO_2-porous carbon with a low loading of 8.32 wt%. MoO_2 interacted with Pt resulting in thermal-neutral hydrogen adsorption energy which improve the intrinsic activity of Pt. 11-times higher mass activity than commercial Pt/C was achieved.[66] Besides Pt, CuS was combined with $NiCo_2O_4$ to fabricate non-Pt catalysts. It shows excellent durability in acidic aqueous solution as long as 50 h and onset overpotential of 31.1 mV.[67]

In alkaline condition, noble metals are still the first choice. Ultrathin platinum nanowires grown on single layer $Ni(OH)_2$ is expected to take the advantage of high specific surface area of two dimensional nanosheets. Strong interaction between Pt and $Ni(OH)_2$ facilitate charge transport and stabilized the active species during electrochemical reaction. It presents 4-5 times higher activity than commercial Pt/C.[68] Dong *et al.* fabricated subnano-sized Ru species on SnO_2 surface by micro-etching techniques. The valence state of Ru species was demonstrated lower than Ru(III), which coupled with SnO_2 resulting in optimal hydrogen binding energy.[69] Slightly cheaper Ag nanodots are also decorated onto porous Cu_2O for HER catalysis. Plenty of active sites, fast mass transportation, and synergistic effect between Ag and Cu_2O and Cu substrate give rise to η_{10} of 108 mV and Tafel slope of 58 mV dec^{-1}.[70]

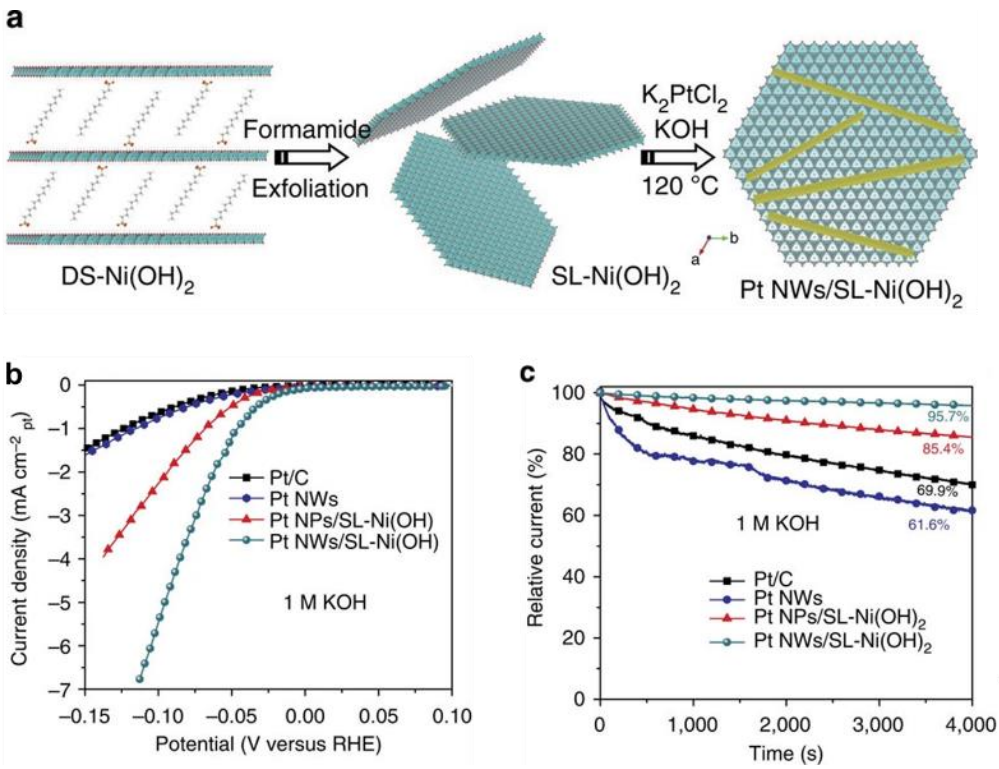


Figure 1. 5 (a) Scheme for synthesis of Pt NWs/SL-Ni(OH)$_2$, (b) HER activity of Pt NWs/SL-Ni(OH)$_2$, Pt NPs/SL-Ni(OH)$_2$, pure Pt NWs and commercial Pt/C (20 wt%) in 1 M KOH at room temperature, (c) current-time chronoamperometric responses for HER at Pt NWs/SL-Ni(OH)$_2$, Pt NPs/SL-Ni(OH)$_2$ Pt NWs and commercial Pt/C (20 wt%) electrodes in 1 M KOH solution.[68] Copyright © 2015, Springer Nature

1.4 Metal oxides/hydroxides for Oxygen Evolution Reaction

In the past decades, a wide range classes of OER electrocatalysts have been designed and studied. Precious metals and its relevant oxides – ruthenium, ruthenium dioxide, iridium and iridium oxide are the star catalysts which present the highest, acceptable efficiency in OER process.[71, 72] The normal crystalline structure of ruthenium and iridium dioxide are classified in rutile-type, with electronic configuration of ruthenium $4d^7 5s^1$ and iridium $5d^7 6s^2$. RuO_2 has in metallic characteristics, showing a resistivity of 35.2 ± 0.5 μΩ·cm at room temperature.[73] Such high electronic conductivity and unique electronic configuration of RuO_2 render it a most active electrocatalyst towards OER. Reier *et al.* conducted a comparative investigation of carbon supported precious metal

of bulk materials and nanoparticles.[71] The intrinsic OER activities for them are Ru > Ir > Pt. To reveal the true OER activities of Ru and Ir oxides nanoparticles, Lee *et al.* performed a systematical study of Rutile RuO_2 and IrO_2. Nanoparticles with diameter of ~ 6 nm have been synthesized and electrochemically examined in acid and alkaline solution.[74] RuO_2 nanoparticle exhibits slightly higher intrinsic and mass OER activities than IrO_2. These two nanoparticles show higher stability than commercial Ru/C and Ir/C catalyst. Besides the size effect, crystallographic orientation is another factor essential to catalytic activity. The (100) surface of IrO_2 and RuO_2 have been demonstrated more active in alkaline solution than the most thermodynamically stable (110) surface. The OER activity is fairly dependent on the density of coordinatively undersaturated metal sites of each crystallographic facet.[75]

Despite the highly intrinsic acidity of RuO_2 and IrO_2, the problems of scarcity of precious metal and solubility of ruthenium oxide severely impede the further scalable industrial production. In terms of cost, both RuO_2 and IrO_2 are one of the scarcest metals in the earth's crust and are typically as side products during Pt or Ni mining.[31] They are also unstable at high anodic potential, suffered from oxidation to high valence and then dissolved in solution.[76-78] Easy corrosion under anodic oxidized potential has drew serious concerns on the stability, especially in practical application. In this context, substantial interest has been paid to explore new types of catalysts with high efficiency and low cost.

In acidic condition, most transition metal oxide are not stable because of the dissolution of metal atoms. The OER performance of crystalline cobalt oxide films with relatively slow corrosion rate has been studied in 0.5 M H_2SO_4. Although 570 mV overpotential is required to afford 10 mA cm^{-2} current density, near-quantitative Faradaic yields was maintained as long as 12h.[79] This catalyst along with manganese oxide (MnO_x) providing possibility to employ earth abundant metal oxide towards acidic OER.[80, 81]

Recently a great progress was made by Mascaros's group with Co based polyoxometalate showing both excellent activity and stability in strong acidic media.[82] Both Cs and Ba cation countered polyoxometalates show superior OER activity over reference IrO_2. The best catalyst 40% Ba[Co-POM], an overpotential of only 189 mV is required for 1 mA cm^{-2}. Chronoamperometric test show that after 24 h reaction, Ba[Co-POM] still exhibit ten times higher current density than IrO_2.

In alkaline conditions, replacing expensive and scarce precious metals by common transition metals is feasible and attractive. Transition metal oxides are a great family with distinct performance determined by their electronic configuration. Single oxides[83-85] (Co, Mn, oxides), layer single hydroxides[86, 87] (Ni/$Co(OH)_2$, Ni/CoOOH), layered double oxides[88, 89] (NiFe LDH, NiCo LDH), and the perovskite[90, 91] ($Ba_{0.5}Sr_{0.5}Co_{0.8}Fe_{0.2}O_{3-\delta}$) are all selected for electrocatalysis reaction of oxygen evolution. In the following, extensive (hydro)oxides catalysts will be collected and summarized.

1.4.1 Layered metal oxide

Layered metal oxides are a great family with tunable properties and abundant diversity of chemical compositions and crystal structures.[92-95] Two-dimensional (2D) layers with atomic/molecular thickness are stacked in layer-by-layer form. The host layers typically composed of edge/corner sharing octahedral MO_6 subunits based on Ti, Mn, Nb, Mo, W etc., showing active redox activity. Layered metal oxides are ideally feasible for electrochemical reactions due to their high specific surface area and unique electronic structure. To date, considerable attentions have been paid on such material but they are still far from being fully explored.

Manganese oxides have a long history in functioning as an OER catalyst under alkaline conditions, because of its abundance, non-toxic nature, multiple valence states and structural diversity.[96-99] Among the manganese oxide polymorphs, δ-MnO_2 (Birnessite)

present a typical layered form. Negative charged Mn-O host layer pack along the c axis, with positively charged alkali cations (Na^+, K^+, Cs^+ *etc.*) inserted in the interlayer gallery. Multivalence is another feature of Birnessite, Mn (II), Mn (III) and Mn (IV) substitute with each contributing to the complex electronic structure. High spin Mn (III) with d^4 electronic structure where one unit electron filling the e_g orbital, has always been considered as the active sites for electrocatalysis of water.[100-102] However, compared with those most active non-precious metal oxides like Ni, Fe, Co and its (oxy)hydroxide relatives, Birnessite exhibits moderate electrocatalytic activity in water oxidation, with overpotential labeled in the range of 500-800 mV at current density of 10 mA cm^{-2}.[103] To improve this plight, Zhao *et al.* introduced defects into Birnessite nanosheet arrays which grow on Ni foam substrate. Defects give rise to semiconductor-half metallic transformation that significantly enhance the conductivity. Abundant oxygen vacancies increase the percentage of Mn^{3+}, enhancing H_2O adsorption.[104]

Other layered transition metal oxides have been largely explored.[105, 106] Through electrochemical delithiation of layered $LiNiO_2$, Ni-rich surface transform to NiOOH, lead to a large fraction of surface exposed.[107] It improves the electron transfer rate from the solution, enriching $LiNiO_2$ with lithium vacancies that can optimize the electronic structure of surface NiOOH. After deprotonation, OER active NiOO* species with higher Ni valence state are formed and stabilized, giving rise to superior OER activity. Unusually short O–O separation is demonstrated in layered oxide $Na_{0.67}CoO_2$ that favors the formation of peroxide ions *via* O^-– O^- interactions. O_2 can be produced directly through the O-O combination (LOM mechanism) instead of conventional WNA mechanism. Combined with the strong hybridization of O-2p band and low spin Co(III)/Co(IV) state, the catalysts show better OER activity than IrO_2 reference.[108]

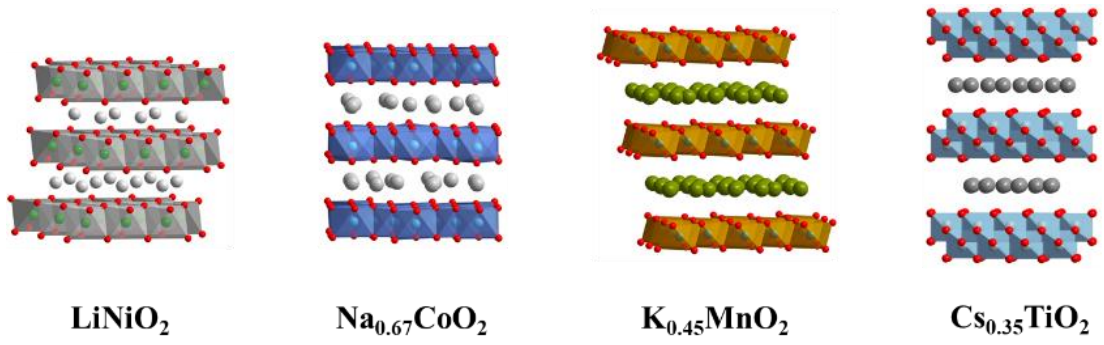


Figure 1. 6 Crystal structures of typical layered metal oxides.

1.4.2 Layered double hydroxides (LDHs)

Layered double hydroxides are a class of two-dimensional (2D) material consisting of metal hydroxide layers and inorganic/organic gallery anions/molecules.[109] The general formula of LDHs is $[M^{2+}_{1-x}M^{3+}_{x}(OH)_2]^{x+}(A^{n-})_{x/n}\cdot mH_2O$, M^{2+} = Mn, Fe, Co, Al, Cu, Zn etc., M^{3+} = Al, Ga, Ti, Cr, Fe, Co *etc.* A^{n-} is a charge-balancing anion intercalated between the brucite-like metal hydroxide layers, e.g. CO_3^{2-}, Cl^-, SO_4^{2-}, RCO^{-2}, the x is normal between 0.2-0.4. Such layered materials can be directly exfoliated into multi-layer or single layer sheets by soft exchange chemistry. Anions or water molecules intercalated in the interlayer are exchangeable. The two-dimensional structure feature, coexisting dual metal cations in the host layer, high specific surface area, tunable electronic structure, and inexpensive cost make LDHs the most promising catalyst for OER in basic condition.[105, 110, 111] Plenty of strategies can be carried out for catalyst design. For example, (I) intercalation of expected anions between the interlayer spacing; (II) tuning the distance of interlayer; (III) doping exotic element in the host layer; (IV) exfoliating into single/few layers; (V) constructing superlattice/composites with other two-dimensional layers. However, the LDHs suffer from some drawbacks such as inferior electrical conductivity, low efficiency in exploiting active sites, and weak combination with the electrodes. Substantial efforts have been made to tackle the issues that improve the OER activity.[112-116]

Regarding the insufficient conductivity of LDH, Dai's group introduced carbon

nanotubes (CNTs) as support where ultrathin NiFe-LDH directly grew on. Interaction between them enhancing electron transport, resulted in improved OER activity as compared to bare NiFe-LDH.[117] Compared to one dimensional CNTs, reduced graphene oxide (rGO) with two dimensional form can be matched with LDH in layer-by-layer mode. Long *et al.*[113] and Ma *et al.*[118] separately reported that NiFe-LDH-rGO hybrid/superlattice boosted OER activity of η_{10} = 195 mV and 230 mV in 1M KOH, respectively. Electrostatic attraction tightly binding the LDH layers and rGO layers, lead to strong synergetic reaction between them. Fast electron transport from rGO maximumly exploit the catalytic activity of NiFe-LDH. Beyond that, NiFe LDH/rGO superlattice in Ma's work also exhibited considerable HER activity. In alkaline electrolyte, one 1.5 V AA battery can drive the electrolytic cell for total splitting of water. Likewise, various LDHs have been employed to couple with rGO or graphene derivates. For instance, CoAl-LDH nanosheets on 3D graphene network,[119] NiMn-LDH nanosheets with graphene,[120] and NiFe-LDH nanosheet with defective graphene.[121] All of these composite catalysts showed excellent performance as a result of synergetic effect between the LDHs and graphene.

Beside coupling with conductive materials, exfoliation of bulk LDHs into ultrathin nanosheets can increase exposed active sites and conductivity. Song and Hu thoroughly studied the OER activity of exfoliated Co-Co, Ni-Co, Ni-Fe LDHs single-layer nanosheets with comparison to their bulk phase.[89] All the nanosheets showed superior performance than their parent phase. Increased number of active sites at the edge and defect that originated from exfoliation mainly contribute to OER improvement. Different to wet chemistry exfoliation, Wang's group developed Ar plasma technique to delaminate bulk LDHs in dry environment.[122] Plasma etching break the bond of bulk material, facilitating surface atoms escaping from the lattice. Exfoliated nanosheets enrich with vacancies and defects, tuning the surface electronic structure, decreasing the coordination numbers and increasing the disorder in nanosheets. In this way, ultrathin exfoliated CoFe-LDH nanosheets with multiple vacancies (including O, Co,

and Fe vacancies) show significantly improve OER activity of η_{10} = 266 mV.

Since LDHs layers consist of two different cations, manipulating cations with regard to the type, content and valence state is a feasible way to tailor the electronic structure of active centers. Yang *et al.* studied the synergetic effect of Co, Fe in LDH matrix by varying Fe percentage, suggesting the optimal value of 35 at%.[123] Further comparison of the effect of trivalence Al and Fe on catalytic activity show that Al^{3+} suppressed the OER activity whereas the Fe^{3+} enhanced the activity. In another work, high spin Fe(IV) with d^4 electrons leads to efficient formation of an active O radical intermediate, synergistically coupled with the closed shell d^6 Ni(IV) to catalyze the subsequent O-O combination. Such cooperation between the coexisted metal delivers the optimal OER performance.[124]

Cations were not merely limited in two elements, introducing a third part further strengthened the synergetic cooperation among cations. Cr was incorporated into NiFe-LDH by Jin's group aiming to tune electronic structure.[125] The molar ratio Ni:Fe:Cr = 6:2:1 exhibited the optimal intrinsic catalytic activity, achieving a current density of 25 mA cm^{-2} only at the 225 mV overpotential. Likewise, Zhou *et al.* synthesized ternary NiCoFe-layered double hydroxide, which further combined with the nitrogen-doped graphene oxide *via* in-situ growth route.[126] In 0.1 M KOH media, tri-cations catalyst present ultralow onset overpotential of 180 mV. In addition to the prominent OER activity, this composite also exhibited excellent ORR performance. Onset potential of 0.88 V was achieved, fundamentally due to the dispersion of Co(III) into NiFe layers. High valence state Co, N doped graphene and the highly exposed Ni, Fe active sites together contribute to the excellent bifunction of the oxygen reaction. Doping with Ir^{4+} opened the window for bifunctional water splitting catalysis. In 1 M KOH electrolyte, the Ir-NiFe LDH only requires an overpotential of 200 mV for OER and 34 mV for HER at 10 mA cm^{-2}, respectively. This rational strategy addressed the issue of poor HER activity of LDHs, facilitating the adsorption of proton that rendered it Pt-like

performance.[127] A small potential of 1.41 V is sufficient to drive the water splitting and can maintain a relatively stable at 20 mA cm^{-2} for more than 50 h.

1.4.3 Cation modified metal oxide/hydroxide

In this section, we focus on cation modification in following two aspects: cations intercalation within the interlayer gallery and cation decoration on the outer surface. These two routes are different to the doping of foreign elements into the layer matrix that lead to interesting phenomenon or enriching the functions of the pristine material. Ni was selected as the intercalation cations to layered manganese oxide.[128] Firstly, a $[Ni(N_2H_2)_x(H_2O)_y]^{2+}$ complex was prepared by reacting of the aqueous cation with hydrazine. Small amounts of the cation-hydrazine complexes were inserted *via* ion exchange protocol. Negatively shifted pre-OER redox of $Ni^{2+/3+}$ suggested changed electronic structure of Ni. Intercalated Ni complex exhibited an overpotential of 400 mV to reach anodic current density of 10 mA cm^{-2}. Combined with theoretical calculation, enhanced OER activity can be attributed to confined environment and orientational ordering of interlayer H_2O. This strategy was applied to other transition metal such as Co and Cu.[129, 130] Moreover, Strongin's group studied Co intercalated NiFe-LDH for OER by experimental and theoretical combination.[84] Introduction of Co tunes the electronic structure of NiFe-LDH so that the optimal binding energy of OER reaction intermediates could be achieved. Co modified NiFe LDH exhibit the best activity, requiring overpotential of 265 mV at 10 mA cm^{-2}. In another work molybdate was intercalated between the interlayer of NiFe-LDH.[112] Four times higher density of electrochemically active sites gives rise to boosting OER current density that is three times higher than regular NiFe-LDH. Highly active catalytic performance is companied by remarkable durability at different current density levels.

OER inactive Au single atoms was decorated on the surface of NiFe-LDH.[131] Six-fold OER activity enhancement was obtained at an overpotential of 208 mV. Theoretical and experimental results uncovered the activity origin of Au@NiFe-LDH: Fe atoms are

active sites in NiFe marix during OER catalysis, the decoration of Au atoms on the surface can transfer electrons from Au to LDH, changing surrounding environment of Fe thus improves the activity. OER active Ru single atoms was also anchored on the surface of CoFe-LDH.[132] The Ru oxidation state in as-synthesized catalyst is only 1.6+, while the operando X-ray absorption spectroscopy showed that the Ru atoms kept oxidation states of 4+ at OER anodic potential. Theoretical calculation reveals the strong electronic coupling between Ru and CoFe-LDH.

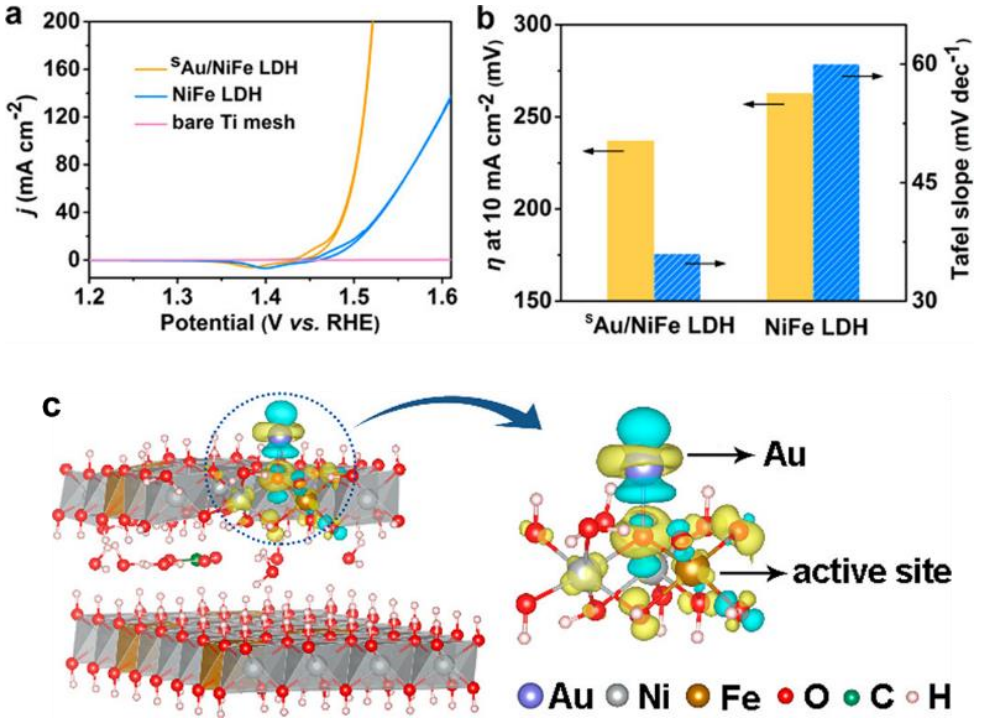


Figure 1. 7 (a) Cyclic voltammetry (CV) curves of Au/NiFe LDH, pure NiFe LDH and bare Ti mesh in 1 M KOH. (b) Overpotential (η) at 10 mA cm^{-2} (left) and Tafel slope (right) for sAu/NiFe LDH and pure NiFe LDH. (c) Differential charge densities of NiFe LDH with and without Au atom.[131] Copyright © 2018, American Chemical Society

References

1. Z. Wei, J. Sun, Y. Li, A. K. Datye and Y. Wang, *Chemical Society Reviews*, 2012, **41**, 7994-8008.
2. Y. Pu, Q. Chen, Z. Sun, P. Rodriguez and L. Huang, *Crystal Growth & Design*, 2019, **19**, 3298-3304.
3. Y. Pu, M. J. Lawrence, V. Celorrio, Q. Wang, M. Gu, Z. Sun, L. A. Jácome, A. E. Russell, L. Huang and P. Rodriguez, *Journal of Materials Chemistry A*, 2020, **8**, 13340-13350.
4. Y. Pu, V. Celorrio, J. M. Stockmann, O. Sobol, Z. Sun, W. Wang, M. J. Lawrence, J. Radnik, A. E. Russell, V.-D. Hodoroaba, L. Huang and P. Rodriguez, *Journal of catalysis*, 2021, **396**, 304-314.
5. S. Chu, Y. Cui and N. Liu, *Nature Materials*, 2017, **16**, 16-22.
6. Z. W. Seh, J. Kibsgaard, C. F. Dickens, I. Chorkendorff, J. K. Nørskov and T. F. Jaramillo, *Science*, 2017, **355**, eaad4998.
7. J. H. Montoya, L. C. Seitz, P. Chakthranont, A. Vojvodic, T. F. Jaramillo and J. K. Nørskov, *Nature Materials*, 2017, **16**, 70-81.
8. V. R. Stamenkovic, D. Strmcnik, P. P. Lopes and N. M. Markovic, *Nature Materials*, 2017, **16**, 57-69.
9. L. Li, P. Wang, Q. Shao and X. Huang, *Chemical Society Reviews*, 2020.
10. H. A. Gasteiger and N. M. Marković, *Science*, 2009, **324**, 48-49.
11. J. Hwang, R. R. Rao, L. Giordano, Y. Katayama, Y. Yu and Y. Shao-Horn, *Science*, 2017, **358**, 751.
12. J. Kibsgaard and I. Chorkendorff, *Nature Energy*, 2019, **4**, 430-433.
13. J. Zhu, L. Hu, P. Zhao, L. Y. S. Lee and K.-Y. Wong, *Chemical Reviews*, 2020, **120**, 851-918.
14. X. Tian, P. Zhao and W. Sheng, *Advanced Materials*, 2019, **31**, 1808066.
15. N. Eliaz and E. Gileadi, *Physical Electrochemistry: Fundamentals, Techniques, and Applications*, John Wiley & Sons, 2019.
16. I. Ledezma-Yanez, W. D. Z. Wallace, P. Sebastián-Pascual, V. Climent, J. M. Feliu and M. T. M. Koper, *Nature Energy*, 2017, **2**, 17031.
17. H. Dau, C. Limberg, T. Reier, M. Risch, S. Roggan and P. Strasser, *ChemCatChem*, 2010, **2**, 724-761.
18. I. C. Man, H.-Y. Su, F. Calle-Vallejo, H. A. Hansen, J. I. Martínez, N. G. Inoglu, J. Kitchin, T. F. Jaramillo, J. K. Nørskov and J. Rossmeisl, *ChemCatChem*, 2011, **3**, 1159-1165.
19. I. C. Man, H. Y. Su, F. Calle-Vallejo, H. A. Hansen, J. I. Martinez, N. G. Inoglu, J. Kitchin, T. F. Jaramillo, J. K. Nørskov and J. Rossmeisl, *ChemCatChem*, 2011, **3**, 1159-1165.
20. R. L. Doyle and M. E. Lyons, in *Photoelectrochemical solar fuel production*, Springer, 2016, pp. 41-104.
21. M. S. Burke, M. G. Kast, L. Trotochaud, A. M. Smith and S. W. Boettcher, *Journal of the American Chemical Society*, 2015, **137**, 3638-3648.
22. Y. Surendranath, M. W. Kanan and D. G. Nocera, *Journal of the American Chemical Society*, 2010, **132**, 16501-16509.
23. Z. Xu, J. Rossmeisl and J. R. Kitchin, *The Journal of Physical Chemistry C*, 2015, **119**, 4827-4833.
24. N.-T. Suen, S.-F. Hung, Q. Quan, N. Zhang, Y.-J. Xu and H. M. Chen, *Chemical Society Reviews*, 2017, **46**, 337-365.
25. J. T. Mefford, X. Rong, A. M. Abakumov, W. G. Hardin, S. Dai, A. M. Kolpak, K. P. Johnston and K. J. Stevenson, *Nature communications*, 2016, **7**, 11053.
26. A. Grimaud, O. Diaz-Morales, B. Han, W. T. Hong, Y.-L. Lee, L. Giordano, K. A. Stoerzinger, M.

T. M. Koper and Y. Shao-Horn, *Nature Chemistry*, 2017, **9**, 457-465.
27. S. Geiger, O. Kasian, M. Ledendecker, E. Pizzutilo, A. M. Mingers, W. T. Fu, O. Diaz-Morales, Z. Li, T. Oellers, L. Fruchter, A. Ludwig, K. J. J. Mayrhofer, M. T. M. Koper and S. Cherevko, *Nature Catalysis*, 2018, **1**, 508-515.
28. X. Rong, J. Parolin and A. M. Kolpak, *ACS Catalysis*, 2016, **6**, 1153-1158.
29. J. Hessels, R. J. Detz, M. T. M. Koper and J. N. H. Reek, *Chemistry – A European Journal*, 2017, **23**, 16413-16418.
30. W. Sheng, H. A. Gasteiger and Y. Shao-Horn, *Journal of The Electrochemical Society*, 2010, **157**, B1529.
31. P. C. K. Vesborg and T. F. Jaramillo, *Rsc Advances*, 2012, **2**, 7933-7947.
32. T. Zhang, M.-Y. Wu, D.-Y. Yan, J. Mao, H. Liu, W.-B. Hu, X.-W. Du, T. Ling and S.-Z. Qiao, *Nano Energy*, 2018, **43**, 103-109.
33. R. S. Datta, F. Haque, M. Mohiuddin, B. J. Carey, N. Syed, A. Zavabeti, B. Zhang, H. Khan, K. J. Berean, J. Z. Ou, N. Mahmood, T. Daeneke and K. Kalantar-zadeh, *Journal of Materials Chemistry A*, 2017, **5**, 24223-24231.
34. Z. Li, Y. Feng, Y.-L. Liang, C.-Q. Cheng, C.-K. Dong, H. Liu and X.-W. Du, *Advanced Materials*, 2020, **32**, 1908521.
35. D. Voiry, H. Yamaguchi, J. Li, R. Silva, D. C. B. Alves, T. Fujita, M. Chen, T. Asefa, V. B. Shenoy, G. Eda and M. Chhowalla, *Nature Materials*, 2013, **12**, 850-855.
36. Y. Kim, D. H. K. Jackson, D. Lee, M. Choi, T.-W. Kim, S.-Y. Jeong, H.-J. Chae, H. W. Kim, N. Park, H. Chang, T. F. Kuech and H. J. Kim, *Advanced Functional Materials*, 2017, **27**, 1701825.
37. J.-X. Feng, J.-Q. Wu, Y.-X. Tong and G.-R. Li, *Journal of the American Chemical Society*, 2018, **140**, 610-617.
38. D. Y. Chung, S. W. Jun, G. Yoon, H. Kim, J. M. Yoo, K.-S. Lee, T. Kim, H. Shin, A. K. Sinha, S. G. Kwon, K. Kang, T. Hyeon and Y.-E. Sung, *Journal of the American Chemical Society*, 2017, **139**, 6669-6674.
39. A.-L. Wang, J. Lin, H. Xu, Y.-X. Tong and G.-R. Li, *Journal of Materials Chemistry A*, 2016, **4**, 16992-16999.
40. H. Fei, J. Dong, C. Wan, Z. Zhao, X. Xu, Z. Lin, Y. Wang, H. Liu, K. Zang, J. Luo, S. Zhao, W. Hu, W. Yan, I. Shakir, Y. Huang and X. Duan, *Advanced Materials*, 2018, **30**, 1802146.
41. H. Ang, H. Wang, B. Li, Y. Zong, X. Wang and Q. Yan, *Small*, 2016, **12**, 2859-2865.
42. B. Zhang, L. Zhang, Q. Tan, J. Wang, J. Liu, H. Wan, L. Miao and J. Jiang, *Energy & Environmental Science*, 2020, **13**, 3007-3013.
43. W.-F. Chen, K. Sasaki, C. Ma, A. I. Frenkel, N. Marinkovic, J. T. Muckerman, Y. Zhu and R. R. Adzic, *Angewandte Chemie International Edition*, 2012, **51**, 6131-6135.
44. H. Jin, Q. Gu, B. Chen, C. Tang, Y. Zheng, H. Zhang, M. Jaroniec and S.-Z. Qiao, *Chem*, 2020, **6**, 2382-2394.
45. X. Tan, S. Geng, Y. Ji, Q. Shao, T. Zhu, P. Wang, Y. Li and X. Huang, *Advanced Materials*, 2020, **32**, 2002857.
46. J. Mao, C.-T. He, J. Pei, W. Chen, D. He, Y. He, Z. Zhuang, C. Chen, Q. Peng, D. Wang and Y. Li, *Nature communications*, 2018, **9**, 4958.
47. Y. Wang, J. Li and Z. Wei, *Journal of Materials Chemistry A*, 2018, **6**, 8194-8209.
48. D. A. Kuznetsov, B. Han, Y. Yu, R. R. Rao, J. Hwang, Y. Román-Leshkov and Y. Shao-Horn, *Joule*, 2018, **2**, 225-244.

49. Y. Zhu, Q. Lin, Y. Zhong, H. A. Tahini, Z. Shao and H. Wang, *Energy & Environmental Science*, 2020, **13**, 3361-3392.
50. A. Ruiz Puigdollers, P. Schlexer, S. Tosoni and G. Pacchioni, *ACS Catalysis*, 2017, **7**, 6493-6513.
51. Y. J. Sa, C. W. Lee, S. Y. Lee, J. Na, U. Lee and Y. J. Hwang, *Chemical Society Reviews*, 2020, **49**, 6632-6665.
52. Y. H. Li, P. F. Liu, L. F. Pan, H. F. Wang, Z. Z. Yang, L. R. Zheng, P. Hu, H. J. Zhao, L. Gu and H. G. Yang, *Nature communications*, 2015, **6**, 8064.
53. T. Zheng, W. Sang, Z. He, Q. Wei, B. Chen, H. Li, C. Cao, R. Huang, X. Yan, B. Pan, S. Zhou and J. Zeng, *Nano Letters*, 2017, **17**, 7968-7973.
54. L. Li, T. Zhang, J. Yan, X. Cai and S. Liu, *Small*, 2017, **13**, 1700441.
55. S. Geng, Y. Liu, Y. S. Yu, W. Yang and H. Li, *Nano Research*, 2020, **13**, 121-126.
56. X. Zhong, Y. Sun, X. Chen, G. Zhuang, X. Li and J.-G. Wang, *Advanced Functional Materials*, 2016, **26**, 5778-5786.
57. H. Zeng, S. Chen, Y. Q. Jin, J. Li, J. Song, Z. Le, G. Liang, H. Zhang, F. Xie, J. Chen, Y. Jin, X. Chen and H. Meng, *ACS Energy Letters*, 2020, **5**, 1908-1915.
58. T. Ling, D.-Y. Yan, H. Wang, Y. Jiao, Z. Hu, Y. Zheng, L. Zheng, J. Mao, H. Liu, X.-W. Du, M. Jaroniec and S.-Z. Qiao, *Nature communications*, 2017, **8**, 1509.
59. C. Zhong, Z. Han, T. Wang, Q. Wang, Z. Shen, Q. Zhou, J. Wang, S. Zhang, X. Jin, S. Li, P. Wang, D. Gao, Y. Zhou and H. Zhang, *Journal of Materials Chemistry A*, 2020, **8**, 10831-10838.
60. X. Yu, Z.-Y. Yu, X.-L. Zhang, P. Li, B. Sun, X. Gao, K. Yan, H. Liu, Y. Duan and M.-R. Gao, *Nano Energy*, 2020, 104652.
61. T. Ling, T. Zhang, B. Ge, L. Han, L. Zheng, F. Lin, Z. Xu, W.-B. Hu, X.-W. Du, K. Davey and S.-Z. Qiao, *Advanced Materials*, 2019, **31**, 1807771.
62. L. Huang, D. Chen, G. Luo, Y.-R. Lu, C. Chen, Y. Zou, C.-L. Dong, Y. Li and S. Wang, *Advanced Materials*, 2019, **31**, 1901439.
63. G. Chen, T. Wang, J. Zhang, P. Liu, H. Sun, X. Zhuang, M. Chen and X. Feng, *Advanced Materials*, 2018, **30**, 1706279.
64. R. Fan, Q. Mu, Z. Wei, Y. Peng and M. Shen, *Journal of Materials Chemistry A*, 2020, **8**, 9871-9881.
65. C. Xie, W. Chen, S. Du, D. Yan, Y. Zhang, J. Chen, B. Liu and S. Wang, *Nano Energy*, 2020, **71**, 104653.
66. Y. Jiang, M. Yang, M. Qu, Y. Wang, Z. Yang, Q. Feng, X. Deng, W. Shen, M. Li and R. He, *Journal of Materials Chemistry A*, 2020, **8**, 10409-10418.
67. L. An, L. Huang, P. Zhou, J. Yin, H. Liu and P. Xi, *Advanced Functional Materials*, 2015, **25**, 6814-6822.
68. H. Yin, S. Zhao, K. Zhao, A. Muqsit, H. Tang, L. Chang, H. Zhao, Y. Gao and Z. Tang, *Nature communications*, 2015, **6**, 6430.
69. W. Dong, Y. Zhang, J. Xu, J.-W. Yin, S. Nong, C. Dong, Z. Liu, B. Dong, L.-M. Liu, R. Si, M. Chen, J. Luo and F. Huang, *Cell Reports Physical Science*, 2020, **1**, 100026.
70. C. Song, Z. Zhao, X. Sun, Y. Zhou, Y. Wang and D. Wang, *Small*, 2019, **15**, 1804268.
71. T. Reier, M. Oezaslan and P. Strasser, *ACS Catalysis*, 2012, **2**, 1765-1772.
72. Y. Lee, J. Suntivich, K. J. May, E. E. Perry and Y. Shao-Horn, *The Journal of Physical Chemistry Letters*, 2012, **3**, 399-404.
73. W. Ryden, A. Lawson and C. Sartain, *Physics Letters A*, 1968, **26**, 209-210.

74. Y. Lee, J. Suntivich, K. J. May, E. E. Perry and Y. Shao-Horn, *J Phys Chem Lett*, 2012, **3**, 399-404.
75. K. A. Stoerzinger, L. Qiao, M. D. Biegalski and Y. Shao-Horn, *J Phys Chem Lett*, 2014, **5**, 1636-1641.
76. R. Kötz, H. Lewerenz and S. Stucki, *Journal of The Electrochemical Society*, 1983, **130**, 825-829.
77. E. Antolini, *ACS Catalysis*, 2014, **4**, 1426-1440.
78. O. Kasian, J.-P. Grote, S. Geiger, S. Cherevko and K. J. J. Mayrhofer, *Angewandte Chemie International Edition*, 2018, **57**, 2488-2491.
79. J. S. Mondschein, J. F. Callejas, C. G. Read, J. Y. C. Chen, C. F. Holder, C. K. Badding and R. E. Schaak, *Chemistry of Materials*, 2017, **29**, 950-957.
80. M. Huynh, D. K. Bediako and D. G. Nocera, *Journal of the American Chemical Society*, 2014, **136**, 6002-6010.
81. A. Li, H. Ooka, N. Bonnet, T. Hayashi, Y. Sun, Q. Jiang, C. Li, H. Han and R. Nakamura, *Angewandte Chemie International Edition*, 2019, **58**, 5054-5058.
82. M. Blasco-Ahicart, J. Soriano-López, J. J. Carbó, J. M. Poblet and J. R. Galan-Mascaros, *Nature Chemistry*, 2018, **10**, 24-30.
83. B. S. Yeo and A. T. Bell, *Journal of the American Chemical Society*, 2011, **133**, 5587-5593.
84. Q. Kang, L. Vernisse, R. C. Remsing, A. C. Thenuwara, S. L. Shumlas, I. G. McKendry, M. L. Klein, E. Borguet, M. J. Zdilla and D. R. Strongin, *J Am Chem Soc*, 2017, **139**, 1863-1870.
85. Y. Zhao, C. Chang, F. Teng, Y. Zhao, G. Chen, R. Shi, G. I. N. Waterhouse, W. Huang and T. Zhang, *Advanced Energy Materials*, 2017, **7**, 1700005.
86. J. Huang, J. Chen, T. Yao, J. He, S. Jiang, Z. Sun, Q. Liu, W. Cheng, F. Hu, Y. Jiang, Z. Pan and S. Wei, *Angewandte Chemie International Edition*, 2015, **54**, 8722-8727.
87. M. Gao, W. Sheng, Z. Zhuang, Q. Fang, S. Gu, J. Jiang and Y. Yan, *J Am Chem Soc*, 2014, **136**, 7077-7084.
88. F. Song and X. Hu, *J Am Chem Soc*, 2014, **136**, 16481-16484.
89. F. Song and X. Hu, *Nature communications*, 2014, **5**, 1-9.
90. J. Suntivich, K. J. May, H. A. Gasteiger, J. B. Goodenough and Y. Shao-Horn, *Science*, 2011, **334**, 1383-1385.
91. A. Vojvodic and J. K. Norskov, *Science*, 2011, **334**, 1355-1356.
92. V. Nicolosi, M. Chhowalla, M. G. Kanatzidis, M. S. Strano and J. N. Coleman, *Science*, 2013, **340**, 1226419.
93. X. Zhang and Y. Xie, *Chemical Society Reviews*, 2013, **42**, 8187-8199.
94. R. Ma and T. Sasaki, *Acc Chem Res*, 2015, **48**, 136-143.
95. K. Kalantar-zadeh, J. Z. Ou, T. Daeneke, A. Mitchell, T. Sasaki and M. S. Fuhrer, *Applied Materials Today*, 2016, **5**, 73-89.
96. J. E. Post, *Proceedings of the National Academy of Sciences*, 1999, **96**, 3447-3454.
97. F. Cheng, Y. Su, J. Liang, Z. Tao and J. Chen, *Chemistry of Materials*, 2010, **22**, 898-905.
98. D. M. Robinson, Y. Go, M. Mui, G. Gardner, Z. Zhang, D. Mastrogiovanni, E. Garfunkel, J. Li, M. Greenblatt and C. G. Dismukes, *Journal of the American Chemical Society*, 2013, **135**, 3494-3501.
99. D. A. Kitchaev, S. T. Dacek, W. Sun and G. Ceder, *Journal of the American Chemical Society*, 2017, **139**, 2672-2681.
100. T. Takashima, K. Hashimoto and R. Nakamura, *Journal of the American Chemical Society*, 2012, **134**, 1519-1527.
101. Z. Chan, D. A. Kitchaev, J. Weker, C. Schnedermann, K. Lim, G. Ceder, W. Tumas, M. F. Toney

and D. G. Nocera, *Proceedings of the National Academy of Sciences*, 2018, **115**, 201722235.
102. A. Bergmann, I. Zaharieva, H. Dau and P. Strasser, *Energy & Environmental Science*, 2013, **6**, 2745-2755.
103. Y. Meng, W. Song, H. Huang, Z. Ren, S.-Y. Chen and S. L. Suib, *Journal of the American Chemical Society*, 2014, **136**, 11452-11464.
104. Y. Zhao, C. Chang, F. Teng, Y. Zhao, G. Chen, R. Shi, G. I. Waterhouse, W. Huang and T. Zhang, *Advanced Energy Materials*, 2017, **7**, 1700005.
105. Y. Wang, D. Yan, S. El Hankari, Y. Zou and S. Wang, *Advanced Science*, 2018, **5**, 1800064.
106. M. P. Browne, Z. Sofer and M. Pumera, *Energy & Environmental Science*, 2019, **12**, 41-58.
107. X. Ren, C. Wei, Y. Sun, X. Liu, F. Meng, X. Meng, S. Sun, S. Xi, Y. Du, Z. Bi, G. Shang, A. C. Fisher, L. Gu and Z. J. Xu, *Advanced Materials*, 2020, **32**, 2001292.
108. H. Wang, J. Wu, A. Dolocan, Y. Li, X. Lü, N. Wu, K. Park, S. Xin, M. Lei, W. Yang and J. B. Goodenough, *Proceedings of the National Academy of Sciences*, 2019, **116**, 23473-23479.
109. Q. Wang and D. O'Hare, *Chemical Reviews*, 2012, **112**, 4124-4155.
110. X. Lu, H. Xue, H. Gong, M. Bai, D. Tang, R. Ma and T. Sasaki, *Nano-Micro Letters*, 2020, **12**, 86.
111. X. Long, Z. Wang, S. Xiao, Y. An and S. Yang, *Materials Today*, 2016, **19**, 213-226.
112. N. Han, F. Zhao and Y. Li, *Journal of Materials Chemistry A*, 2015, **3**, 16348-16353.
113. X. Long, J. Li, S. Xiao, K. Yan, Z. Wang, H. Chen and S. Yang, *Angewandte Chemie International Edition*, 2014, **53**, 7584-7588.
114. F. Song and X. Hu, *Nature communications*, 2014, **5**, 4477.
115. X. Lu and C. Zhao, *Nature communications*, 2015, **6**, 6616.
116. M. Luo, Z. Cai, C. Wang, Y. Bi, L. Qian, Y. Hao, L. Li, Y. Kuang, Y. Li, X. Lei, Z. Huo, W. Liu, H. Wang, X. Sun and X. Duan, *Nano Research*, 2017, **10**, 1732-1739.
117. M. Gong, Y. Li, H. Wang, Y. Liang, J. Z. Wu, J. Zhou, J. Wang, T. Regier, F. Wei and H. Dai, *Journal of the American Chemical Society*, 2013, **135**, 8452-8455.
118. W. Ma, R. Ma, C. Wang, J. Liang, X. Liu, K. Zhou and T. Sasaki, *ACS Nano*, 2015, **9**, 1977-1984.
119. J. Ping, Y. Wang, Q. Lu, B. Chen, J. Chen, Y. Huang, Q. Ma, C. Tan, J. Yang, X. Cao, Z. Wang, J. Wu, Y. Ying and H. Zhang, *Advanced Materials*, 2016, **28**, 7640-7645.
120. W. Ma, R. Ma, J. Wu, P. Sun, X. Liu, K. Zhou and T. Sasaki, *Nanoscale*, 2016, **8**, 10425-10432.
121. Y. Jia, L. Zhang, G. Gao, H. Chen, B. Wang, J. Zhou, M. T. Soo, M. Hong, X. Yan, G. Qian, J. Zou, A. Du and X. Yao, *Advanced Materials*, 2017, **29**, 1700017.
122. Y. Wang, Y. Zhang, Z. Liu, C. Xie, S. Feng, D. Liu, M. Shao and S. Wang, *Angewandte Chemie International Edition*, 2017, **56**, 5867-5871.
123. F. Yang, K. Sliozberg, I. Sinev, H. Antoni, A. Bähr, K. Ollegott, W. Xia, J. Masa, W. Grünert, B. Cuenya, W. Schuhmann and M. Muhler, *ChemSusChem*, 2017, **10**, 156-165.
124. H. Xiao, H. Shin and W. A. Goddard, *Proceedings of the National Academy of Sciences*, 2018, **115**, 201722034.
125. Y. Yang, L. Dang, M. J. Shearer, H. Sheng, W. Li, J. Chen, P. Xiao, Y. Zhang, R. J. Hamers and S. Jin, *Advanced Energy Materials*, 2018, **8**, 1703189.
126. D. Zhou, Z. Cai, X. Lei, W. Tian, Y. Bi, Y. Jia, N. Han, T. Gao, Q. Zhang, Y. Kuang, J. Pan, X. Sun and X. Duan, *Advanced Energy Materials*, 2018, **8**, 1701905.
127. Q.-Q. Chen, C.-C. Hou, C.-J. Wang, X. Yang, R. Shi and Y. Chen, *Chemical Communications*, 2018, **54**, 6400-6403.
128. A. C. Thenuwara, E. B. Cerkez, S. L. Shumlas, N. H. Attanayake, I. G. McKendry, L. Frazer, E.

Borguet, Q. Kang, R. C. Remsing, M. L. Klein, M. J. Zdilla and D. R. Strongin, *Angewandte Chemie International Edition*, 2016, **55**, 10381-10385.
129. A. C. Thenuwara, S. L. Shumlas, N. H. Attanayake, Y. V. Aulin, I. G. McKendry, Q. Qiao, Y. Zhu, E. Borguet, M. J. Zdilla and D. R. Strongin, *ACS Catalysis*, 2016, **6**, 7739-7743.
130. A. C. Thenuwara, S. L. Shumlas, N. H. Attanayake, E. B. Cerkez, I. G. McKendry, L. Frazer, E. Borguet, Q. Kang, M. J. Zdilla, J. Sun and D. R. Strongin, *Langmuir*, 2015, **31**, 12807-12813.
131. J. Zhang, J. Liu, L. Xi, Y. Yu, N. Chen, S. Sun, W. Wang, K. M. Lange and B. Zhang, *Journal of the American Chemical Society*, 2018, **140**, 3876-3879.
132. P. Li, M. Wang, X. Duan, L. Zheng, X. Cheng, Y. Zhang, Y. Kuang, Y. Li, Q. Ma, Z. Feng, W. Liu and X. Sun, *Nature communications*, 2019, **10**, 1711.

Chapter 2. Aim and Objectives

Chapter 1 presented the current situation of the demand for clean energy H_2, the potential solution – electrochemical water splitting and the bottleneck of the electrocatalyst development. To alleviate the high cost of noble metal used and to improve the efficiency of electrocatalyst, we paid attention to the layered metal oxides. Layered metal oxides are a big family comprised by transition metals with tunneled nanostructures, tunable valence states and flexible phase structures. Its low price and earth-abundance meet the requirement of lowering cost thus to be potential for large-scale industrialization. In addition, from the perspective of scientific research, the tunneled structure particularly facilitates ion exchange and new species accommodation; the nature of multivalence makes the possibility of engineering electronic structure via the redox reaction; targeted physical properties can be regulated through the phase structure engineering. The underlaying correlation between the structure-catalytic performance is necessarily to be studied so as to provide guidelines for rational design of new catalyst.

On the basis of the background, this Ph.D. project focus on *i*) developing highly active electrocatalysts based on layered transition metal oxides for efficient water splitting, e.g. hydrogen evolution and oxygen evolution. *ii*) reveal the correlation between electronic/coordination structure of the catalyst and electrochemical behavior and activity, which provide fundamental guidelines for catalysts design. Detailed characterizations and measurements on catalyst compositions, morphologies, crystal structures and electrochemical performance are presented in the following chapters of this thesis.

The objectives of this Ph.D. project are:

(1) To design Pt, Ni, Co supported catalysts based on layered metal oxides for the hydrogen evolution reaction and oxygen evolution reaction, exploring the underlying mechanism of active species formation, including phase transition, intercalation and surface redox reaction.

(2) Systematic analysis of the physical features of synthesized catalysts by various techniques, including scanning electron microscopy (SEM), High-resolution transmission electron microscopy (HR-TEM), high-angle annular dark-field scanning transmission electron microscopy (HAADF-STEM), Powder X-ray diffraction (PXRD), X-ray fluorescence spectroscopy (XRF), X-ray photoelectron spectroscopy (XPS), X-ray absorption spectroscopy (XAS) and X-ray emission spectroscopy (XES), Raman spectroscopy, infrared spectroscopy and Thermogravimetry analysis (TGA).

(3) To study the electrochemical performance of the synthesized catalysts using different electrochemical techniques such as cyclic voltammetry (CV), chronoamperometry (CA), Tafel analysis and turnover analysis, exploring the effect of pHs and cations.

(4) To gain fundamental understanding of the mechanism of hydrogen/oxygen evolution on the surface of designed catalysts.

(5) To clarify the effect of composition, morphologies and coordination/electronic structure on hydrogen evolution and oxygen evolution, build the correlations of electronic/coordination structure of the catalyst and electrochemical behavior and performance.

Chapter 3. Theory and Techniques

In this chapter, basic principle of various electrochemical techniques and physical characterizations are summarized and presented. All the experimental results in following ***Chapters 4 - 6*** *over the whole Ph.D course are based on these techniques.*

3.1 Electrochemical theory

3.1.1 Overpotential

Ideally, the voltage applied on the electrodes for an OER reaction should at least be equal to the potential of the reaction at equilibrium. While in a real case, over potential is always needed because there is an additional barrier to overcome due to the electrode polarization. The applied potential can be expressed by the Nernst equation[1]:

$$E_{eq} = E^0 + \frac{RT}{nF} ln \frac{C_O}{C_R} \quad [3.1]$$

T denotes absolute temperature, R is the ideal gas constant, F is faraday constant, n is the transferred electrons in the reaction, C_O and C_R are the concentration of oxidized and reduced reagents, respectively. E_{eq} is the equilibrium potential, and E^0 is the formal potential of reaction. The overpotential is equal to the difference of equilibrium potential E_{eq} and applied potential E.

$$\eta = E - E_{eq} \quad [3.2]$$

usually, the overpotential at a current density of 10 mA cm^{-2} (normalized by geometry) is used as a criterion for different catalyst comparison.

3.1.2 Tafel slope

According to the polarization curve, the relationship of current density j and overpotential η can be express by the Butler-Volmer equation[2]:

$$j_a = j^0 \left[\exp\left(\frac{\beta F}{RT}\eta_a\right) - \exp\left(-\frac{\alpha F}{RT}\eta_a\right) \right] \quad [3.3]$$

j_a denotes anode current, j^0 is exchange current, α and β are external factor, $\alpha + \beta = 1$. R is the ideal gas constant, T is temperature. When $j >> j^0$, the equation can be written:

$$\eta_a = -\frac{2.3RT}{\beta F} log j^0 + \frac{2.3RT}{\beta F} log j_a \quad [3.4]$$

Hence, the Tafel slope is defined as the following:

$$\frac{dlg(j)}{d\eta} = \frac{2.3\times RT}{\alpha zF} \quad [3.5]$$

where F is the Faraday constant and α is transfer efficient and z is the number of transferred electrons in the rate-determining step (RDS). The value of the Tafel slope is an important parameter to estimate the catalytic performance of one catalyst because it indicates the rate of current density changes with increasing overpotential. A smaller Tafel slope means the current density can increase faster with smaller overpotential change.

3.1.3 Exchange current density (j^0)

Exchange current density is defined as the absolute reaction rate on the electrode. When the electrode potential is equal to the equilibrium potential, no net reaction occurs on the electrodes. Whereas in microscopic sense, the oxidation and reduction are in dynamic equilibrium, *i.e*. anode current j_a and cathodic current j_c are equal. At the equilibrium potential, current/potential relationship is:[3]

$$j^0 = F\vec{K}C_o \exp\left(-\frac{\alpha F\varphi_{eq}}{RT}\right) = F\overleftarrow{K}C_R \exp\left(\frac{\beta F\varphi_{eq}}{RT}\right) \quad [3.6]$$

j^0 is a function of electrode material, surface structure, reactant concentration and temperature. For the normalization of electrode area, exchange current density is a good parameter for catalytic activity comparison. Higher exchange current density indicates fast intrinsic oxidation/reduction reaction rate of the catalyst surface, which possessing strong capability in such target reaction.

3.1.4 Turnover frequencies (TOF)

The authentic reflection of a catalyst's intrinsic activity would be TOF, which contributes to exposed surface atoms that participate in an electrochemical reaction. According to the definition, TOF quantifies the specific activity of a catalytic center for a special reaction per number of active center per unit time.[4] The calculation of TOF is given by:

$$\mathrm{TOF} = \frac{j \times A}{4 \times F \times m} \qquad [3.7]$$

j is the current density of a given overpotential, A is the surface area of the electrode, F is the Faraday constant, m is the number of moles of metal on the electrode. It should be noted that, the TOF calculation method can not obtain accurate values because of the difficulty of determining real active species and the population of active sites under catalytic conditions.

3.1.5 Electrochemical active surface area (ECSA)

ECSA usually reflects the area that contributes to the catalysis, which is different from the geometric area. There are several methods to determine the ECSA depending on the type of catalyst. Two methods are usually adopted for the metal electrocatalyst: hydrogen underpotential deposition (HUPD) and CO stripping. The HUPD is widely used for noble metals such as Pt, Pd, Rh, Ir and their alloys.[5-7] A monolayer H atoms adsorption/desorption can occur on the metal surface *via* a sweep of voltage, as shown at the CV curves (**Figure 3.1**). By subtracting the double layer region, the integrated area correlate to the charges that contributes to H adsorption/desorption, which equals to the population of H atoms. Further, it is commonly divided by the specific charge (210 μC cm_{Pt}^{-2}) for a monolayer.[5]

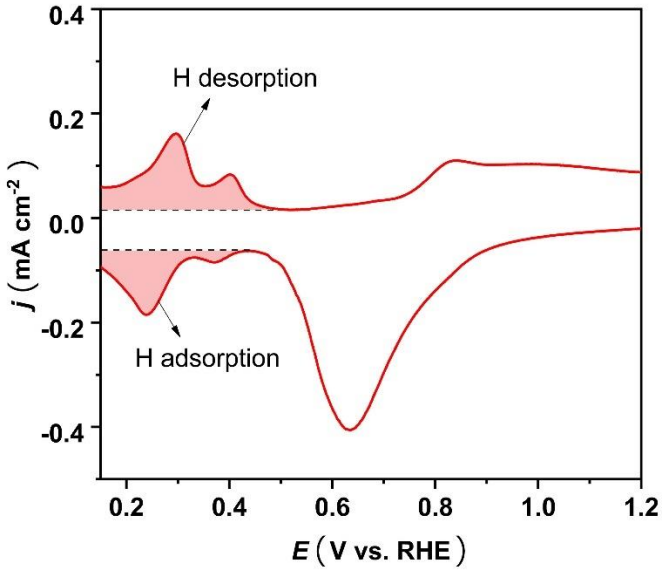


Figure 3. 1 Cyclic voltammetry of Pt nanoparticles at 20 mV s^{-1} in Ar-saturated 0.1 M

NaOH, shaded regions are H adsorption/desorption area.

As for the metal oxides, surface redox reaction and double layer capacitance (C_{dl}) are two candidates for measuring ECSA. Many kinds of metal oxides lack the redox process before the OER, and so double-layer capacitance is the most popular used method. Once the electrode is in contact with electrolyte, a quasi-equilibrium is built on the solid-liquid interface. At this interface, the electrical double-layer region is considered to be the accommodation for catalytic reaction. Thus, ECSA can be acquired by:

$$ECSA = C_{dl}/C_{oxide} \quad [3.8]$$

C_{oxide} denotes ideal oxide capacitance. It should be noted that this value varied with various metal oxides, with significant difference among them.[8] The C_{dl} can be determined by two methods: extract from EIS or CV at non faradic region. For the EIS, modified Randles circuit fitted complex impedance (Nyquist plot) can generate C_{dl} directly. Compare to that, CV sweep at non-faradic regions is more frequently used. By considering the equation:

$$C_{dl} = dQ/dE \approx \Delta j/\Delta \upsilon \quad [3.9]$$

where current density differences ($\Delta j = j_a - j_c$), the plot of Δj v*ersus* the scan rates provides the slope of the linear regression which is equivalent to the double layer capacitance ($2C_{dl}$).[8]

3.2 Electrochemical techniques

3.2.1 Cyclic Voltammetry (CV) and Linear Scanning Voltammetry (LSV)

Cyclic voltammetry is the most widely used technique for acquiring qualitative information about electrochemical reactions. To get a voltammogram of an electrochemical process, linearly varying potential is applied to the working electrode at a fixed scan rate. When the voltage reaches the maximum (minimum) value, it then reverses and back to the minimum (maximum) side, as shown in **Figure 3.2**.[9] The potential change presents a triangular shape signal. This cycle can be repeated several

times, according to a preset value. With a closed loop of potential sweep, redox characteristics or double layer region can be recorded. The information of potential peaks, difference between redox peak and integrated area help us study the electrochemical behaviors elaborately. Reversibility and reaction mechanism also can be examined by variation of scan rates.

A simple example of Ni^{2+}/Ni^{3+} redox voltammogram (as shown in **Figure 3.2b**) is based on the reversible reaction:

$$Ni^{2+} \rightleftharpoons Ni^{3+} + e^{-1} \qquad [3.10]$$

the potential sweep from point A with a positive direction, surface Ni^{2+} sites are assumed to access OH^- from the electrolyte. When the potential reaches ~1.3 V vs. RHE, Ni^{2+} starts to be oxidized to Ni^{3+}. The reaction rate keeps fast until the faradic current reaches the summit, at potential E_p^{ox}. During this process, the electrochemical reaction is controlled by electrode polarization, *i.e.* by the electron transfer.[10] As potential increase higher than E_p^{ox}, faradic current start to go downhill. The transformation of Ni^{2+} to Ni^{3+} keeps moving but with a slower reaction rate until it reaches to point B. In this region, the electrochemical reaction is controlled by mass transfer. From point B to C, the potential reverses to a negative direction, giving rise to a reductive current. Similar to the anodic oxidation process, the reducing of Ni^{3+} to Ni^{2+} rapidly increase to E_p^{re} and then transfer to slow transformation until the reaction finishes. At point C, the whole cycle finished.

Similar to CV, LSV means that the voltage is changed from a fixed potential range (point A to point B) in linear increasing with time. The scan rate can be tuned by changing the time, which usually is set as 1-5 mV s^{-1} to get a quasi-steady state of the electrode process, to minimize the effect from double-layer current. The current recorded is the sum of currents for the redox reaction and charged for electric double layer.

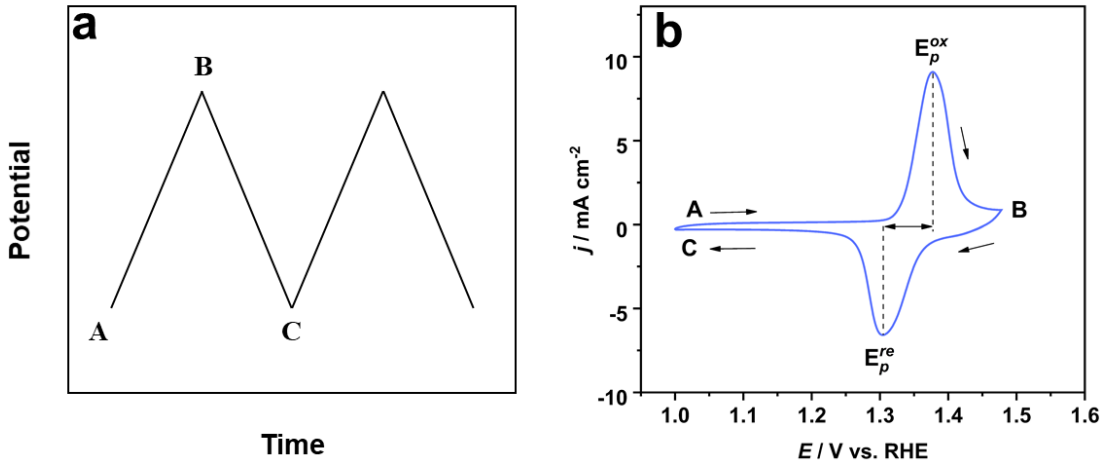


Figure 3. 2 (a) Repetitive triangular wave signal of potential variation during the cyclic voltammetry, (b) typical voltammogram of Ni^{2+}/Ni^{3+} redox in 1 M NaOH with scan rate $\upsilon = 20$ mV s^{-1}.

3.2.2 Chronoamperometry (CA) and Chronopotentiometry (CP)

Chronoamperometry is carried out by applying a potential signal on the working electrode, to get the current response as function of time.[11] It has been one of the most frequently used techniques in evaluating the stability of catalysts. Take the OER as an example, three steps are set to implement the CA. The applied voltage is held on pre-OER potential E_1 for several minutes. Then, the potential sharply jumps to E_2, at which the expected oxygen evolution reaction takes place with a reaction current. A long time is set for this period to get the current variation that evaluates the stability. Afterwards, the potential goes back to E_1 and CA finish.

Chronopotentiometry means applying a current pulse on the working electrode to acquire the potential variation as a function of time.[11] There are different types of Chronopotentiometric techniques according to the applied current. For example, the applied current on the electrode is constant; the applied current can be linearly increased or decreased; the applied current can be reversed repeatedly in cycles. In particular, a constant current is usually implemented in catalyst stability tests.

3.3 Physical characterization techniques

3.3.1 Electron microscopy

Scanning electron microscopy (SEM)

SEM is the most used technique to study the morphology of solid samples.[12] A beam of focused electrons scans the sample surface, with the detector receive high-energy backscattered electrons and low-energy secondary electrons which are scattered by the irregular surface of the sample. In this way, the image processor outputs the 3D morphology.

Transmission electron microscopy (TEM)

High energy electron beam (accelerated by 200-300 kV voltage) is used in TEM to penetrate the tested sample.[13] In this regard, a specimen is required to be thin enough (less than 100 nm) that electron can transmit. A two-dimensional image is formed after the electron interacting with the specimen. Selected area electron diffraction (SAED) and energy dispersion spectroscopy (EDS) mounted on TEM can be used for crystallographic and elements analysis.

3.3.2 X-ray based techniques

X-ray diffraction (XRD)

XRD is a rapid analytical technique used for phase identification of natural or synthesized materials.[14] It is well known that the atoms or ions are in periodic arrangement of a crystal. For a polycrystal, it is composed of different planes of atoms exposed with specific lattice distance. These lattice planes are in several angstroms scale which can be compared to the wavelength of the X-rays. When the incident rays reach the sample surface, the diffraction would happen if incident rays and corresponding contractive interference satisfy Bragg's Law, $2d_{hkl}\bullet\sin\theta = n\lambda$ (**Figure 3.3**). The *d*-spacing of a specific lattice plane therefore will be obtained. In a powder sample, sufficient crystal planes should be included in all possible orientations. By scanning the sample in a range of θ, all lattice planes in possible axes of the tested

sample can be acquired, despite their random orientations. Phase identification can be operated by matching the diffraction patterns with database. By applying Rietveld refinement analysis of the structure high-quality diffraction data, precise crystal structure, cell parameters, bond length/angle and the atomic occupancy can be obtained.

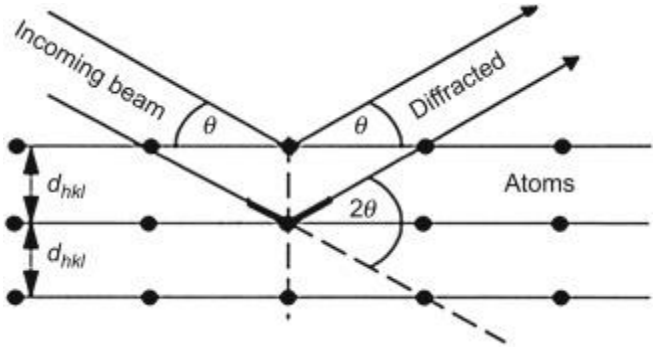


Figure 3. 3 Schematic graph of the diffraction that occurs on a crystal surface.[15] Copyright ©2016, Elsevier

X-Ray Fluorescence (XRF)

It is well known that the various techniques are principally based on the interaction between X-ray and matter, such as adsorption, emission of fluorescence, scattering and diffraction.[16] XRF technique depends on the fundamental principles of X-ray excited fluorescence, which is common to energy dispersive spectroscopy (EDS) used for elements analysis, *i.e.* species and quantity.[17] Once atoms in a bulk material receive high energy X-rays radiation, the adsorption can strengthen the oscillation of lattice and electrons in inner shells would be excited and emitted with vacancies left. Electrons at higher energy level tend to refill the holes and at the same time a pulse of electro-magnetic radiation is released, called the characteristic X-ray (**Figure 3.4**). This emitted fluorescence energy is characteristic for specific energy level of a specific elements. According to Moseley's law:

$$E = C_1 \times (Z - C_2) \qquad [3.12]$$

C_1, C_2 correspond to involved electron shells. At all X-ray series (K, L, M) the energy of characteristic X-ray is directly dependent on atomic number Z. Thus, qualitative and quantitative analysis can be performed to determine elemental composition.

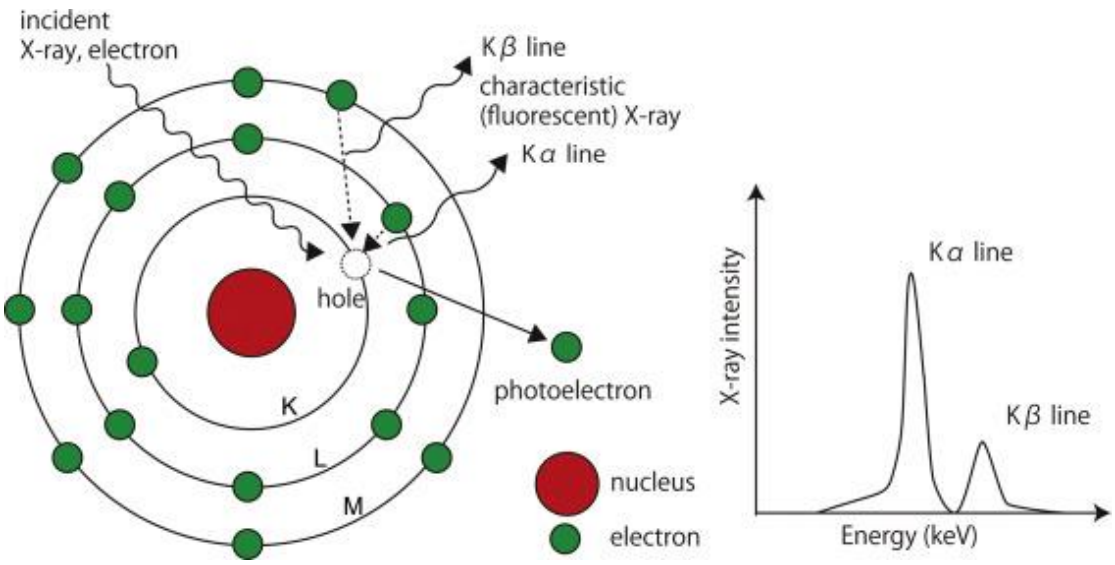


Figure 3. 4 Schematic graph of the principle on characteristic X-ray generation.[18] Copyright ©2015, Elsevier

X-ray absorption spectroscopy (XAS)

XAS plays a pivotal role in catalysis study since it provides electronic properties and local coordination information of a catalyst. High energy X-rays on a sample can excite electrons from core level to an unoccupied state. Electron transition in metal center from 1s to 4p band is called hard XAS, associated with the K-edge. As shown in **Figure 3.4b**, a typical absorption spectrum consists of two regions: X-ray absorption near-edge structure region (XANES) and extended X-ray absorption fine structure (EXAFS).[19] The former provides oxidation states of the metal center by analysis of edge position. Stronger electrostatic interaction between metal center and ligands correspond to higher photon energy position, which is associated with higher oxidation state. The dependence of energy position and oxidation state can be expressed linearly. In addition, the pre-edge feature at XANES region also provides important information. Since the pre-edge peaks are originated from 1s to 3d transition, they would be inhibited in a symmetry field. For example, the ubiquitous octahedra field of transition metal oxides hold a symmetry feature that pre-edge peaks show weak intensity. If tetrahedra exist in bulk materials (spinel), the hybridization of 3d and 4p would break the prohibition that promotes the transition. Intense pre-edge peaks can be detected. Besides symmetry

configuration, the shape and position of pre-edge peaks also link to oxidation state and ligand types. EXAFS spectrum affords the coordination information of samples. At Fourier transformed R space spectrum, the first peak corresponds to the nearest light atoms (O, N, C *etc*.) around central metal atoms (ions) in the first shell. The second peak is linked to the nearest metal atoms (homo or hetero) around the central metal atoms in the second shell. Based on analysis of the two main peaks, the ligand type, bond distance and symmetry configuration can be obtained. Moreover, coordination numbers (CN) can be estimated by spectrum fitting, which is of great importance in the catalytic activity studied.

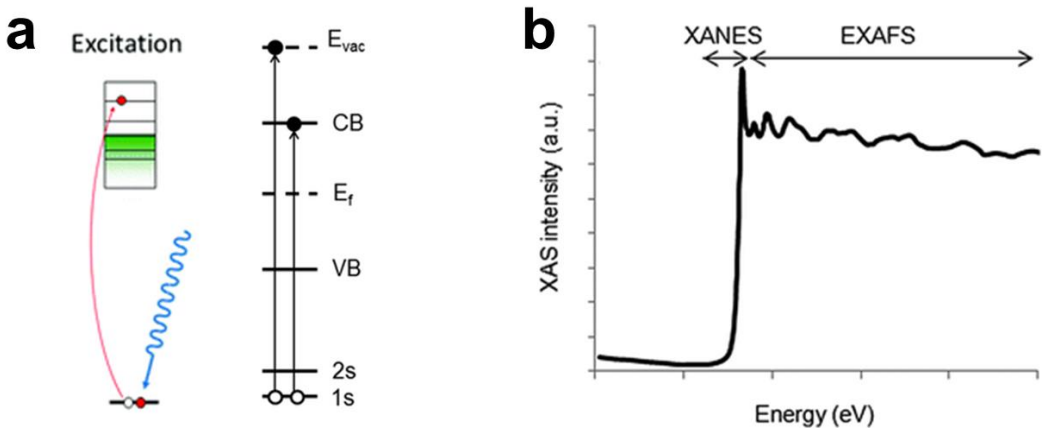


Figure 3. 5 (a) Schematic graph of XAS excitation and energy diagram, (b) typical XAS spectrum.[19] Copyright © 2017, Royal Society of Chemistry

X-ray photoelectron spectroscopy (XPS)

XPS is widely used to study the composition and chemical state of samples.[20] It is a surface sensitive technique that reflects the information on the solid's outer surface of only 1-10 nm. When photons irradiate the sample electrons initially bound to atoms (for example K shell) would be excited and escape from the solid through the photo-electron interaction. The kinetic energy (E_K) of the emitted electron can be measured and confirmed, thus binding energy E_B can be acquired by:

$$E_B = h\nu - (E_K + \Delta\Phi) \quad [3.13]$$

$h\nu$ is photon energy, $\Delta\Phi$ is the work function of a spectrometer. Therefore, most elements in the periodic table (except H, He) present characteristic peaks due to

different binding energy (*B.E.*). Peak intensity is proportional to elements content. Based on these features, XPS can be used to identify and quantify the elemental composition, and reveal the chemical environment.

3.3.3 Raman and Infrared Spectroscopy

The Raman effect focuses on the interaction of incident light and targeted phonon mode from atoms vibration. The interaction is commonly classified as elastic scattering and inelastic scatting.[21, 22] The latter was first discovered by Chandrasekhara Venkata Raman, describing an energy transition phenomenon. When a strong monochromatic light incident on the specimen surface, it will cause excitation of molecules to a 'virtual state'. The excited molecules can be viewed as a new radiation source, which releases photon as falling back to ground state. Energy equal to initial incident photon is called Rayleigh scattering; different to initial energy is Raman scattering. Since the electron cloud of molecules is polarized at the 'virtual state', it is characteristic of specific elements with a specific crystal arrangement. The Raman shift, the energy difference between incoming and scattering photon, is used as a fingerprint signal for species identification.

Infrared spectroscopy is a technique reflecting the vibration or rotation of a molecule. It originates from the change of dipole moment of a molecule.[23, 24] When the infrared radiation is exposed on matter (solid or liquid), a certain degree of energy would be absorbed by the molecules that excited the molecules into a higher energy level. The difference between energy levels is the fingerprint for a special matter, which can be used for material identification. As the wavenumber consecutively varies from 0 - 4000 cm^{-1}, molecules that absorb frequencies at different positions can be indexed to the characteristic vibration.

3.3.4 Thermal Gravimetric Analysis and Differential Thermal Analysis

Both Thermal gravimetric Analysis (TGA) and Differential scanning calorimetry (DSC) are used to study the endothermic/exothermic reaction of compounds at varying temperature.[25, 26] They are working in the same principle, with differences in measuring method. TGA, describes the dependence of mass change on temperature; DSC, depicts the correlation of heat flow with temperature. Usually they cooperate with each other to give a comprehensive evaluation of tested samples. For instance, the mass loss in a certain temperature window could be attributed either to water loss or organic decomposition or crystal phase transition. The DSC curve in the same temperature range with or without endothermic/exothermic can help determine which reaction happens.

References

1. A. J. Bard, L. R. Faulkner, J. Leddy and C. G. Zoski, *Electrochemical methods: fundamentals and applications*, wiley New York, 1980.
2. E. Fabbri, A. Habereder, K. Waltar, R. Kötz and T. J. Schmidt, *Catal. Sci. Technol.*, 2014, **4**, 3800-3821.
3. F. Barbir, in *PEM Fuel Cells (Second Edition)*, ed. F. Barbir, Academic Press, Boston, 2013, DOI: https://doi.org/10.1016/B978-0-12-387710-9.00003-5, pp. 33-72.
4. M. Boudart, *Chemical Reviews*, 1995, **95**, 661-666.
5. W. Sheng, M. Myint, J. G. Chen and Y. Yan, *Energy & Environmental Science*, 2013, **6**, 1509-1512.
6. J. Zheng, W. Sheng, Z. Zhuang, B. Xu and Y. Yan, *Science Advances*, 2016, **2**, e1501602.
7. I. E. L. Stephens, A. S. Bondarenko, U. Grønbjerg, J. Rossmeisl and I. Chorkendorff, *Energy & Environmental Science*, 2012, **5**, 6744-6762.
8. C. C. L. McCrory, S. Jung, J. C. Peters and T. F. Jaramillo, *Journal of the American Chemical Society*, 2013, **135**, 16977-16987.
9. J. Heinze, *Angewandte Chemie International Edition in English*, 1984, **23**, 831-847.
10. D. Pletcher, R. Greff, R. Peat, L. M. Peter and J. Robinson, in *Instrumental Methods in Electrochemistry*, eds. D. Pletcher, R. Greff, R. Peat, L. M. Peter and J. Robinson, Woodhead Publishing, 2010, DOI: https://doi.org/10.1533/9781782420545.76, pp. 76-112.
11. S.-I. Pyun, H.-C. Shin, J.-W. Lee, J.-Y. Go, S.-I. Pyun, H.-C. Shin, J.-W. Lee and J.-Y. Go, *springer*, 2012, DOI: 10.1007/978-3-642-29464-8_2, 11-32.
12. P. S. Kumar, K. G. Pavithra and M. Naushad, in *Nanomaterials for Solar Cell Applications*, eds. S. Thomas, E. H. M. Sakho, N. Kalarikkal, S. O. Oluwafemi and J. Wu, Elsevier, 2019, DOI: https://doi.org/10.1016/B978-0-12-813337-8.00004-7, pp. 97-124.
13. V. S. Kulkarni and C. Shaw, in *Essential Chemistry for Formulators of Semisolid and Liquid Dosages*, eds. V. S. Kulkarni and C. Shaw, Academic Press, Boston, 2016, DOI: https://doi.org/10.1016/B978-0-12-801024-2.00010-8, pp. 183-192.
14. O. D. Neikov and N. A. Yefimov, in *Handbook of Non-Ferrous Metal Powders (Second Edition)*, eds. O. D. Neikov, S. S. Naboychenko and N. A. Yefimov, Elsevier, Oxford, 2019, DOI: https://doi.org/10.1016/B978-0-08-100543-9.00001-4, pp. 3-62.
15. J. Epp, in *Materials Characterization Using Nondestructive Evaluation (NDE) Methods*, eds. G. Hübschen, I. Altpeter, R. Tschuncky and H.-G. Herrmann, Woodhead Publishing, 2016, DOI: https://doi.org/10.1016/B978-0-08-100040-3.00004-3, pp. 81-124.
16. B. K. Agarwal, *X-Ray Spectroscopy: An Introduction*, 1979.
17. G. J. Weltje and R. Tjallingii, *Earth and Planetary Science Letters*, 2008, **274**, 423-438.
18. M. Uo, T. Wada and T. Sugiyama, *Japanese Dental Science Review*, 2015, **51**, 2-9.
19. C. H. M. van Oversteeg, H. Q. Doan, F. M. F. de Groot and T. Cuk, *Chemical Society Reviews*, 2017, **46**, 102-125.
20. P. v. d. Heide, in *X-Ray Photoelectron Spectroscopy: An Introduction to Principles and Practices*, 2011, DOI: 10.1002/9781118162897.ch1, pp. 1-12.
21. N. John and S. George, in *Spectroscopic Methods for Nanomaterials Characterization*, eds. S. Thomas, R. Thomas, A. K. Zachariah and R. K. Mishra, Elsevier, 2017, DOI: https://doi.org/10.1016/B978-0-323-46140-5.00005-4, pp. 95-127.
22. S. Loridant, in *Characterization of Nanomaterials*, eds. S. Mohan Bhagyaraj, O. S. Oluwafemi, N.

Kalarikkal and S. Thomas, Woodhead Publishing, 2018, DOI: https://doi.org/10.1016/B978-0-08-101973-3.00002-X, pp. 37-59.

23. J. Ryczkowski, *Catalysis Today*, 2001, **68**, 263-381.

24. H. Günzler and H.-U. Gremlich, *IR Spectroscopy: An Introduction*, 2002.

25. M. Wagner, in *Thermal Analysis in Practice*, ed. M. Wagner, Hanser, 2018, DOI: https://doi.org/10.3139/9781569906446.001, pp. 10-15.

26. J. Abraham, A. P. Mohammed, M. P. Ajith Kumar, S. C. George and S. Thomas, in *Characterization of Nanomaterials*, eds. S. Mohan Bhagyaraj, O. S. Oluwafemi, N. Kalarikkal and S. Thomas, Woodhead Publishing, 2018, DOI: https://doi.org/10.1016/B978-0-08-101973-3.00008-0, pp. 213-236.

Chapter 4. Study of anomalous phase transition of layered lepidocrocite titania nanosheets to anatase and rutile, and their electrochemical HER performance with Pt decoration

Preface to Chapter 4

Format: The first part of this chapter: Phase transition of layered titanate oxide to anatase has been published.[1] The second part of this chapter about the electrochemical HER study on photochemical-deposited Pt on TiO_2 synthesized by phase transition, is under preparation for another submission.

Article information: Yayun Pu, Qianwen Chen, Zongzhao Sun, Paramaconi Rodriguez* and Limin Huang*, Anomalous Phase Transition of Layered Lepidocrocite Titania Nanosheets to Anatase and Rutile, *Cryst. Growth Des.* 2019, 19, 6, 3298–3304. https://doi.org/10.1021/acs.cgd.9b00147

Overview: Hydrogen evolution, the half reaction of water splitting, occurs on the cathode and requires cheap, robust and highly efficient electrocatalysts to drive. For the supported catalyst, a deep understanding of the interaction between active species and metal oxide support is essentially important, in terms of electronic structure and chemical state. To study such interaction, a phase transition based on a layered titanate oxide was first examined. pH-dependent TiO_2 nanoparticles on morphology and exposed crystal facet were prepared, which displayed different photo-response under UV-Vis irradiation. By means of this new finding, ~1 wt% Pt species were photochemically deposited on the as synthesized TiO_2 surface, aiming at exploring the interaction of Pt and the support, and the effect on electrochemical HER performance. The study provides useful information on the rational design of electrocatalysts.

Author contribution: Pu. Y performed the experiments and data analysis. P.R and L.H supervise the work. C. Q and Z. Sun performed the TEM characterization. All authors contributed to the drafting and revision of the article.

4.1 Introduction

Titanium oxides with various polymorphs, such as anatase, rutile, brookite and lepidocrocite-type layered structure, have been among the most studied material systems in energy relevant applications such as photoelectrochemical solar cells, photocatalysis and electrode materials for Li/Na-ion batteries.[2-8] To meet the ever-increasing energy demand, intensive efforts have been devoted to developing the titanium oxides with tunable compositions, morphologies and structures.[9-12] Understanding the properties of the materials as a function of the crystallographic structure and the phase transition amongst these polymorphs, *e.g.* the transformation of lepidocrocite-type TiO_2 nanosheets into rutile or anatase is essential to establish protocols of synthesis of these materials and their subsequent applications. Among the well-developed protocols, solution-based methods are suitable to control the size, morphology and crystallographic orientation of nanocrystals providing a broad spectrum of physical, chemical and electronic properties that have found interest in diverse areas.[13-15] For example, Pan *et al*. prepared specifically exposed facets of anatase TiO_2 nanorod using the hydrothermal method and layered $Cs_{0.68}Ti_{1.83}O_4$ as a precursor.[16] This material found later application on dye-sensitized solar cells. The transition of layered titanate nanosheets to anatase at different pHs and above 100 °C was first reported by Wen *et al*.[17, 18] The authors found that the formation of rutile is only favorable in strongly acidic environment (pH < 2). However, these studies do not provide a clear understanding of the phase transition and phase morphonology as the function of temperature and pH, thus there is still lack of a fully established transition map for an overall view. Energy relevant applications such as water splitting, solar conversion and lithium storage require precise control of the crystal phase, particles size, the special dominant facet and the morphology, all of which are exclusively based on the complete and deep understanding of such transition.

Metal oxides, especially TiO_2, are ideal supports for anchoring various hetero atoms/clusters/nanoparticles for catalysis.[19] The strong metal support interactions

(SMSI) is defined between decorated metal/metal oxide and the support due to the variety of composition, crystal phase, particles size, interplanar spacing of support oxides.[20-23] For example, by means of electrochemical lithiation/delithiation special crystalline lattice spacing where Pt nanoparticles anchored on, can be changed. The varied crystal lattice induced tensile/compressive strain to adsorbed platinum nanoparticles, which tune the d-band center of Pt that give rise to different ORR activity.[22] Mobini *et al* studied the effect of ZrO_2, CeO_2, MgO, SiO_2, and Al_2O_3 support with MnO_x decoration towards CO oxidation reaction. High ability to supply oxygen by CeO_2 during the catalytic process makes it the highest activity.[24]

Here, this work provides a coherent and insightful investigation on the phase transition of titanium oxides polymorphs, featuring the dependence of temperature and pH change and to provide important information for the optimization parameters of dominant (101) facet of anatase single crystal. By employing the pre-synthesized TiO_2 as supports, Pt species were introduced on the Ti-O surface by photochemical reduction reaction. Due to the fact that different capability of TiO_2 supports response to the UV-Vis irradiation, the interaction between deposited Pt and TiO_2 are varied. Charge transfer from Ti to adjacent Pt can reduce the valence state which facilitate electrochemical HER.

4.2 Methods

4.2.1 Preparation of layered lepidocrocite-type TiO_2 nanosheets suspension

The $Cs_{0.35}TiO_2$ precursor was prepared by a solid-state reaction according to the previous report.[25] Typically, an intimate mixture of titanium dioxide and cesium carbonate (99.9% metals basis, Aladdin) with a molar ratio of 1:5.3 were placed in a crucible and was heated at 800 ºC for 1 h for decarbonation. After cooling down, the powder was ground carefully and then was allowed for two cycles of heating at 800 ºC, 20 h. During that process, the powder was also ground four times. The as-synthetized $Cs_{0.35}TiO_2$ powder was then subjected to acidic exchange by 1 M HCl with a solution-solid ratio of 100 cm^3/g. After 24 h, the solution was decanted and replaced by a fresh one. It was repeated 3 times. The obtained solid was filtered, rinsed with water 3 times and dried at 60 ºC. A weighed amount of H_xTiO_2 (0.1 g) was dispersed into 25 ml aqueous tetrabutyl ammonium hydroxide (TBAOH) solution (40 wt.%) under ultrasonic treatment for 4h, with H^+/TBA^+=1:5.

4.2.2 Hydrothermal treatment of colloidal suspension

First, 8 mL of the L-TiO_2 nanosheet suspension was diluted in 24 ml of water and the pH was adjusted to pH=1, 3, 6 or 9 by HCl and TBAOH solution. In the following step, the TiO_2 nanosheet solution was transferred to a Teflon-lined stainless steel vessel with an internal volume of 50 ml. The reactor was sealed and kept for 24 h at different temperatures: 50 ºC, 80 ºC, 120 ºC, 180 ºC, 220 ºC. After the hydrothermal treatment, the product of the reactions was collected by centrifuging and was washed with distilled water five times. Finally, the nanoparticles s were dried in a conventional oven at 50 ºC overnight.

Freeze-drying steps were performed using two different protocols: *i)* freeze-drying was applied directly after centrifuging; or *ii)* a small amount of the samples were diluted with water after centrifuging, and then the freeze-drying step was applied.

4.2.3 Preparation of Pt@TiO_2 after phase transition by photochemical reduction reaction

Firstly, 1 mg mL^{-1} H_2PtCl_6 aqueous solution was prepared by chloroplatinic acid and ultrapure water. A series of Ti oxide nanoparticles (100 mg for each), including as-synthesized HTO nanoflakes, exfoliated L-TiO_2 nanosheets, A-TiO_2@pH=3, 9, 12 and commercial TiO_2 (anatase, Aladdin®), were separately dispersed in 6 separate beakers containing 20 mL ultrapure water, then under ultrasonic treatment for 10 min. Note that, basic L-TiO_2 nanosheets were firstly centrifuged at 18000 rpm, washed with water several times to get neutral pH, and then redispersed in ultrapure water. Then, 1 mL prepared H_2PtCl_6 aqueous solution was added to pre-made TiO_2 suspension dropwise, with magnetic stirring under ice-bath. After violently stirring for 1 h, the suspension was irradiated by a UV lamp for 1 h, keeping stirring and under ice-bath. After UV irradiation, the obtained Pt@TiO_2 suspensions were centrifuged, washed with water and then freeze-dried. All the samples were placed in a tube furnace annealing for 1 h under N_2 atmosphere.

4.2.4 Physicochemical and structural characterization

The particle morphology was characterized using scanning electron microscopy (SEM, Zeiss with Oxford Instruments EDS attachment) with an acceleration voltage of 15 kV and probing current of 1 nA. Transmission electron microscopy (TEM) was performed on a FEI Tecnai G2 F30 with acceleration voltage of 300 kV. High-angle annular dark field scanning transmission electron microscopy (HAADF-STEM) imaging experiments were carried out on a FEI Talos F200X microscope operated at 200 kV. X-ray diffraction (XRD) patterns were acquired by a Rigaku Smartlab-9Kw X-ray diffractometer. Raman scattering spectra were collected by a confocal Laser Raman Spectrome (HORIBA LabRAM) with 532 nm He-Ne laser, a laser power of 0.2 mW was used to avoid sample damage. The intensity was enhanced with optimum exposure time (10 s) and multicycles (5) that produce good quality spectra. Thermogravimetry analysis (TGA) was performed in the temperature range of 25-550 ^oC by Shimadzu

TGA-50 with a heating rate of 10 ^{o}C /min, the nitrogen gas flow was 30 ml/min. The Differential Scanning Calorimeter (DSC) was performed using a Shimadzu DSC-60 Plus with a heating rate of 10 ^{o}C /min, a nitrogen gas flow of 30 ml/min within the temperature window between 25-500 ^{o}C. UV-Vis absorption spectra of the colloidal suspensions were recorded by a Shimadzu UV-3101PC UV/Vis spectrometer. Zeta-potential data were obtained by a Zetasizer Nano ZS. Inductively Coupled Plasma Mass Spectrometry (ICP-MS) measurement was carried out in an Agilent 7700x equipment. To dissolve the Pt decorated TiO_2 samples, concentrated HNO_3 and HF were mixed as solvent. The XPS analyses were performed on a PHI 5000 VersaProbe III spectrometer using a monochromatic Al K(alpha) X-ray source, with the most used X-ray settings being 200 um, 50 W, 15 kV. The PHI 5000 VersaProbe III charge neutralization system was used on all specimens. Charge neutralization was deemed to have been fully achieved by monitoring the C 1s peak positions which remained unchanged throughout the whole experiment. High resolution analyses were carried out at 69.0 eV for analyzer pass energy and step size of 0.125 eV. The data were analyzed using the PHI MultiPak software (version 9.8). Spectra have been charge corrected to the main line of the carbon 1s spectrum (adventitious carbon) and set to BE of 284.8 eV.

4.2.5 Electrochemical characterization

Electrochemical cell setup: All the electrochemical measurements were performed in a three-electrode setup. Before each electrochemical measurement, the electrochemical cell system was stored in permanganate solution overnight. Before testing, the cell was rinsed with ultrapure water and diluted piranha solution to remove permanganate, followed by filling with ultrapure water and heating to ~70 ^{o}C. The hot water was replaced with fresh ultrapure water and reheated five times. Electrochemical measurements were performed with a CHI 760e electrochemical workstation, with carbon rod as the counter electrode (CE) and Ag/AgCl (3.5 M KCl) as the reference electrode (RE). The CE was rinsed with water several times before immersed in electrolyte. iR resistance was measured by the '*iR compensation*' function of CHI

electrochemical workstation, test potential: 0 V vs. RHE, step amplitude: 50 mV. The measured resistance was 3.5 Ω. The acidic electrolyte was freshly prepared by mixing of 98% concentrated H_2SO_4 (Sinopharm) with ultrapure water. The prepared electrolytes were purged with high purity argon (99.99%) for at least 30 min prior to measurements. Ar stream acted as a protective medium above the electrolyte, was employed during measurements.

Electrode preparation: Sample powders were dispersed in ultrapure water with a concentration of 1 mg mL^{-1}, followed by sonication (~30 min) to achieve a good dispersion. The glassy carbon (GC) rotating disk electrode (RDE, 5 mm diameter, geometric area = 0.196 cm^{-2}) was polished with 1 μm and 0.3 μm Al_2O_3 slurry in sequence to get a refining surface then rinsed abundantly with ultrapure water. 4 x 10 μL of the prepared ink were drop-casted onto the GC and dried in an oven at 50 ºC to deposit ~0.04 mg catalyst; the loading was ~0.2 mg cm^{-2}. 10 μL Nafion D-521 solution (Alfa Aesar, 5% w/w in H_2O and 1-propanol) was dispersed in 1 mL ultrapure water. After catalyst deposition, 10 μL prepared diluted Nafion solution was dropped on the surface of electrode.

Cyclic voltammetry (CV): CVs were recorded in a potential window of -0.4 to 0.1 V vs. RHE, with a scan rate of 20 mV s^{-1}. After the curves stabilized, LSV with scan rate of mV s^{-1} was recorded. GC RDE was rotated at 1600 rpm to remove generated H_2 bubbles. The Ohmic resistances of the electrochemical system were obtained from CHI 760e. Amperometric i-t measurement was kept at -0.35 V vs. RHE for 24 h.

4.3 Results and Discussion

4.3.1 Phase transition of L-TiO_2

The characterization of as-prepared lepidocrocite-type TiO_2 nanosheets (L-TiO_2) is presented in **Figure 4.1**. The SEM and TEM images show well-defined single layer nanosheets with an average lateral size between 200-300 nm. The faded contrast in the TEM image and the AFM image in **Figure 4.2** certify the molecular-level thickness (~1.5 nm) of the nanosheets.[25, 26] Prior to the solvothermal treatment, the photochemical properties and stability of the colloidal solution of the exfoliated TiO_2 nanosheets were evaluated as a function of the pH by UV-Vis spectroscopy and the Zeta-potential (**Figure 4.1d,e**). As can be seen, the absorption peak at 266 nm is associated with the presence of colloidal suspension of polydisperse TiO_2 nanosheets, the peak weakens as the pH decreases from alkaline to acid until it disappears at pH=3. Such a decrease of the signal is directly associated with the accelerated flocculation of the suspension of nanoparticles in a range of pH between 5.0-6.0 (see an optical image in **Figure 4.1c**). The flocculation of the nanoparticles can be explained in terms of the attractive and repulsive interaction of the particles and the surface charge as a function of the pH. As can be seen in **Figure 4.1e**, the Zeta-potential measurements reveal that the variation trend of exfoliated nanosheets on pH is similar to the UV-Vis spectra variation. Because of the negatively charged surface of L-TiO_2, well dispersed nanosheets show a potential of -30 mV under alkaline conditions. The potential starts to change positively as the pH decreases, indicating that the nanosheets follow an accelerated assembly or restacking. At pH=3, the surface charge of the nanoparticles becomes positive, the Zeta-potential reaches a potential of +6 mV, suggesting the full restacking of the TiO_2 single-layer nanosheets. The change of the zeta potential and the change of charge is consistent with the precipitation process observed in the optical images and the trend observed on the UV-Vis spectra.

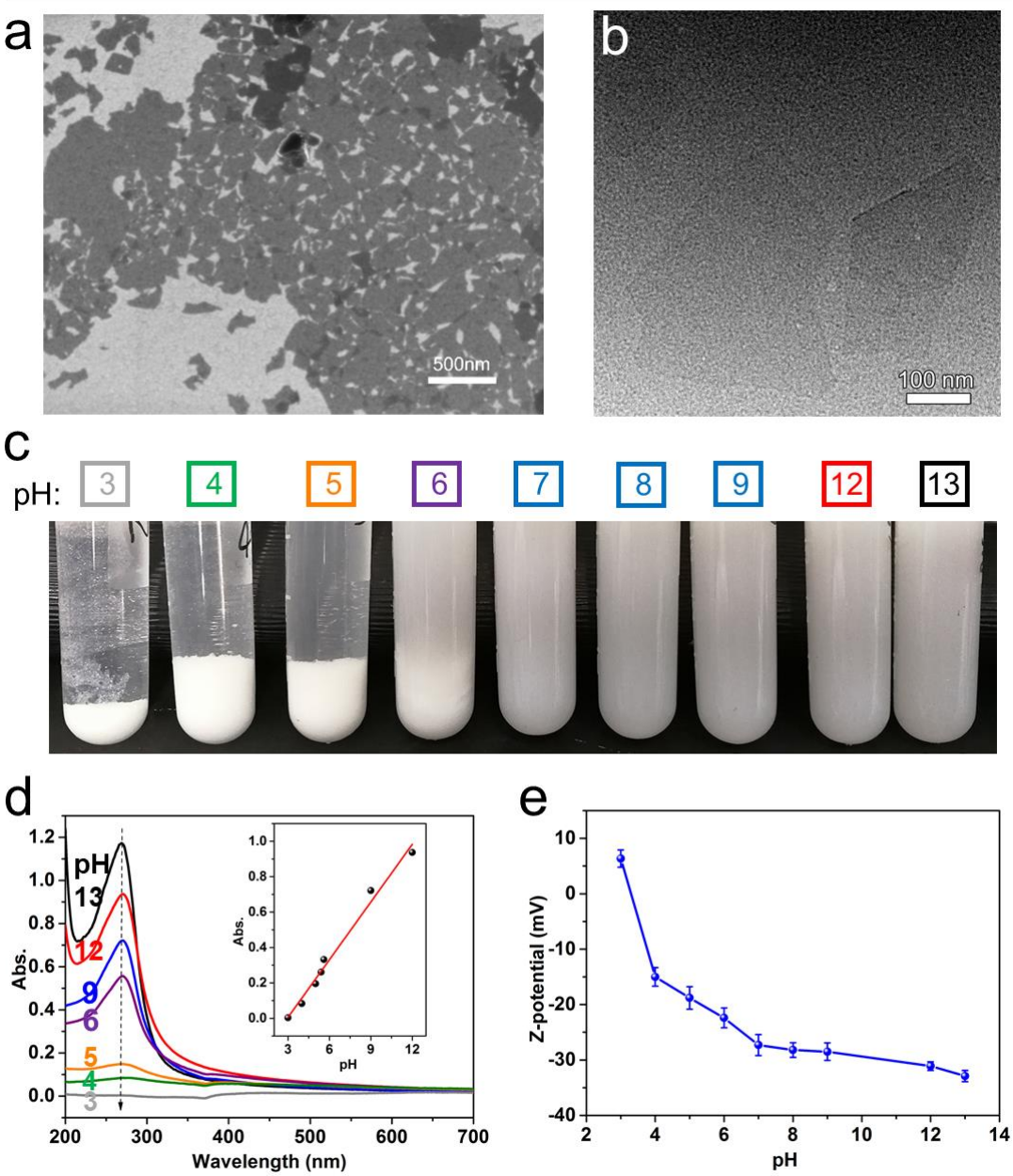


Figure 4. 1 Characterization of L-TiO_2 nanosheets by a) SEM image and b) TEM image. Photographs of colloidal solution of L-TiO_2 nanosheets at different pH (c) and their corresponding UV-Vis spectra (d) and Zeta-potentials (e). The inset in figure (d) corresponds to the plot of the intensity at 266 nm as a function of the pH.

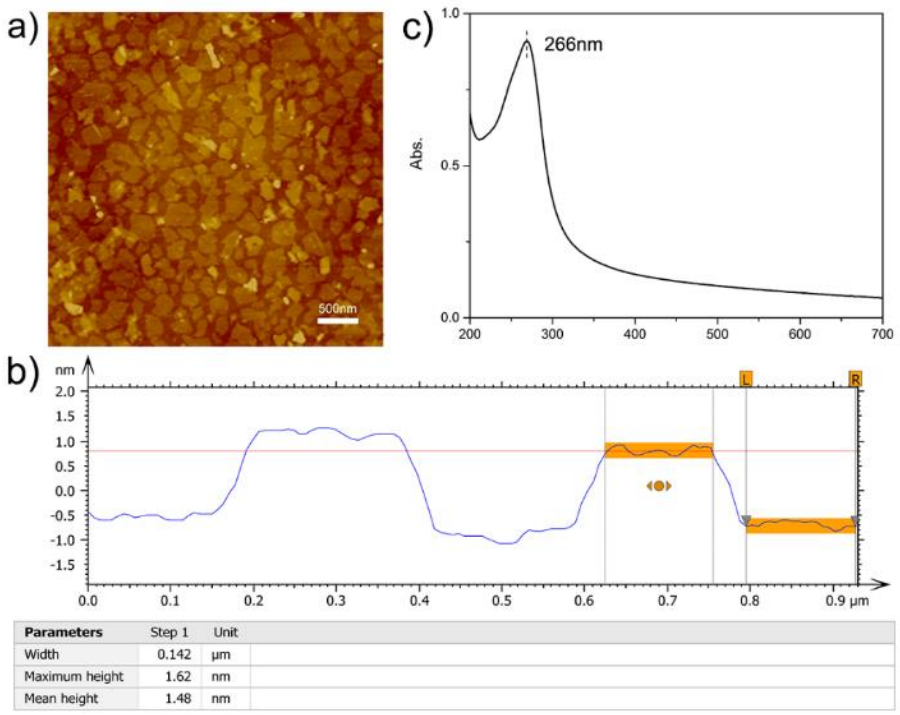


Figure 4. 2 a) AFM image and b) height profile of the L-TiO_2 nanosheets supported on Si wafer, c) UV-Vis spectrum of a colloidal solution of as synthesized L-TiO_2 nanosheets at pH = 12.

Once the presence of exfoliated L-TiO_2 nanosheet and the stability of the suspension of the nanosheets as a function of the pH was confirmed, the hydrothermal phase transition of the nanosheets as a function of the temperature was evaluated at different pHs. The XRD patterns in **Figure 4.3** show no correlation between the phase transition and the pH. On the other hand, this process is exclusively determined by the temperature. The effect of the temperature on the phase transition is shown in **Figure 4.5**. As shown in **Figure 4.5a**, L-TiO_2 nanosheets retain the 2D structure and restack randomly in a layered structure after the following freeze-drying protocol *(i)*. The signals at low angles 2θ = 6.4º, 12.56º, and 18.56º are characteristic of reassembled nanosheets.[25] Following the freeze-drying protocol *(ii)*, an unexpected transition to rutile TiO_2 (R-TiO_2) can be indexed by diffraction peaks at 2θ = 27.56º, 36.14º, and 41.38º, which correspond to (110), (101), and (111) lattice planes (JCPDS 78-1509), respectively. As the temperature increases from 50 ºC to 180 ºC, XRD results clearly show how a new

peak evolves at $2\theta = 25.4^{o}$ and the intensity further increases. In addition, the peaks at $2\theta = 27.56^{o}$, 36.14^{o} gradually weaken and finally disappear. When the temperature reaches 220 ^{o}C, the peaks of the R-TiO_2 phase have completely disappeared and the pure anatase TiO_2 (A-TiO_2) phase is obtained. The signals at $2\theta = 25.4^{o}$, 37.9^{o} and 48.1^{o} correspond to the lattice planes of (101), (004), and (200) (JCPDS 73-1764), respectively.

Generally, rutile, anatase and brookite are the three stable polymorphs of TiO_2 crystals. They are constructed by TiO_6 octahedral but differs to each other in the spatial arrangement of the building blocks. From thermodynamic point, rutile is the most stable form which exhibits tetragonal structure with space group of *P*42/mnm. In the solid annealing reaction, rutile started to form under the temperature being heated to higher than 580 °C. On the contrary, the anatase phase, a tetragonal structure with space group of *I*41/amd, is commonly formed below 450 °C. However, an intriguing abnormal phase transition occurred in this work. Under hydrothermal condition, lepidocrocite titanate nanosheets transformed into rutile phase at lower temperature and then gradually to the anatase phase along the elevated temperature.

To get more information of crystal structure evolution, the XRD refinement of representative TiO_2 transition at 80 °C was performed (**Figure 4.4**). The refinement was performed by Rietveld method. Rutile and anatase phase were used for the fit. The peak at ~48.1° should be assigned to the incompletely transformed L-TO phase. Refined cell parameters are collected in **Table 4.1-4.4**. The rutile obtained from phase transition shows nearly identical a, b, c values (faint enlargement), with negligible expansion of volume. However, a significant compression in the c axis was found on the transformed anatase phase. Compared to the reference, the value of c in anatase shrink from 9.509 Å to 9.165 Å. At the same time, the value of a, b slightly increased. It suggested that remarkable stress was introduced during the transformation of intermediate rutile to anatase, due to the lattice mismatch.

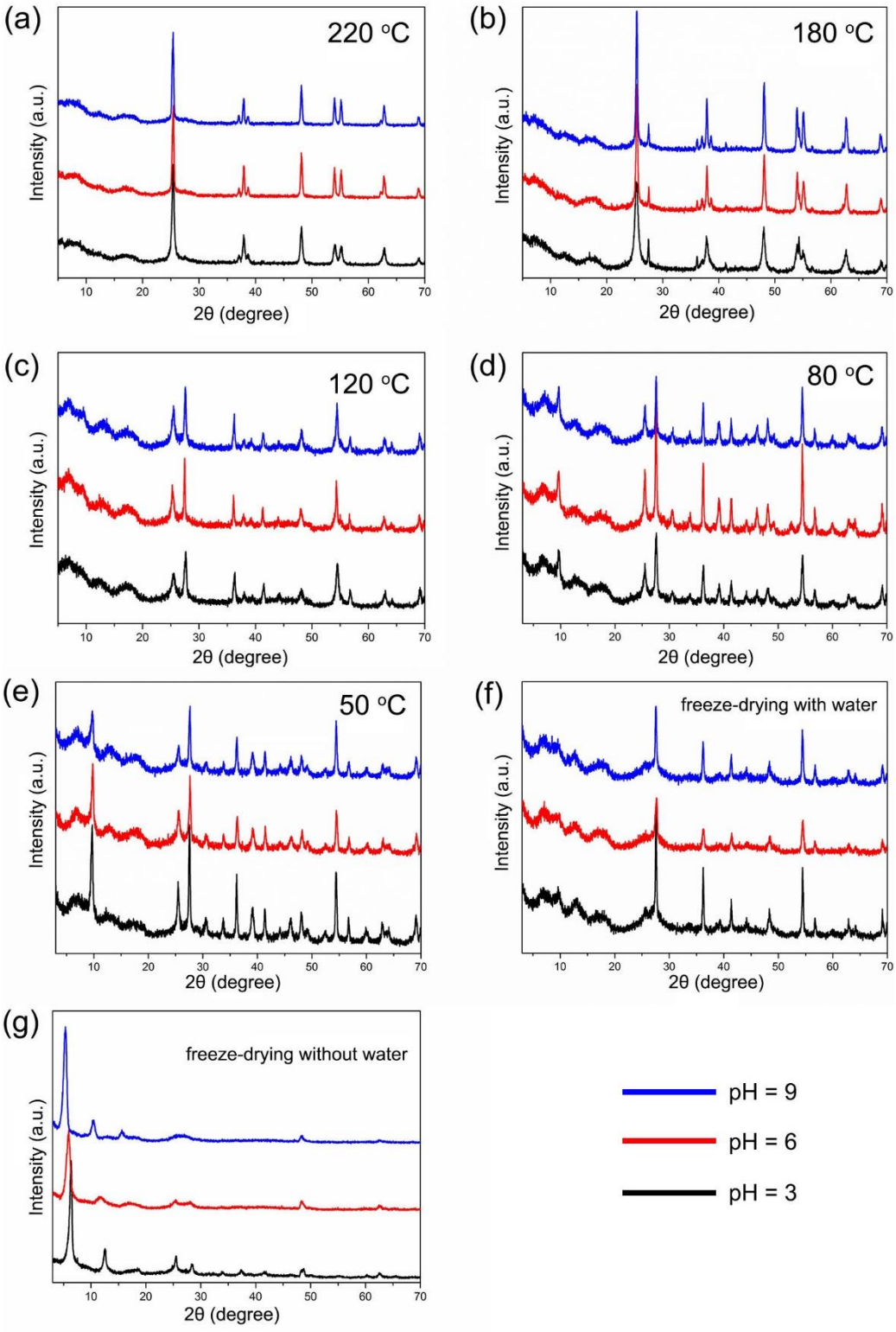


Figure 4. 3 X-ray patterns of different exfoliated L-TiO_2 nanosheets (pH = 3, 6, 9) under different heat treatment as indicated in the figures. (f) freeze-drying with water, (g) freeze-drying without water.

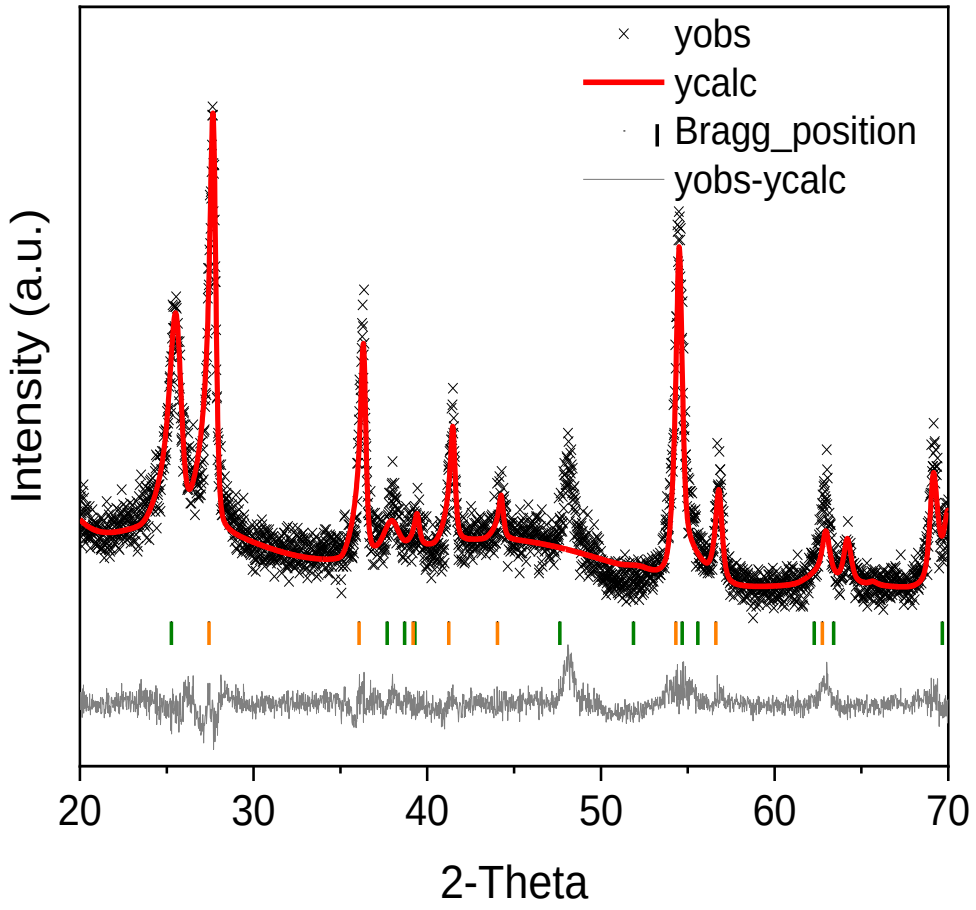


Figure 4. 4 Observed, calculated, and difference profiles from the refinement XRD data of L-TO to A-TO/R-TO transition at 80 °C.

Table 4. 1 Refined cell parameters of Rutile.

	Ref.	Fit
a (Å)	4.5941(1)	4.6060 (1)
b (Å)	4.5941(1)	4.6060 (1)
c (Å)	2.9589(1)	2.9644 (1)
c/a	0.6441	0.6436
V($Å^3$)	62.45	62.89 (4)

R_bragg=6.136

Table 4. 2 Refined structural parameters for rutile using XRD data

Atom	x	y	z	Occupancy	U_{iso}
Ti	0	0	0	1	1
O	0.3057	0.3057	0	1	1

Table 4. 3 Refined cell parameters of Anatase.

	ref	fit
a (Å)	3.799(1)	3.815 (3)
b (Å)	3.799(1)	3.815 (3)
c (Å)	9.509(3)	9.165 (2)
c/a	2.5030	2.4024
V	137.24(8)	133.39 (3)

R_bragg=3.861

Table 4. 4 Refined structural parameters for rutile using XRD data

Atom	x	y	z	Occupancy	U_{iso}
Ti	0	0.25	0.291(5)	1	1
O	0	0.25	0.143(3)	1	1

The phase transition L-TiO_2 nanosheets as a function of the temperature observed by XRD was consistently confirmed using Raman spectroscopy (**Figure 4.5b**). In the Raman spectra of figure 2b, the bands observed at 143, 444 and 609 cm^{-1} are associated with B_{1g}, E_g and A_{1g} active modes of the R-TiO_2 phase. The signal at 240 cm^{-1} can be attributed to the two-phonon scattering mode[27] and the bands at 701 and 2930 cm^{-1} can be attributed to the incomplete conversion of L-TiO_2 nanosheets, as they are similar to the bands of the sample obtained after the freeze-drying protocol (*i*). In the temperature range from 50 °C to 120 °C, the main bands of samples remain unaltered, except that the band at 143 cm^{-1} gradually increases. This indicates that the main structure maintains as R-TiO_2 phase but A-TiO_2 phase starts to be formed. Similar to the results obtained from XRD, as the temperature increases higher than 180 °C, the bands at 444 cm^{-1} (E_g) and 609 cm^{-1} (A_{1g}) of the rutile phase becomes weaker, while the bands at 197, 395, and 515 cm^{-1} associated with the Raman active modes of E_g and B_{1g} of the A-TiO_2 phase[28] appear and their intensities increase as the temperature increases. Same as in the case of the XRD, no further changes were observed when the temperature reached 220 °C, as the bands at 144, 197, 395, 515 and 635 cm^{-1} associated with the A-TiO_2 phase reached full intensity.

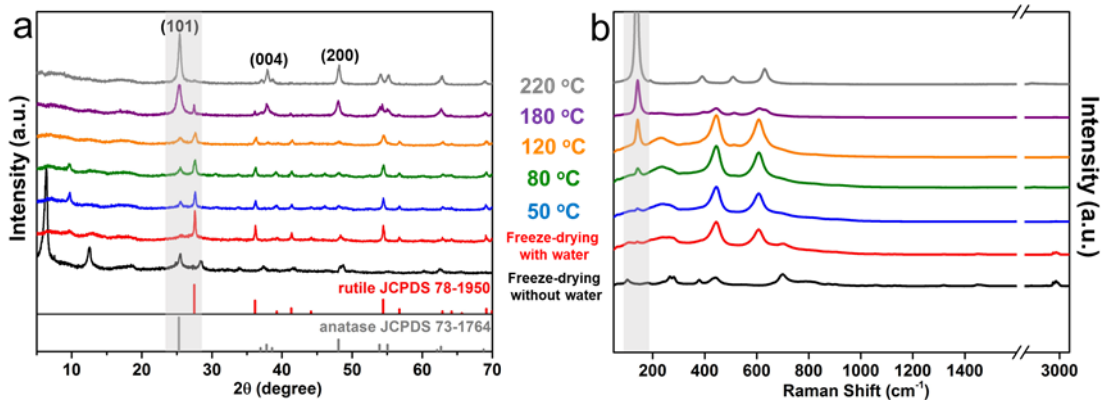


Figure 4. 5 a) XRD diffraction patterns and b) Raman scattering spectra of hydrothermally treated L-TiO_2 nanosheets at pH=3 and at different temperatures as indicated in the figure.

TEM and SEM images of the samples were recorded in order to visualize the

morphological changes of the TiO_2 nanostructures as a function of the temperature. **Figure 4.6** shows electron microscopy images of the restacked L-TiO_2 nanosheets and nanoparticles obtained at 180 ^oC hydrothermal treatment. As can be seen the pH of the synthesis strongly impact on the size and morphology of TiO_2 nanoparticles. The nanoparticles of the sample prepared in pH=3 show granular shape particles with a diameter of ~30 nm (**Figure 4.6d, g, j**). On the other hand, both samples prepared at pH=6 and pH=9, shows A-TiO_2 nanoparticles with a rhomboid-like morphology and a particle size of ~120 nm for the particles prepared at pH=9 and that of ~70 nm for those prepared at pH=6. This suggest that the phase transition and crystal growth is favored under alkaline conditions. A lattice spacing of 0.35 nm was determined from the HRTEM images of the A-TiO_2 nanocrystal prepared at pH=6 and pH=9. This lattice spacing corresponds to the plane (101) of anatase (**Figure 4.7**) confirming the results obtained by XRD on **Figure 4.5a**.

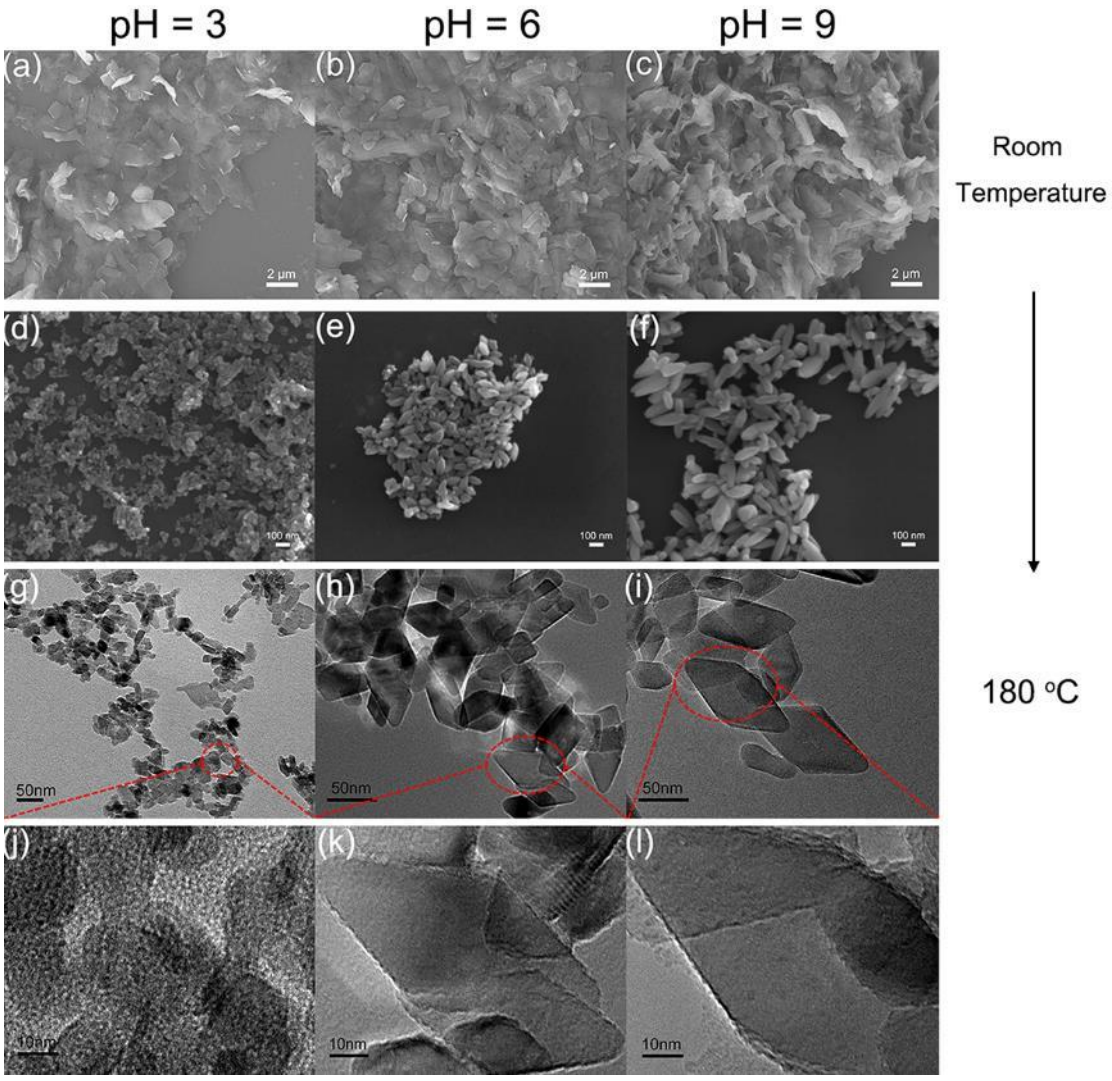


Figure 4. 6 (a-f) SEM images of stacked L-TiO_2 nanosheets and A-TiO_2 nanoparticles at different temperatures and pHs as indicated in the figure. (g-l) TEM images and HRTEM images of A-TiO_2 nanoparticles prepared at different pHs and after treatment at different temperatures as indicated in the figure.

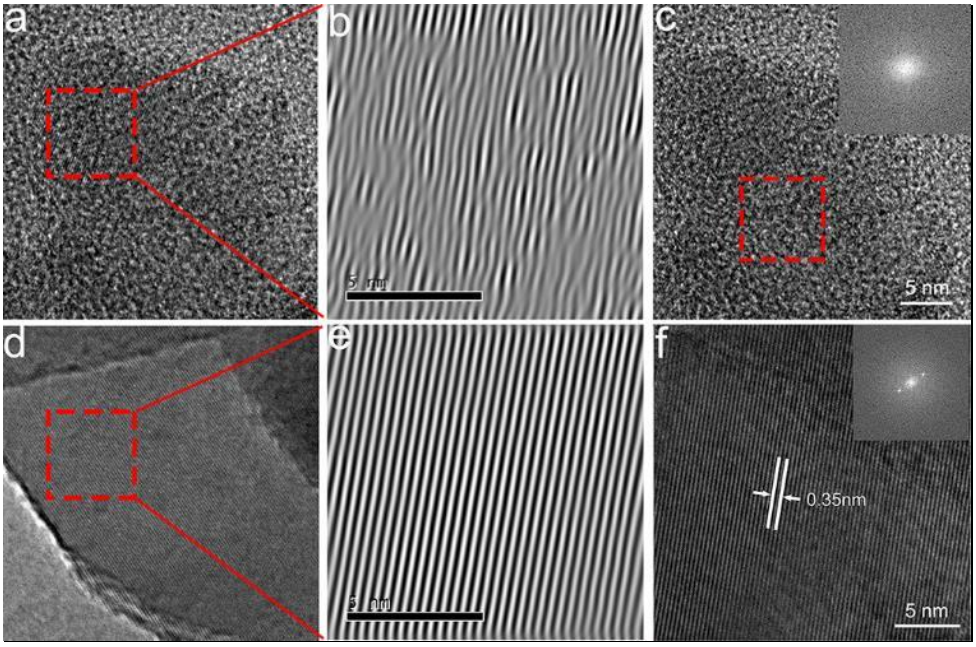


Figure 4. 7 (a), (c) HRTEM image and (b) Inverse FFT image of A-TiO_2 at 180 ºC of pH=3; (d), (f) HRTEM image and (e) Inverse FFT image of A-TiO_2 at 180 ºC of pH=9. The insert in (c), (f) is FFT patterns.

Based on these results, we propose two pH-dependent transition mechanisms of A-L-TiO_2 nanosheets towards the formation of other polymorphs of TiO_2 particles (**Figure 4.8**). In acidic media, pH=3, the phase transition proceeds via a dissolution-recrystallization mechanism, while in neutral and alkaline media pH=6 and pH=9 the phase transition is controlled by a topological rolling mechanism. During the process of dissolution-recrystallization, nanosheets are restacked first and then dissolved in the solution under the harsh acidic environment. For example, as the annealing at 180 ºC proceeds, restacked small nanoplatelets with high free energy tend to dissolve into solution, which leads to a supersaturated solution of titanate. Then, A-TiO_2 starts to precipitate on the surface/edge of flake-like nanoplates (L-TiO_2) and grows up into small granular nanoparticles. Nanoplates eventually disappear and are totally transformed into A-TiO_2 nanoparticles with diameters between 30 to 50 nm. The transformation process of the nanoparticles prepared at pH=3 and annealed at 180 ºC as a function of time (6 h to 24 h) is shown in the SEM images in **Figure 4.9**; the

temperature dependence of the same nanoparticles is shown in **Figure 4.10**. At pH=3, the A-TiO_2 nanoplates undergo structure transformation at 50 ^oC due to dissolution. Such transformation process is enhanced even further at higher temperatures. At 80 ^oC, the SEM images indicate a significant increase in the rugosity of nanoparticles and a gradual transformation of the nanoplates into a round shape are observed. When the annealing temperature reaches 120 ^oC, only smaller amorphous particles were observed in the SEM images. The evidence and poor crystallization of the resulted A-TiO_2 nanoparticles confirmed by the HRTEM image (**Figure 4.7**) strongly support such recrystallization process.

In the case of the samples prepared at neutral/alkaline pH (pH=6 to 9), the phase transition is dominated by the topological rolling mechanism.[29, 30] HRTEM and SEM images show highly oriented shuttle-like nanocrystals with a large aspect ratio of length to thickness. The lattice spacing of d_{101} = 0.35 nm related to the (101) plane is the most preferentially exposed (**Figure 4.7**). The XRD results (**Figure 4.11**) confirm that the L-TiO_2 precursor exhibit a typical interlayer plane of (010), which is responsible for the (101) plane of resultant nanocrystals owing to topological rolling.[31] The temperature dependence of the nanoparticles is shown in **Figure 4.10**. Two-dimensional nanosheets with high surface energy could not maintain good dispersion any more as being suffered from heat treatment. They started to split and roll in order to reduce the Gibbs free energy. As shown in **Figure 4.8,** these smaller nanoplates are finally transformed into single nanocrystals via topologically rolling into shuttle-like particles.

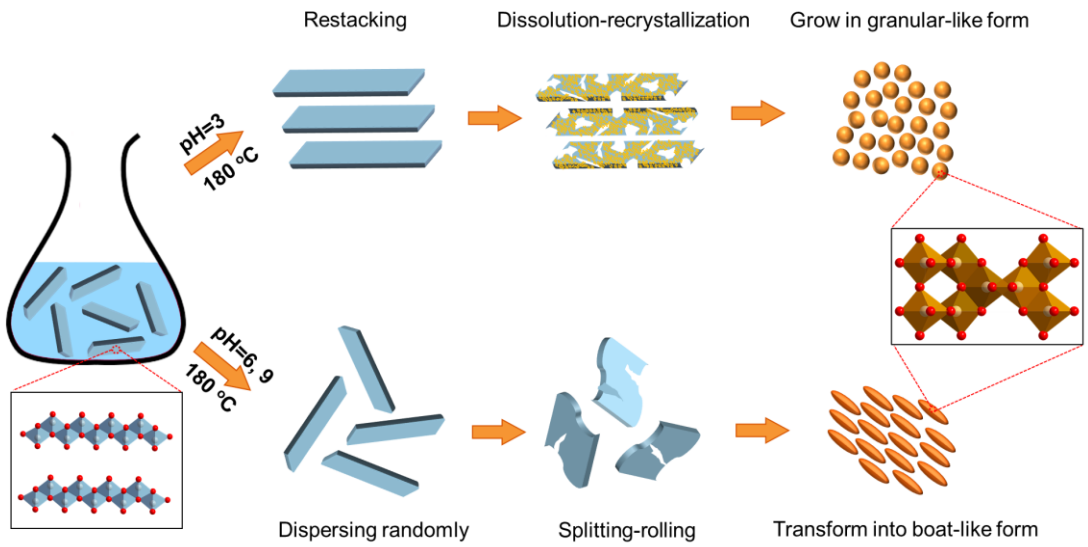


Figure 4. 8 Schematic illustrations for the pH-dependence transition mechanism of L-TiO_2 to A-TiO_2 nanoparticles.

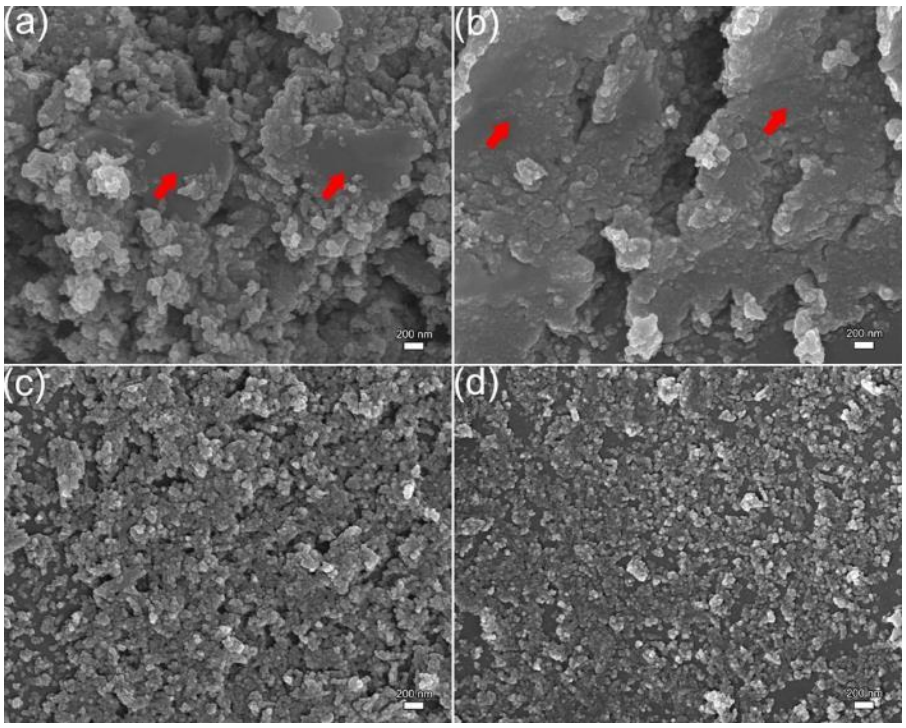


Figure 4. 9 SEM images of the L-TiO_2 samples prepared at pH=3 and annealed at 180 ^{o}C at different times (a) 6 h, (b) 12 h, (c) 18 h, and (d) 24 h.

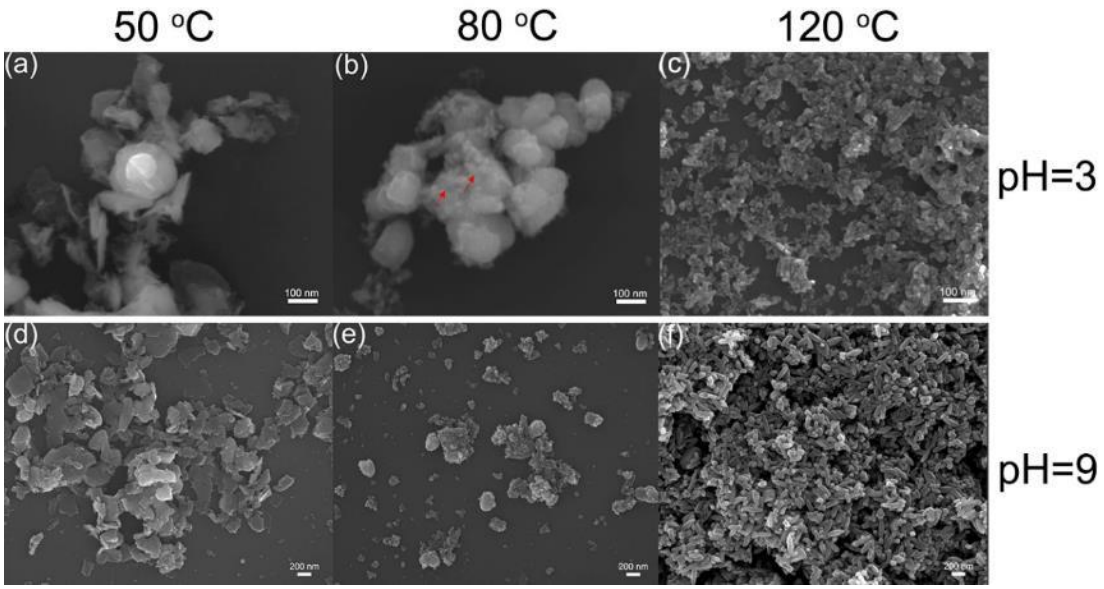


Figure 4. 10 SEM images of hydrothermal treatment of L-TiO_2 (pH=3) and pH=9 at different annealing temperatures as indicated in the figure.

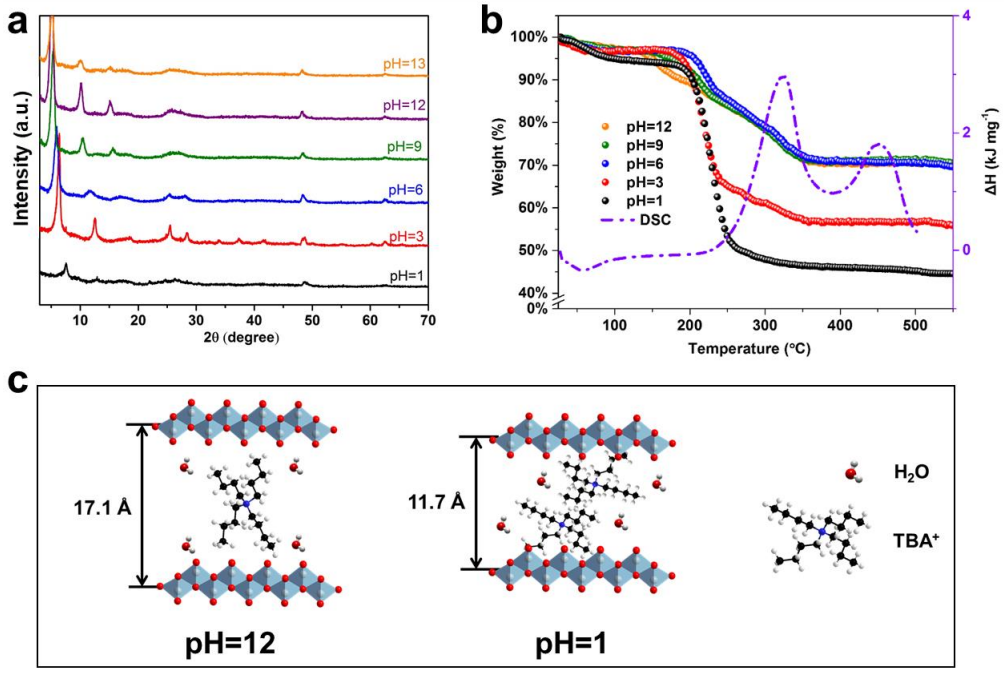


Figure 4. 11 (a) X-ray diffraction patterns of restacked L-TiO_2 nanosheets at different pH's, (b) Thermogravimetric analysis of L-TiO_2 nanosheets adjusted at different pH followed by freeze-drying protocol (ii). (c) Schematic graph of TBA intercalated in L-TiO_2 with different orientations under different pHs.

4.3.2 Characterization of Pt decorated TiO_2

All the Pt decorated samples are synthesized through a photochemical reduction reaction (**Figure 4.12**) under the same parameters except for different TiO_2 supports, including A-TiO_2 from phase transition, exfoliated lepidocrocite TiO_2 (denote as L-TiO_2) and its parent H_xTiO_2 (denote as HTO) and also commercial TiO_2 (denote as TiO_2-C) (details are shown in Methods section 4.2.3). Firstly, XRD patterns in **Figure 4.13** show that the A-TiO_2 samples from different pH phase transitions preserve the crystal structure from their parent counterparts after the photochemical reaction. All of them mainly consist of anatase phase. No extra metal Pt phase was detected. It was also observed that the nanoparticle sizes are different for pH=3 and pH=9 and pH=12. For example, the main peak at 25.35° show clear difference in full width at half maximum (FWHM), with 0.661° for pH=3 and 0.239° for pH=9. According to Scherrer equation:[32]

$$D = K\lambda/\beta\cos\theta \qquad [4.1]$$

where D denote crystal size, K is Scherrer constant which depends on crystal shape, size distribution. λ is the wavelength of incident X-ray, θ is diffraction angle, β is FWHM. It can be calculated that the crystal size of the sample (regarding to plane (101)) at pH=9 is roughly 3-fold larger than that at pH=3, which is consistent with the SEM results (**Figure 4.14-15**).

Different to Pt decorated A-TiO_2 samples that keep the same crystal phase to their parent counterparts during the photochemical reduction reaction, the layered lepidocrocite-TiO_2, both HTO and exfoliated L-TiO_2, were subjected to certain degree of phase transition in response to UV irradiation. As shown in **Figure 4.14**, as-synthesized HTO show ordered stacked layered structure while the L-TiO_2 show randomly stacked layered structure, which is the same as the literatures.[25] After intensified UV irradiation for 1 h, some new phases such as anatase (JCPDS 04-0477) rutile (JCPDS 87-0710), Ti_9O_{17} (JCPDS 50-0791) were detected (**Figure 4.15**). Simultaneously, the layered structure is preserved with signals at low angle regions

corresponding to the interlayer lattice plane. Pt@L-TiO_2 holds the interlayer spacing of 1.71 nm while this value is 0.69 nm for Pt@HTO. Such photochemically induced phase transition can be ascribed to the flexibility of layered structure.

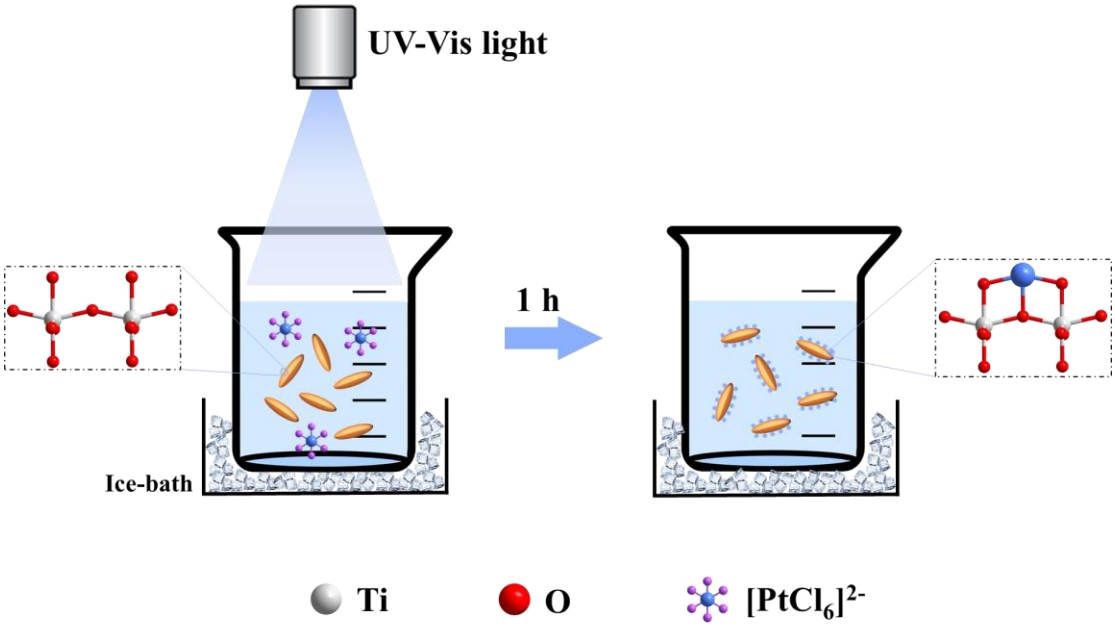


Figure 4. 12 Schematic graphs of photochemical reduction deposition of Pt on A-TiO_2.

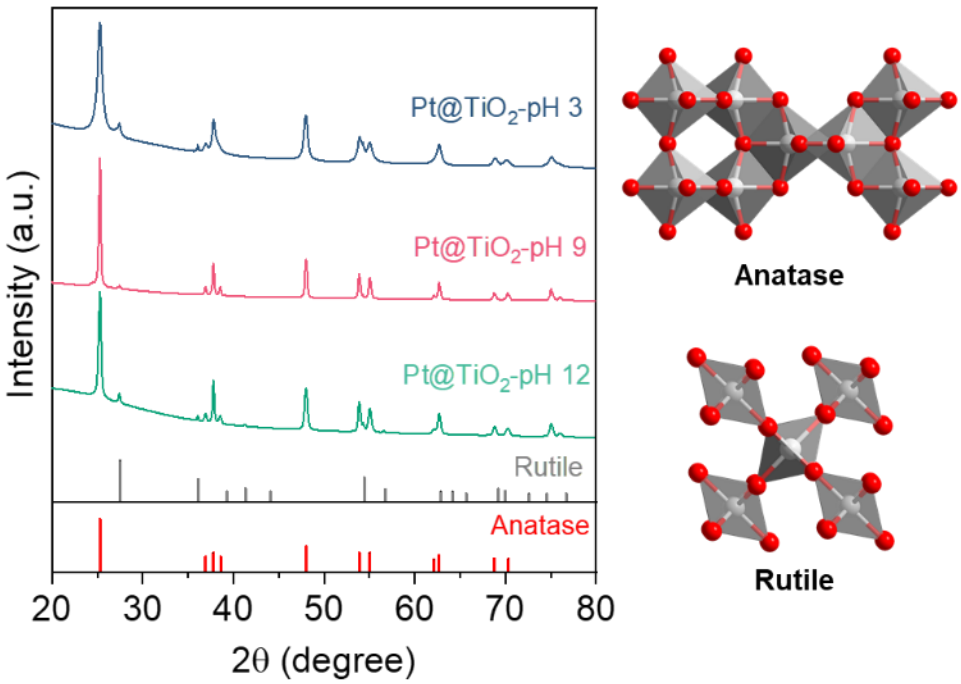


Figure 4. 13 X-ray diffraction patterns of Pt decorated TiO_2 samples synthesized by a photochemical reduction reaction.

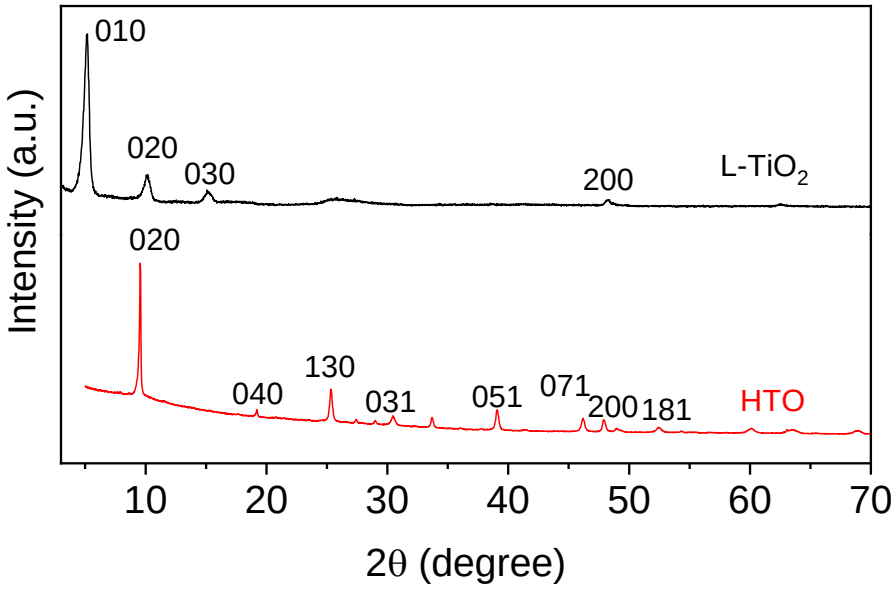


Figure 4. 14 X-ray diffraction patterns of as-synthesized HTO and L-TiO_2.

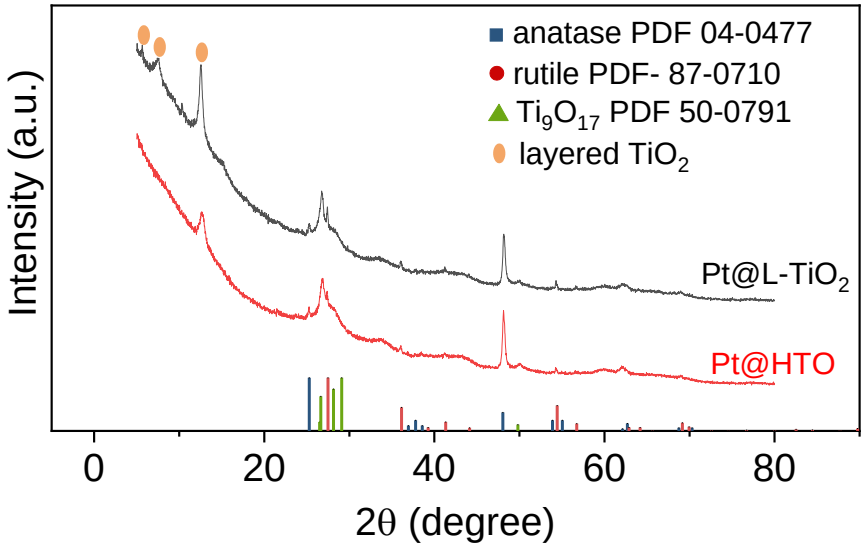


Figure 4. 15 X-ray diffraction patterns of Pt@HTO and Pt@L-TiO_2 after photochemical reduction reaction.

The morphologies of Pt decorated TiO_2 samples at pH=3 and pH=9 are shown in **Figure 4. 16**. They maintain the same shape and size to the pristine phase (**Figure 4. 16a,b** and **Figure 4.17**), of which granular shape at pH=3 and rhomboid-like form at pH=9 are inherited. This implies that the photochemical reduction reaction does not change the

phase morphology of TiO_2 support. The obtained Pt@TiO_2 nanoparticles kept clean surface that metallic Pt nanoparticles had not been found, in accordance with the XRD results. HAADF-STEM images and corresponding EDS mapping in **Figure 4.17** also confirm the low loading of Pt and its homogeneous dispersion on TiO_2 supports. Further annealing at N_2 atmosphere did not remarkably change the morphology, as presented in **Figure 4. 16c, d**. The control sample Pt@TiO_2-pH12 showed the same morphology as Pt@TiO_2-pH9 (**Figure 4.18**), indicating the coherent reaction mechanism in alkaline conditions. Other Pt decorated samples on different TiO_2 supported were also characterized and compared in **Figure 4.19**. Commercial TiO_2 presents a granular shape similar to Pt@TiO_2-pH3, while both Pt@HTO and Pt@L-TiO_2 are in the form of nanoflakes. The difference of these two layered supports is the thickness, size and degree of restacking order. The lateral size of Pt@HTO nanoparticles is 3-4 folds larger than Pt@L-TiO_2.

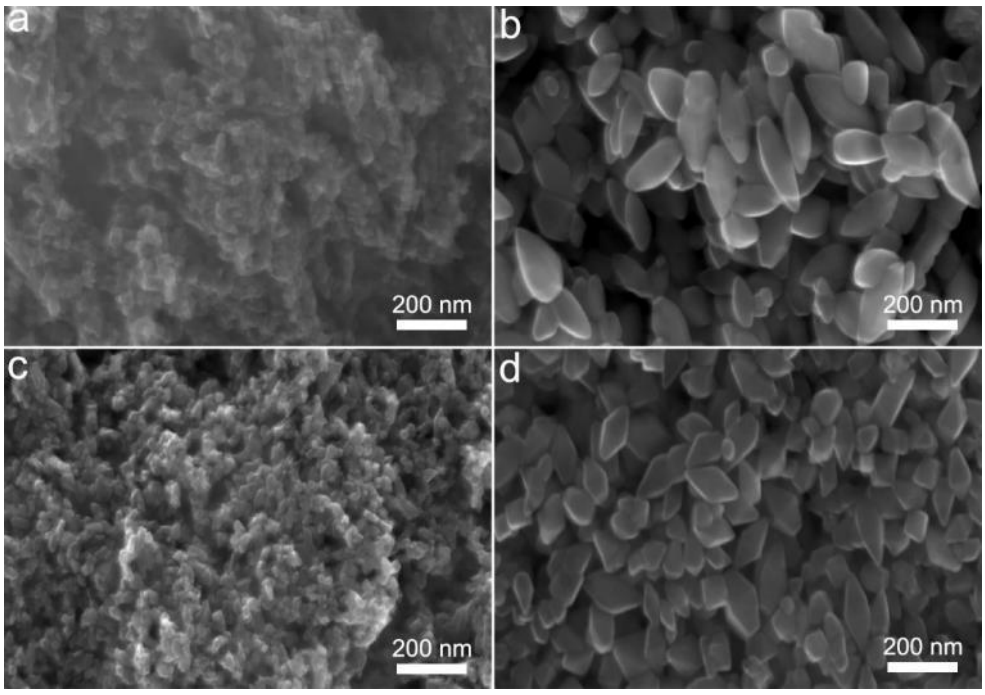


Figure 4. 16 SEM images of (a) Pt@TiO_2-pH3, (b) Pt@TiO_2-pH9, (c) Pt@TiO_2-pH3-N300, (d) Pt@TiO_2-pH9-N300.

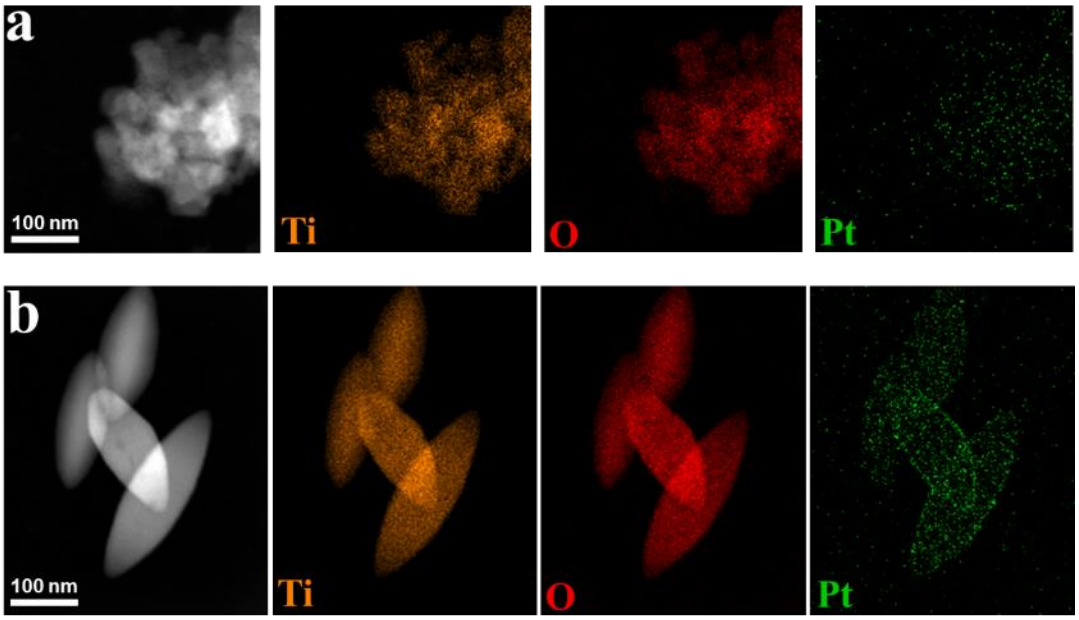


Figure 4. 17 HAADF-STEM images of (a) Pt@TiO_2-pH3, (b) Pt@TiO_2-pH9 with EDS elemental mappings.

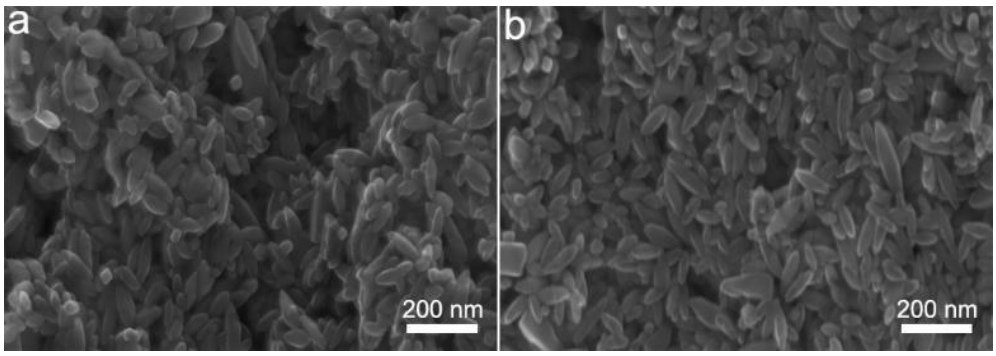


Figure 4. 18 SEM images of (a) Pt@TiO_2-pH12, (b) Pt@TiO_2-pH12-N300.

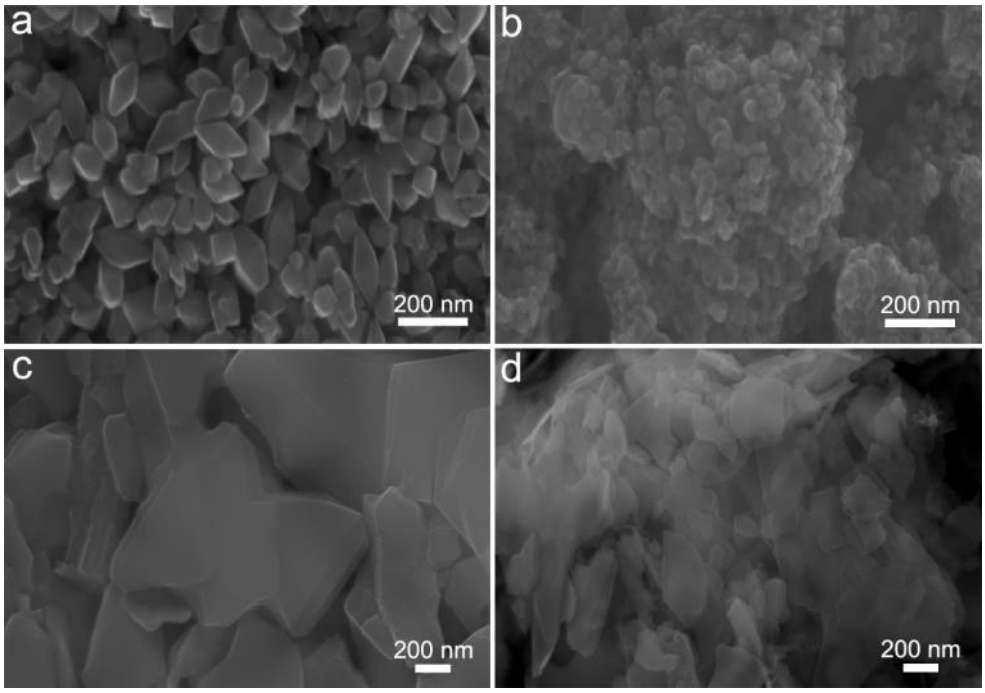


Figure 4. 19 SEM images of (a) Pt@TiO_2-pH9-N300, (b) Pt@TiO_2-C, (c) Pt@HTO, (d) Pt@L-TiO_2.

Besides size and morphology differences, the Raman vibration models were recorded for Pt@TiO_2 samples to extract the Ti-O bond information. Raman spectra in **Figure 4.20a** show the same vibration models of all samples, indicating the same crystal phase, which is consistent with the XRD results. Moreover, all the samples maintain the same vibration models when compares with the pristine phase (**Figure 4.5**). The fingerprint signals at 144, 197 and 636 cm^{-1} can be assigned to E_g models, while 396 and 521 cm^{-1} are associated with B_{1g} model and last 513 cm^{-1} associated with A_{1g} model.[33] Since Raman scattering is very sensitive to crystallinity and microstructures of materials, the peak intensity and position reflects vibration details that are directly correlated to structure. Comparison of the most intense E_g vibration model in **Figure 4.20b** shows the frequency redshift and intensity increase of Pt@TiO_2-pH9, demonstrating better crystallinity in line with XRD results. The vibration models are summarized in **Figure 4.21** for detailed analysis. By integrating peak area, the ratio of each vibration model can be obtained. **Table 4.5** collects all the calculated vibration percentages. The E_g and A_{1g} models of Pt@TiO_2-pH9 increase while the B_{1g} model decreases when compared

to Pt@TiO_2-pH3. It suggests that Ti-O bending strengthened in the a and b axis and weakened in the c axis. FTIR spectra in **Figure 4.22** show consistent results with the Raman data. The broad absorption band at 648 cm^{-1} for Pt@ TiO_2-pH3 was shifted to 671 cm^{-1} for Pt@TiO_2-pH9, which corresponds to the Ti-O-Ti stretching model.[34] Higher vibration energy of Pt@TiO_2-pH9 indicates strengthened Ti-O stretching.

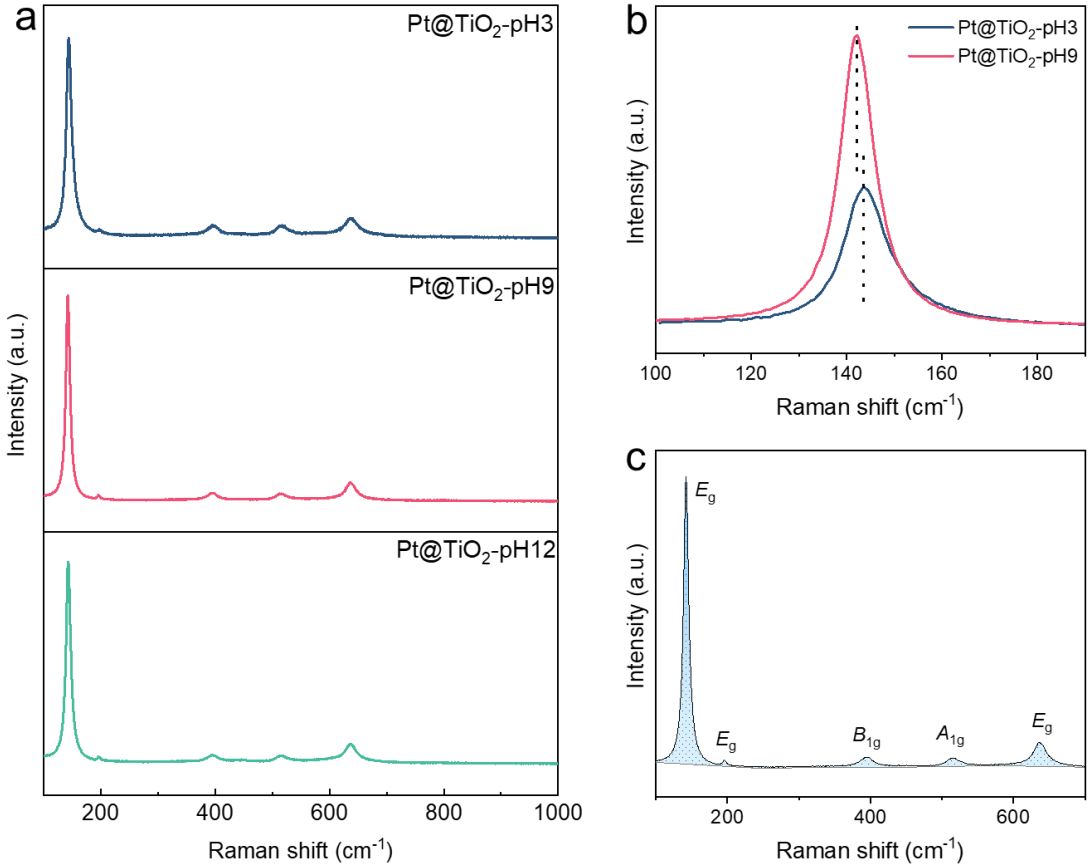


Figure 4. 20 (a) Raman spectrums of Pt@TiO_2 at different pHs, (b) enlarged area of E_g model at *ca.* 142 cm^{-1} of Pt@TiO_2-pH3 and Pt@TiO_2-pH9, (c) integration of each vibration models.

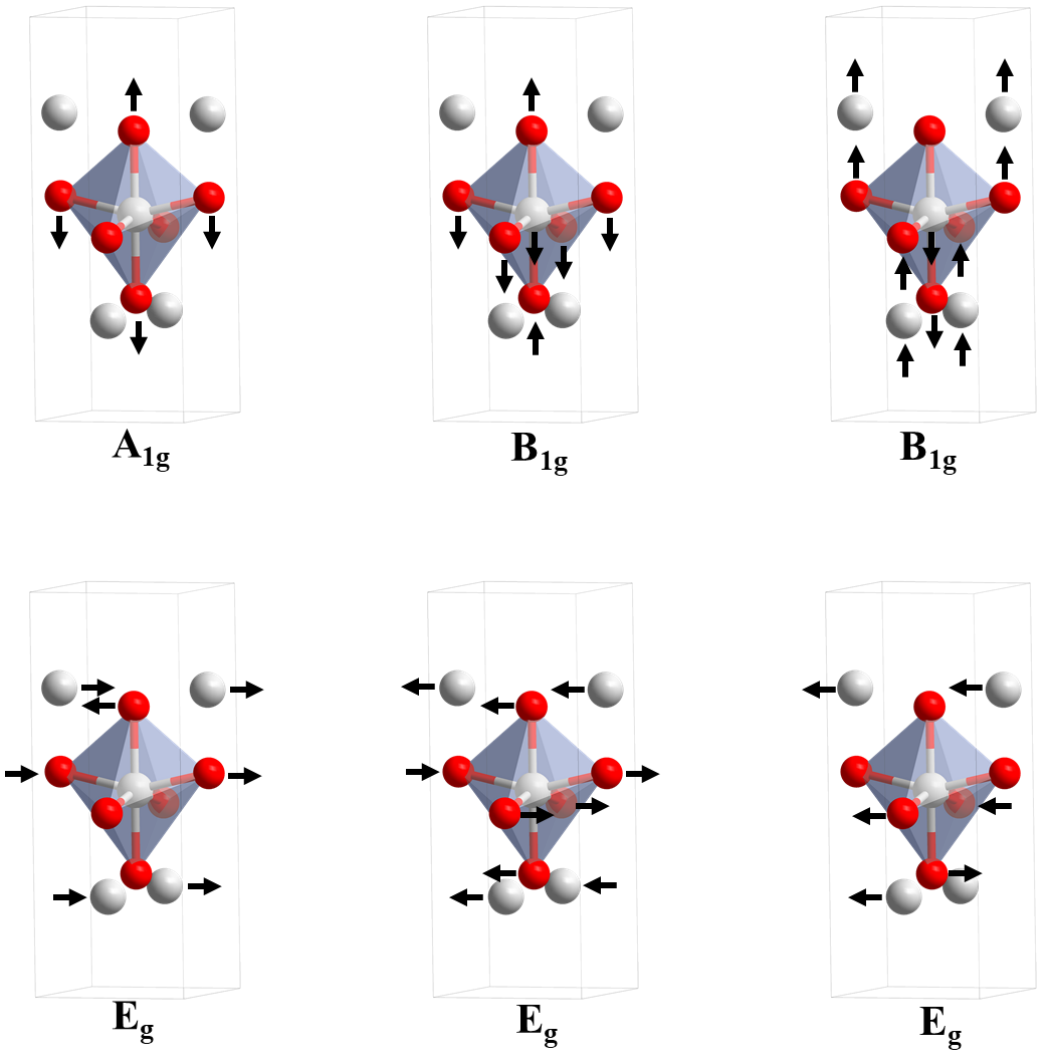


Figure 4. 21 Vibration models of anatase TiO_2.[28]

Table 4. 5 Integral areas of different vibration models of Pt@TiO_2 at different pHs.

	E_g	A_{1g}	B_{1g}
Pt@TiO_2-pH3	39443.12	1102.95	5136.29
	86.34%	2.41%	11.24%
Pt@TiO_2-pH9	62314.46	1966.87	7176.64
	87.20%	2.75%	10.04%

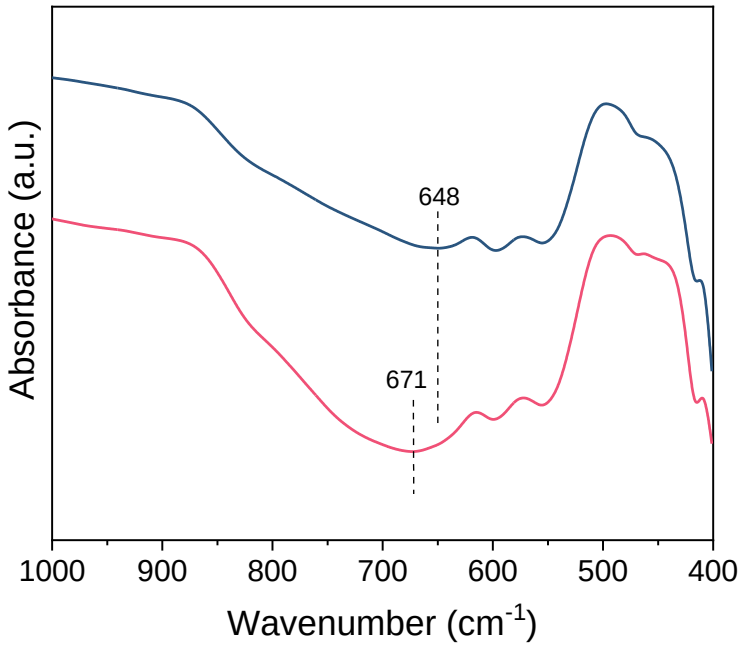


Figure 4. 22 FTIR spectra of Pt@TiO_2-pH3 (blue) and Pt@TiO_2-pH9 (red).

Since the absorption associated d-d transition strongly depends on the electronic stucture, UV-Vis spectra were recorded to evaluate the electronic structure of Pt decorated TiO_2 samples.[35] As shown in **Figure 4.23**, pristine TiO_2-pH9 show red-shifted UV-Vis spectra when compared to the TiO_2-pH3, indicating a different absorption behavior. A discernable absorption peak was found at *ca*. 336 nm in TiO_2-pH9 and *ca*. 266 nm in TiO_2-pH3. After the photochemical reaction, obvious change was found on both samples. The absorption of Pt decorated TiO_2 samples shift from UV region to visible light region as compared to the unreacted A-TiO_2. Specifically, the absorption shoulder of Pt@TiO_2-pH3 shifts from 381 nm (pristine TiO_2-pH3) to 412 nm, with the band gap changed from 3.25 eV to 3.0 eV. While the Pt@TiO_2-pH9 presents a wide broad absorption curve in the visible light region, indicating considerable electronic structure modification. The UV-Vis absorption spectra are in line with the sample colour (inserted optical images in **Figure 4.23**). Since Pt@TiO_2 samples at different pHs have the same crystal phase, the difference in UV absorption properties after the photochemical reaction can be associated with the morphology and exposed lattice plane. Highly exposed (101) plane of TiO_2-pH9 has stronger interaction

with UV-Vis light irradiation than amorphous nanoparticles prepared at pH=3, leading to the different electronic structures of TiO_2 support. Different electronic structure of the support further employs different interactions with the decorated Pt species. This intepretation is demonstrated by the comparison of Pt@TiO_2-pH3 and reference sample Pt@TiO_2-C. Both show nearly identical crystal phase (anatase) and morphology and particle size (**Figure 4.16&4.19**). The UV-Vis spectra in **Figure 4.24** show that they hold the nearly identical absorption properties after photochemical reduction of Pt.

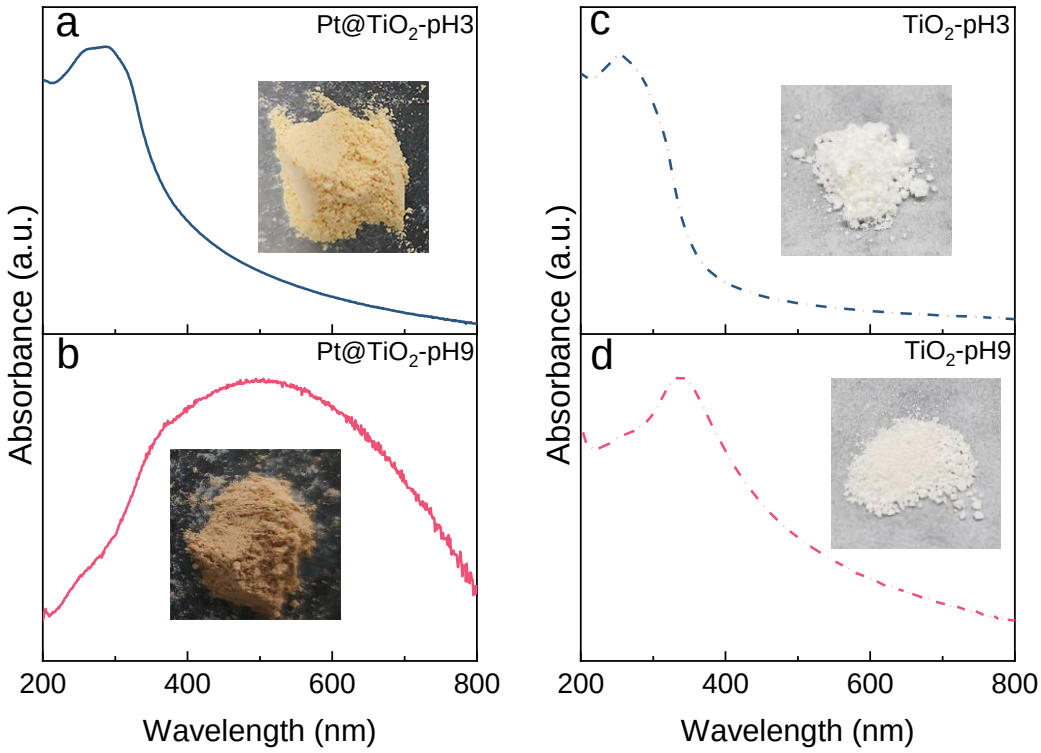


Figure 4. 23 UV-Vis spectra of Pt decorated A-TiO_2 samples prepared at different pHs. Insert images are photographs of corresponding samples.

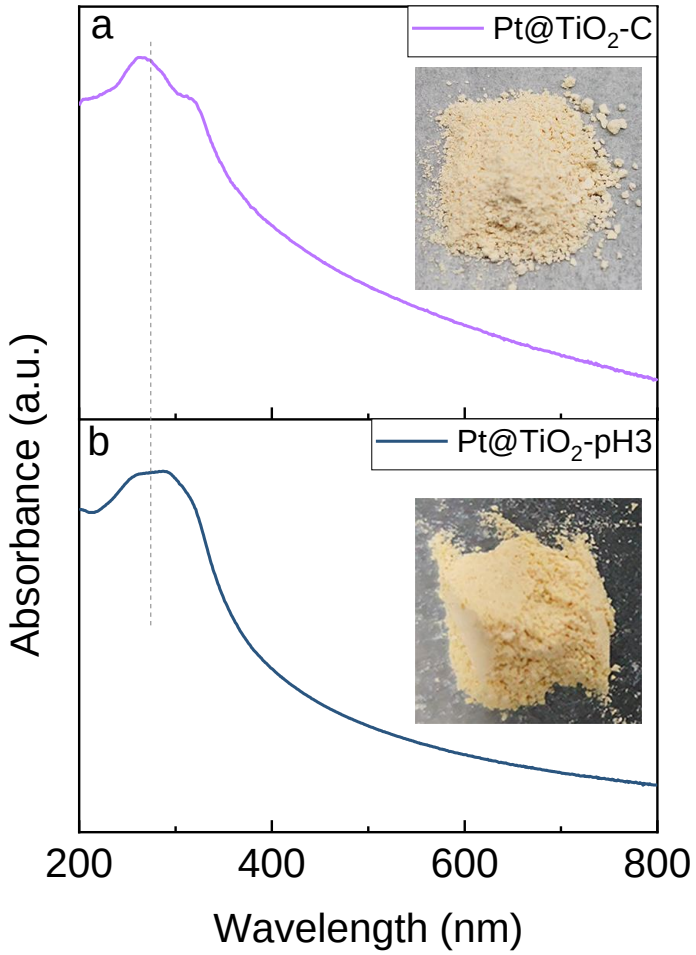


Figure 4. 24 UV-Vis spectra of (a) Pt@TiO_2-C and (b) Pt@TiO_2-pH3. Inset images are photographs of corresponding samples.

In addition, XPS was carried out to characterize the chemical composition of Pt decorated TiO_2 samples. As shown in **Figure 4.25**, the high-resolution spectra of Pt 4f, O 1s, and Ti 2p of Pt@TiO_2 at pH=3 and 9 are compared. Two prominent peaks at *ca*. 458.69 eV and 464. 44 eV of Pt@TiO_2-pH3 can be assigned to Ti $2p_{3/2}$ and $2p_{1/2}$ due to the spin-orbital coupling effect. The doublet binding energy with splitting $\Delta = 5.75$ eV indicates typical anatase TiO_2 characterization.[36] In contrast, the Ti $2p_{3/2}$ peak of Pt@TiO_2-pH9 positively shifted by 0.2 eV with regard to Pt@TiO_2-pH3. As for the photochemical deposited Pt species, the $4f_{7/2}$ peak of Pt@TiO_2-pH3 at *ca*. 72.5 eV implies a Pt(II) oxidation state, which is lower than that at 74.9 eV for PtO_2 and higher than that at 71.0 eV for metallic Pt.[37, 38] Oxidized Pt was obtained instead of metallic

Pt, which can be rationally interpreted by the strong interaction between decorated species and oxide support.[39, 40] Compared to that of Pt@TiO_2-pH3, Pt 4f spectra of Pt@TiO_2-pH9 is shifted to lower energy direction, at which the $4f_{7/2}$ peak locates around 71.88 eV, implying an oxidation state lower than Pt(II). The variation of Ti and Pt spectra clearly suggests the charge transfer from the Ti atoms to adjacent Pt species at the Ti-O-Pt configuration, which gives rise to enhanced Ti and weakened Pt binding energy in Pt@TiO_2-pH9. Detailed fit results are presented in **Figure 4.26**. In Pt@TiO_2-pH9 sample, the Pt^0 species count for the largest proportion of 45.5%, and outperforms the Pt^{2+} of 35.2% and Pt^{4+} of 19.3% (summarized in **Table 4.6**). Pt^0 species as the majority confirms the lower average oxidation state. In addition, the comparison of Ti 2p, O 1s, and Pt 4f spectra in Pt@TiO_2-pH3 and the reference sample Pt@TiO_2-C was also performed. As shown in **Figure 4.27**, the Pt 4f, Ti 2p and O 1s spectra are identical between the two samples, indicating comparable chemical status. It is consistent with the UV-Vis absorption and associated with the electrochemcial results in below.

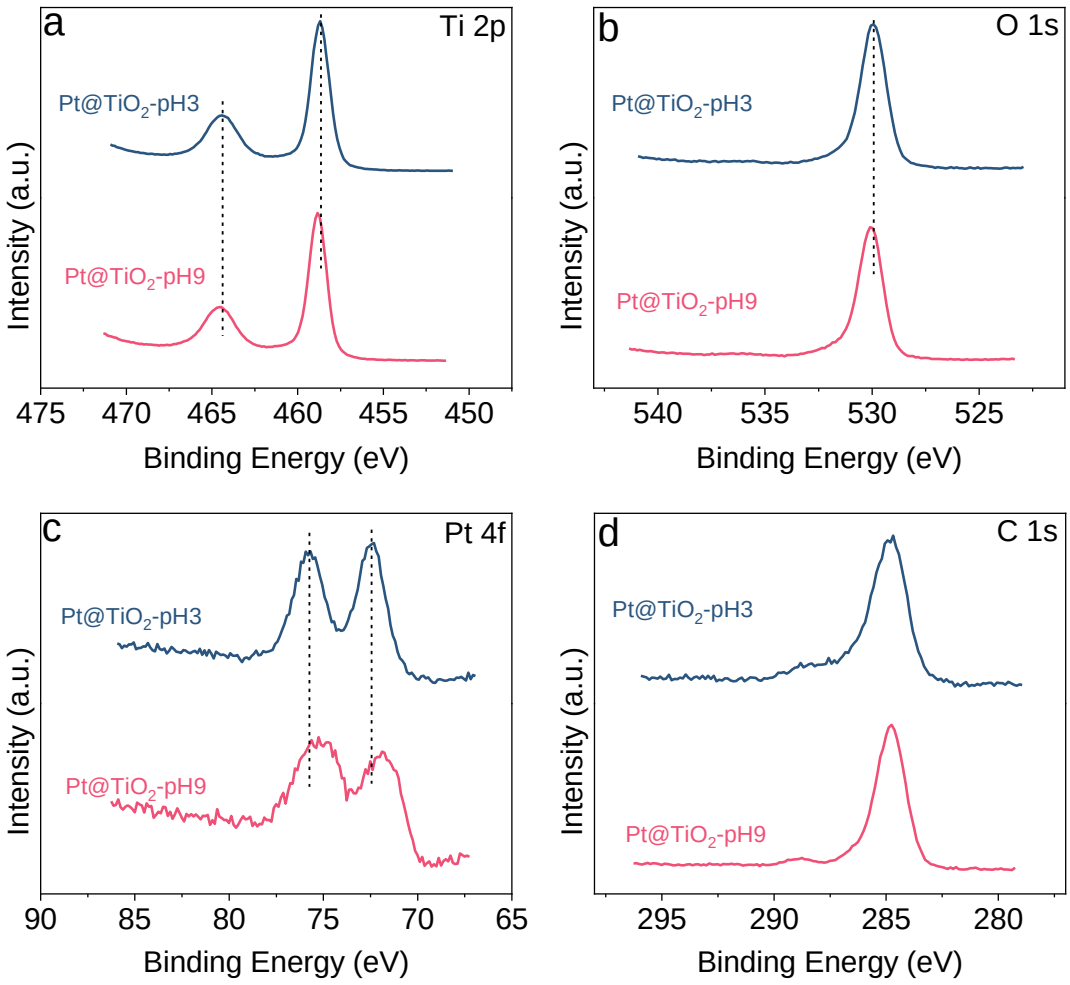


Figure 4. 25 High resolution XPS of Pt@TiO_2 at different pHs, (a) Pt 4f, (b) O 1s, (c) Ti 2p, (d) C 1s.

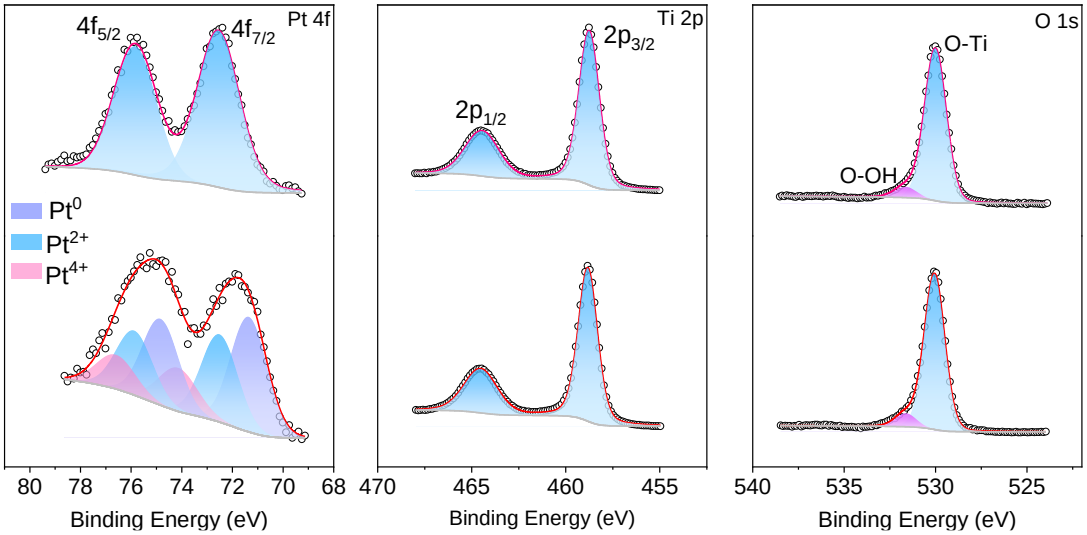


Figure 4. 26 Fit results of high-resolution XPS of Pt 4f, Ti 2p, O 1s on Pt@TiO_2-pH3 and Pt@TiO_2-pH9. All of the baselines are Shirley curve.

Table 4. 6 Binding energies, FWHM and area percentage of each component of Pt(4f) fit spectra on Pt decorated A-TiO_2 samples from Figure 4.25.

Catalyst	Species	$4f_{7/2}$ (eV)	$4f_{5/2}$ (eV)	FWHM	%Area
Pt@TiO_2-pH3	Pt^{2+}	72.55	75.84	1.98	100
Pt@TiO_2-pH9	Pt^0	71.35	74.84	1.70	45.5
	Pt^{2+}	72.51	75.87	1.70	35.2
	Pt^{4+}	74.15	76.61	1.82	19.3

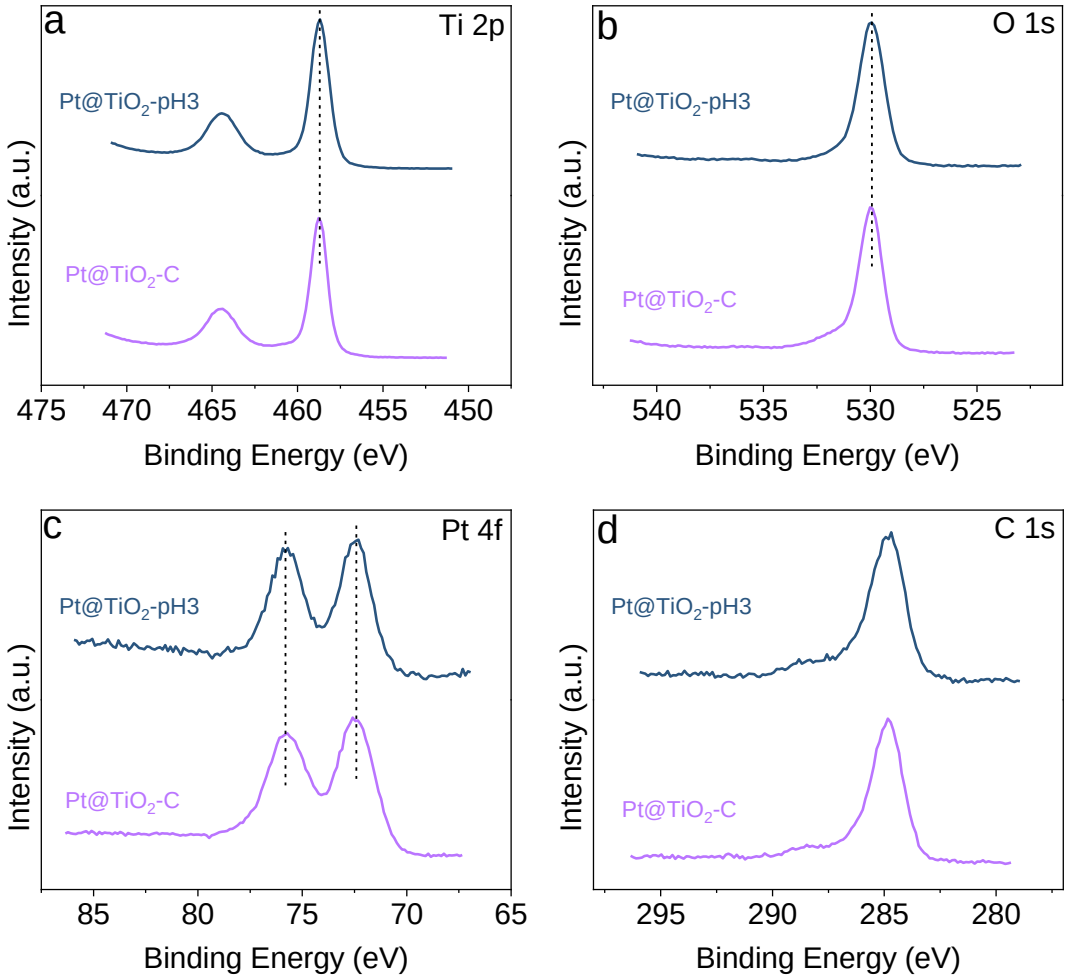


Figure 4. 27 High resolution XPS of Pt@TiO_2-pH3 and Pt@TiO_2-pH3-C, (a) Pt 4f, (b) O 1s, (c) Ti 2p, (d) C 1s.

4.3.3 Electrochemical study of Pt decorated TiO_2

The electrochemical HER performances of Pt decorated samples were evaluated in Ar-saturated 0.5 M H_2SO_4 aqueous solution using a three-electrode system. As shown in **Figure 4.28a**, Pt@TiO_2 samples synthesized at different pHs show different HER catalytic activity. Compared to Pt@TiO_2-pH3, Pt@TiO_2-pH9 displays clearly lower onset overpotential to initiate the hydrogen evolution, indicating higher intrinsic activity. To yield a current density of 10 mA cm^{-2}, Pt@TiO_2-pH9 requires an overpotential (η_{10}) of 86 mV, superior to Pt@TiO_2-pH3 (125 mV). Moreover, the Pt@TiO_2 samples prepared at pH=9 and pH=12 exhibit nearly identical performance. Based on the physical characterizations above, the TiO_2 support synthesized in alkaline medium has the same crystal phase and morphology, regardless of the pH difference. This led to an identical UV-Vis response which induced interaction between Pt species and TiO_2 support. Thus, nanoparticles with the same morphology can correspond to the same photochemical properties, giving rise to identical HER activity.

On the other hand, compared to the amorphous nanoparticle of TiO_2 obtained at pH=3, highly exposed (101) plane on TiO_2-pH9 has a stronger response to UV irradiation during the photochemical reduction process. It is confirmed by the UV-Vis spectra and the optical images of Pt decorated TiO_2 samples after the photochemical reaction (**Figure 4.23**). The narrow band gap of TiO_2-pH9 led to broader adsorption range of the UV-Vis light, which excited larger electron population to higher energy level. These photogenerated electrons migrated to the surface of TiO_2 to reduce the Pt-containing precursor. The reduced Pt species, therefore, has a strong interaction with the TiO_2 support through chemical bonding, which determines the final chemical state of Pt and can be reflected by the nanoparticle color. The chemical states of Pt on different TiO_2 supports and Pt-O-Ti interaction were confirmed by XPS in **Figure 4.25-26**. Enhanced charge transfer from support Ti atoms to decorated Pt species was found on Pt@TiO_2-pH9. The outer surface of the support itself, in turn experienced chemical state modification during the photochemical deposition of Pt. Thus, it can be concluded that

the Pt species on Pt@TiO_2-pH9 with modified electronic structure favors H adsorption, which gives rise to better HER activity.

After being subjected to annealing at 300 °C for 1 h under N_2 atmosphere, all the HER activities of three samples are improved. Specifically, the η_{10} of Pt@TiO_2-pH3-N300 was reduced to 97 mV, while the values of Pt@TiO_2-pH9-N300 and Pt@TiO_2-pH12-N300 were 30 mV and 35 mV, respectively. With the annealing treatment, the catalytic performance of Pt@TiO_2-pH9 and Pt@TiO_2-pH12 were still kept identical and superior to that of Pt@TiO_2-pH3. All the η_{10} values are summarized in **Figure 4.29**.

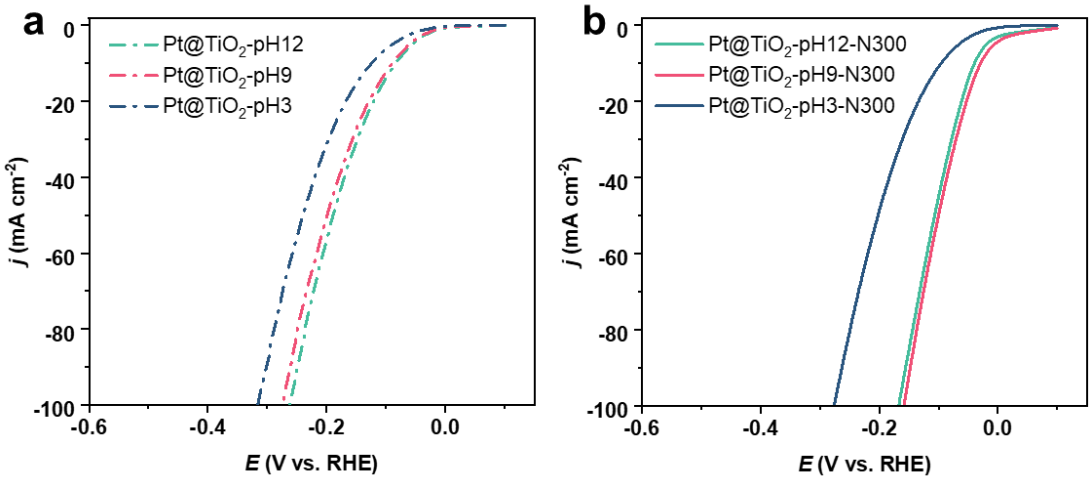


Figure 4. 28 LSV curves of Pt@TiO_2 samples prepared in different pHs: (a) as-synthesized, (b) annealing at 300 °C in N_2 atmosphere. The samples were measured in 0.5 M H_2SO_4 solution with scan rates υ = 5 mV s^{-1}.

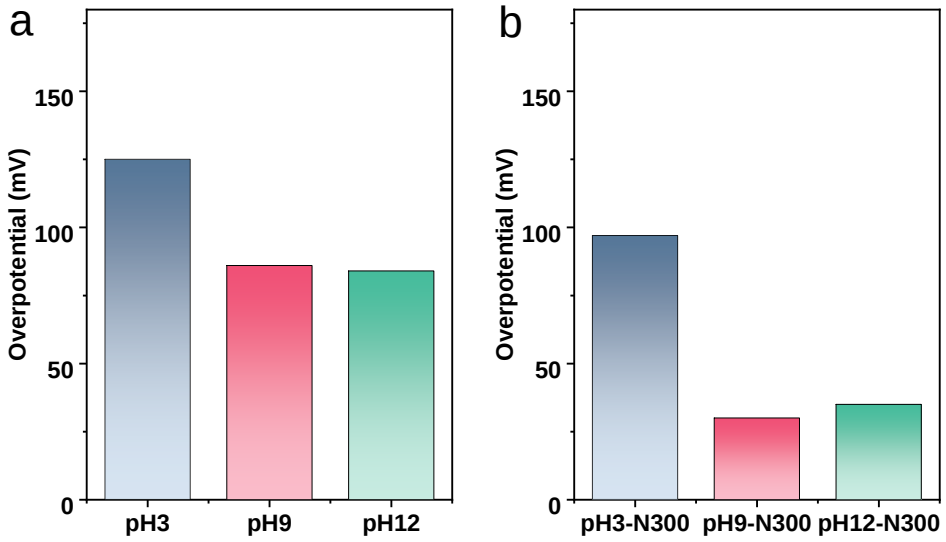


Figure 4. 29 Overpotentials at 10 mA cm^{-2} for Pt@TiO_2 samples prepared at different pHs, (a) as-synthesized, (b) after annealing at 300 °C in N_2 atmosphere.

In addition to TiO_2 prepared by phase transition under different pHs, some other TiO_2 supports are also included for comparison. The layered structured HTO, exfoliated L-TiO_2 nanosheets, commercial TiO_2 nanoparticles were selected. As shown in **Figure 4.30**, the LSV (normalized by geometric area) of Pt@TiO_2-pH9-N300 is nearly overlapping to commercial Pt/C (20 wt%), indicating the excellent HER activity. Slight differences in the HER onset region can be reflected by Tafel slopes, showing 43 mV dec^{-1} for Pt@TiO_2-pH9-N300 and 40 mV dec^{-1} for the commercial Pt/C. The η_{10} of Pt@TiO_2-pH9-N300 is 30 mV, slightly smaller than Pt/C (as seen in **Figure 4.31**). Among the Pt decorated TiO_2 samples, Pt@TiO_2-pH9-N300 displayed best HER performance followed by the activity trend of Pt@HTO > Pt@TiO_2-C > Pt@L-TiO_2. Both Pt@HTO and Pt@L-TiO_2 with the layered structure, where (010) lattice plane is mostly exposed, are less active for HER than Pt decorated A-TiO_2 prepared by phase transition.

In order to evaluate the long-term stability, chronoamperometry of Pt@TiO_2-pH9-N300 and commercial Pt/C were performed under -0.03 V vs. RHE in 0.5 M H_2SO_4. As seen in **Figure 4.30c**, after unintermittent 24 h hydrogen evolution catalysis under harsh

acidic condition, Pt@TiO_2-pH9-N300 retains a current density of 88.5%. In contrast, the current density of commercial Pt/C dropped fast to 56.7% in the initial 1 h and then kept a slow decrease rate in the following 10 h. LSV of Pt@TiO_2-pH9-N300 after chronoamperometry show η_{10} of 87 mV, which is 57 mV higher than the initial one. Pt@TiO_2-pH9-N300 with degradation of ~10% displayed superior durability than the tested Pt/C in our work and the literature.[41]

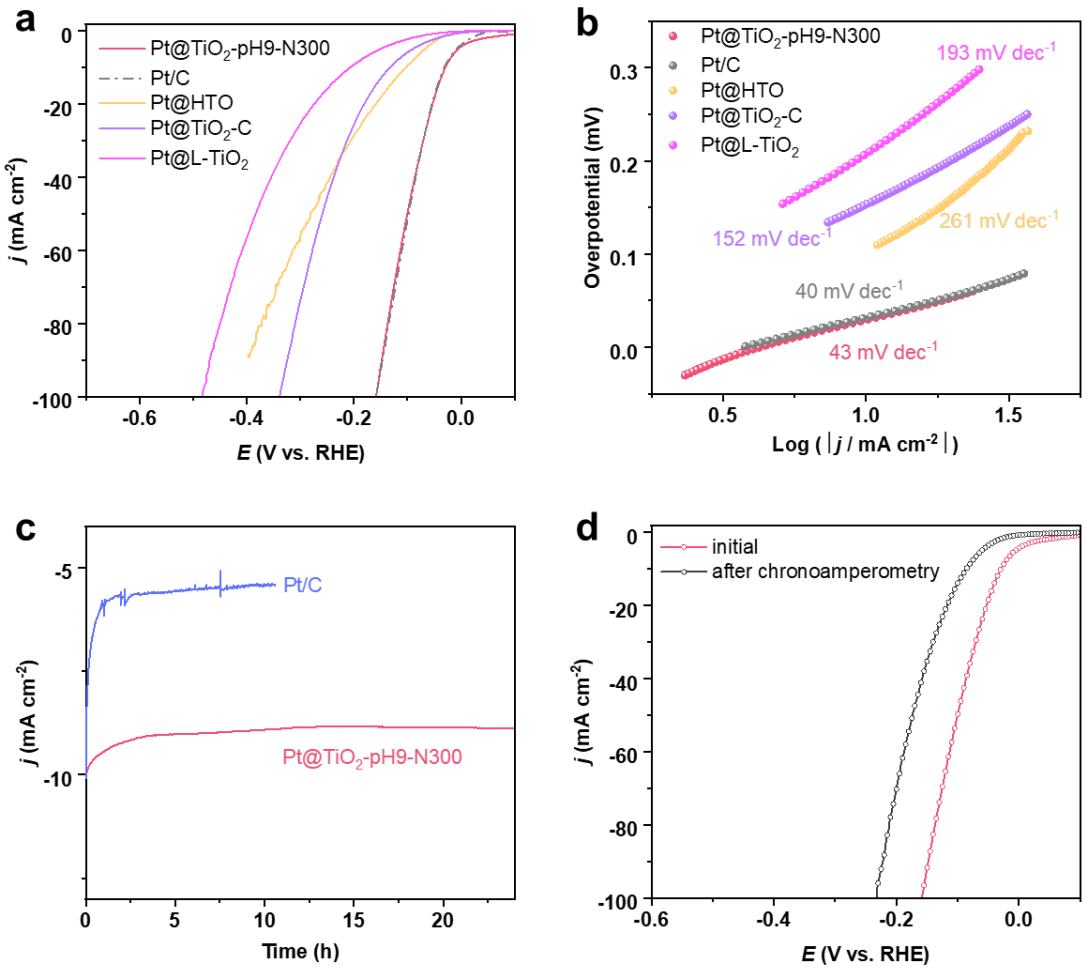


Figure 4. 30 (a) LSV curves (b) Tafel slopes of Pt@TiO_2-pH9-N300, Pt@HTO, Pt@TiO_2-C and Pt@L-TiO_2 in 0.5 M H_2SO_4, with a scan rate of υ = 5 mV s^{-1}. (c) Chronoamperometry for 24 h, (d) LSV before/after chronoamperometry test of Pt@TiO_2-pH-N300.

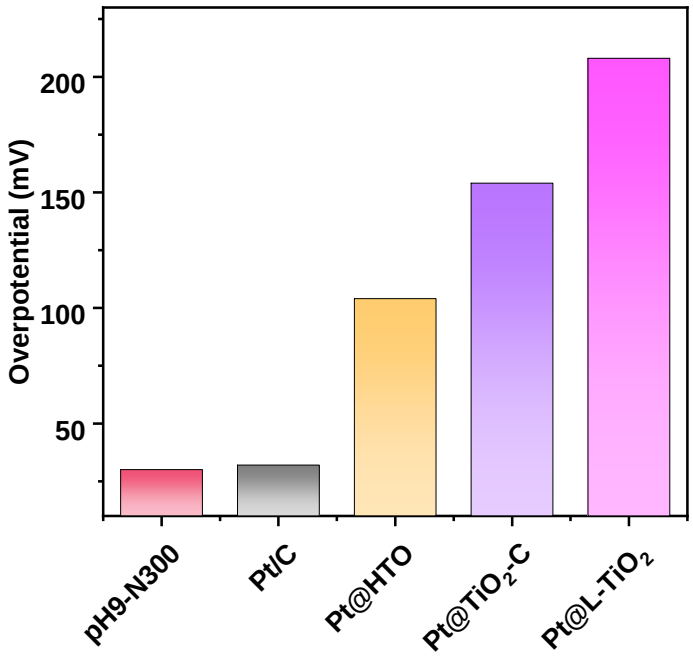


Figure 4. 31 Overpotentials η_{10} (mV) for different Pt-decorated TiO_2 supports and the Pt/C reference.

The control sample Pt decorated commercial-TiO_2 (Pt@TiO_2-C) was introduced for comparison, which has the same crystal phase (anatase), morphology and particle size to the Pt@TiO_2-pH3 (**Figure 4.16** and **Figure 4.19**). Correspondingly, these two samples showed the same response to the UV-Vis light and exhibited same color (**Figure 4.24**). Pt@TiO_2-pH3 and Pt@TiO_2-C in **Figure 4.32** exhibited almost the same HER activity. In detail, the η_{10} is 125 mV for Pt@TiO_2-pH3 while Pt@TiO_2-C requires 133 mV to reach 10 mA cm^{-2}. At the same time, Tafel curves suggest that the increased current density of Pt@TiO_2-pH3 and Pt@TiO_2-C was kept the same. These results combined with the XPS data in **Figure 4. 27** support our interpretation that HER activity is directly associated with the chemical state of Pt, which is determined by the interaction between Pt and TiO_2 support where the charge transfer from Ti to Pt was confirmed. The interaction is controlled by the photochemical properties of TiO_2 support, on which photogenerated electrons dominated the reduction reaction. The morphology and exposed lattice plane are directly related to the photochemical property of the TiO_2.[42, 43] Therefore, the correlation between electrochemical HER activity and

morphology can be found.

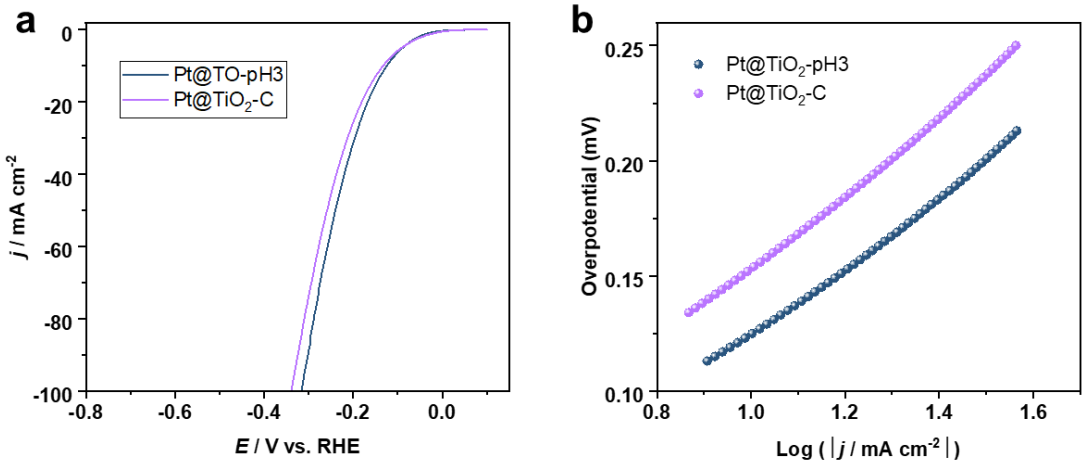


Figure 4. 32 (a) LSV curves (b) Tafel slope of Pt@TiO_2-pH3 and Pt@TiO_2-C.

It should be note that the ECSA of Pt species are not directly measured in this work. In regards to the electrochemical activity normalized by electrode areas (geometric activity), the ECSA can be an important factor in addition to the electronic effects. Highly dispersed Pt species might expose more surface sites than the commercial Pt/C that can contribute to the catalytic current. Under this circumstance, mass activity (normalized by the loading of Pt) can provide more accurate information to evaluated the catalyst performance.

We performed ICP-MS to detect the loading of Pt species on TiO_2 support. **Figure 4. 32** show the linear fitted standard curves of reference samples, which is used for determining the content of measured sample which falls in the range of 0-1000 ppb. Thus, the acquired Pt, Ti content are collected in **Table 4.7**. The Pt loading of Pt@TiO_2-pH9 is 1.12 wt%, this value is 1.26 wt% for Pt@TiO_2-pH3, 0.78 wt% for Pt@TiO_2-C, and 0.84 wt% for Pt@L-TiO_2. Compared to the commercial Pt/C (20 wt%) catalyst, Pt@TiO_2-pH9 show 17.8-fold less Pt. This, in turn, gives rise to higher mass activity. **Figure 4.33** shows the activity normalized by Pt loading at an overpotential of 30 mV, and almost all the Pt decorated TiO_2 samples outperform the commercial Pt/C. The annealed Pt@TiO_2-pH9 exhibit the highest specific activity of 3954 A g_{Pt}^{-1} that attributes

to the low loading of Pt species (1.12 wt%).

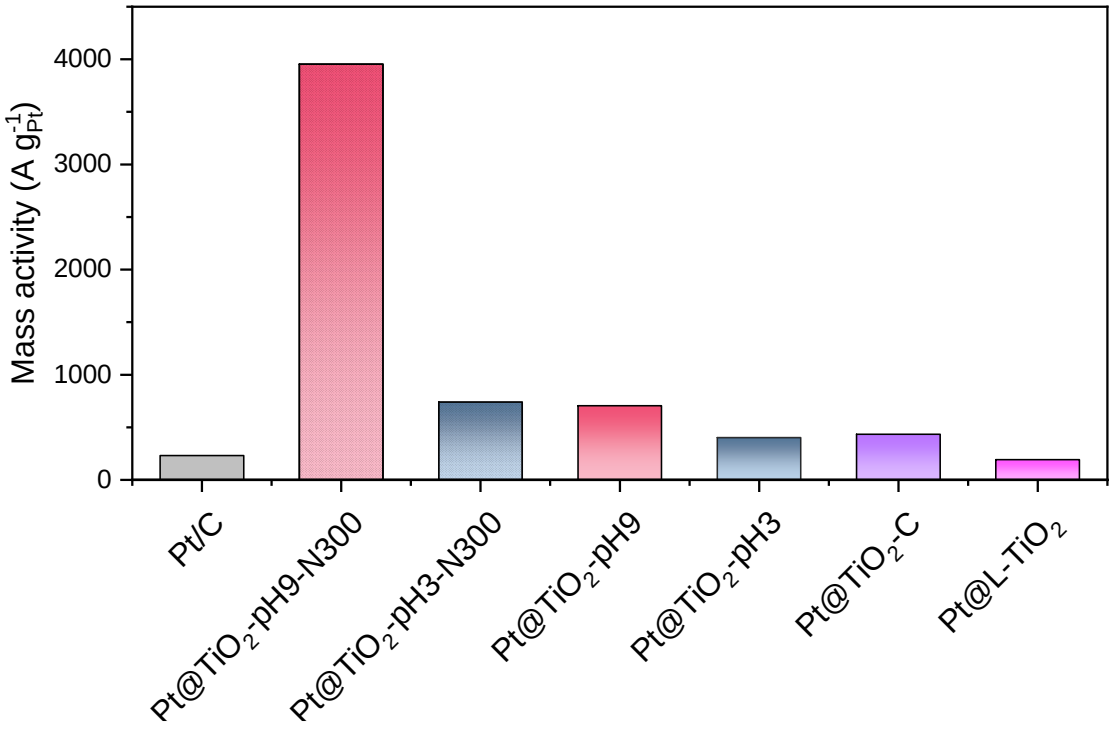


Figure 4. 33 Mass activity of Pt decorated samples, at the overpotential of 30 mV.

Table 4. 7 ICP-MS results of selected Pt decorated samples.

	Ti (ppb)	Pt (ppb)	Pt (wt%)
Pt@TiO_2-pH9	1104.385	20.758	1.12
Pt@TiO_2-pH3	537.759	11.334	1.26
Pt@TiO_2-C	680.159	9.038	0.78
Pt@L-TiO_2	851.564	12.211	0.84

4.4 Conclusions

In this study, the phase transformation from L-TiO_2 nanosheets to R-TiO_2 and A-TiO_2 has been systematically investigated as well as their electrochemical HER performance with Pt decoration. Our study on the transition phase of the L-TiO_2 nanosheets as a function of temperature and pH reveals that the temperature determines the final phase-structure of the TiO_2 nanoparticles, while the pH mostly influences the morphology and particle size. Photochemical reduced Pt anchored on the as-synthesized nanoparticles with different morphology and exposed lattice plane exhibit different electrochemical HER activity.

It was found that anatase is the dominant phase at a critical temperature of 180 °C. Under these conditions, particles sizes increase as the pH increases from 3 to 9. The obtained A-TiO_2 particles in pH=3 solution are granular-like while those in pH=6-9 are shuttle-like, in contrast to the initial sheet form L-TiO_2. Because the electron microscopy images and the XRD did not show significant differences in morphology for the samples prepared in pH=6 and pH=9, it is speculated that the phase transition and morphology evolution follow the same mechanism. Two different transition pathways of dissolution-recrystallization and topologically rolling transition have been proposed to give a detailed insight into such phase transition process. In acidic solution, pH=3, it follows the dissolution-recrystallization mechanism caused by the corrosive environment and strengthened interlayer reaction between nanosheets. The strengthened interlayer reaction caused by decreased interlayer spacing and increased uptake of TBA ions is favorable to the stability of the restacked structure. Thus, the L-TiO_2 precursor prefers dissolution-recrystallization rather than topological rolling transition, which requires the individual nanosheets are dispersed well and can be rolling freely. Our results give a full map of phase transition and morphology evolution of L-TiO_2 to R-TiO_2/A-TiO_2 that can provide a guideline to new materials design, especially for the catalysts with morphology control can based on our optimal parameters.

A-TiO_2 synthesized in acidic/alkaline conditions showed different UV-Vis responses due to their band gap difference, which can be related to the morphology and exposed lattice plane. By means of this property, atomic dispersed Pt species were deposited on the pre-synthesized A-TiO_2 surface via photochemical reduction reaction. XPS and UV-Vis measurements show that the chemical state of Pt species of Pt@TiO_2-pH9 and Pt@TiO_2-pH3 are different due to the SMSI effect. Pt@TiO_2-pH9 with a stronger response to UV-Vis light irradiation leads to greater charge transfer from Ti atoms to adjacent Pt, which further lowers the oxidation state of Pt. Such optimal electronic structure facilitates the adsorption of protons, thus promotes the HER. In 0.5 M H_2SO_4, the HER performance of Pt@TiO_2-pH9 with highly exposed (101) plane outperforms all of other Pt decorated TiO_2, including amorphous A-TiO_2 obtained at pH=3, plate-like lepidocrocite HTO and its exfoliated counterpart L-TiO_2 with most exposed (010) plane as well as commercial anatase. After annealing in N_2 atmosphere, the Pt@TiO_2-pH9 only requires an overpotential of 30 mV to reach 10 mA cm_{geo}^{-2}. In addition, with regard to the mass activity, all the Pt decorated TiO_2 samples show excellent HER performance superior to commercial Pt/C due to ultralow loading of Pt. The best Pt@TiO_2-pH9-N300 presents a current density of 3954 A g_{Pt}^{-1} at an overpotential of 30 mV, which is 17-fold higher than benchmark Pt/C. By employing this strategy, the loading of precious metal is significantly reduced, and better stability is obtained than the commercial Pt/C.

References

1. Y. Pu, Q. Chen, Z. Sun, P. Rodriguez and L. Huang, *Crystal Growth & Design*, 2019, **19**, 3298-3304.
2. D.-D. Qin, Y.-P. Bi, X.-J. Feng, W. Wang, G. D. Barber, T. Wang, Y.-M. Song, X.-Q. Lu and T. E. Mallouk, *Chemistry of Materials*, 2015, **27**, 4180-4183.
3. I. S. Cho, J. Choi, K. Zhang, S. J. Kim, M. J. Jeong, L. Cai, T. Park, X. Zheng and J. H. Park, *Nano Letters*, 2015, **15**, 5709-5715.
4. R. Li, Y. Weng, X. Zhou, X. Wang, Y. Mi, R. Chong, H. Han and C. Li, *Energy & Environmental Science*, 2015, **8**, 2377-2382.
5. Z. Li, W. Luo, M. Zhang, J. Feng and Z. Zou, *Energy & Environmental Science*, 2013, **6**, 347-370.
6. M. H. Han, E. Gonzalo, G. Singh and T. Rojo, *Energy & Environmental Science*, 2015, **8**, 81-102.
7. M. A. Tsiamtsouri, P. K. Allan, A. J. Pell, J. M. Stratford, G. Kim, R. N. Kerber, P. C. Magusin, D. A. Jefferson and C. P. Grey, *Chemistry of Materials*, 2018, **30**, 1505-1516.
8. J. Zhang, P. Zhou, J. Liu and J. Yu, *Physical Chemistry Chemical Physics*, 2014, **16**, 20382-20386.
9. M. J. Lawrence, V. Celorrio, X. Shi, Q. Wang, A. Yanson, N. J. Adkins, M. Gu, J. Rodríguez-López and P. Rodriguez, *ACS Applied Energy Materials*, 2018, **1**, 5233-5244.
10. S. Bilmes, P. Mandelbaum, F. Alvarez and N. Victoria, *The Journal of Physical Chemistry B*, 2000, **104**, 9851-9858.
11. M. J. Lawrence, A. Kolodziej and P. Rodriguez, *Current Opinion in Electrochemistry*, 2018, **10**, 7-15.
12. M. L. Kromer, J. Monzo, M. J. Lawrence, A. Kolodziej, Z. T. Gossage, B. H. Simpson, S. Morandi, A. Yanson, J. Rodríguez-López and P. Rodríguez, *Langmuir*, 2017, **33**, 13295-13302.
13. B. Zhao, L. Lin and D. He, *Journal of Materials Chemistry A*, 2012, **1**, 1659-1668.
14. H. Y. Zhu, Y. Lan, X. P. Gao, S. P. Ringer, Z. F. Zheng, D. Y. Song and J. C. Zhao, *Journal of the American Chemical Society*, 2005, **127**, 6730-6736.
15. H. Yuan, R. Besselink, Z. Liao and E. Johan, *Scientific reports*, 2014, **4**, 4584.
16. J. Pan, X. Wu, L. Wang, G. Liu, G. Q. Lu and H. M. Cheng, *Chemical Communications*, 2011, **47**, 8361-8363.
17. P. Wen, H. Itoh, W. Tang and Q. Feng, *Langmuir*, 2007, **23**, 11782-11790.
18. P. Wen, Y. Ishikawa, H. Itoh and Q. Feng, *The Journal of Physical Chemistry C*, 2009, **113**, 20275-20280.
19. S. Bagheri, N. Muhd Julkapli and S. Bee Abd Hamid, *The Scientific World Journal*, 2014, **2014**, 727496.
20. Q. Fu and T. Wagner, *Surface Science Reports*, 2007, **62**, 431-498.
21. P. Hu, Z. Huang, Z. Amghouz, M. Makkee, F. Xu, F. Kapteijn, A. Dikhtiarenko, Y. Chen, X. Gu and X. Tang, *Angewandte Chemie International Edition*, 2014, **53**, 3418-3421.
22. H. Wang, S. Xu, C. Tsai, Y. Li, C. Liu, J. Zhao, Y. Liu, H. Yuan, F. Abild-Pedersen, F. B. Prinz, J. K. Nørskov and Y. Cui, *Science*, 2016, **354**, 1031-1036.
23. M. Xu, S. He, H. Chen, G. Cui, L. Zheng, B. Wang and M. Wei, *ACS Catalysis*, 2017, **7**, 7600-7609.
24. S. Mobini, F. Meshkani and M. Rezaei, *Chemical Engineering Science*, 2019, **197**, 37-51.
25. T. Sasaki, M. Watanabe, H. Hashizume, H. Yamada and H. Nakazawa, *Journal of the American Chemical Society*, 1996, **118**, 8329-8335.
26. T. Sasaki and M. Watanabe, *The Journal of Physical Chemistry B*, 1997, **101**, 10159-10161.

27. J. Zhang, M. Li, Z. Feng, J. Chen and C. Li, *The Journal of Physical Chemistry B*, 2006, **110**, 927-935.
28. T. Ohsaka, F. Izumi and Y. Fujiki, *Journal of Raman Spectroscopy*, 1978, **7**, 321-324.
29. P. Wen, Y. Ishikawa, H. Itoh and Q. Feng, *The Journal of Physical Chemistry C*, 2009, **113**.
30. H. Yuan, R. Besselink, Z. Liao and J. E. Ten Elshof, *Sci Rep*, 2014, **4**, 4584.
31. R. Ma, A. Yoshio Bando and T. Sasaki, *Cheminform*, 2004, **35**, 2115-2119.
32. R. J. Farrauto and M. C. Hobson, in *Encyclopedia of Physical Science and Technology (Third Edition)*, ed. R. A. Meyers, Academic Press, New York, 2003, DOI: https://doi.org/10.1016/B0-12-227410-5/00087-9, pp. 501-526.
33. W. F. Zhang, Y. L. He, M. S. Zhang, Z. Yin and Q. Chen, *Journal of Physics D: Applied Physics*, 2000, **33**, 912-916.
34. J. Rubio, J. L. Oteo, M. Villegas and P. Duran, *Journal of Materials Science*, 1997, **32**, 643-652.
35. H. Khan and I. K. Swati, *Industrial & Engineering Chemistry Research*, 2016, **55**, 6619-6633.
36. L. Q. Wang, K. F. Ferris, A. N. Shultz, D. R. Baer and M. H. Engelhard, *Surface Science*, 1997, **380**, 352-364.
37. P. Bera, K. R. Priolkar, A. Gayen, P. R. Sarode, M. S. Hegde, S. Emura, R. Kumashiro, V. Jayaram and G. N. Subbanna, *Chemistry of Materials*, 2003, **15**, 2049-2060.
38. C. D. Wagner, *NIST Standarad Reference Database 20*, 2000.
39. J. A. Horsley, *Journal of the American Chemical Society*, 1979, **101**, 2870-2874.
40. R. T. K. Baker, S. J. Tauster and J. A. Dumesic, *accounts of chemical research*, 1986, **20**, 389-394.
41. M. Sheng, B. Jiang, B. Wu, F. Liao, X. Fan, H. Lin, Y. Li, Y. Lifshitz, S.-T. Lee and M. Shao, *ACS Nano*, 2019, **13**, 2786-2794.
42. T. Fröschl, U. Hörmann, P. Kubiak, G. Kučerová, M. Pfanzelt, C. K. Weiss, R. J. Behm, N. Hüsing, U. Kaiser, K. Landfester and M. Wohlfahrt-Mehrens, *Chemical Society Reviews*, 2012, **41**, 5313-5360.
43. H. G. Yang, C. H. Sun, S. Z. Qiao, J. Zou, G. Liu, S. C. Smith, H. M. Cheng and G. Q. Lu, *Nature*, 2008, **453**, 638-641.

Chapter 5. Nickel confined in layered metal oxide layers for highly efficient and durable oxygen evolution catalysts

Preface to Chapter 5

Format: published manuscript.

Article information: Yayun Pu, Matthew J. Lawrence, Veronica Celorrio, Qi Wang, Meng Gu, Zongzhao Sun, Leonardo Agudo Jacome, Andrea E. Russell, Limin Huang* and Paramaconi Rodriguez*, Nickel confined in 2D earth-abundant oxide layers for highly efficient and durable oxygen evolution catalysts, *J. Mater. Chem. A*, 2020, 8, 13340. https://doi.org/10.1039/D0TA04031B

Overview: As the counter reaction to hydrogen evolution, oxygen evolution – a half reaction of water splitting, is a more complicated process due to the four-electron transfer steps and multiple intermediates: *OH, *O, *OOH. Electrocatalysts used upon cheap, abundant elements are promising for practical applications in terms of atomic efficiency. Low loading active Ni species confined in layered manganese oxide with extraordinary mass activity is reported in this chapter. Due to such specific confinement effect, different Ni coordination structures in layered metal oxides were confirmed and associated to the electrochemical behavior and OER performance. Confinement effect related electrochemical features were systematically recorded and analyzed.

Author contribution: Y.P. performed the electrochemical experiments, XRD, XRF, SEM characterization and analyses. P.R and L.H supervised the work. XANES and EXAFS characterization and analyses were performed by M.L and V.C. STEM characterization and analyses was performed by Q.W, Z. S and M.G. All authors contributed to the analysis of the results, discussion, writing and revision of the manuscript.

5.1 Introduction

The availability of a carbon neutral sustainable energy supply has become remarkably urgent in recent decades. Electrochemical water splitting, using renewable energy sources, offers an attractive route to chemical energy storage. However, one of the current limitations for the implementation of this technology is related to the inefficiency of the oxygen evolution reaction (OER) catalyst.[1-3] Metal oxide catalysts based on precious metals such as IrO_2 and RuO_2 have been commonly used. However, their high cost and low abundance is a significant hindrance. Therefore, in the last decade there has been an enormous effort from the scientific community towards the development of inexpensive and earth-abundant OER catalysts.[4-9]

Amongst a number of different catalysts reported, layered metal oxide/hydroxide nanoparticles of earth abundant elements are of particular interest in electrochemical water splitting. Compared with the more typically employed RuO_2 and IrO_2 electrocatalysts, the M-based oxides/hydroxides (M= Ni, Co, Fe, Mn), as well as their oxyhydroxide and double metal hydroxides, are attractive as they possess extremely high surface areas, providing a large number of exposed active sites, and enhanced electronic conductivity after exfoliation.[10, 11] Such layered oxide/hydroxides consist of MO_6 host layers stabilized by charge-balancing ions accommodated into the interlayer spacing. The M-O layers fulfill both roles of skeleton, for architecture, and active sites, leading to insufficient atomic efficiency. To enhance the performance and efficiency of these catalysts previous reports have presented the preparation of ultrathin two-dimensional (2D) nanosheets, aiming at the exposure of more active sites.[5] Improving the atomic efficiency of active atoms, such as Ru, Ir, Ni or Co, is economically attractive for large-scale industrial applications.[12, 13] In the literature a variety of strategies have been implemented, including synthesis of nanoclusters and even single atoms anchored on carbon-based and metal oxides-based supports,[14, 15] although, to date, very little attention has been dedicated to the ions in the channels formed between the 2D layered oxide structures. Catalytic ions in between the layers can be arranged *in-plane*

and immobilized by the opposite charge of the 2D host layer (**Fig. 4.1a**).[16] The 2D channels fundamentally act as ideal electrochemical nanoreactors providing ample interlayer spacing for free transportation of reactants and products and confinement of the under-coordinated active atoms.[17]

An important parameter affecting the electrochemical performance of catalysts during the OER is the pH. It is well known that the pH and composition of the electrolyte have a significant impact on the performance and durability of the catalyst during the OER. Establishing correlations between pH and measured voltammetric profiles facilitates the deduction of the active sites for OER and the evolution of adsorption/desorption processes and species on the surface. Takashima et al. reported that the instability of active Mn^{3+} at pH < 9 is the key factor in the observed poor activity of δ-MnO_2 toward the OER, which requires additional potential to electrochemically oxidize Mn^{2+} to Mn^{3+}.[18] Koper's group proposed the surface deprotonation mechanism of NiOOH during OER catalysis based on the pH sensitivity observed.[19] With that in mind, the catalytic activity of confined catalysts in layered structures, where reactant diffusion is rigorously restricted, would be strongly affected by the pH dominated deprotonation kinetics.

The aim of this work is to develop Ni-based electrocatalysts in which the Ni ions are confined to the inter-layer space in 2D interlayered MnO nanoparticles. The manuscript describes the synthesis and full characterization of the catalyst prepared via a facile ion exchange strategy. It also demonstrates the catalytic activity towards the OER and the long-term durability of the catalyst. We also present the reaction mechanism for the OER on the Ni-confined catalyst based on an exhaustive study of the catalyst under different conditions, *e.g.* pH and scan rate.

5.2 Methods

5.2.1 Materials synthesis

Preparation of $K_{0.45}MnO_2$: The $K_{0.45}MnO_2$ (KMO) was prepared by the solid reaction method.[20, 21] K_2CO_3 (99%, Aladdin), Mn_2O_3 (98%, Aladdin) were mixed at stoichiometric ratios and then ground carefully using an agate mortar. The mixture was placed in a crucible and was heated at 800 ^oC for 1 h for decarbonation. After cooling down naturally, the powder was carefully ground and subsequently heated at 800 ^oC for 30 h. The obtained black powder was rinsed with ultrapure water (Milli-Q, 18.4 MΩ cm^{-1}) and dried overnight at 60 ^oC.

Preparation of Ni-exchanged KMO (Ni-KMO): 50 mg of KMO was mixed with 0.5 M $NiCl_2$ solution (20 mL), followed by sonication for 10 min. The resultant suspension was allowed to stand for a given time (10 min, 30 min, 2h, 6 h, 24 h, and 48 h) at room temperature. The powder-solution was separated by centrifugation at 4000 rpm and rinsed with ultrapure water. The process was repeated at least five times. The obtained powder was dried at 50 ^oC overnight.

Preparation of Ni exchanged $H(K)MnO_2$ (Ni-H(K)MO): KMO was reacted with 1 M HCl to extract the K ions. 50 mg of the obtained H(K)MO was mixed with 0.5 M $NiCl_2$ solution (20 mL) followed by sonication for 10 min and thereafter allowed to stand for 24h. The powder-solution was separated by centrifugation at 4000 rpm, washed with ultrapure water and repeated at least five times. The obtained powder was dried at 50 ^oC overnight.

Preparation of Ni-exchanged $HTi_{0.91}O_2$ (Ni-HTO): Layered titanate $HTi_{0.91}O_2$ was prepared using the same method in our previous work.[22] 50 mg of $HTi_{0.91}O_2$ was mixed with 0.5 M $NiCl_2$ solution (20 mL) followed by sonication for 10 min and thereafter allowed to stand for 24 h. The powder-solution was separated by centrifugation at 4000 rpm, washed with ultrapure water and repeated at least five times. The obtained powder

was dried at 50 ºC overnight.

5.2.2 Materials characterizations

Powder X-ray diffraction (PXRD) was performed on a Bruker D8 Advance X-ray diffractometer with Cu Kα radiation (λ=1.5406 Å) at room temperature. XRD data were recorded between 10º-50º with a step size of 0.02º. X-ray fluorescence spectroscopy (XRF) was performed using a Bruker S8 Tiger 4 kW spectrometer under a He atmosphere. The particle morphology was analyzed by scanning electron microscopy (SEM, Philips XL3 30 environmental (E)SEM instrument) under an accelerating voltage of 15 kV, with Oxford Instruments energy dispersive X-ray spectroscopy (EDS) attachment. For the coupled bright field (BF-), high-angle annular dark field scanning transmission electron microscopy (HAADF-STEM) imaging and energy filtered selected area diffraction (EFSAD), a JEOL JEM-2200FS transmission electron microscope TEM, equipped with a field emission gun (FEG), an in-column omega-type energy filtered, Jeol STEM detectors and a Gatan Ultrascan 1000, was operated at an acceleration voltage of 200 kV. For the spatial resolution and distribution of Ni distribution, HAADF-STEM imaging experiments were carried out on a double Cs-corrected FEI Themis G2 operated at an acceleration voltage of 300 kV, coupled with an EDS detector of the type. Thermogravimetry analysis (TGA) was performed in the temperature range of 25-500 ºC by Shimadzu TGA-50 with a heating rate of 10 ºC /min, the nitrogen gas flow was 20 ml/min. X-ray absorption spectroscopy (XAS) measurements were performed on beamline B18 at Diamond Light Source, operating with a ring energy of 3 GeV and at a current of 300 mA.[23] The monochromator comprises Si(311) crystals operating in Quick EXAFS mode. Calibration of the monochromator was conducted using the respective metal foils prior to the measurements. Pellets of the different samples were collected in transmission and fluorescence modes at the Mn K-edge (6539 eV) and Ni K-edge (8332 eV) simultaneously with the foils. The data was analysed using Athena and Artemis programs,[24] which implement the FEFF6 and IFEFFIT codes.[25] X-ray emission

spectroscopy (XES) measurements were conducted at Beamline I20-scanning, of Diamond Light Source.[26, 27] The XES spectra have been normalized with respect to their total area using the range 6456-6500 eV.

5.2.3 Electrochemical characterization

Electrochemical cell setup: All the electrochemical measurements were performed in a three-electrode setup. Before each electrochemical measurement, the electrochemical cell system was stored in permanganate solution overnight. Before testing, the cell was rinsed with ultrapure water and diluted piranha solution to remove permanganate, followed by filling with ultrapure water and heating to ~70 ^{o}C. The hot water was replaced with fresh ultrapure water and reheated five times. Electrochemical measurements were performed by an Autolab PGSTAT100N potentiostat, with Au foil as counter electrode (CE) and Hg/HgO (0.1 M NaOH) as reference electrode (RE), connected via a luggin capillary. The CE was flame annealed and rinsed with water before immersed in electrolyte. Alkaline electrolyte was freshly prepared by dissolution of NaOH beads (Alfa Aesar, semiconductor grade, 99.99%) or KOH pellets in ultrapure water. Concentrations of 1 M, 0.1 M, 0.01 were prepared for pH=14, 13, and 12, respectively. (Alfa Aesar, 99.98%). For pH=8, electrolyte was prepared by adjusting the 0.01 M NaOH solution with $HClO_4$ (Merck KGaA, Suprapur, 70%). The prepared electrolytes were purged with high purity argon for at least 30 min prior to measurements and an Ar stream, acting as a protective layer above the electrolyte, was employed during measurements.

Electrode preparation: Sample powders were dispersed in 5 mL ultrapure water with a concentration of 0.5 mg mL^{-1}, followed by sonication (~30 min) to achieve a good dispersion. Then, 10 μL Nafion D-521 solution (Alfa Aesar, 5% w/w in H_2O and 1-propanol) was added. Glassy carbon (GC) rotating disk electrode (RDE, diameter 5 mm, geometric area = 0.196 cm^{-2}) was polished with 4000 grit wet polish paper to get a fresh surface, followed by polishing with 0.5 μm diamond slurry (Kemet) for refining and

then rinsed abundantly with ultrapure water. 4 x 20 μL of the prepared ink were drop-casted onto the GC and dried in an oven at 75 ºC to deposit ~0.04 mg catalyst; the loading was ~0.2 mg cm^{-2}.

Cyclic voltammetry (CV): CVs were recorded in a potential window of 0.8 - 1.76 V, with a scan rate of 20 mV s^{-1}. GC RDE was rotated at 1600 rpm to remove generated O_2 bubbles. The Ohmic resistances of the electrochemical system were obtained via positive feedback mode of Autolab PGSTAT100N, the iR corrected CVs are presented in **Figure 5.32**. To determine the true moles of redox active Ni atoms, integration of the anodic/cathodic waves of the Ni^{2+}/Ni^{3+} couple was performed with varying scan rate. Double layer capacitance was measured in non-Faradaic region between 1.1 - 1.2 V (vs. RHE), with scan rates of 10, 20, 30, 40, 50 60, 70 and 80 mV s^{-1}.

Chronoampermetry: Chronoamperometric measurements were performed after 30 CV cycles, after which the voltammetric profiles became stable. The procedure consisted of an applied potential of 0.8 V for 10 s, followed by electrolysis at a specific OER potential (1.48 V, 1.40 V, 1.38 V or 1.36 V vs RHE) for 3600 s and then back to 0.8 V for 10 s. The long term stability test was the same procedure except keeping at 1.48 V for 10 h.

Calculations:

Mass activity: 1) Ni mass activity, 2) catalyst mass activity were calculated by using the equation of measured current *i* being divided by Ni or catalyst loading *m*:

$$j_{\text{mass}} = \frac{i}{m} \qquad [5.1]$$

Turnover frequency (TOF): the TOF value was calculated by the equation:

$$\text{TOF} = \frac{jS}{4Fn} \qquad [5.2]$$

where *j* is the measured current density, *S* is geometric surface area 0.196 cm^2, number 4 means the number of electrons transferred in OER per O_2, *F* is faradic constant of

96486 C mol^{-1}, *n* is the moles of active atoms participated in OER. In this work, the active sites are Ni atoms, which can be calculated by integration of pre-OER peak and mass loading from XRF results.

5.3 Results and Discussion

5.3.1 Characterization of Ni-confined KMO

Ni-KMO was prepared by mixing K-rich birnessite ($K_{0.45}MnO_2$) and $NiCl_2$ solution at ambient temperature, as described in the experimental section (Supporting Information). **Figure 5.1b** presents the XRD patterns of the as-prepared KMO and after Ni exchange. From the XRD pattern it was determined that the K-birnessite possessed a layered structure with an interlayer spacing of 0.69 nm (AMCSD 0001302).[28] The same layered structure was retained after the Ni exchange process, with XRF measurements suggesting that Ni cations partially replaced K ions in the interlayer spacing (**Table 5.1**). Such intercalation resulted in the enlargement of the interlayer distances (001) and (002) along the c axis, demonstrated by the decrease in 2θ values for those diffraction signals at $2\theta = 12.43^{o}$ and 24.84^{o}. The SEM **(Figure 5.1c**) and STEM images (**Figure 5.1d,e,g-i)** of Ni-KMO show plate-like nanoparticles with facets with dimensions between 300 - 400 nm with near-identical morphology to that of KMO (**Figure 5.2)**. The bright field (BF) and high angle annular darkfield (HAADF) images in Figure 4.1e and f show a single nanoparticle comprising stacked layers of KMO. In **Figure 5.1d**, the selected area diffraction (SAD) pattern shows a splitting of the reflections, which can be interpreted as an in-plane rotation of 4.5° (marked at the Ni-KMO (110) reflection) between two sets of layers in the nanoparticle. The HAADF-STEM image in **Figure 5.1h** suggests that the Mn-O framework retained a layered structure, which is consistent with the XRD results. In addition to the Ni atoms inserted into the interlayer channels, aggregation of Ni at the edges of the nanoplate crystals, generating a few nanometer-thick region, is observed in the HAADF images and EDS elemental maps (**Figure 5.1i (**contrast the Ni and Mn HAADF images) and **Figure 5.3**). The additional XRD signals observed for Ni-KMO at 37.4º and 43.4º, which can be assigned to (111) and (200) of

NiO (JCPDS 73-1519), are in agreement with STEM results.

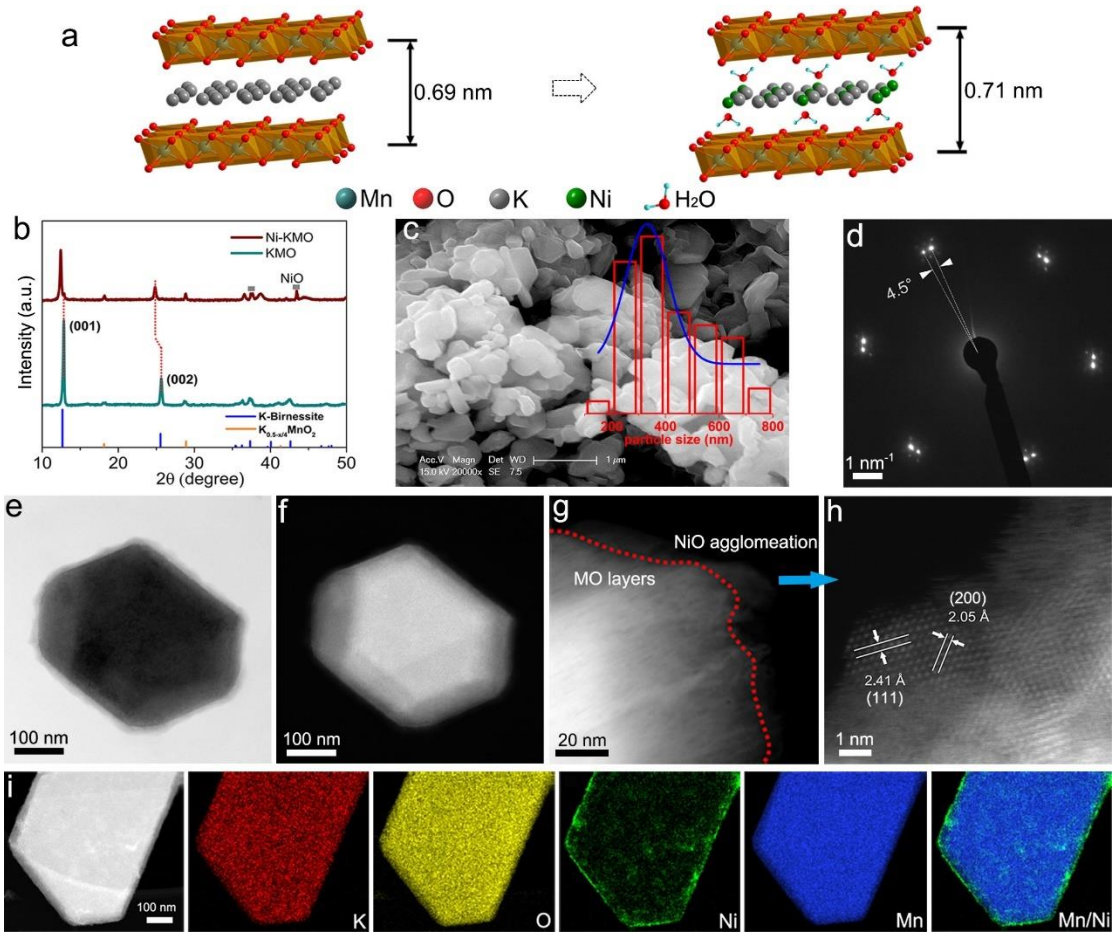


Figure 5. 1 (a) Schematic illustration of the impact of Ni intercalation into layered K-birnessite manganese oxide. (b) X-ray diffraction patterns of Ni-KMO and pristine KMO. (c) SE-SEM image of Ni-KMO nanoplates. The particle size distribution histogram is inset. (f) SAD diffraction pattern (ZA= $[001]_{Ni\text{-}KMO}$) of particle in (e). (e) Bright field (BF) and (f) HAADF-STEM images of Ni-KMO nanoparticle seen along [001]. zone axis (ZA). HAADF-STEM images (g), and (h) enlarged Ni agglomeration at the edge of a Ni KMO nanoplate. (i) HAADF-STEM image of single Ni-KMO nanoplate with corresponding EDS elemental mapping.

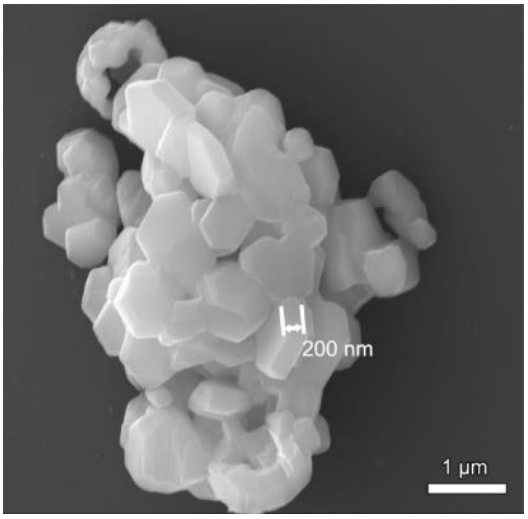


Figure 5. 2 SEM image of $K_{0.45}MnO_2$ nanoparticles synthesized by solid state calcination.

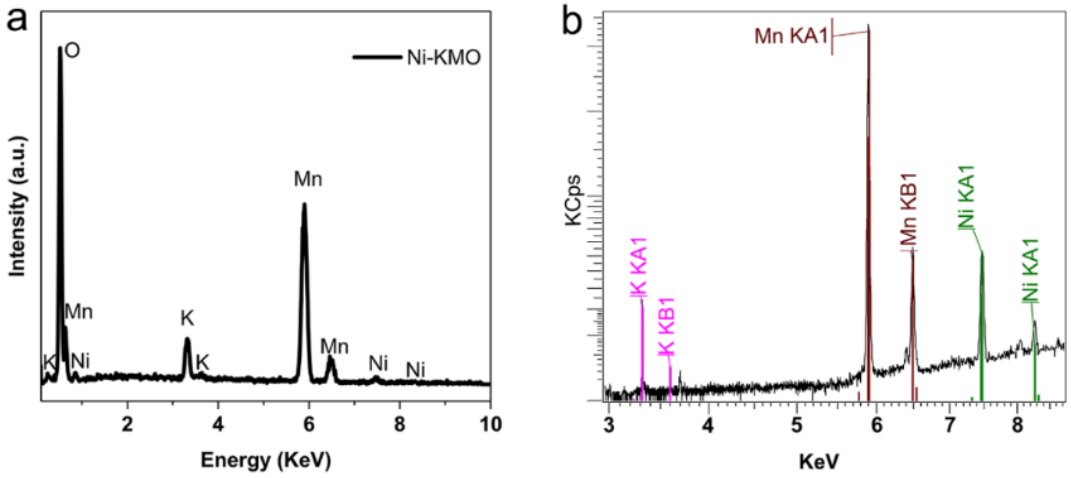


Figure 5. 3 (a) STEM-EDS spectrum, (b) XRF spectrum of Ni-KMO.

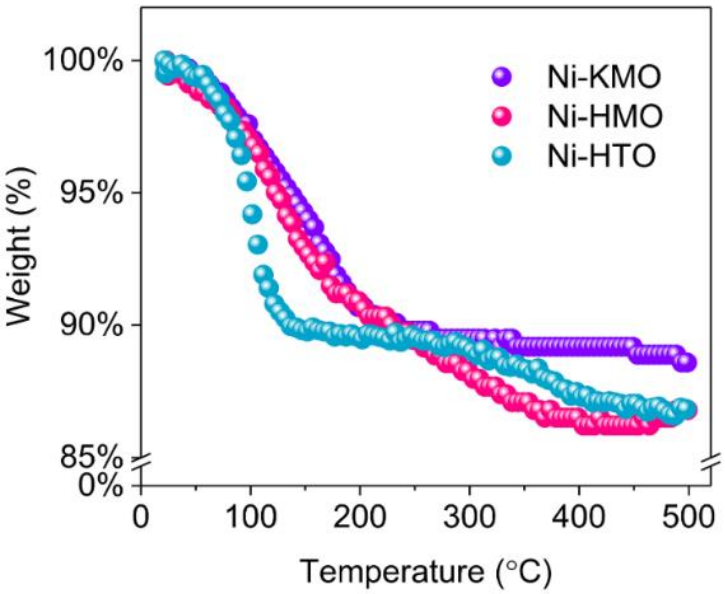


Figure 5. 4 TGA curves of as-synthesized Ni exchanged layered metal oxides.

Table 5. 1 XRF results of Ni-KMO, Ni-H(K)MO and Ni-HTO

Samples	Ni (*at.*%)	K (*at.*%)	Mn (*at.*%)	Ti (*at.*%)
$Ni_{0.16}K_{0.2}MnO_2 \cdot 0.7H_2O$	11.67 ± 0.18	14.46 ± 0.2	73.87 ± 0.37	-
$Ni_{0.33}K_{0.04}MnO_2 \cdot 0.9H_2O$	24.1 ± 0.4	2.69 ± 0.09	71.26 ± 0.5	-
$Ni_{0.033}Ti_{0.91}O_2 \cdot 0.6H_2O$	3.60 ± 0.07	-	-	96.40 ± 0.07

*TGA was performed to determine the water amount in Ni-intercalated layered metal oxides (**Figure 5. 4**).

5.3.2 XAS analysis of Ni intercalated metal oxides

The adsorption energies of *OH and O* are predominantly dependent on the electronic configuration of the Ni surfaces.[29] Therefore, the local environment of the Ni sites and associated species determine the corresponding electrochemical activity of these materials. X-ray absorption spectroscopy (XAS) was implemented to determine the oxidation state and coordination enviroment of Ni and the Mn-oxide host structure and to enable correlatin of these parameters with the underlying OER performance of Ni-

KMO. The characteristic XANES spectra of metallic Mn, standard Mn-oxide compounds with oxidation states spanning the range Mn^{2+} to Mn^{4+} and the synthesized Ni-K(H)MO nanoplates are presented in **Figure 5.5a**.

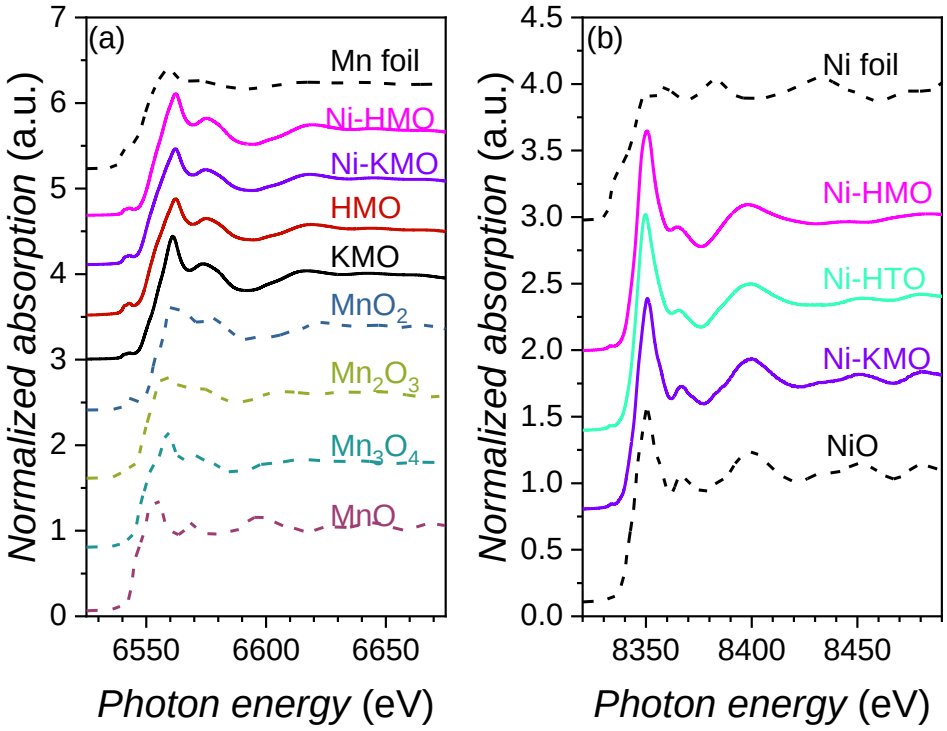


Figure 5. 5 Normalized XANES spectra measured at the (a) Mn K-edge and (b) Ni K-edge for KMO, HMO, Ni-KMO, Ni-HMO and Ni-HTO catalysts, in addition to relevant standard oxide compounds and metal foils. References, represented by dashed lines, are shown for comparison.

The edge positions, determined by the maximum of the first derivative, for Mn foil, MnO, Mn_3O_4, Mn_2O_3 and MnO_2 were observed at 6539.0, 6544.2, 6546.7, 6547.7 and 6552.5 eV, respectively, in agreement with existing literature values.[30-32] The measured edge positions for KMO, HMO and Ni-KMO and Ni-HMO were 6549.3, 6550.3, 6549.6 and 6552.0 eV, respectively. The normalised absorption pre-edge features of the manganese oxide derivatives and relevant Mn K-edge reference oxide compounds are presented in **Figure 5.6**. An increase in pre-edge peak energy is observed with an increase in Mn oxidation state (**Figure 5.6a**). The nature of the pre-edge features of the spectra at the Mn K-edge suggest that there is a contribution from Mn^{2+}, Mn^{3+} and Mn^{4+}

to the overall structure and the intermediate mean Mn oxidation state is between +3 and +4. Thus, X-ray emission spectroscopy (XES) was employed to obtain more accurate Mn oxidation state information. The measured XES spectra and corresponding fits, a function of the sum contributions of the standard Mn^{n+} oxide compounds, are presented in **Figure 5.7**. The mean Mn oxidation state of pristine KMO was determined as +3.9 (**Table 5.2**). A decrease in mean oxidation state was observed upon cation exchange with both H^+ and Ni^{2+}, with the greatest decrease observed for HMO. The fraction of Mn^{4+} is effectively the same for Ni-KMO and KMO, while the Mn^{3+} fraction decreases upon Ni-exchange. This suggests that Ni^{2+} intercalation is more favorable at those Mn^{3+} sites, which are commonly accompanied by defects that contribute to the overall negative charge of Mn-O layers.[8] The defects with higher Gibbs energy favor the ion exchange reaction of K with Ni. The concentration of Mn^{3+} increases significantly in HMO relative to KMO, thus more Ni cations were intercalated into Ni-HMO, as confirmed by the XRF analysis (**Table 5.1**).

The characteristic XANES spectra measured of metallic Ni, Ni-oxide reference compound, Ni-KMO, Ni-HTO and Ni-HMO are presented in **Figure 5.5b**. The edge position of the Ni foil and NiO reference were determined as 8333.0 eV and 8345.2 eV, respectively. The absorption edges of Ni-KMO, Ni-HTO and Ni-HMO were determined as 8345.3, 8345.9 and 8346.0 eV respectively, suggesting a Ni oxidation state of +2. For Ni-KMO the XANES spectrum appears identical to that of the NiO reference, indicative of the presence of NiO structure in Ni-KMO. While slightly different spectrum of Ni-HMO compared to Ni-KMO suggesting a different Ni^{2+} structure, as confirmed by the fitted EXAFS results below. There are no significant differences in pre-edge features observed at the Ni K-edge (**Figure 5.6b**).

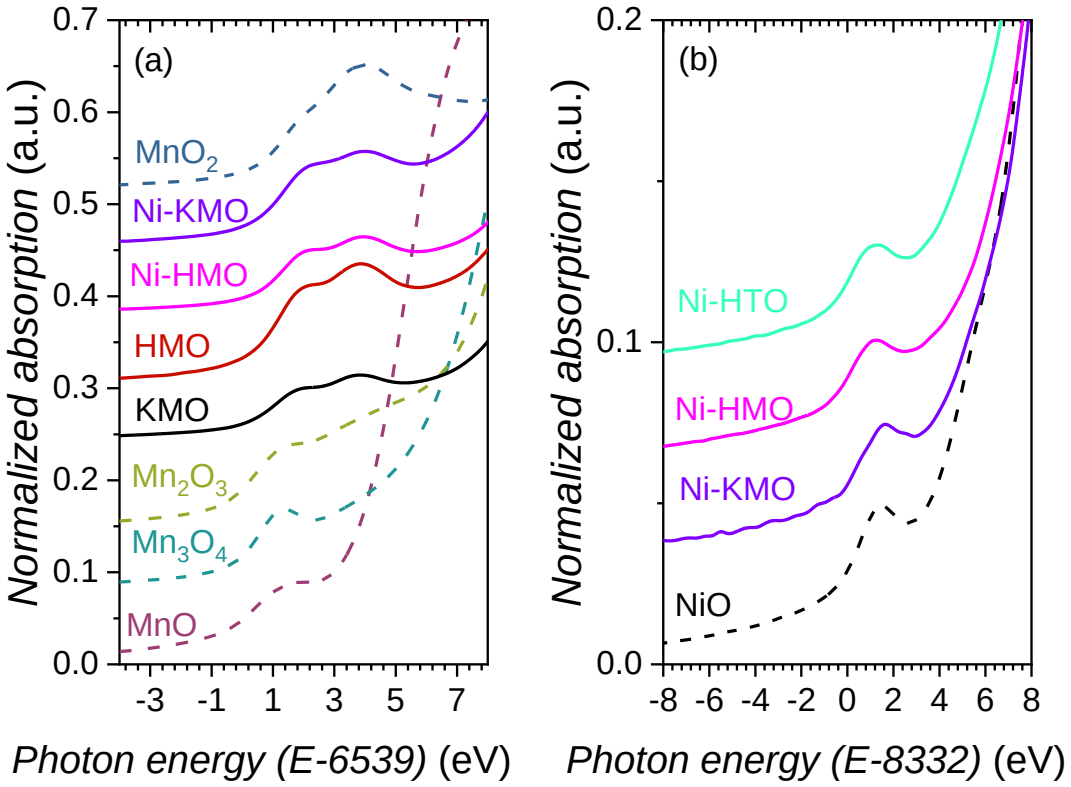


Figure 5. 6 Normalised absorption pre-edge features of X-KMO nanoplates (where M= H or Ni) and oxide reference compounds at (a) Mn K-edge and (b) Ni K-edge. The edge position of the metallic foils, in eV, has been subtracted from the measured spectra presented.

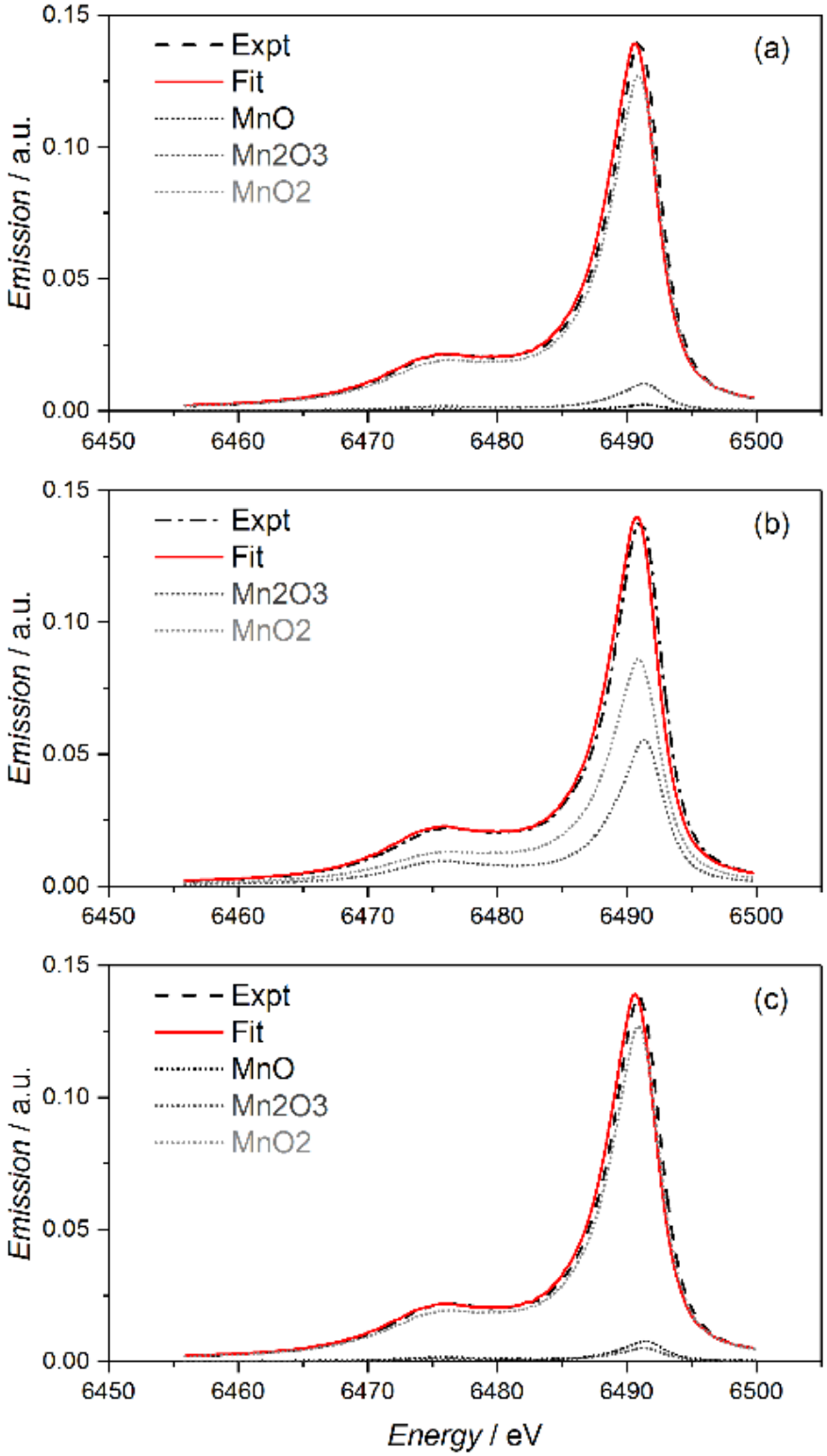


Figure 5. 7 Measured experimental XES spectra of (a) KMO, (b) H(K)MO and (c) Ni-KMO with corresponding fitting contributions from MnO, Mn_2O_3 and MnO_2 standard oxide compounds.

Table 5. 2 Ratio of Mn^{n+} species and corresponding mean Mn oxidation state of prepared KMO derivatives determined by XES.

	% Mn^{4+}	% Mn^{3+}	% Mn^{2+}	Mean Mn oxidation state
KMO	90.5 ± 1.1	7.2 ± 2.7	1.6 ± 1.7	3.9
HMO	61.3 ± 0.9	38.7 ± 0.9	0	3.6
Ni-KMO	90.4 ± 1.2	3.6 ± 2.9	5.1 ± 1.8	3.8

The Mn K-edge EXAFS Fourier transforms (FTs) of the synthesised KMO, H(K)MO, Ni-KMO and Ni-HMO nanosheets and reference samples are presented in **Figure 5.8a**. The first peak at ~1.5 Å (not phase shift corrected) is due to the Mn-O scattering and the second peak at ~ 2.5 Å (not phase shift corrected) is due to Mn-Mn/Mn-Ni scattering (**Tables 5.3 & 5.4 & 5.7**). The two Mn scattering distances are generated by the two distinct Mn birnessite lattice sites: edges and face-centers. The Ni K-edge EXAFS FT of Ni-KMO is near-identical to the NiO reference compound (**Figure 5.8b**). The first shell coordination at ~1.7 Å (not phase shift corrected) corresponds to Ni-O whilst the second shell coordination at ~ 2.6 Å (not phase shift corrected) corresponds to Ni-Ni scattering (**Table 5.5**). The relative amplitude of the second shell peak for Ni-KMO compared to NiO suggests that the former comprises NiO nanoparticles. This is not the case for Ni-HTO and Ni-HMO, where the relative amplitude of the second shell peak differs from that of NiO, suggesting the formation of a different structure (**Tables 4.6 & Table 4.8**).

In summary, the *ex-situ* XAS/XES results clarify the importance of Mn^{3+} on the Ni-exchange intercalation. The Ni-content in each of the samples is proportional to the concentrations Mn^{3+} sites. For all the prepared samples, Ni is present in the oxidation state (+2), but different Ni coordination/structures were obtained for Ni-KMO and Ni-HMO.

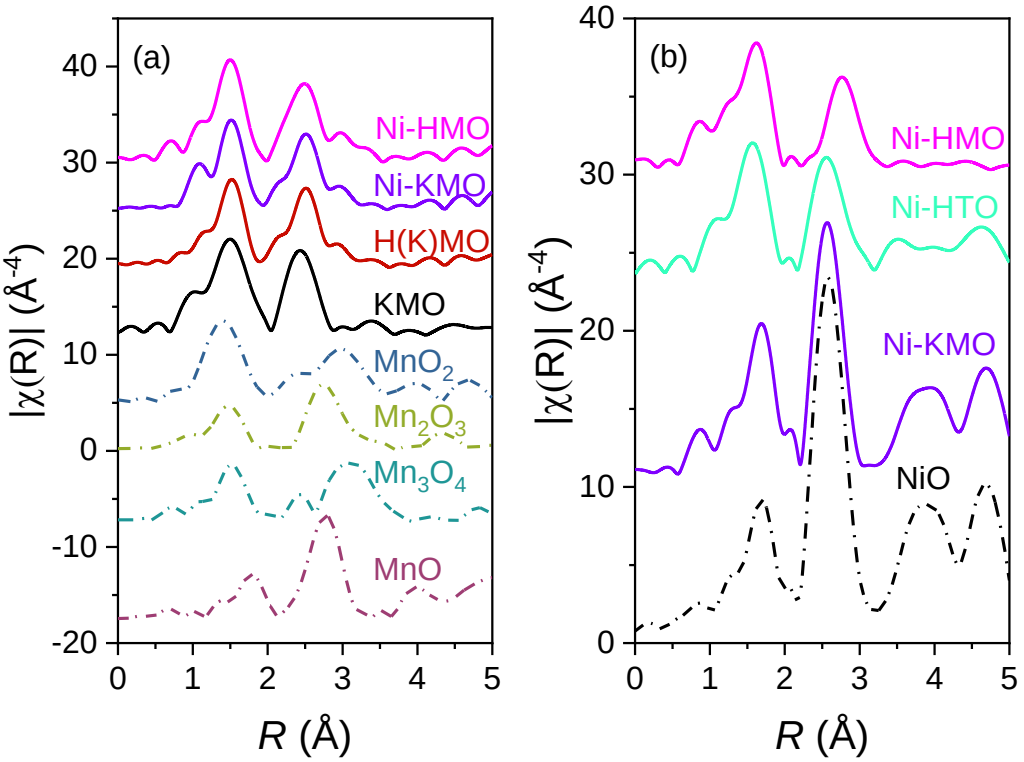


Figure 5. 8 EXAFS FTs of $k^3\chi(k)$ functions for KMO, H(K)MO, Ni-KMO, Ni-HMO and Ni-HMO nanosheets and standard oxide reference compounds at (a) Mn K-edge and (b) Ni K-edge. References are shown for comparison.

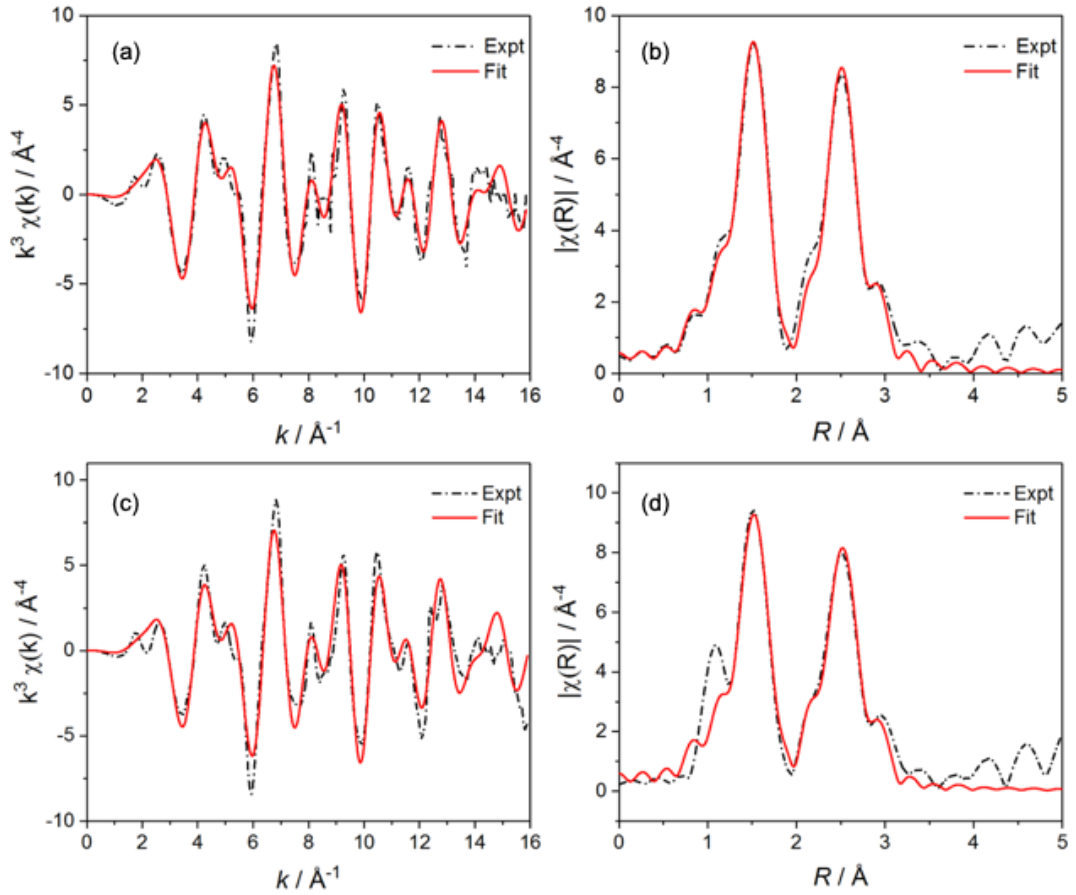


Figure 5. 9 k^3 weighted χ data (a, c) and k^3 weighted Fourier transform EXAFS data (b, d) fits of H(K)MO and Ni-KMO.

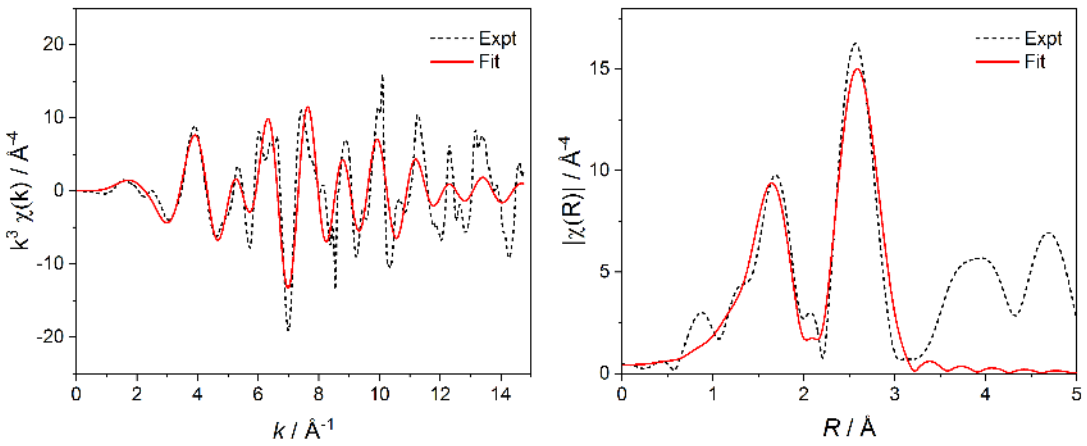


Figure 5. 10 k^3 weighted χ data (left) and k^3 weighted Fourier transform EXAFS data (right) fits for the Ni-KMO catalysts measured at the Ni K-edge.

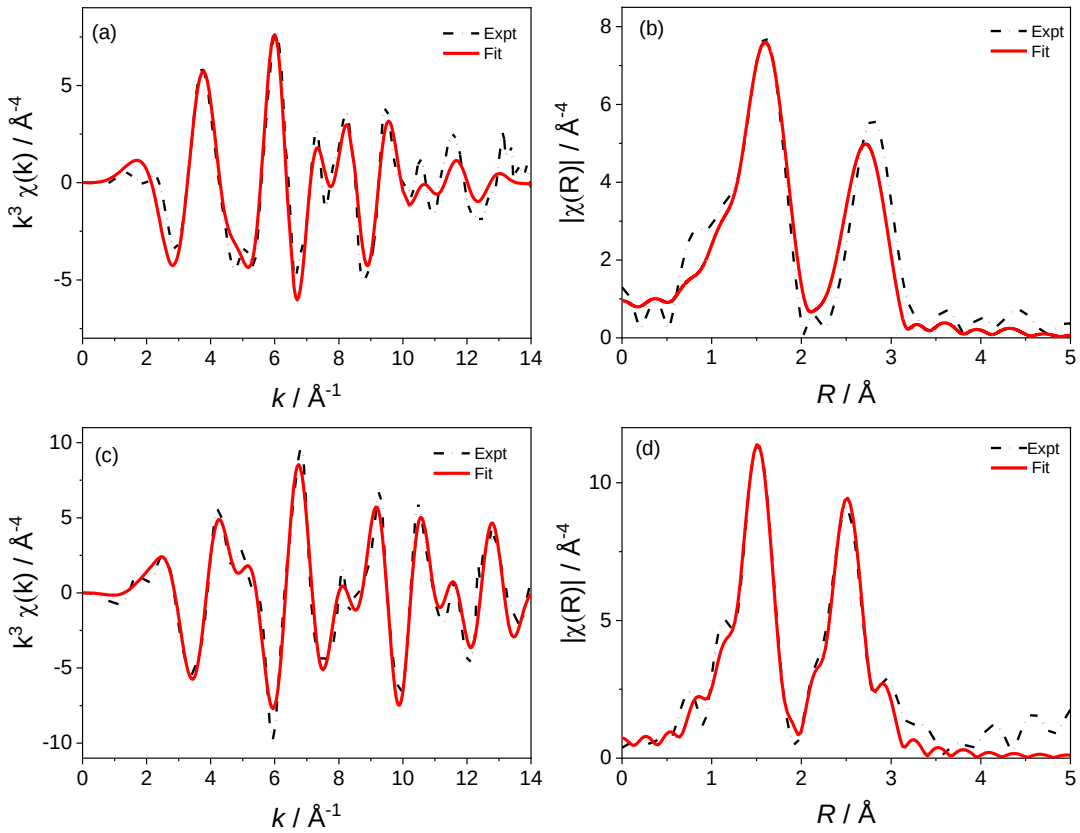


Figure 5. 11 k^3 weighted χ data (left) and k^3 weighted Fourier transform EXAFS data (right) fits for the Ni-HMO catalysts collected at the Ni K edge (a, b) and the Mn K edge (c, d).

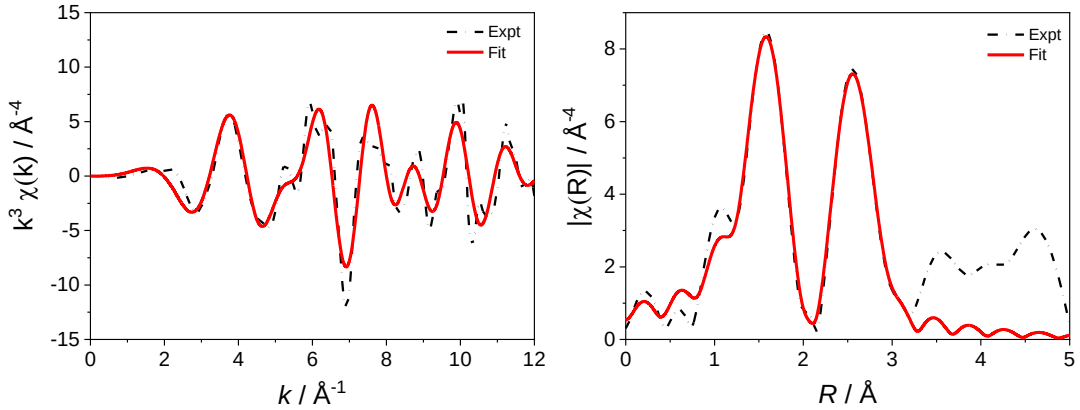


Figure 5. 12 k^3 weighted χ data (left) and k^3 weighted Fourier transform EXAFS data (right) fits for the Ni-HTO catalysts collected at the Ni K edge.

Table 5. 3 EXAFS distances and fitting parameters for the HMO catalyst. Fitting

parameters: $S_0^2 = 0.8$ calculated using a Mn foil standard; fit range $3.0 < k < 13.8$, $1.2 < R < 3.5$. $\Delta E_0 = 0.2 \pm 0.7$ eV; $R_{factor} = 0.008$

Scattering	CN	R / Å	$\sigma^2 \times 10^3$ / Å^2
Mn–O	3.3 ± 0.2	1.90 ± 0.01	2.5 ± 0.7
Mn–Mn_1	5.5 ± 0.8	2.90 ± 0.01	8.2 ± 1.7
Mn–Mn_2	1.6 ± 0.8	3.14 ± 0.02	4.0 ± 3.4

Table 5. 4 EXAFS distances and fitting parameters for the Ni-KMO catalyst at the Mn K-edge. Fitting parameters: $S_0^2 = 0.8$ calculated using a Mn foil standard; fit range $3.0 < k < 13.9$, $1.2 < R < 3.5$. $\Delta E_0 = 0.5 \pm 0.7$ eV; $R_{factor} = 0.006$

Scattering	CN	R / Å	$\sigma^2 \times 10^3$ / Å^2
Mn–O	2.9 ± 0.2	1.90 ± 0.01	1.8 ± 0.6
Mn–$(Ni/Mn)_1$	6.4 ± 0.9	2.91 ± 0.01	9.9 ± 1.7
Mn–$(Ni/Mn)_2$	1.6 ± 0.8	3.16 ± 0.02	3.8 ± 3.0

Table 5. 5 EXAFS distances and fitting parameters for the Ni-KMO catalyst at the Ni K-edge. Fitting parameters: $S_0^2 = 0.8$ calculated using a Ni foil standard; fit range $3.0 < k < 12.1$, $1.0 < R < 3.2$. $\Delta E_0 = -0.4 \pm 1.0$ eV; $R_{factor} = 0.022$

Scattering	CN	R / Å	$\sigma^2 \times 10^3$ / Å^2
Ni–O	6.9 ± 1.0	2.07 ± 0.01	6.2 ± 2.4
Ni–Ni/Mn	12.0 ± 2.3	2.95 ± 0.01	9.2 ± 1.7

Table 5. 6 EXAFS distances and fitting parameters for the Ni-HMO catalyst at the Ni edge. Fitting parameters: $S_0^2 = 0.8$ calculated using a Ni foil standard; fit range $3.2 < k < 12.9$, $1.0 < R < 3.2$. $\Delta E_0 = -4.0 \pm 1.7$ eV; $R_{factor} = 0.027$

Scattering	CN	R / Å	$\sigma^2 \times 10^3$ / Å^2
Ni–O	8.0 ± 1.4	2.06 ± 0.02	9.2 ± 2.6
Ni–Ni/Mn	7.0 ± 2.9	3.08 ± 0.03	12.4 ± 4.1

Table 5. 7 EXAFS distances and fitting parameters for the Ni-HMO catalyst at the Mn edge. Fitting parameters: $S_0^2 = 0.8$ calculated using a Mn foil standard; fit range $3.0 < k < 13.9$, $1.2 < R < 3.5$. $\Delta E_0 = -0.1 \pm 0.7$ eV; $R_{factor} = 0.008$

Scattering	CN	R / Å	σ^2 x 10^3 / Å^2
Mn–O	4.1 ± 0.2	1.90 ± 0.01	2.7 ± 0.7
Mn–(Ni/Mn)$_1$	6.6 ± 1.0	2.90 ± 0.01	9.1 ± 1.9
Mn–(Ni/Mn)$_2$	1.7 ± 0.9	3.14 ± 0.03	3.7 ± 3.6

Table 5. 8 EXAFS distances and fitting parameters for the Ni-HTO catalyst at the Ni edge. Fitting parameters: $S_0^2 = 0.8$ calculated using a Ni foil standard; fit range $3.2 < k < 11.1$, $1.0 < R < 3.2$. $\Delta E_0 = -6.4 \pm 0.7$ eV; $R_{factor} = 0.004$

Scattering	CN	R / Å	σ^2 x 10^3 / Å^2
Ni–O	6.6 ± 0.5	2.05 ± 0.01	6.2 ± 1.1
Ni–Ni/Ti	4.9 ± 0.8	2.95 ± 0.01	7.5 ± 1.4

5.3.3 Evaluation of the electrochemical activity and durability

The catalytic activity of Ni-KMO was evaluated over the pH range 8 – 14, to provide both assessment of the activity of the electrocatalysts for the OER and enable deeper understanding of the mechanism behind this activity. **Figure 5.13a-c** show the stable iR-corrected voltammetric profiles of the Ni-KMO catalyst as a function of the pH, with the voltammograms shown being those obtained after 30 consecutive cycles; the evolution of the curves over the 30 scans is presented in **Figure 5.14**. Current densities are reported as mA cm^{-2} normalized by the geometric area of the electrode. As can be seen, the OER onset overpotential (η_{onset}) increases with decreasing pH, from 130 mV at pH 14 to 220 mV at pH 12. (Note that all voltammetric responses are reported vs. RHE and, thus, differences are not attributable to changes to the potential of the reference electrode.) At the same time, at pH 14 the overpotential at 10 mA cm^{-2} (η_{10}) was 240 mV, which is significantly smaller than the η_{10} = 1090 mV observed at pH 12. The marginal difference in measured η_{onset} and sharp contrast at η_{10} confirm the lower reaction rate of the OER at lower pH due to the lower concentration and availability of OH^-. **Figure 5.13b** summarizes the observed trends.

The redox activity of the confined Ni clusters is evident in the voltammograms as a quasi-reversible peak in the region between 1.2 - 1.5 V was observed at pH 14 and 12 (**Figure 5.13c**). This peak has previously been ascribed to the $Ni^{2+} \leftrightarrow Ni^{3+}$ couple of Ni based catalysts.[33, 34] Interestingly, at pH=14 the oxidation peak of $Ni^{2+} \rightarrow Ni^{3+}$ appears at 1.24 V, which is significantly more cathodic relative to previous reports in the literature (~1.4 V vs. RHE on carbon electrode). This unusual cathodic shift of oxidation peak to 1.24 V is beneficial for subsequent catalytic oxygen evolution. As seen in **Figure 5.13c**, a direct relationship between the position of the $Ni^{2+} \rightarrow Ni^{3+}$ oxidation peak on the Ni-KMO and the OER onset potential was observed as a function of pH. Increasing the pH of the solution from 12 to 14 results in the shift of the peroxidation $Ni^{2+} \rightarrow Ni^{3+}$ peak together with a shift of the onset potential of OER towards less positive potentials. This is a clear indicator that the Ni^{3+} are active sites for

the OER. Moreover, the correlation between redox peaks and OER activity over multiple cycles is shown in **Figure 5.14**. At any one pH, the $Ni^{2+} \rightarrow Ni^{3+}$ oxidation peak shifts cathodically and the OER current density increases as a function of the number of cycles, confirming the role of $Ni^{2+} \rightarrow Ni^{3+}$ transformation on OER catalysis. This behavior is in agreement with previous work that established the relationship between the peak position of the redox couple on Ni-Fe(OOH) and the OER catalytic activity.[35]

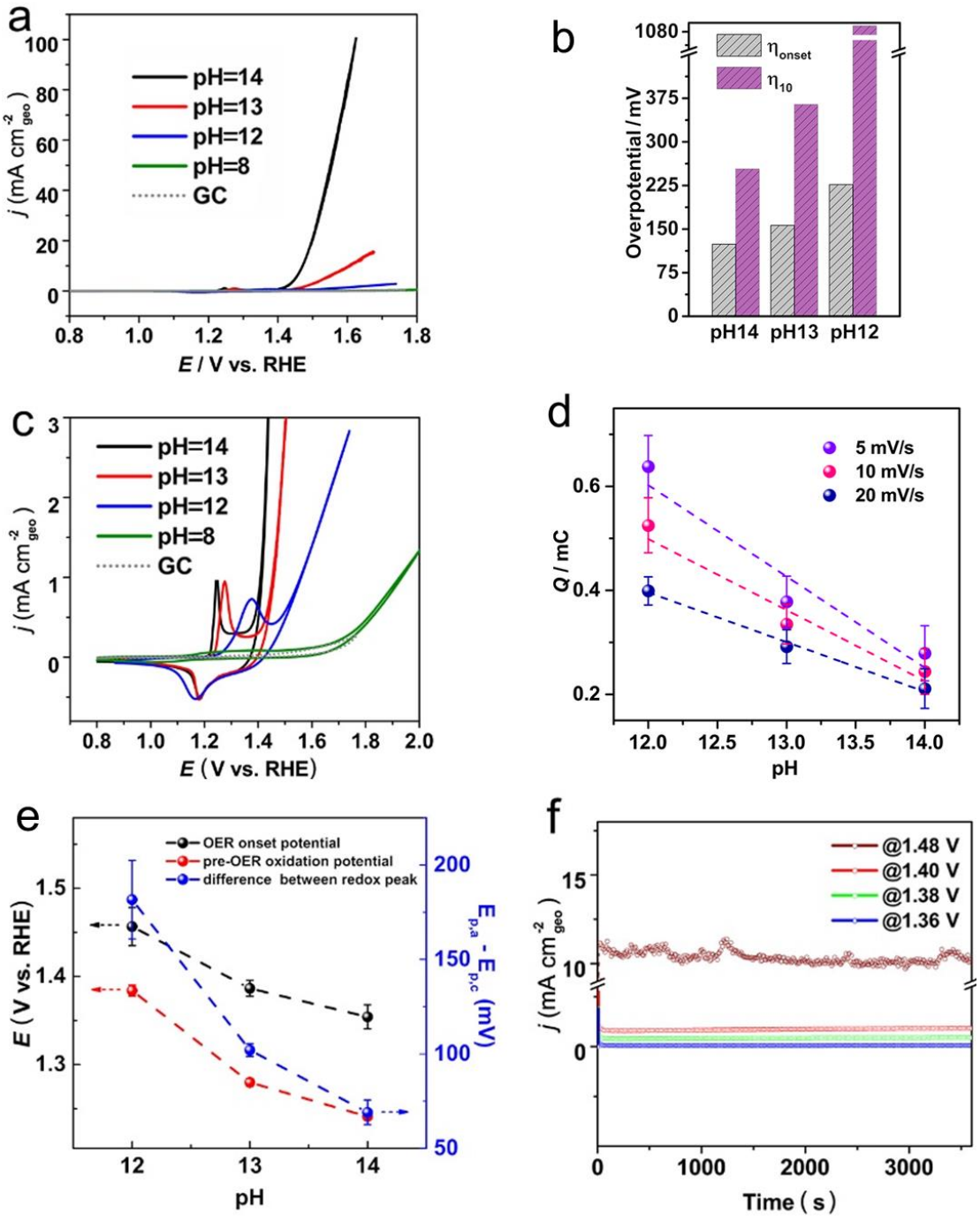


Figure 5. 13 (a) Stable cyclic voltammograms of Ni-KMO at various pHs after 30 consecutive scans in NaOH electrolyte, with a scan rate of 20 mV s^{-1}. The profile of the glassy carbon (GC) support is included for comparison. All the curves are iR-corrected. (b) The onset overpotential (η_{onset}) and overpotential at j = 10 mA cm^{-2} (η_{10}) obtained from (a). (c) Enlarged region showing the $Ni^{2+} \rightarrow Ni^{3+}$ redox peaks at various pHs. (d) Integrated charge of Ni^{2+}/Ni^{3+} oxidation peak as a function of pH at various scan rates. (e) OER onset potential, pre-OER oxidation peak potential and Ni^{2+}/Ni^{3+} ΔE variation with pH. (f) Chronoamperometry profiles of Ni-KMO at pH=14 at various applied potentials as indicated in the figure.

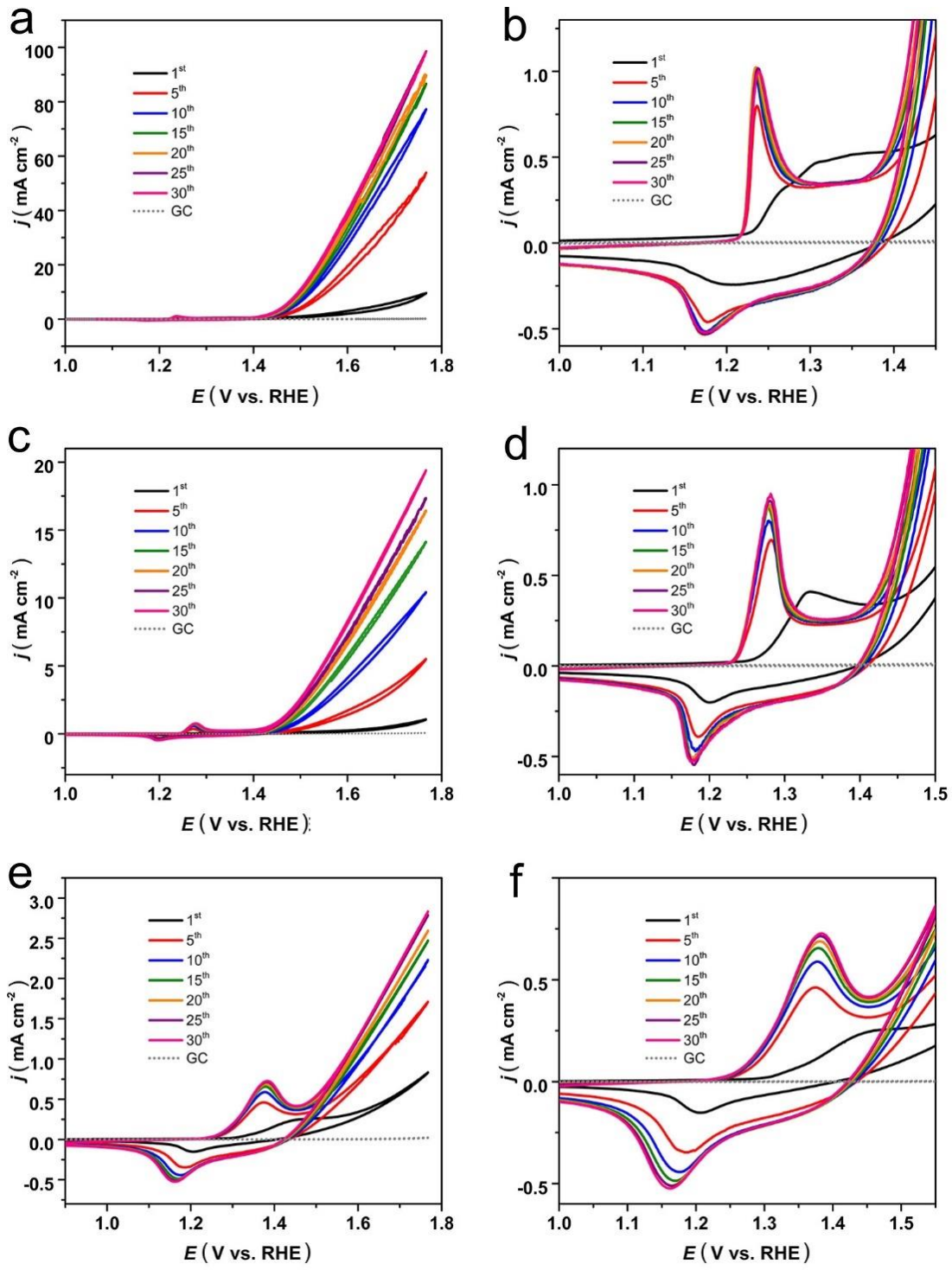


Figure 5. 14 Evolution of Ni-KMO voltammograms over 30 cycles at (a) pH=14, (c) pH=13, (e) pH=12. Corresponding enlarged redox peaks of Ni^{2+}/Ni^{3+} redox couple at (b) pH=14, (d) pH=13, (f) pH=12.

Since the OER catalytic activity is directly correlated to the nature of the Ni centers,

understanding the redox peak of the Ni in the cyclic voltammograms may contribute to greater understanding of the reaction mechanism as well as in the development of better catalyst. Voltammetric profiles of the Ni^{2+}/Ni^{3+} redox peaks were recorded at different pHs (**Figure 5.15**). At pH=14 the presence of two discrete processes, Ox1/Re1 and Ox2/Re2, were observed. Previous reports assigned the process Ox1 ↔ Re1 to the phase transition α-$Ni(OH)_2$/γ-NiOOH, while the process labelled Ox2 ↔ Re2 has been associated with the transition of β-$Ni(OH)_2$ to the active phase β-NiOOH.[36, 37] A schematic illustration of the phase transitions is presented in **Figure 5.16**. When the pH is decreased to 13, only one oxidation peak is observed (Ox1) and the peak labelled Re2 shifts towards more positive potentials and its current density decreases (**Figure 5.15**). At pH=12, the Re2 peak is not observable and only the redox peak Ox1/Re1 is visible. The absence of the β-NiOOH transformation at pH=12 was accompanied by a significant reduction in measured OER activity.

To explore the underlying mechanism, we thoroughly examined the relationship between the Ni^{2+}/Ni^{3+} redox peaks and the scan rates. The linear relationship between peak current density and scan rate at pH=14 was indicative that the surface reaction kinetics were dominated by charge transfer steps, whereas the linear relationship between peak current density and the square root of the scan rate at pH=12 was indicative that the diffusion limitation was the dominating factor (**Figure 5.17**).

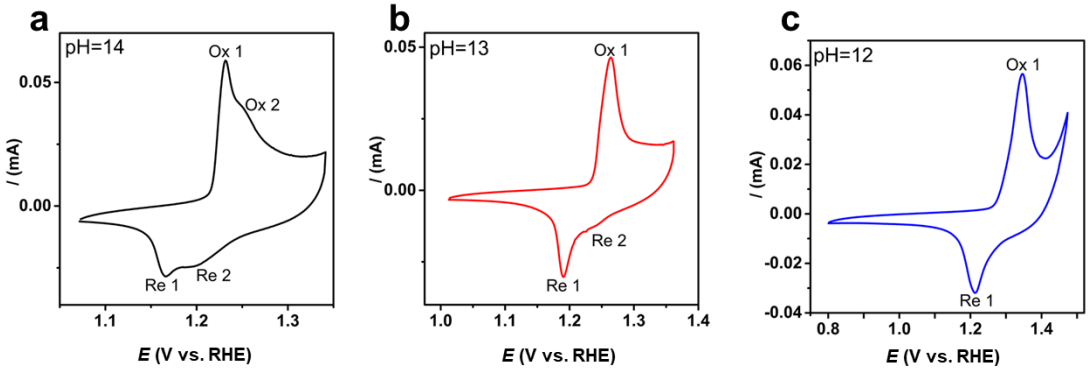


Figure 5. 15 Redox peak correlated NiOOH structure evolution of Ni-KMO at (a) pH=14. (b) pH=13. (c) pH=12, with scan rate v = 5 mV s^{-1}.

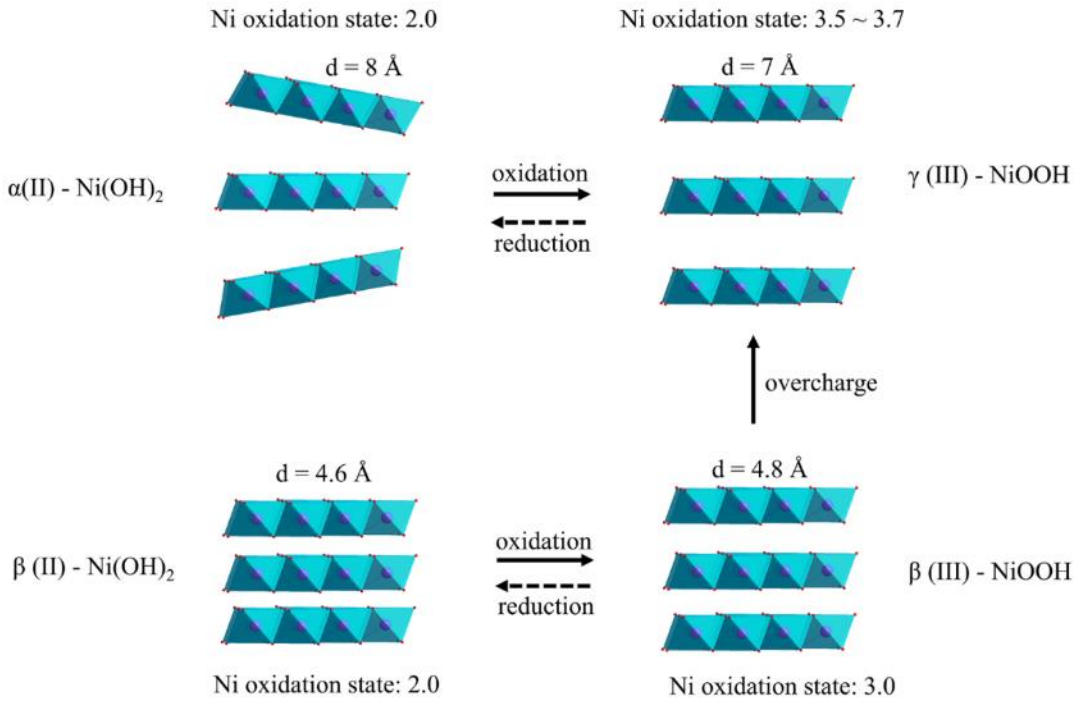


Figure 5. 16 Schematic graphs of Ni based phase transition.[38]

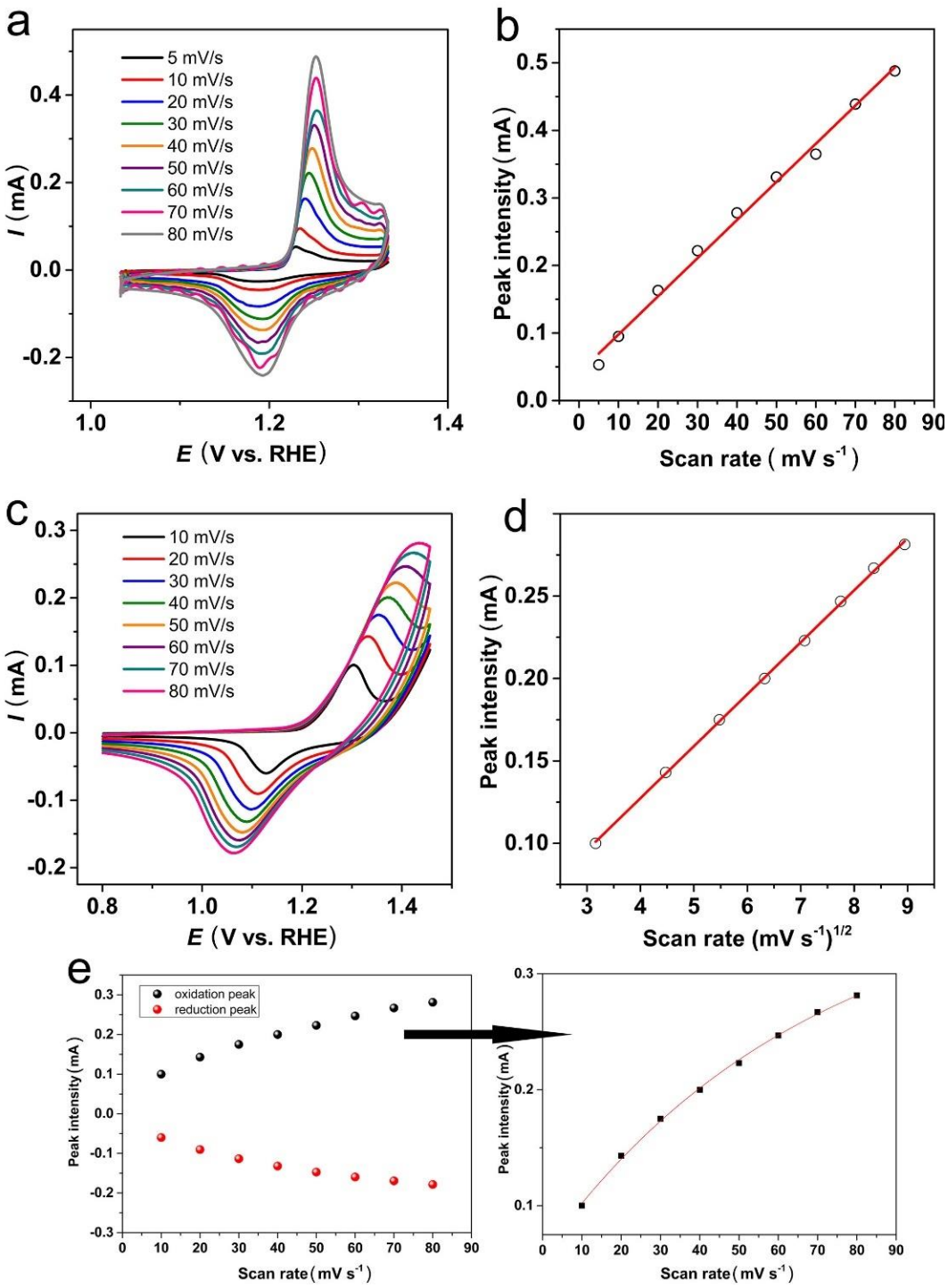


Figure 5. 17 Cyclic voltammograms of Ni-KMO in NaOH, (a) Ni^{2+}/Ni^{3+} redox peaks of Ni-KMO with varying scan rates at pH=14, (b) corresponding linear fitting of peak value against scan rate. (c) Ni^{2+}/Ni^{3+} redox peaks against scan rate of Ni-KMO at pH=12, (d) corresponding linear fitting of peak current value against the square root of scan rate, (e) asymptotic independence of peak currents against scan rate at pH=12.

The charge associated with the redox peaks as function of the pH is also shown in **Figure 5.13d** and **Figure 5.18**. As can be seen, opposite to the literature,[35] the charge associated to the redox peak of Ni^{2+}/Ni^{3+} increases as the pH decreases. We further explore this phenomenon by analyzing the charges of the redox peak at pH=12 and pH=14 as a function of the number of cycles. **Figure 5.19** shows the comparison between the charge of the redox peaks of the 1st scan and 30th scan for the different pHs. The first observation is that slightly larger charges are observed at pH=14 and pH=13. As can be seen, the charge of the oxidation peak increases after electrochemical cycling across the pH range explored. However, the increase of the charge of the redox peak is significantly larger at pH=12 and after 30 cycles. Charge of the redox peak at pH=12 (399 μC) is 1.89-fold that of the same peak at pH=14 (211 μC). According to the discussion above, and the XAS results (section 2.2) the Ni-clusters intercalated between the KMO layers must undergo an "*activation process*", which is attributed to a phase transformation of the Ni oxide species. While at pH=14, Ni sites with OH^- adsorption are fully transformed into the *β*-NiOOH active form, at pH=12 most of the catalyst is only transformed into the *γ*-NiOOH phase. Considering that the oxidation state of the *β*-NiOOH is +3 and the *γ*-NiOOH is ~3.7 (**Figure 5.19**), the transformation from Ni^{2+} to *γ*-NiOOH requires ~1.7 fold more charges than that to the *β*-NiOOH. Therefore, our results suggest that at pH=14 the active phase for the OER is the *β*-NiOOH and at pH=12, the active phase for the OER is the *γ*-NiOOH. The unique structure of the Ni confined in 2D layer structure with flexibly adjustable interlayer spacing gives rise to such phenomenon.

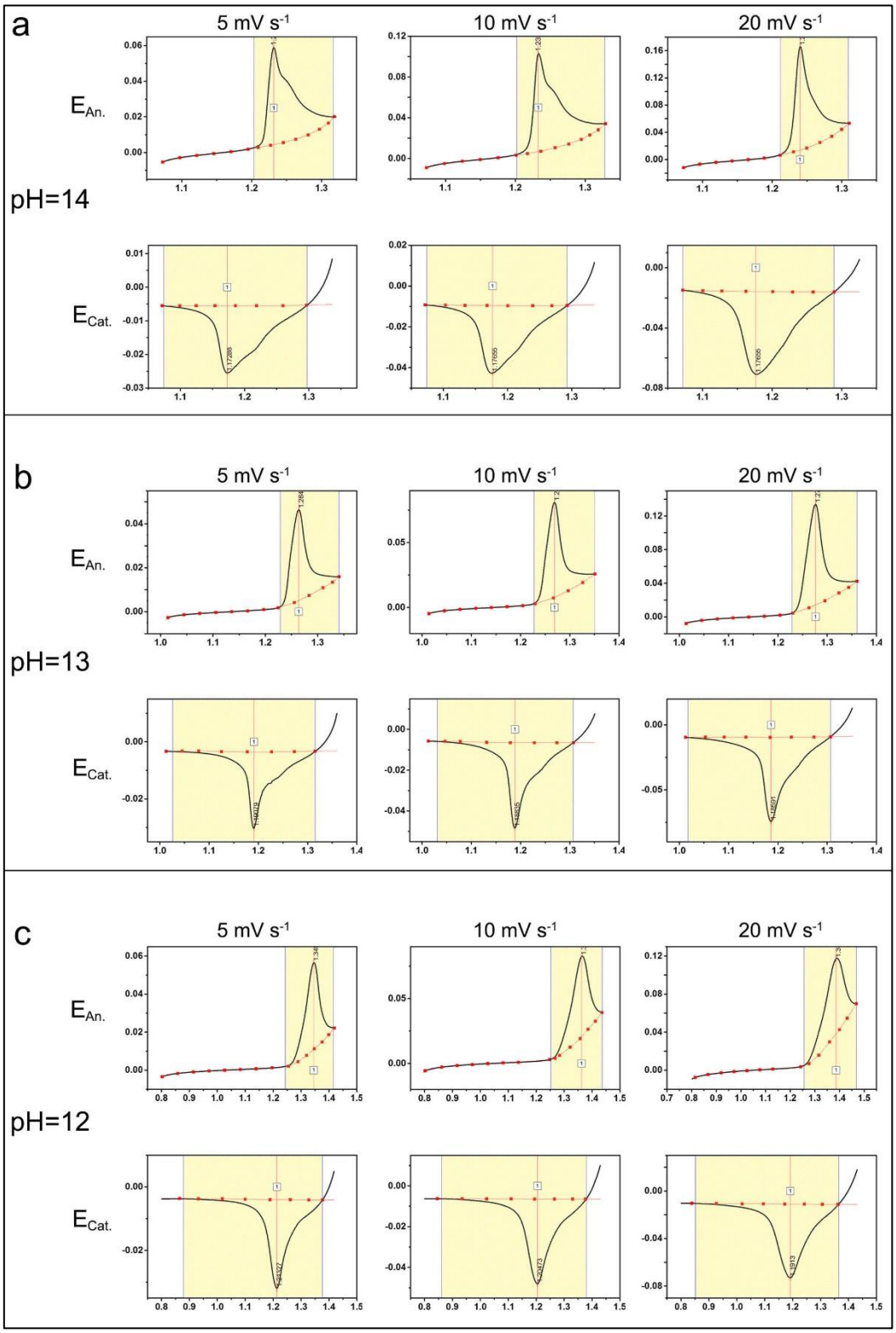


Figure 5. 18 Graphic demonstration of the potential limits and base line for the integration of the charge associated with the Ni redox peaks of Ni-KMO at (a) pH=14, (b) pH=13, (c) pH=12 and different scan rates.

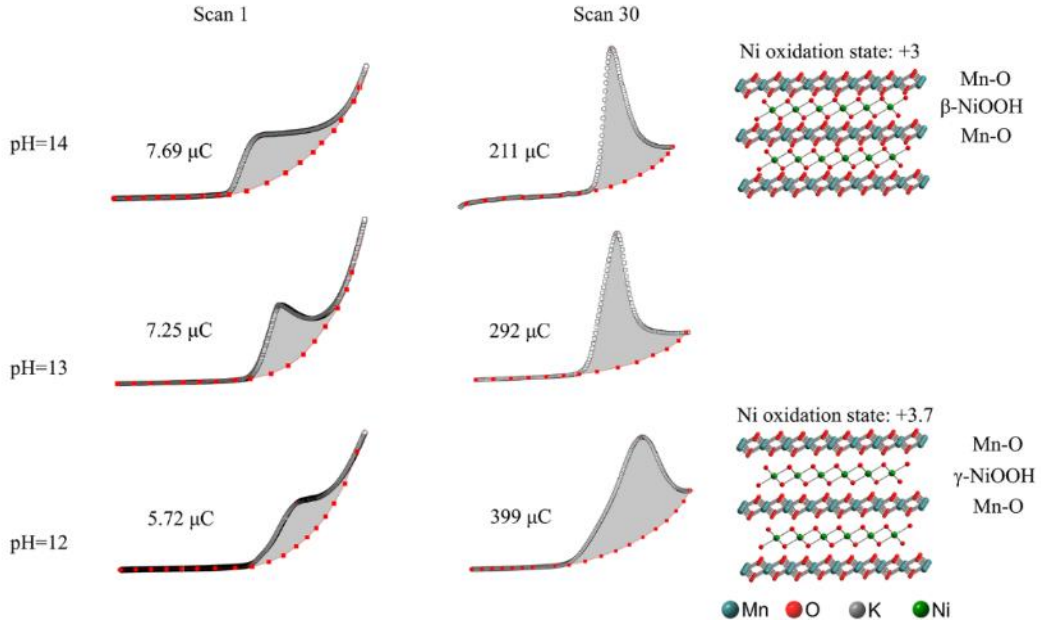


Figure 5. 19 Integration charge of scan1 and scan 30 at pH=14, pH=13 and pH=12 with the corresponding schematical crystal structures.

In order to obtain more information on the reaction mechanism, Tafel analysis of the OER curves at different pHs was performed. Note that all voltammograms were iR corrected prior to the Tafel analysis. It has been previously proposed that the overall mechanism of OER catalysis on Ni sites in alkaline media involve four proton-electron-transfer steps.[39] Tafel plots for the OER on Ni-KMO at different pHs are presented in **Figure 5.20**. The following equations are used for the determination of rate-determining step (RDS) by Tafel slope[40],

$$b = \frac{2.3RT}{a\,F} \qquad [5.3]$$

$$a = \frac{n_f}{v} + n_r\beta \qquad [5.4]$$

R is the gas constant, T is temperature, F is faraday's constant, n_f is the number of electrons transferred before the RDS, v is the stoichiometric number with a typical value of 1, n_r is the number of electrons transferred in a single RDS, β is the symmetry factor with a typical value of 0.5. If the first electron transfer (Eqn. 5.5) is rate-determining, the Tafel slope can be calculated as 120 mV dec^{-1}. Accordingly, Tafel slopes show values of 40 mV dec^{-1} and 24 mV dec^{-1} as the RDS are the second and the third electron

transfer (Eqn. 5.6 and Eqn. 5.7), respectively.[7] For the case of Tafel slope of 60 mV dec^{-1}, the RDS involves a chemical step subsequent to the first electron transfer, with n_r = 0 and n_f = 1. Thus, Ni-KMO at pH=14, RDS is chemical deprotonation; at pH=12, RDS is the adsorption of OH^-.

The Tafel slope, at pH=14, is 60 mV dec^{-1} suggesting that the rate-determining step (RDS) was the deprotonation of adsorbed hydroxyl species (Eqn. 5.6), in agreement with previous works on Ni hydroxide/oxide catalyst.[41] On the other hand, a Tafel slope of 232 mV dec^{-1} was obtained at pH 12, suggesting that the RDS at lower pH was the adsorption of OH^- species. This can be rationalized by consideration of the nature of Ni sites. A higher concentration gradient is required to promote the transport of the OH^- species from electrolyte through the channels of the layered oxide structure to the confined Ni nanoreactor sites. This diffusion-dependent process gives rise to the significant difference in OER activity observed for Ni-KMO with varying pHs.

$$Ni^* + OH^- \rightarrow Ni^*OH + e^- \quad [5.5]$$

$$Ni^*OH + OH^- \rightarrow Ni^*O + H_2O + e^- \quad [5.6]$$

$$Ni^*O + OH^- \rightarrow Ni^*OOH + e^- \quad [5.7]$$

$$Ni^*OOH + OH^- \rightarrow Ni^* + O_2 + H_2O + e^- \quad [5.8]$$

The evaluation of the electrochemical performance of a catalyst should not only be based on its catalytic activity but also on the durability of the catalyst. Long-term stability of the Ni-KMO was recorded at pH=14 *via* chronoamperometry at various applied potentials (**Figure 5.13**). As can be seen, the current density during the OER remained stable over 1 h of electrolysis at different relevant potentials. In order to gain insight into the structural and compositional stability of the catalyst, SEM and HAADF-EDS images of the Ni-KMO catalyst were collected after electrolysis (**Figure 5.21**). Interestingly, no significant changes in the morphology or the element distribution of the catalyst were detected confirming the excellent stability of the catalyst after 10 h of electrolysis.

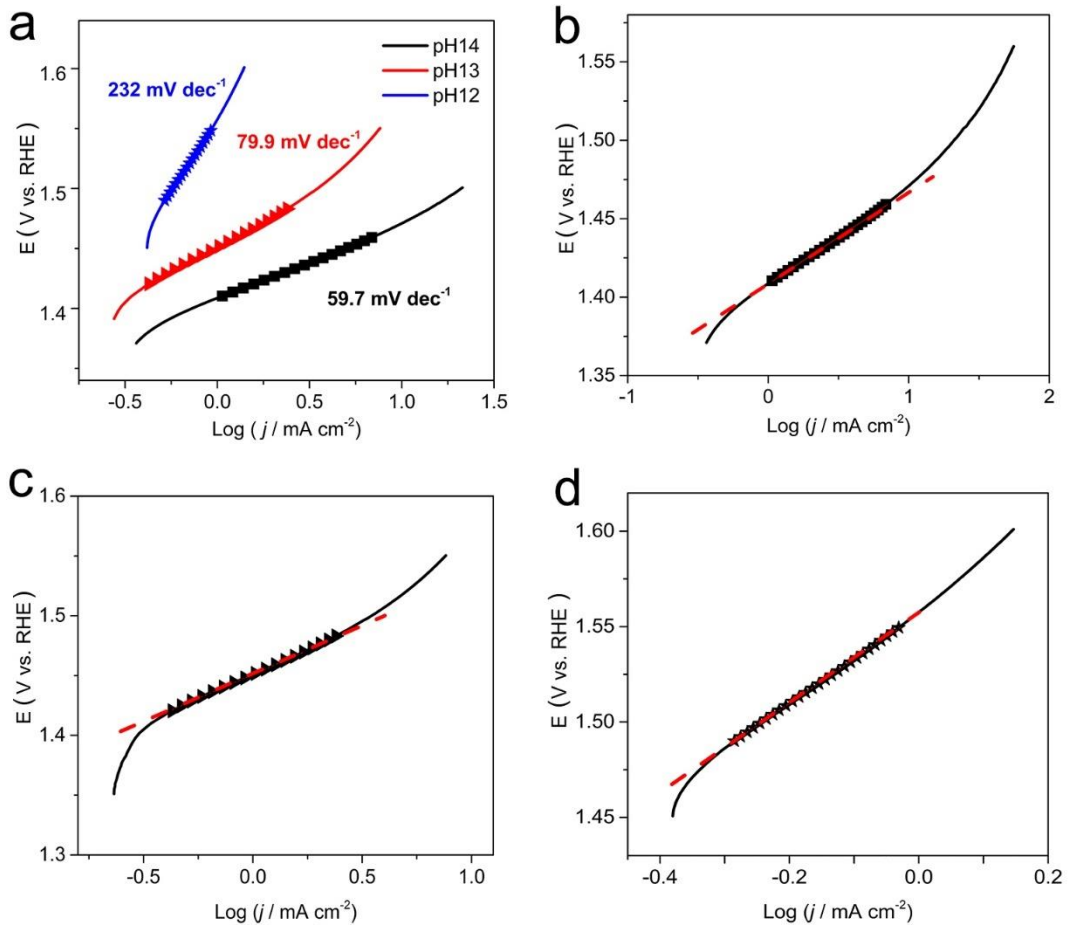


Figure 5. 20 (a) Tafel slopes of Ni-KMO, with corresponding slope fitting at (b) pH=14, (c) pH=13, (d) pH=12.

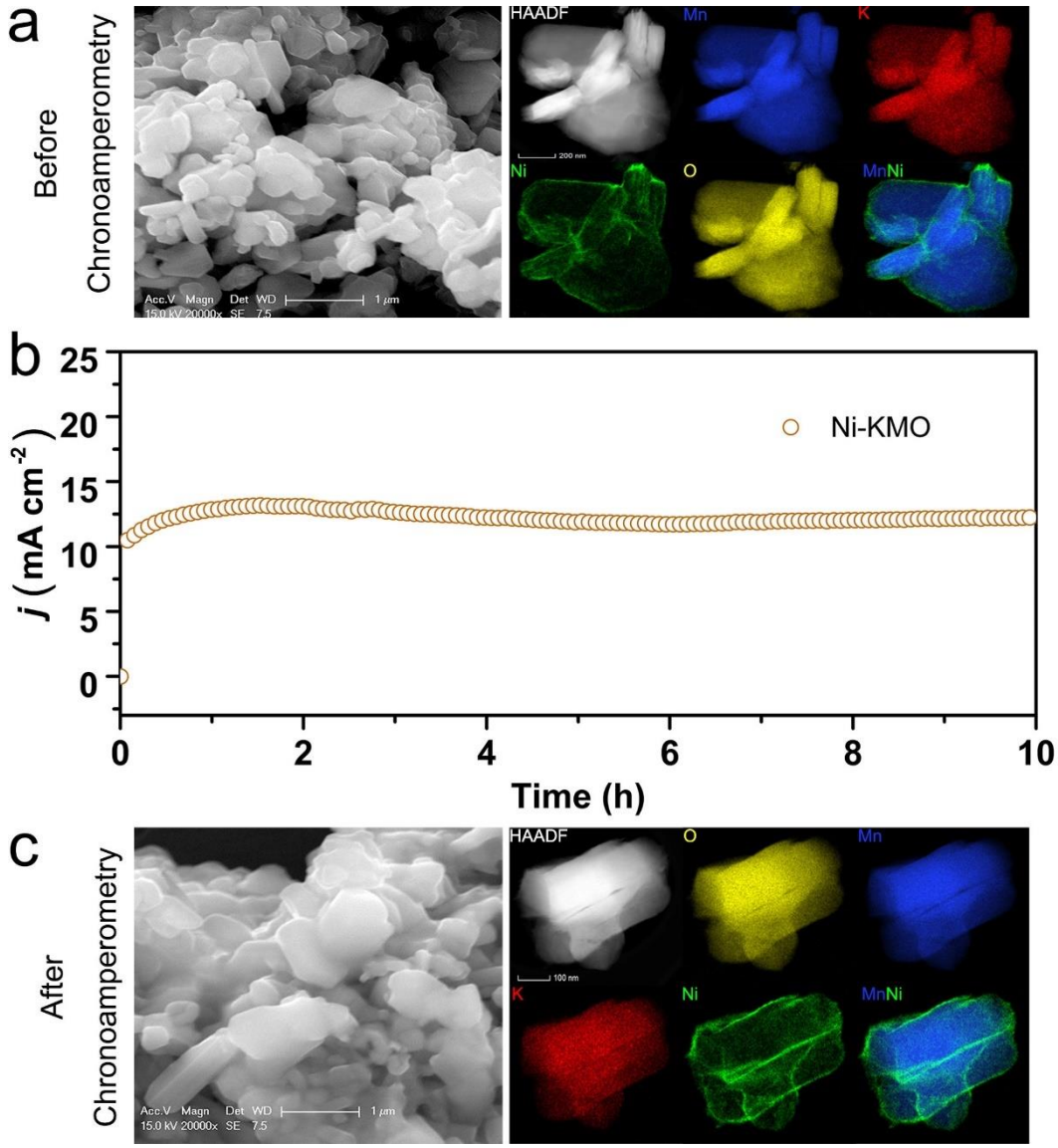


Figure 5. 21 (a) SEM and STEM-EDS images of Ni-KMO before electrochemical evaluation, (b) chronoamperometry of Ni-KMO at 1.48 V over 10 h, (c) SEM and STEM-EDS images of Ni-KMO after electrochemical evaluation.

5.3.4 Effect of the cations on the OER catalytic activity

Previous works have also demonstrated that in addition to the pH, the nature of the electrolyte cation also affects the observed activity and selectivity of electrochemical processes, especially in alkaline media.[42, 43] We investigated the effect of K^+ and Na^+ cations on the electrochemical activity of Ni-KMO towards the OER (**Figure 5.22**). As can be seen, although a slightly different shape of the $Ni^{2+} \rightarrow Ni^{3+}$ redox peaks was

observed, the charges for the Ni^{2+}/Ni^{3+} redox peaks are almost identical, 261 μC in NaOH and 263 μC in KOH respectively. Ni-KMO presents lower η_{onset} and η_{10} for the OER in KOH (η_{onset} = 100 mV and η_{10} = 206 mV) relative to the respective values in NaOH (η_{onset} = 130 mV and η_{10} = 240 mV). It has been previously demonstrated, that the nature of the cations affects the catalytic activity of the OER and the ORR. In particular, those reports indicate that potassium enhance the catalytic activity.[44-46] This effect has been associated to the non-covalent interaction between $K^+(H_2O)_x/Na^+(H_2O)_x$ clusters and the active Ni-oxygenated species at the surface Ni-OH*, Ni-O*, Ni-OOH*. **Figure 5.22** shows that the onset of the Ni^{2+}/Ni^{3+} oxidation reaction is independent of the cation present in the electrolyte (KOH or NaOH) which indicates similar adsorption reaction of OH^- on Ni sites. On the other hand, at slight more positive potentials a slight cathodic shift of OER onset in KOH suggests that the subsequent deprotonation step is favorable in KOH. Suntivich *et al*. suggested that charged $K^+(H_2O)_x/Na^+(H_2O)_x$ clusters would modified the energy of M-oxygenated species, thus change their stability.[44]

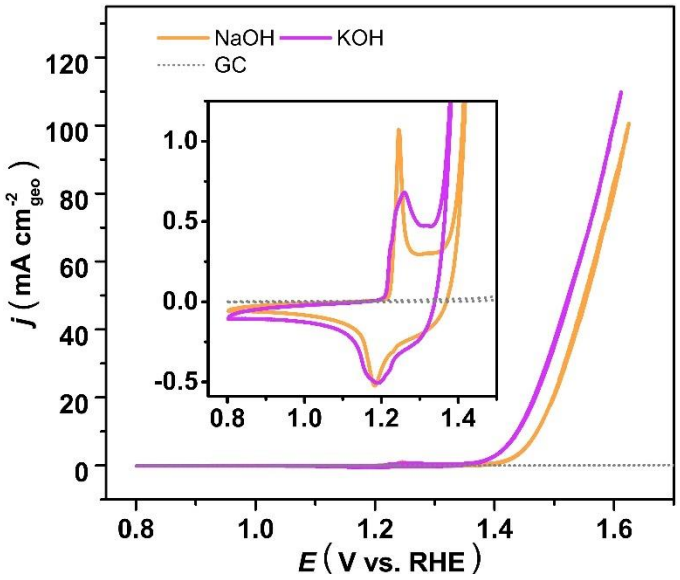


Figure 5. 22 Voltammetric profiles of Ni-KMO in 1 M KOH and NaOH electrolyte, as indicated in the figure, inset is the enlarged redox features. Glassy carbon shown for comparison. Scan rate υ = 20 mV s^{-1}.

5.3.5 Investigation of the coordination of active Ni on the catalytic activity

In order to further investigate the specific role of Ni coordination in the performance of the catalyst, Ni-exchanged $HMnO_2$ (Ni-HMO) and Ni-exchanged $HTi_{0.91}O_2$ (Ni-HTO) were prepared and evaluated towards the OER. Both materials, HMO and HTO, present the same layered structure (**Figure 5.23**), therefore any observable differences in the catalytic activity would suggest differences in the interaction between the Ni and species such as Mn/Ti and K/H_2O around. Both Ni-HMO and Ni-HTO catalysts display notable OER activity (**Figure 5.24a**) in comparison with the pristine HMO and HTO (**Figure 5.25**). As can be seen on **Table 5.9**, Ni-KMO shows the greatest OER catalytic activity (η_{10} = 240 mV) of the three Ni-exchanged layered oxide catalysts in regard to geometrical activity. Despite the remarkable difference of Ni redox peaks for the 3 catalysts, the OER η_{onset} values are nearly identical, indicating that confined Ni is truly the active component in the observed activity of Ni-exchanged HMO and HTO. Tafel slopes of three Ni confined samples are shown in **Figure 5.27**. Ni-HTO with a value of 50 mV dec^{-1} is smaller than Ni-KMO (60 mV dec^{-1}) and Ni-HMO (113 mV dec^{-1}). These data suggest that the chemical deprotonation process is the RDS for both Ni-HTO and Ni-KMO, whilst for Ni-HMO it is the adsorption of OH^-. To obtain further information on the nature of the differences in the shape of the redox peaks and the catalytic activity the Ni content in each of the catalysts was determined by XRF (**Table 5.9**). It was found that Ni-HMO had the greatest Ni loading (16 wt.%), followed by Ni-KMO (8 wt.%) and Ni-HTO (2 wt.%). Therefore, the differences in the shape of the redox peaks could be attributed to the differences in Ni loading and coordination, but the larger catalytic activity of the Ni-KMO could not be directly correlated to the Ni loading. This implies that Ni coordination plays the predominant role in water catalysis. Identical crystal structure (**Figure 5.23**) combined with EXAFS (**Figure 5.5**), XRF and TGA results (**Table 5.1**) indicate chemical environment difference of Ni-KMO and Ni-HMO is the coordination of H_2O/K. As compared to Ni-KMO, more H_2O intercalated in Ni-HMO that led to the replacement of K/H_2O-Ni by H_2O-Ni. Thenuwara reported that highly ordered water molecules lowering the potential barrier that facilitated the

OER.[47] Our study here suggested that appropriate amount of water promote the OER by the optimal orientation, whereas excess interlayer water would alter such alignment thus reduce the promotion effect.

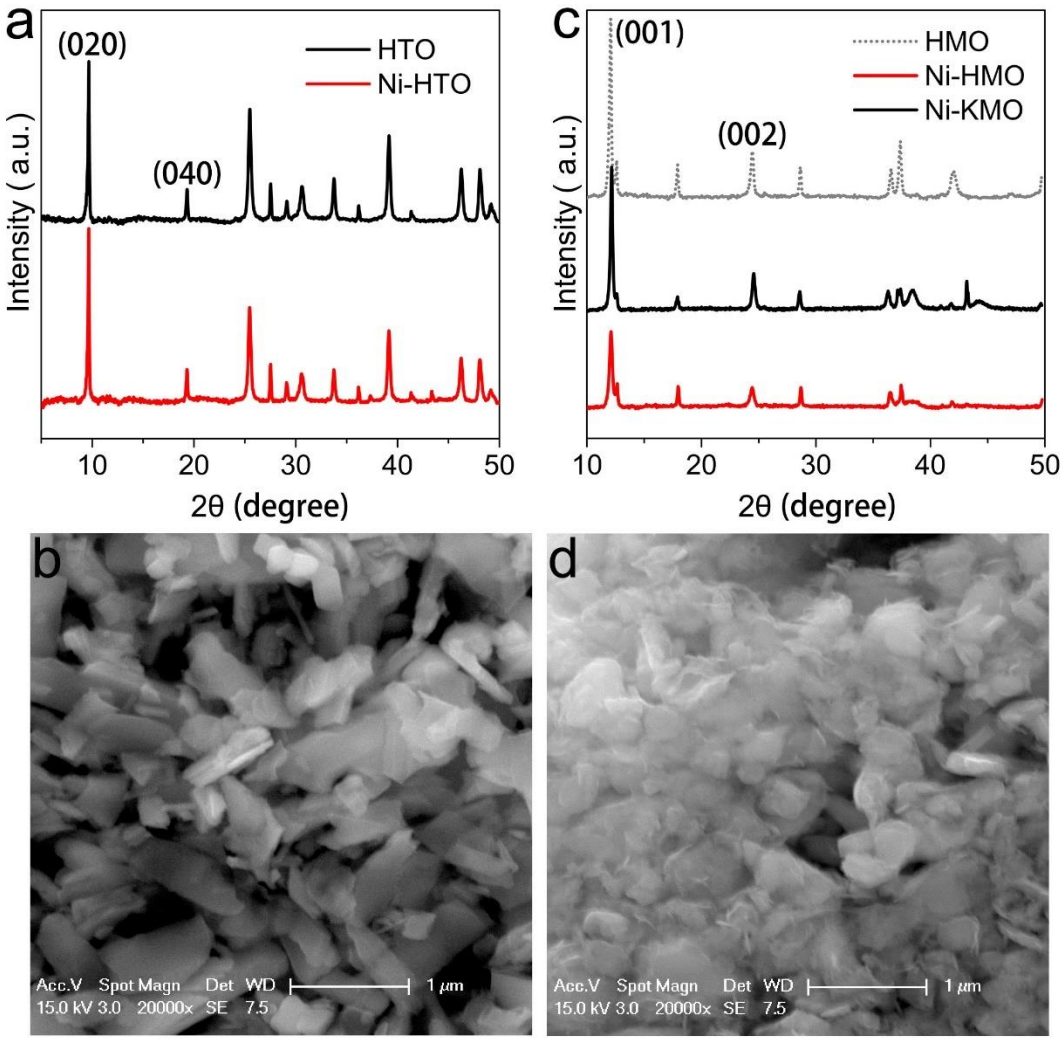


Figure 5. 23 XRD patterns of pristine (a) HTO and (c) HMO, and after Ni-exchange intercalation. SEM images of (b) Ni-HTO, (d) Ni-HMO.

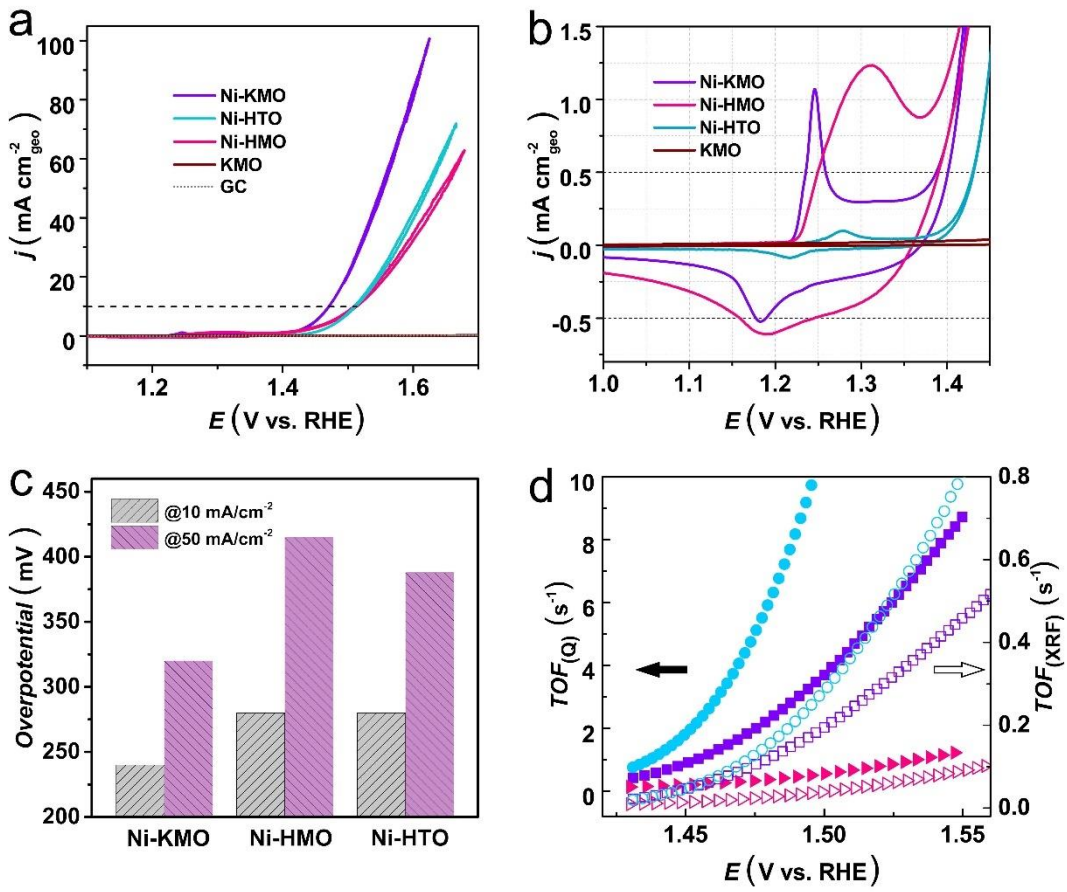


Figure 5. 24 (a) iR-corrected voltammetric profiles of Ni-KMO, Ni-HMO and Ni-HTO after 30 consecutive scans at pH=14, in 1 M NaOH at 20 mV s^{-1}. The evolution of the voltammograms as a function of the number of scans can be found in **Figure 5.25**. (b) Enlarged region showing the $Ni^{2+} \rightarrow Ni^{3+}$ redox peaks and OER onset. (c) η_{50} and η_{10} obtained from (a). (d) TOF as a function of potential calculated using the content of Ni content on Ni-KMO, Ni-HMO and Ni-HTO determined by the Ni^{+2}/Ni^{+3} redox charge and the XRF.

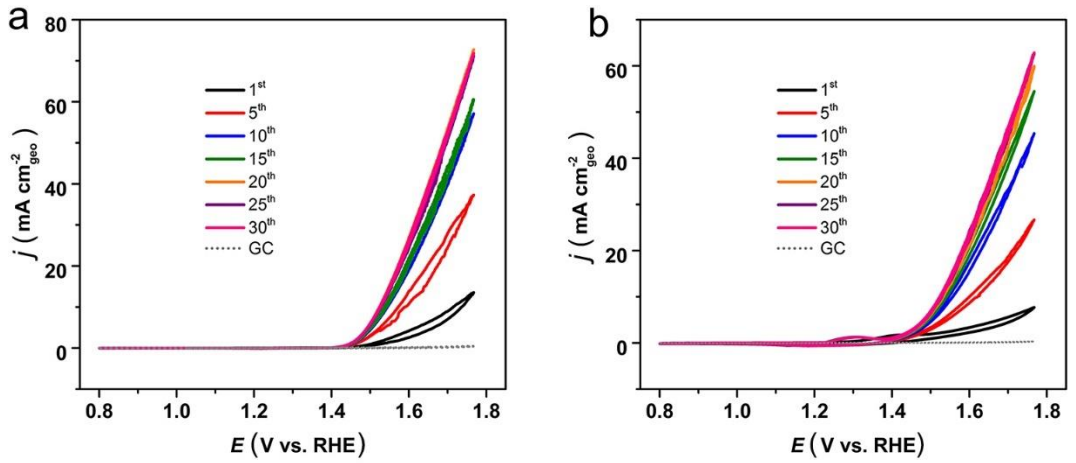


Figure 5. 25 Voltammetric profiles of (a) Ni-HTO and (b) Ni-HMO evolved in 30 cycles in 1 M NaOH.

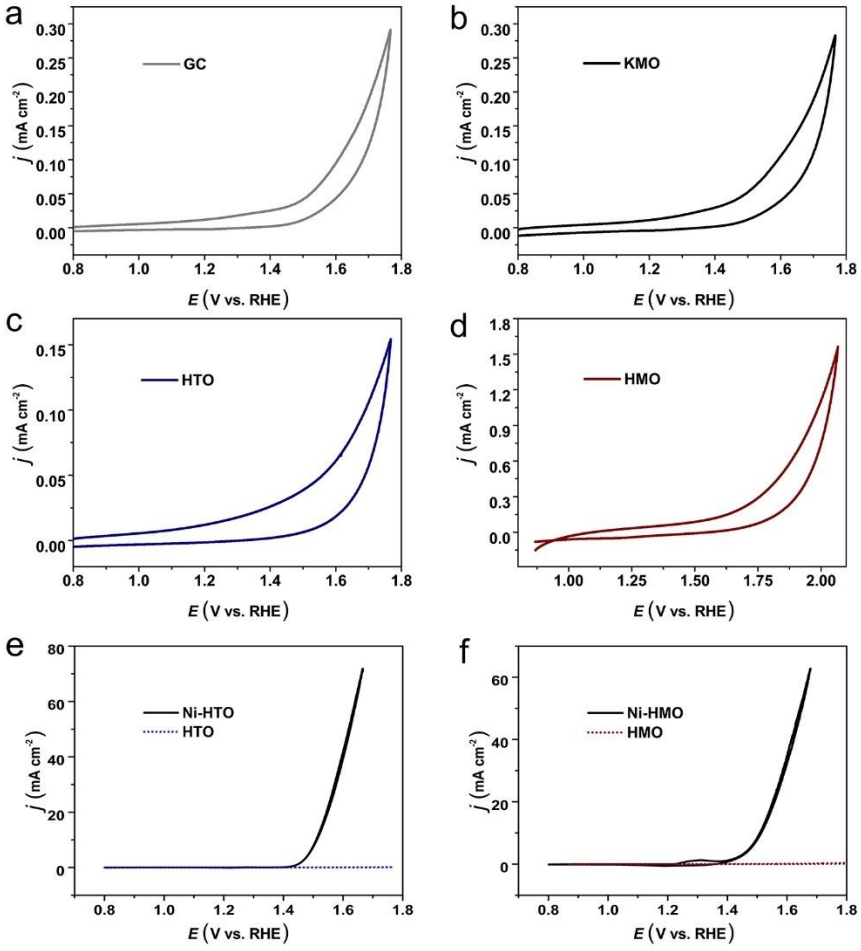


Figure 5. 26 CV of (a) GC electrode and pristine (b) KMO, (c) HTO and (d) HMO, (e) Ni-HTO and HTO for comparison, (f) Ni-HMO and HMO for comparison at pH=14.

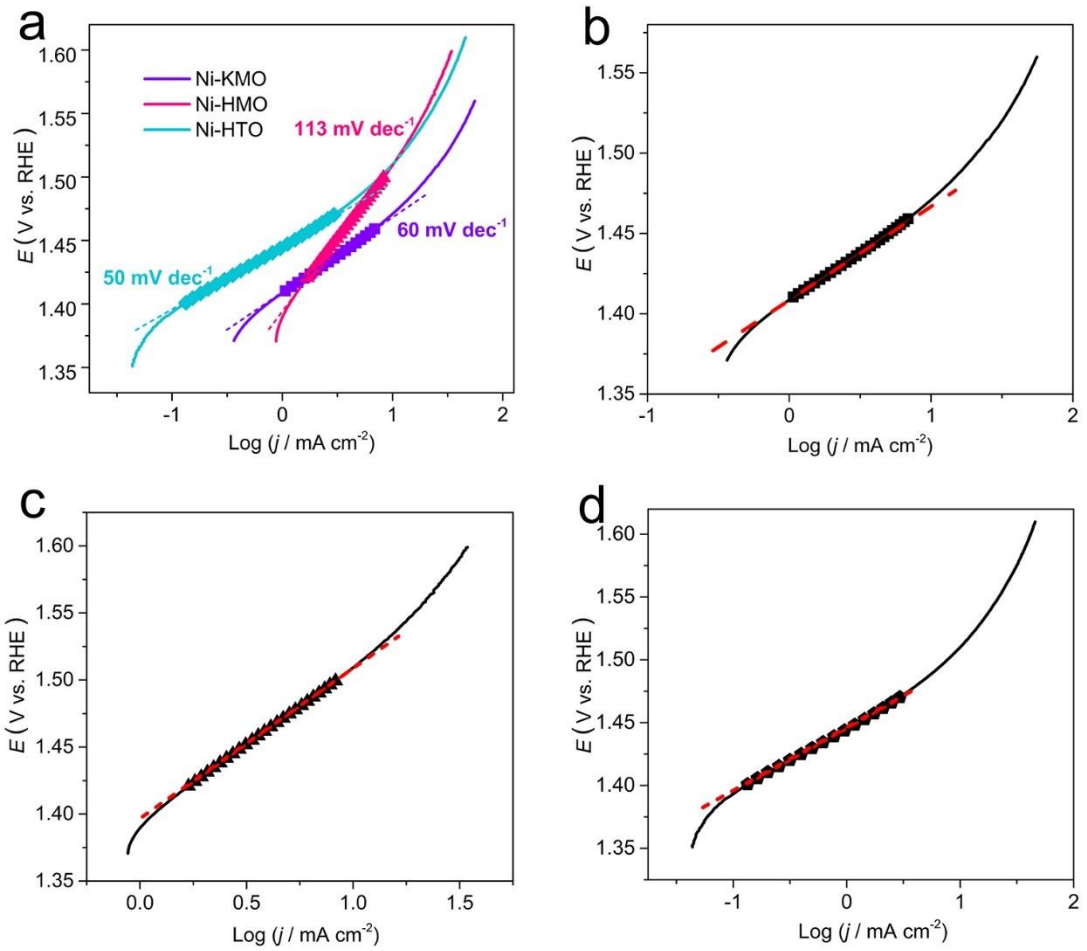


Figure 5. 27 (a) Tafel plots of Ni-exchanged layered metal oxides, corresponding fitting of (b) Ni-KMO, (c) Ni-HMO, (d) Ni-HTO at pH=14.

So far we have demonstrated that the Ni sites solely give rise to the observed OER activity of the Ni-confined layered metal oxide catalysts, thus, the Ni content allows us to determine the turnover frequency (TOF) of the catalyst, a key indicator of the intrinsic activity of a catalyst. However, two possible strategies can be adopted in this case. The TOF was determined using the total Ni content obtained from XRF measurements (TOF_{XRF}) and by use of the wt %Ni determined by the charge of Ni^{2+}/Ni^{3+} redox peak (TOF_Q), as previously demonstrated by Nakagawa[41] and Chen[42] (**Figure 5.24d**). Whilst the two methods give different absolute values of the TOF, the trend Ni-HTO > Ni-KMO > Ni-HMO is the same. Interestingly, despite the results above indicating that the Ni-KMO had the larger catalytic activity per geometrical

surface area, Ni-HTO displays better TOF values (**Table 5.9**), indicating that it possesses the highest active atom efficiency. Determination of the %Ni from the integrated charges and XRF measurements both strongly support our claim of low-loading of active catalysts for OER catalysis. For example, as the XRF result is overall evaluation of Ni content in catalyst, TOF calculation based on XRF display the lower limitation. 2 wt.% Ni in Ni-HTO shows a TOF_{XRF} of 0.1090 ± 0.0067 s^{-1} at 1.47 V vs. RHE. While the TOF_Q of Ni-HTO is 4.22 ± 0.05 s^{-1} based on integrated charge, which is an order of magnitude higher than TOF_{XRF} (**Figure 5.28**).

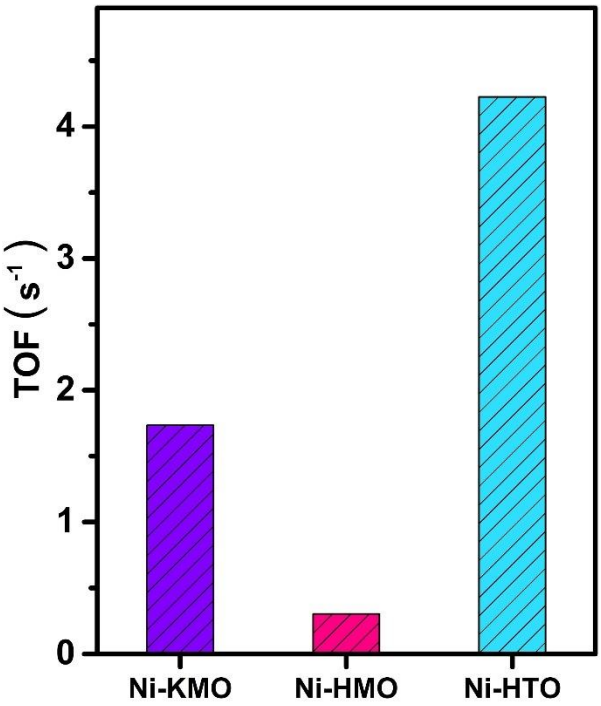


Figure 5. 28 Calculated TOFs normalized by the integrated charge of Ni-exchanged samples at η_{10} = 240 mV.

Table 5. 9 Summary of electrochemical data of Ni-KMO, Ni-HMO, Ni-HTO.

	$Ni_{0.16}K_{0.2}MnO_2 \cdot 0.7H_2O$	$Ni_{0.33}K_{0.04}MnO_2 \cdot 0.9H_2O$	$Ni_{0.033}Ti_{0.91}O_2 \cdot 0.6H_2O$
η_{10} / mV	**240**	**280**	**280**
Integration charge / mC	**0.278**	**0.743**	**0.0342**
Corresponding Ni content / μg	**0.169**	**0.452**	**0.020**
Tafel slope / mV dec^{-1}	**60**	**113**	**50**
Ni content [XRF] / wt.%	**8**	**16**	**2**
j_{mss} at η = 240 mV / A g_{Ni}^{-1}	**602**	**140**	**710**

The mass activities of our ion-exchanged catalysts **Figure 5.29** are compared with other Ni-based catalysts previously reported in the literature, including a variety of Ni structures (Ni foam, self-supported NiOOH nanocatalysts). Ni-KMO and Ni-HTO were found to have the largest mass activities by a factor of 4 or more. The mass activities of these 2D Ti-O and Mn-O Ni catalysts surpasses the state-of-the-art Ni-based catalysts, such as NiV-LDH (144 g_{Ni}^{-1} @300 mV)[48] or single Au atoms anchored on NiFe-LDH (117 g_{Ni}^{-1} @280 mV)[49].

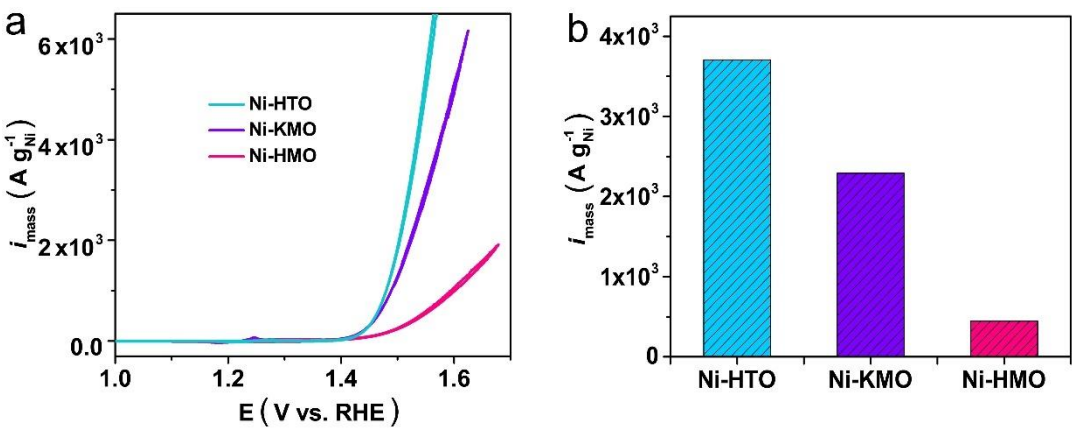


Figure 5. 29 (a) Voltammetric mass activity of Ni-KMO, Ni-HMO, and Ni-HTO measured in 1 M NaOH. Scan rate of 20 mV s^{-1}, (b) corresponding activity at 1.53 V vs RHE.

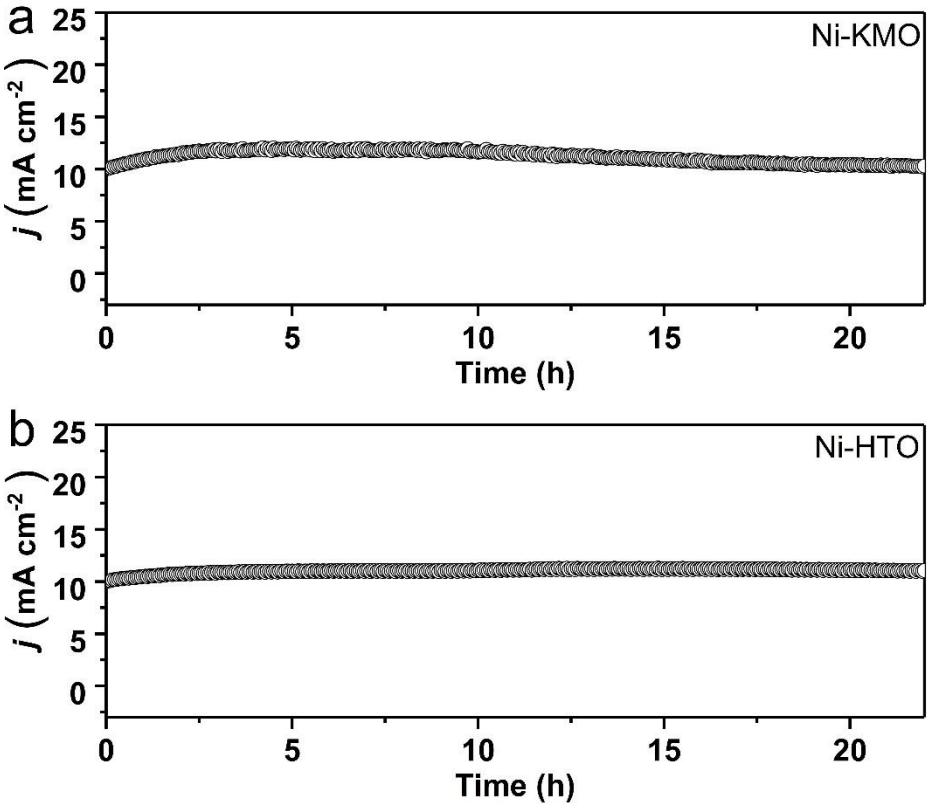


Figure 5. 30 Chronoamperometry of (a) Ni-KMO at 1.48 V and (b) Ni-HTO at 1.51 V in 1 M NaOH at least 20 h.

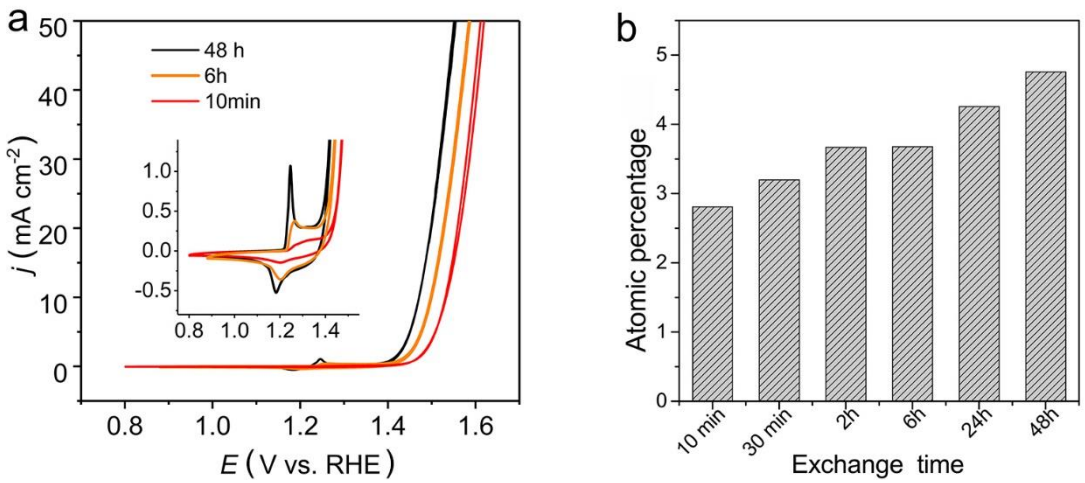


Figure 5. 31 (a) Cyclic voltammetry of Ni-KMO with different exchange time in 1 M KOH, scan rate of 20 mV s^{-1}. Inset shows the potential range between 0.8 and 1.5V showing the Ni^{2+}/Ni^{3+} redox peaks (b) Ni content of Ni-KMO determined by XRF analysis as a function of the Ni-exchange time.

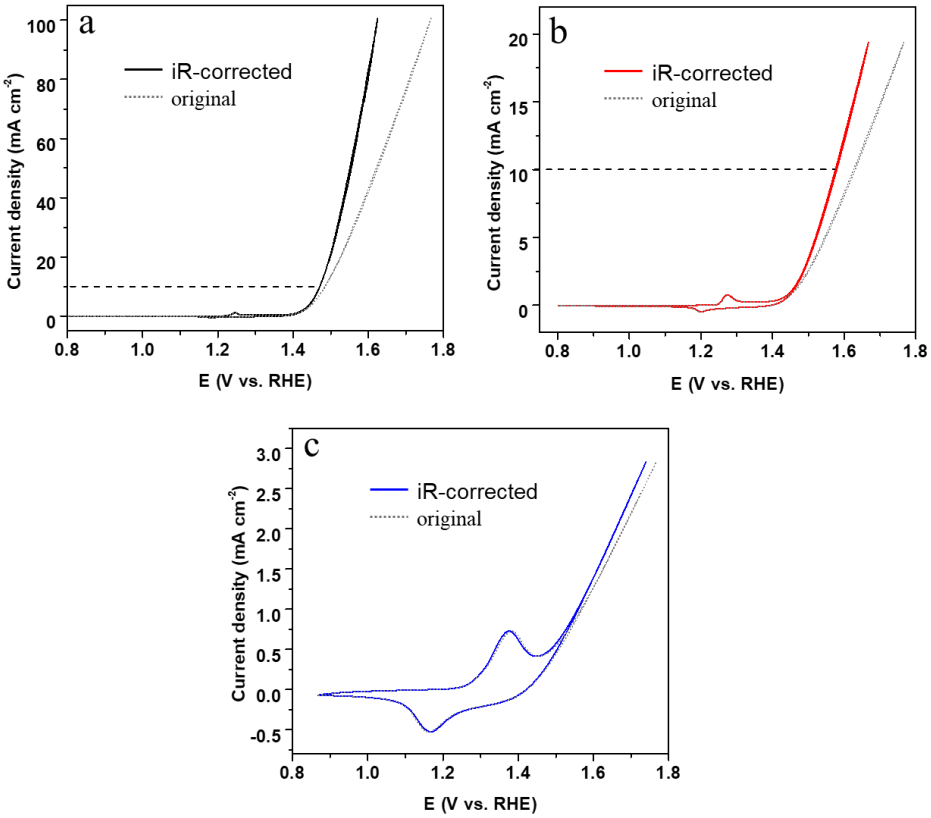


Figure 5. 32 iR-correction of CVs of Ni-KMOs at different pHs: (a)1 M NaOH, (b) 0.1 M NaOH, and (c) 0.01 M NaOH.

5.4 Conclusions

This work described the preparation and characterization of highly active OER catalysts based on the facile ion-exchange of Ni atoms into the 2D birnessite and lepidocrocite titanate structures. A direct correlation between the Ni redox peaks and the OER activity was demonstrated. After the evaluation of different catalysts as a function of the Ni content it was found that Ni-KMO and Ni-HTO show excellent mass activity of 602 A g_{Ni}^{-1} and 710 A g_{Ni}^{-1} at overpotential of 240 mV, respectively. Ni-HTO shows a 6-fold increase in catalytic activity per mass of Ni in comparison with the state-of-the-art Ni-based nanocatalysts (Au@$Ni_{7/8}Fe_{1/8}$ LDH). By evaluating the electrochemical performance at varying pHs in NaOH, it was found that the catalytic activity was enhanced at higher pH and in the presence of K cations, η_{onset} = 100 mV and η_{10} = 206 mV were obtained in comparison with those in the presence of Na cations (η_{onset} = 130 mV, η_{10} = 240 mV). The intercalation mechanism and oxidation state of Ni and Mn have been explored by the XAS technique. Our results demonstrate that Ni intercalation occurs at the Mn^{3+} sites by reducing Mn^{3+} to Mn^{2+}. As mentioned above, the *ex-situ* XAS/XES results shown that the Ni-content in each of the samples is proportional to the concentrations Mn^{3+} sites. Even though, Ni is present in the oxidation state (+2) for all the samples, the Ni coordination/structures were obtained for Ni-KMO and Ni-HMO was different. We associate the differences OER activity to the differences in coordination/structures between Ni-KMO and Ni-HMO. It was also demonstrated that while the intercalated Ni is the active site for oxygen evolution reaction, Mn sites do not contribute to the OER. Thus, the evaluation of intrinsic activity such as TOFs and mass activity by using the Ni content offers reliable results.

In brief, highly efficient catalysts with Ni confined in 2D layered metal oxides towards OER have been synthesized by ion exchange reactions. Our synthesis protocol provides evidence for the broader applicability of our employed methodology to other layered metal oxide structures and to compositions other than manganese oxides.

References

1. J. Kibsgaard and I. Chorkendorff, *Nature Energy*, 2019, **4**, 430.
2. C. Wei, R. R. Rao, J. Peng, B. Huang, I. E. Stephens, M. Risch, Z. J. Xu and Y. Shao-Horn, *Advanced Materials*, 2019, **31**, 1806296.
3. F. Song, L. Bai, A. Moysiadou, S. Lee, C. Hu, L. Liardet and X. Hu, *Journal of the American Chemical Society*, 2018, **140**, 7748-7759.
4. M. P. Browne, Z. Sofer and M. Pumera, *Energy & Environmental Science*, 2019, **12**, 41-58.
5. W. Zhang and K. Zhou, *Small*, 2017, **13**, 1700806.
6. R. Subbaraman, D. Tripkovic, K.-C. Chang, D. Strmcnik, A. P. Paulikas, P. Hirunsit, M. Chan, J. Greeley, V. Stamenkovic and N. M. Markovic, *Nature Materials*, 2012, **11**, 550-557.
7. M. S. Burke, M. G. Kast, L. Trotochaud, A. M. Smith and S. W. Boettcher, *Journal of the American Chemical Society*, 2015, **137**, 3638-3648.
8. Y. Zhao, C. Chang, F. Teng, Y. Zhao, G. Chen, R. Shi, G. I. Waterhouse, W. Huang and T. Zhang, *Advanced Energy Materials*, 2017, **7**, 1700005.
9. C. Luan, G. Liu, Y. Liu, L. Yu, Y. Wang, Y. Xiao, H. Qiao, X. Dai and X. Zhang, *ACS Nano*, 2018, **12**, 3875-3885.
10. F. Song and X. Hu, *Nature communications*, 2014, **5**, 1-9.
11. H. Wang, J. Zhang, X. Hang, X. Zhang, J. Xie, B. Pan and Y. Xie, *Angewandte Chemie*, 2015, **127**, 1211-1215.
12. V. Vij, S. Sultan, A. M. Harzandi, A. Meena, J. N. Tiwari, W.-G. Lee, T. Yoon and K. S. Kim, *ACS Catalysis*, 2017, **7**, 7196-7225.
13. A. Bergmann, T. E. Jones, E. M. Moreno, D. Teschner, P. Chernev, M. Gliech, T. Reier, H. Dau and P. Strasser, *Nature Catalysis*, 2018, **1**, 711-719.
14. Y. Hou, M. Qiu, M. G. Kim, P. Liu, G. Nam, T. Zhang, X. Zhuang, B. Yang, J. Cho and M. Chen, *Nature communications*, 2019, **10**, 1-9.
15. A. Munir, T. u. Haq, A. Qurashi, H. u. Rehman, A. Ul-Hamid and I. Hussain, *ACS Applied Energy Materials*, 2019, **2**, 363-371.
16. R. Ma and T. Sasaki, *Advanced Materials*, 2010, **22**, 5082-5104.
17. D. Deng, K. Novoselov, Q. Fu, N. Zheng, Z. Tian and X. Bao, *Nature nanotechnology*, 2016, **11**, 218-230.
18. T. Takashima, K. Hashimoto and R. Nakamura, *Journal of the American Chemical Society*, 2012, **134**, 1519-1527.
19. O. Diaz-Morales, D. Ferrus-Suspedra and M. T. Koper, *Chemical Science*, 2016, **7**, 2639-2645.
20. Y. Omomo, T. Sasaki and M. Watanabe, *Solid State Ionics*, 2002, **151**, 243-250.
21. J.-P. Parant, R. Olazcuaga, M. Devalette, C. Fouassier and P. Hagenmuller, *Journal of Solid State Chemistry*, 1971, **3**, 1-11.
22. Y. Pu, Q. Chen, Z. Sun, P. Rodriguez and L. Huang, *Crystal Growth & Design*, 2019, **19**, 3298-3304.
23. A. J. Dent, G. Cibin, S. Ramos, A. D. Smith, S. M. Scott, L. Varandas, M. R. Pearson, N. A. Krumpa, C. P. Jones and P. E. Robbins, *Journal of Physics: Conference Series*, 2009, **190**, 012039.
24. B. Ravel and M. Newville, *Journal of synchrotron radiation*, 2005, **12**, 537-541.
25. M. Newville, *Journal of synchrotron radiation*, 2001, **8**, 96-100.
26. S. Diaz-Moreno, M. Amboage, M. Basham, R. Boada, N. E. Bricknell, G. Cibin, T. M. Cobb, J.

Filik, A. Freeman and K. Geraki, *Journal of synchrotron radiation*, 2018, **25**, 998-1009.
27. S. Hayama, G. Duller, J. P. Sutter, M. Amboage, R. Boada, A. Freeman, L. Keenan, B. Nutter, L. Cahill and P. Leicester, *Journal of synchrotron radiation*, 2018, **25**, 1556-1564.
28. J. E. Post and D. R. Veblen, *American mineralogist*, 1990, **75**, 477-489.
29. J. C. Conesa, *The Journal of Physical Chemistry C*, 2016, **120**, 18999-19010.
30. M. Belli, A. Scafati, A. Bianconi, S. Mobilio, L. Palladino, A. Reale and E. Burattini, *Solid State Communications*, 1980, **35**, 355-361.
31. P. Ghigna, G. Flor and G. Spinolo, *Journal of Solid State Chemistry*, 2000, **149**, 252-255.
32. J.-K. Chang, M.-T. Lee and W.-T. Tsai, *Journal of Power Sources*, 2007, **166**, 590-594.
33. D. Friebel, M. W. Louie, M. Bajdich, K. E. Sanwald, Y. Cai, A. M. Wise, M.-J. Cheng, D. Sokaras, T.-C. Weng, R. Alonso-Mori, R. C. Davis, J. R. Bargar, J. K. Nørskov, A. Nilsson and A. T. Bell, *Journal of the American Chemical Society*, 2015, **137**, 1305-1313.
34. M. Görlin, P. Chernev, J. Ferreira de Araújo, T. Reier, S. Dresp, B. Paul, R. Krähnert, H. Dau and P. Strasser, *Journal of the American Chemical Society*, 2016, **138**, 5603-5614.
35. M. Görlin, J. Ferreira de Araújo, H. Schmies, D. Bernsmeier, S. Dresp, M. Gliech, Z. Jusys, P. Chernev, R. Kraehnert, H. Dau and P. Strasser, *Journal of the American Chemical Society*, 2017, **139**, 2070-2082.
36. B. S. Yeo and A. T. Bell, *The Journal of Physical Chemistry C*, 2012, **116**, 8394-8400.
37. S. R. Mellsop, A. Gardiner, B. Johannessen and A. T. Marshall, *Electrochimica Acta*, 2015, **168**, 356-364.
38. M. Wehrens-Dijksma and P. H. L. Notten, *Electrochimica Acta*, 2006, **51**, 3609-3621.
39. K. Xu, P. Chen, X. Li, Y. Tong, H. Ding, X. Wu, W. Chu, Z. Peng, C. Wu and Y. Xie, *Journal of the American Chemical Society*, 2015, **137**, 4119-4125.
40. G. Rolando, G. C. Richard, M. F. Juan, G. Eliezer, L. Jacek, S. Wolfgang and T. Sergio, *Pure and Applied Chemistry*, 2014, **86**, 245-258.
41. J. Liu, Y. Zheng, Y. Jiao, Z. Wang, Z. Lu, A. Vasileff and S. Z. Qiao, *Small*, 2018, **14**, 1704073.
42. C. Stoffelsma, P. Rodriguez, G. Garcia, N. Garcia-Araez, D. Strmcnik, N. M. Marković and M. T. M. Koper, *Journal of the American Chemical Society*, 2010, **132**, 16127-16133.
43. G. García, C. Stoffelsma, P. Rodriguez and M. T. M. Koper, *Surface Science*, 2015, **631**, 267-271.
44. J. Suntivich, E. E. Perry, H. A. Gasteiger and Y. Shao-Horn, *Electrocatalysis*, 2013, **4**, 49-55.
45. W. Jin, H. Du, S. Zheng, H. Xu and Y. Zhang, *The Journal of Physical Chemistry B*, 2010, **114**, 6542-6548.
46. M. Xiao, Y. Tian, Y. Yan, K. Feng and Y. Miao, *Electrochimica Acta*, 2015, **164**, 196-202.
47. A. C. Thenuwara, E. B. Cerkez, S. L. Shumlas, N. H. Attanayake, I. G. McKendry, L. Frazer, E. Borguet, Q. Kang, R. C. Remsing, M. L. Klein, M. J. Zdilla and D. R. Strongin, *Angewandte Chemie International Edition*, 2016, **55**, 10381-10385.
48. K. Fan, H. Chen, Y. Ji, H. Huang, P. M. Claesson, Q. Daniel, B. Philippe, H. Rensmo, F. Li, Y. Luo and L. Sun, *Nature communications*, 2016, **7**, 11981.
49. J. Zhang, J. Liu, L. Xi, Y. Yu, N. Chen, S. Sun, W. Wang, K. M. Lange and B. Zhang, *Journal of the American Chemical Society*, 2018, **140**, 3876-3879.

Chapter 6. Surface galvanic formation of Co-OH on layered Birnessite oxide and its catalytic activity for the oxygen evolution reaction

Preface to Chapter 6

Format: published manuscript.

Article information: Yayun Pu, Veronica Celorrio, Jöerg M. Stockmann, Oded Sobol, Zongzhao Sun, Wu Wang, Matthew J. Lawrence, Jörg Radnik, Andrea E. Russell, Vasile-Dan Hodoroaba, Limin Huang* and Paramaconi Rodriguez*, Surface galvanic formation of Co-OH on Birnessite and its catalytic activity for the oxygen evolution reaction, *J. Catal.*, 2021, 396, 304-314. https://doi.org/10.1016/j.jcat.2021.02.025.

Overview: Since the oxygen evolution reaction is regarded as the rate determine step to the overall water splitting, high performance electrocatalysts synthesized by green, clean and large scalable protocol is necessary. In this chapter, ultrathin and high surface area Co-OH nanosheets with 3-4 nm thickness supported on layered manganese oxide via surface redox reaction of hydrated Co^{2+} and crystalline Mn^{4+} is reported. The effect of anions on the chemical state of Co species was characterized and analyzed, which correlated to the electrochemical OER activity. With the tailored electronic structure, the binding energy of OH on active sites was strengthened which further enhanced the catalysis performance.

Author contribution: Y.P. performed the experiments and analyses the data. EXAFS characterization and analyses were performed by VC, ML and AER. XES data were collected and analyzed by VC and AER. STEM characterization was performed by WW and ZS. JMS and JR performed the XPS experiments in BAM and OS performed the ToF-SIMS experiments at BAM. All authors contributed to the analysis of the results, discussion, writing and revision of the manuscript.

6.1 Introduction

Electrochemical oxygen evolution reaction (OER) is one of the most extensively studied reactions in the last 10 years given its importance in the development of water splitting and hydrogen storage technologies.[1-5] Since the OER is a complex four-electron transfer reaction with slow kinetics, the development of highly active electrocatalysts is paramount to improve the efficiency of water electrolyzers. The Ru and Ir oxides are, so far, the most active materials for the OER, however the low abundance and consequently the high cost make the implementation of these materials in broadly use technologies, impervious.[6, 7] Due to the abundance and cost limitation, the use of other transition metal oxide (TMO) catalysts, such as Mn, Co and Ni based oxide catalysts, have been the subject of extensive studies.[8] To our knowledge, the first to report the kinetics of electrode oxygen evolution was Bockris,[9] and then other TMOs such as spinels, perovskites and hydroxides have been widely studied.[10-14] Over the recent years, these investigations have revealed the formation of surface oxo-hydroxide as the active species for the OER with turnover frequencies (TOF) up to 20 times higher than the oxide counterpart.[15-18] Besides all the efforts, one of the main limitations of metal oxide-based catalysts is the low number of active sites exposed on the surface. Such limitation is directly linked to the morphology of the catalyst and the preparation methods of the catalyst such as electrodeposition,[19] co-precipitation,[20] cathodic corrosion,[21] and impregnation-annealing.[22] To fulfil the goal of exposing more active sites, tailoring surface chemistry is a feasible strategy.

Sorption of metal ions on manganese oxide from soils and rocks has long been known, especially on layered birnessite which consists of $Mn^{\delta+}$ ions ($\delta = Mn^{4+}$, Mn^{3+}, Mn^{2+}).[23, 24] Inspired by the interaction between the transition metal ions with the layered manganese oxides, highly active catalysts can be developed.[25-27] For example, our recent work reported a highly efficient OER catalyst by intercalation of Ni^{2+} into $K_{0.45}MnO_2$ (KMO) via ion exchange. Our previous work demonstrated that Mn^{3+} ions in KMO have an essential role in the ion intercalation and that the valence of hydrated

$Ni(H_2O)_n^{2+}$ ions with d^8 subshell remains unchanged during the intercalation.[27]

In this work, we have taken advantage of the stronger reduction ability of hydrated $Co(H_2O)_n^{2+}$ ions (d^7) to promote a surface redox reaction with Mn^{4+} in KMO nanoparticles to form Co oxohydroxides (**Figure 6.1**). The oxidation state and coordination of Co on KMO was analyzed by X-ray absorption spectroscopy (XAS) and X-ray photoelectron spectroscopy (XPS) in order to understand the catalytic activity towards the OER. Moreover, we report on the effect of the anion, chloride, nitrate and sulfate, during the catalyst preparation as well as their effect on the catalytic activity.

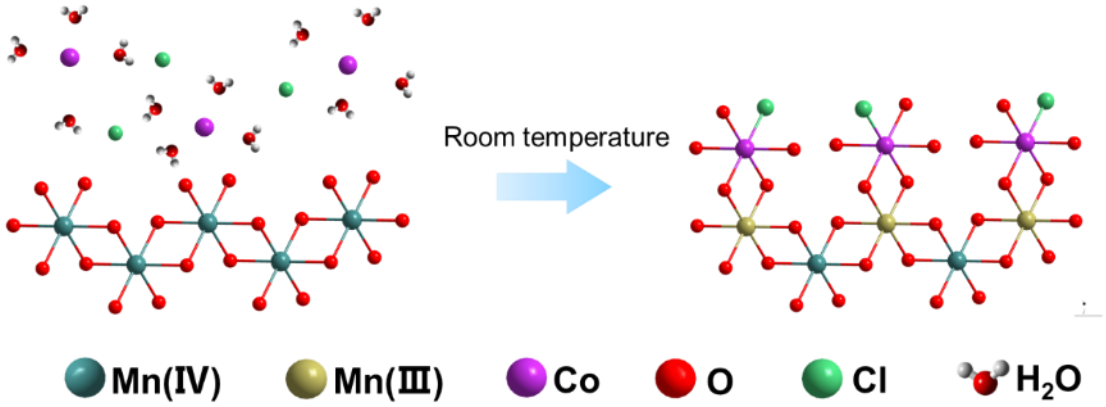


Figure 6. 1 Schematic graph of hydrated Co^{2+} reacting with crystalline Mn^{4+} at room temperature.

6.2 Methods

6.2.1 Synthesis of the materials

Preparation of K-Birnessite (KMO): The $K_{0.45}MnO_2$ was prepared by solid reaction method. K_2CO_3 (99%, Aladdin), Mn_2O_3 (98%, Aladdin) were mixed at stoichiometric ratios and then ground carefully using an agate mortar. The mixture was placed in a crucible and was heated at 800 ^oC for 1 h for decarbonation. After cooling down to ambient temperature, the powder was carefully grounded and subsequently heated at 800 ^oC for 30 h. The resulting black powder was rinsed with ultrapure water (Milli-Q, 18.4 MΩ cm^{-1}) and dried overnight at 60 ^oC.

Preparation of Co@KMO-Clx (X = 0.5, 0.25, 0.05, 0.01), Co@KMO-NO and Co@KMO-SO: 50 mg of KMO was mixed with 0.5 M, 0.25 M, 0.05 M, 0.01 M $CoCl_2$ solution (20 mL) and placed in an ultrasonic bath for 10 min. The suspension was kept at room temperature for 48 h. The powder was separated from the suspension by centrifugation at 4000 rpm and then rinsed with ultrapure water. The process was repeated at least five times to get clean particles. The obtained powder was dried at 50 ^oC overnight.

The same preparation procedure was implemented for the synthesis of Co@KMO-NO and Co@KMO-SO. For these two systems 0.5 M $Co(NO_3)_2$ and $CoSO_4$ were used as precursors instead of $CoCl_2$.

6.2.2 Materials characterization

X-ray diffraction and X-ray fluorescence characterization:

Same as described in *Chapter* 5.

X-Ray photoemission spectroscopy characterization:

The XPS measurements were performed in parallel at SUSTech and BAM. The XPS analyses at SUSTech were performed on a PHI 5000 VersaProbe III spectrometer using monochromatic Al K(alpha) X-ray source, with most used X-ray settings being 200 um,

50 W, 15 kV. The PHI 5000 VersaProbe III charge neutralization system was used on all specimens. Charge neutralization was deemed to have been fully achieved by monitoring the C 1s peak positions which remained unchanged throughout the whole experiment. High resolution analyses were carried out with analyzer pass energy at 69.0 eV and step size of 0.125 eV. The data were analyzed using the PHI MultiPak software (version 9.8). Spectra have been charge corrected to the main line of the carbon 1s spectrum (adventitious carbon) and set to BE of 284.8 eV.

The XPS measurements at BAM were performed with an AXIS Ultra DLD photoelectron spectrometer manufactured by Kratos Analytical (Manchester, UK). The XP-spectra were recorded using monochromatized Al Kα radiation (E = 1486.6 eV) for excitation, the electron emission angle was 0°, and the source-to-analyzer angle was 60°. The measurements were performed in the UHV region (between 10−8 and 10−9 mbar). The binding energy (BE) scale of the instrument was calibrated following a Kratos procedure, which is based on ISO 15472 BE data. Survey and narrow scan spectra were taken by setting the lens mode to hybrid mode. The pass energy was set to 80 eV for survey and to 20 eV for narrow scan spectra. The survey spectra were recorded with a step size of 1 eV and the narrow scan spectra with a step size of 0.1 eV. The focus position was determined according to a procedure provided by Kratos. The spectra were quantified with the CasaXPSsoftware version 2.3.16 Pre-rel 1.4.
Spectra have been charge corrected to the main line of the adventitious carbon at a BE of 284.8 eV. A "Shirley" background subtraction method was used. In addition, a fitting curve line-shape had chosen to utilize the "Gaussian-Lorentzian" function.

Time-of-Flight secondary ion mass spectrometry (ToF-SIMS) characterization:

ToF-SIMS measurements were performed at BAM. The analyses were performed on a ToF-SIMS IV (IONTOF GmbH, Münster Germany) equipped with a 25 kV BiMn primary ion source and a dual source column (DSC) for sputtering with Ar or Cs. Data were acquired in two different modes, spectrometry mode (*i.e.* high-current bunched

mode) enabling good mass resolution and collimated-burst alignment (CBA) mode, enabling good lateral resolution. In each mode both negative and positive secondary ion measurements were performed. For all analyses, 3D imaging and spectrometry, sputtering was utilized using a 1 keV Ar^+ beam for the positive ion data acquisition and 1 keV Cs^+ beam for the negative ion data acquisition. The relevant negative secondary ions had a relatively low sputter yield and therefore Cs was applied as sputter species, as Cs is generally enhancing the negative secondary ionization yield. During the acquisition of the high mass resolution spectra, the sputter gun was operating within the cycle time (interlaced within the cycle time). Sputtering during the acquisition of the image data (*i.e.* 3D reconstruction) was conducted in the non-interlaced mode where the sputtering process is excluded from the acquisition cycle. In other words, for the image data acquisition, the sample was sputtered for 30 seconds after each scan with the primary ion source. The sputter field was adjusted to 300×300 μm^2 for all measurements; the analysis-FoV was adjusted at the center of the sputtered area.

Raman scattering characterization:

Raman scattering spectra were collected using a confocal Laser Raman Spectrome (HORIBA LabRAM) with 532 nm He-Ne laser (0.2 mW). In order to optimize the signal to noise ratio, the acquisition conditions were: 20 s exposure time and 5 cycles.

Electron Microscopy characterization:

The particle morphology was characterized using a scanning electron microscopy (SEM, Zeiss with Oxford Instruments EDS attachment) with an acceleration voltage of 15 kV and probing current of 1 nA. Transmission electron microscopy (TEM) was performed on a FEI Tecnai G2 F30 with acceleration voltage of 300 kV. High-angle annular dark field scanning transmission electron microscopy (HAADF-STEM) imaging experiments were carried out on a FEI Talos F200X microscope operated at 200 kV.

X-ray absorption spectroscopy characterization:

X-ray absorption spectroscopy (XAS) measurements were performed on beamline B18 at Diamond Light Source, operating with a ring energy of 3 GeV and at a current of 300 mA.[28] The monochromator comprises Si (111) crystals operating in Quick EXAFS mode. The calibration of the monochromator was conducted using the respective metal foils prior to the measurements. Pellets of the different samples were collected in transmission and fluorescence modes at the Mn K-edge (6539 eV) and Co K-edge (7709 eV) simultaneously with the foils. The data were analysed using Athena and Artemis programs,[29] which implement the FEFF6 and IFEFFIT codes.[30] X-ray emission spectroscopy (XES) measurements were conducted at Beamline I20-scanning, of Diamond Light Source.[31, 32] The XES spectra have been normalized with respect to their total area using a range of 6456-6500 eV.

6.2.3 Electrochemical characterization:

Electrochemical cell setup:

Same as described in *Chapter* 5.

Electrode preparation:

All the powders were dispersed in 5 mL ultrapure water with a final concentration of 0.5 mg mL^{-1}. The dispersion of nanoparticles in water was placed in an ultrasonic bath (~30 min). Then, 10 μL Nafion D-521 solution (Alfa Aesar, 5% w/w in H_2O and 1-propanol) was added to the dispersed nanoparticles with another 10 min in the ultrasonic bath.

The experiments were carried out on a rotating disk electrode (RDE) configuration. A glassy carbon (GC) with the diameter of 5 mm and a geometric area of 0.196 cm^{-2} was used as a support of the nanoparticles. Prior to each experiment, the GC electrode was polished first with 4000 grit wet polish paper, followed by a fine polishing with 0.5 μm diamond slurry (Kemet) and finally rinsed abundantly with ultrapure water. The catalyst layer was prepared by drop-casting 4 times 20 μL of the prepared ink onto the GC and

dried in a convection oven at 75 ºC. The final loading of each electrode was ~ 0.2 $mg_{catalyst}\ cm^{-2}$.

Cyclic voltammetries:

CVs were recorded same as described in *Chapter* 5.

The ECSA was determined by measuring the double-layer capacitance (dl) of each sample in the non-Faradaic region between 1.1 - 1.2 V (*vs.* RHE), with scan rates (υ) of 10, 20, 30, 40, 50 60, 70 and 80 mV s^{-1}. When considering the equation:

$$C_{dl} = dQ/dE \approx \Delta j/\Delta \upsilon, \quad 6.1$$

where current density differences ($\Delta j = j_a - j_c$), the plot of Δj v*ersus* the scan rates provides the slope of the linear regression which is equivalent to the double layer capacitance ($2C_{dl}$).[33]

The *ECSA* of the catalyst was then estimated by using the relationship between the C_{dl} of our catalyst and the ideal oxide capacitance (C_{oxide} = 27 μF cm^{-2}) obtained from McCrory's work [13] using the equation:

$$ECSA = C_{dl}/C_{oxide} \quad 6.2$$

It should be noted that, a smooth two-dimensional surface of the same materials can give a accurate estimation of materials synthesized in specific condition. Deviation is inevitable since the morphology, surface roughness of materials varied from each other. Under this circumstance, the calculated ECSA in this work is only been used for comparison analysis of our materials.

6.3 Results and Discussion

6.3.1 Synthesis and characterization of Co@KMO-Cl

Co@KMO samples were prepared by mixing synthesized K-rich Birnessite ($K_{0.45}MnO_2$) with different Co salt solutions at ambient temperature (details are given in the experimental section 6.2.1). The morphology and chemical analysis of the products by electron microscopy are shown in **Figure 6.2**. Scanning electron microscopy (SEM) images show the Co@KMO-Cl nanoparticles prepared using 0.5 M $CoCl_2$ as a precursor in **Figure 6.2a, b**. Distinct differences in the morphology can be found compared to pristine KMO nanoparticles (**Figure 6.3)**. In contrast to the flat and smooth surface of KMO, the Co@KMO-Cl nanoflakes show a surface densely covered with a porous structure. The EDS spectrum in **Figure 6.2c,** confirms the incorporation of a significant amount of Co into the KMO framework. HR-TEM and HAADF-STEM confirmed the formation of poorly-crystalline Co-OH nanoflakes at the interface of the layered-structure KMO (**Figure 6.2d, e**). In order to address the concerns of the possibility of electron beam induced lattice fringe, we have performed TEM measurements on Co@KMO-Cl nanoparticles as a function of time, in which the region of sample rich on Co-OH were exposed to the electron beam (dose rate: ~500 e/Å^2/s). The images were recorded in different intervals of time for 50 s. If the lattice fringes were induced by the electron beam, it would be expected to observe changes on the lattice as a function of time. **Figure 6.4** shows the representative images after 1 s, 10 s, 20 s, 30 s, 40 s and 50 s. The lattice fringes of the Co-OH are indicated with yellow circles in the figure. As can be seen, the partial *"crystalline"* structure of the Co-OH nanoflakes remains unchanged during the 50 s of exposure to the electron beam of the TEM, thus we believe that the crystallization is not beam induced. The elemental distribution of Co, O, Mn, shown in **Figure 6.2g**, unambiguously demonstrates the layered KMO support being coated by a Co-OH shell. Noteworthy is the heterogeneous distribution of Cl on the Co@KMO-Cl nanoparticles. Further discussion of the presence of chloride is presented later in the manuscript.

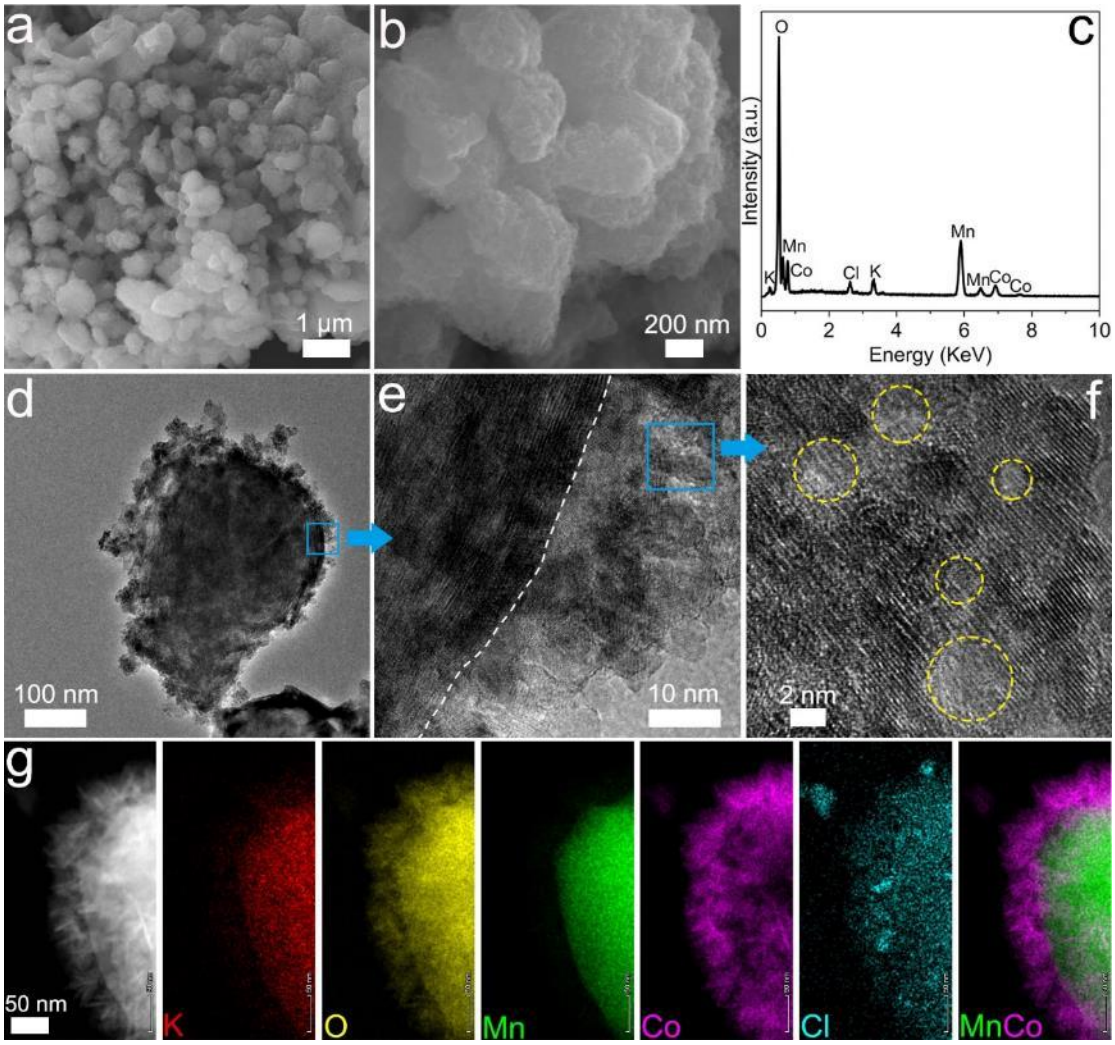


Figure 6. 2 (a-b) SEM images, (c) EDS, (d-e) TEM images of Co@KMO-Cl nanoplates. (f) enlarged area of COOH on the surface of Co@KMO-Cl, (g) HAADF-STEM image of a Co@KMO-Cl nanoplate with corresponding EDS elemental mapping.

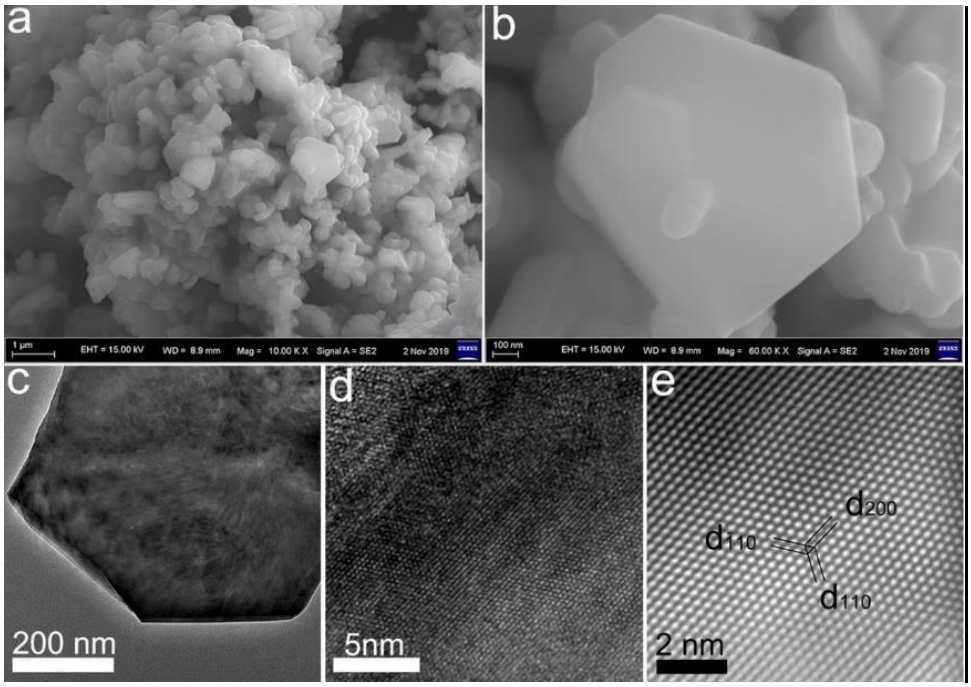


Figure 6. 3 (a-b) SEM images of as synthesized KMO nanoparticles prepared by solid-state calcination, (c) TEM image, (d) high resolution TEM, (e) reversed FFT image of single KMO nanoparticle.

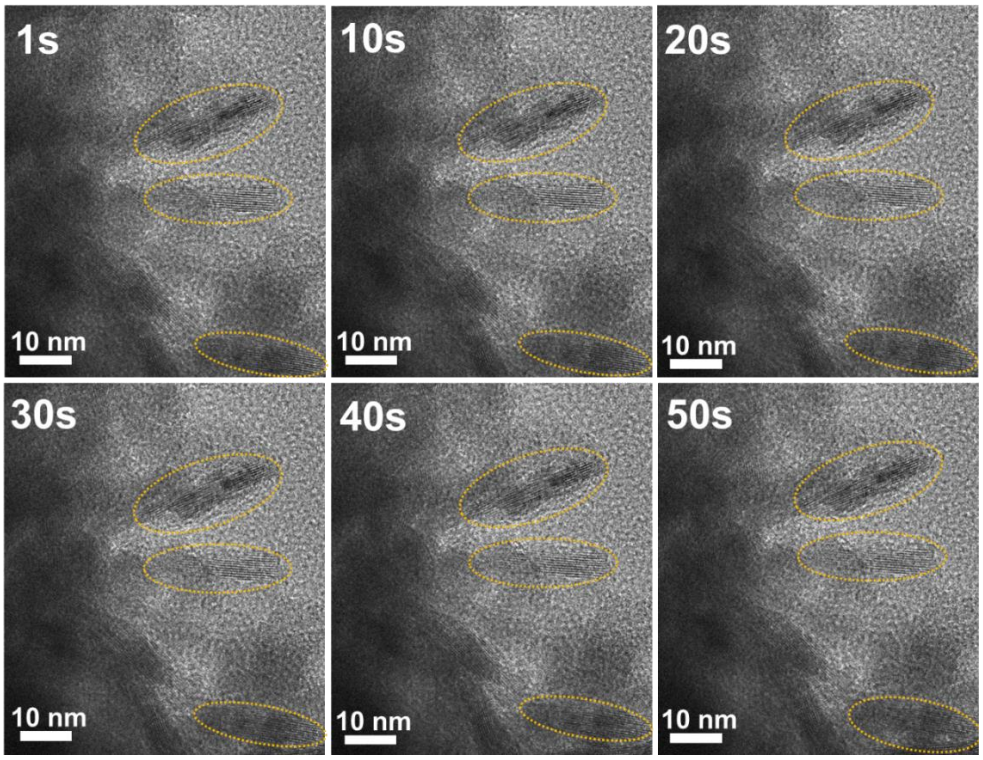


Figure 6. 4 HRTEM images of Co@KMO-Cl exposed on TEM beam for consecutive 50 s, dose rate: ~500 e/Å^2/s.

In order to gain a better insight into the details of the structure and chemical composition of the Co@KMO-Cl nanoplates, XRD, Raman spectroscopy, ToF-SIMS and XAS were performed. XRD patterns in **Figure 6.5a** show that the layered structure of Co@KMO-Cl retained the peaks at 12.4° and 24.8° associated with the (001) and (002) planes of KMO (monoclinic structure with *C*2/*m* space group). However, their intensities were significantly weakened when compared to the pristine KMO, suggesting a reduced degree of crystallinity. **Figure 6.5b** shows the comparison between the Raman spectra of pristine KMO and Co@KMO-Cl (**Figure 6.6**). The fingerprint signals at 634 cm^{-1} and 578 cm^{-1} (A_g modes) are associated with the typical layered structure of Mn oxides. The signal at 634 cm^{-1} corresponds to out-of-plane Mn-O stretching vibrations perpendicular to the layers and the signal at 578 cm^{-1} corresponds to in-plane Mn-O vibration along the layers.[34-36] With surface modification of Co-OH species, the Raman spectra of the Co@KMO-Cl show a red shift of 14 cm^{-1} at 564 cm^{-1} and a blue shift of 22 cm^{-1} at 656 cm^{-1}, as well as a reduced intensity and broadened band width. In addition, the bands observed for KMO at wavenumbers lower than 450 cm^{-1} disappeared after the surface modification with Co. Pure CoOOH phase commonly present two peaks at 503 and 635 cm^{-1}[37, 38], which perfectly overlapped with the KMO signals. The Raman spectra of Co@KMO-Cl are a combination of signals associated to CoOOH phase (503 cm^{-1} and 635 cm^{-1}) and the signals of distorted KMO (564 cm^{-1} and 656 cm^{-1}). These results are in agreement with the observations of the XRD patterns indicating the layered features of KMO were significantly weakened due to Co-OH species formation.

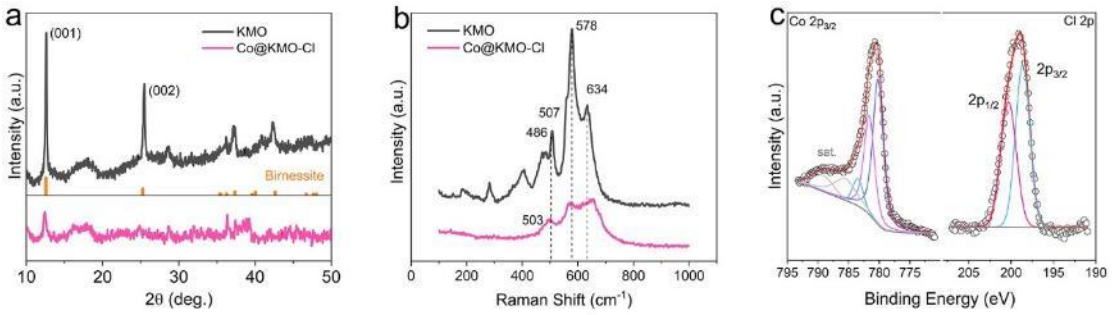


Figure 6. 5 (a) XRD patterns, (b) Raman spectra of pristine KMO and Co@KMO-Cl, (c) XPS of Co@KMO-Cl with fit, left Co 2p3/2, right Cl 2p. Shirley baseline was adopted for the fit in (c).

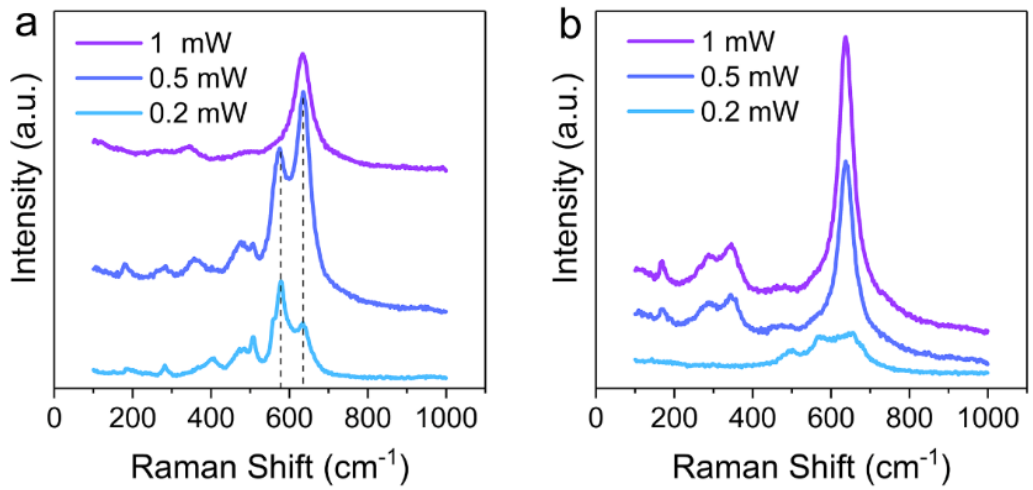


Figure 6. 6 Raman spectra of (a) KMO and (b) Co@KMO-Cl at different laser power intensities.

Since the multiple valence and strong redox ability, KMO is very sensitive to intensified energy input. As triclinic KMO might be transformed to other phases like hausmannite or β-MnO_2, we exposed our samples to varying laser power to determine the authentic Raman features and get the optimal parameters. **Figure 6.6** shows that the discrete brands at 578 cm^{-1} and 634 cm^{-1} (at 0.2 mW) of both pristine KMO and Co@KMO-Cl, gradually changed their intensity and finally merge into a broad, intensified brand at ~634 cm^{-1} (1 mW). Laser induced phase transition was ruled out by recording the data under 0.2 mW laser power).

XPS and XAS were performed to probe the electronic environments of Co@KMO-Cl. The Co $2p_{3/2}$ and Cl 2p XPS spectra and fits to the data are shown in **Figure 6.5c**. The coexistence of divalent and trivalent Co is indicated by deconvolution as well as the satellite features (at 785-793 eV). Detailed analysis is presented below. Moreover, the Cl 2p detailed spectrum shows the binding energy of $2p_{3/2}$ at 198.8 eV and $2p_{1/2}$ at 200.4 eV, with ΔE = 1.6 eV, which can be assigned to a typical lattice Cl bonding with metal atom instead of adsorbed or interlayer Cl species at 198.0 eV.[39, 40] This observation was also supported by ToF-SIMS 3D reconstructed elemental distribution within the Co@KMO-Cl system (**Figure 6.17**). As can be observed, during sputtering of the

nanostructure the signals of the Co and Cl species appear to be homogeneously distributed in the same x-y plane. The combination of the STEM-EDS, XPS, and ToF-SIMS suggest the presence of a strong chemical bond O…Co…Cl on the Co@KMO-Cl.

The changes on the electronic structure and oxidation state were evaluated by XAS. **Figure 6.7a** shows the XANES spectra at the Co K-edge for Co@KMO-Cl and different cobalt oxides, which were used as standard reference compounds. A linear correlation between the K-edge edge position (defined as the maximum of the first derivative) and the metal oxidation state was previously established.[41] The average Co valence of Co@KMO-Cl was estimated to be 2.75+ (**Figure 6.8**). **Figure 6.7b** shows the spectra collected at the Mn K-edge, and the comparison with the pristine KMO. In this case, the analysis is significantly more complex due to the wide pre-edge features (inset of **Figure 6.7b**) and the influence of Mn coordination on the main edge.[42-44] For this reason, we performed X-ray emission spectroscopy (XES) characterization to determine quantitatively the ratios of $Mn^{2+}/Mn^{3+}/Mn^{4+}$ in KMO before and after the Co incorporation (**Figure 6.9** and **Table 6.1**). The results indicate that 78% of the Mn^{4+} ions in KMO were converted to Mn^{3+}, leading to a clear decrease of the mean oxidation state of Mn from 3.9+ on KMO to 3.1+ on Co@KMO-Cl. This change of the reduced Mn^{4+} is consistent with the percentage of oxidized Co^{2+} and demonstrates the proposed reaction pathway:

$$\delta Co^{2+}{}_{(liq.)} + Mn^{4+}{}_{(cryst.)} \rightarrow \delta Co^{3+}{}_{(cryst.)} + Mn^{(4-\delta)+}{}_{(cryst.)} \qquad (0 < \delta < 1) \qquad [6.3]$$

The Co K-edge EXAFS-FT of Co@KMO-Cl and reference samples are shown in **Figure 6.7c**. The first peak at around 1.50 Å (not phased shift corrected) can be assigned to the first coordination shell Co–O, whereas the second peak at 2.50 Å is due to Co–Co and Co–Mn scattering (**Figure 6.10** and **Table 6.2**). **Figure 6.6d** shows the FT of the synthetized Co@KMO-Cl and KMO samples collected at the Mn edge, as well as

the reference compounds. The first peak at ~1.5 Å (not phase shift corrected) is due to the Mn-O scattering and the second peak at ~ 2.5 Å (not phase shift corrected) is due to Mn-Mn and Mn-Co scattering (**Figure 6.11-12** and **Table 6.3 and 6.4**). Nearly identical distances between Mn and its closest neighbor atoms for Co@KMO-Cl and KMO demonstrate the local coordination environment of Mn is largely maintained in the bulk. The Co-Mn redox reaction did not modify the KMO structure, consistent with the HRTEM image in Figure 6.2e but induced point defects in the lattice that lead to the loss of crystallinity, as confirmed by the XRD results.

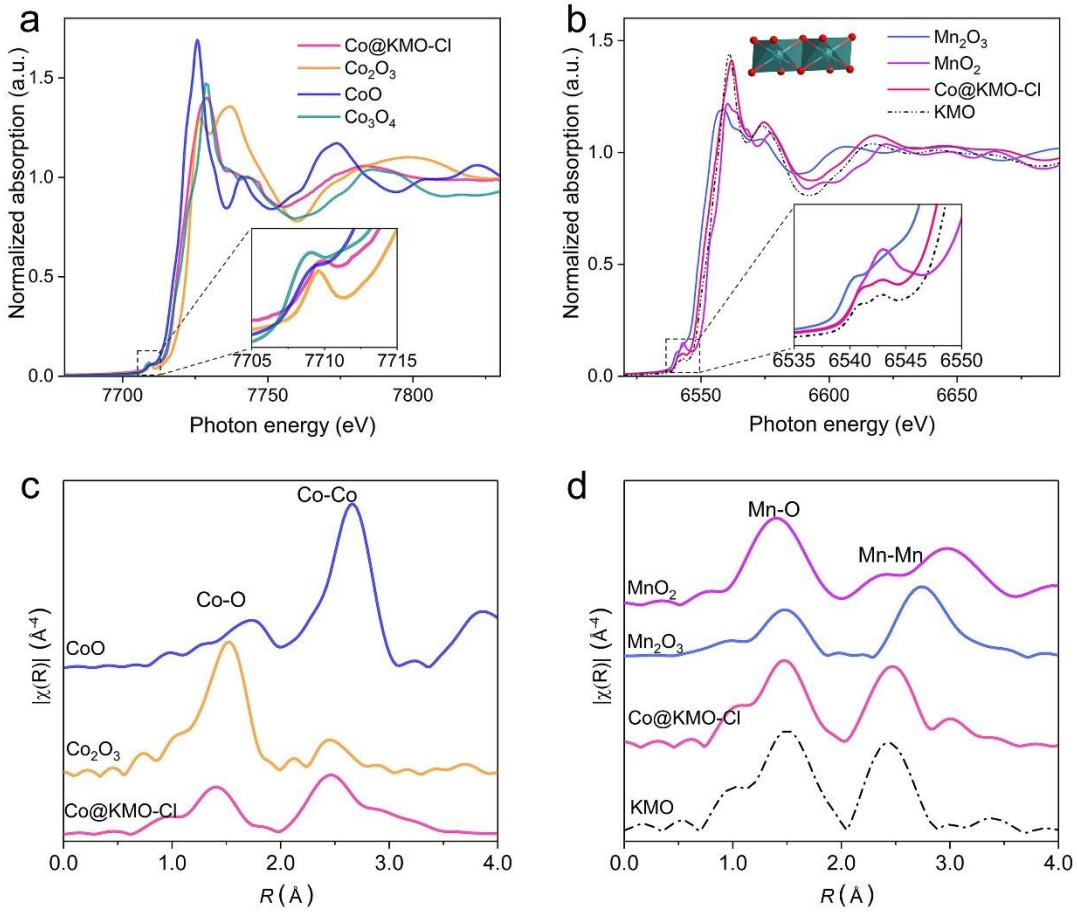


Figure 6. 7 Normalized XANES spectra at the (a) Co K-edge, (b) Mn K-edge of the synthetized electrocatalysts. Spectra for reference compounds have been included as a comparison. Insets show the pre-edge region. Structure in **Figure 6.6b** represents the structure of edge shared M-O octahedra from KMO where the red atoms are O, the dark blue atoms are Mn. EXAFS FTs of $k^3\chi(k)$ functions for the materials from **Figure 6.6a** at the (c) Co K-edge, and (d) Mn K-edge.

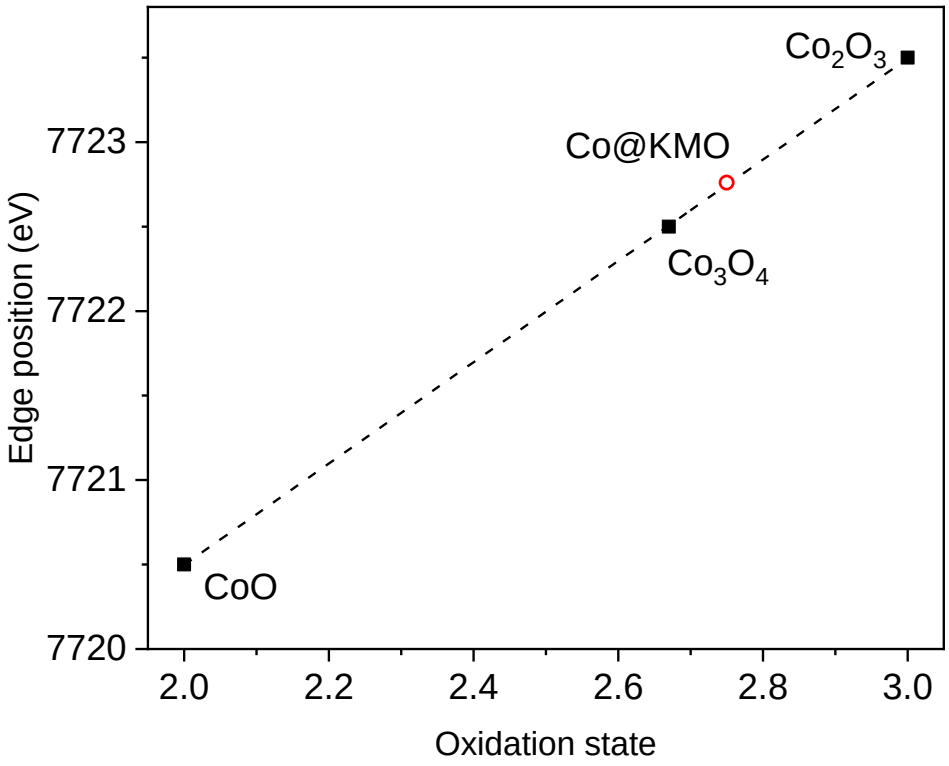


Figure 6. 8 Mean Co oxidation state as a function of the Co K-edge position for the prepared Co@KMO catalysts.

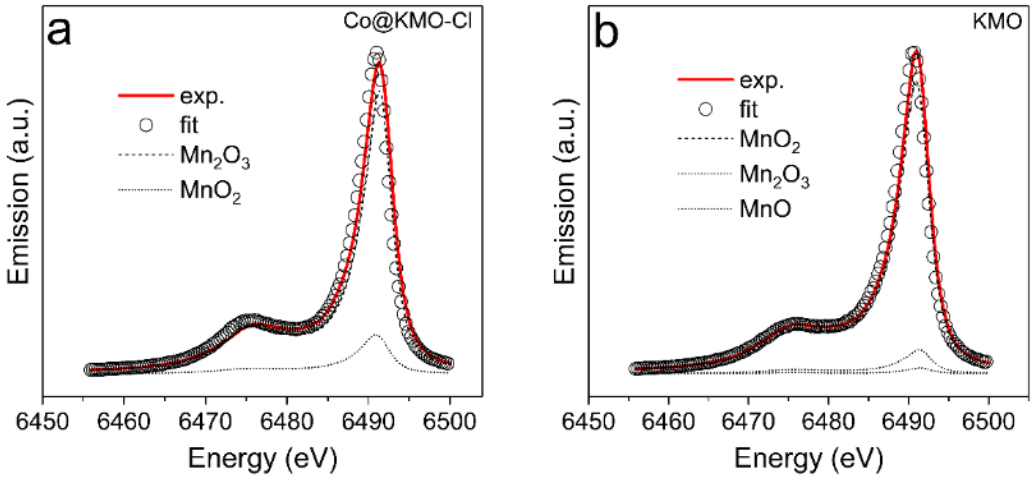


Figure 6. 9 Measured experimental XES spectra of (a) Co@KMO-Cl, (b) KMO with corresponding fitting contributions from MnO, Mn_2O_3 and MnO_2 standard oxide compounds.

Table 6. 1 Ratio of Mn^{n+} fractions and corresponding mean Mn oxidation state of prepared CoKMO-Cl determined by XES.				
	Mn^{4+} (%)	Mn^{3+} (%)	Mn^{2+} (%)	Mean oxidation state
KMO	90.5 ± 1.1	7.2 ± 2.7	1.6 ± 1.7	3.9 ± 0.2
Co@KMO-Cl	12.5 ± 2.5	87.5 ± 2.6	-	3.1 ± 0.3

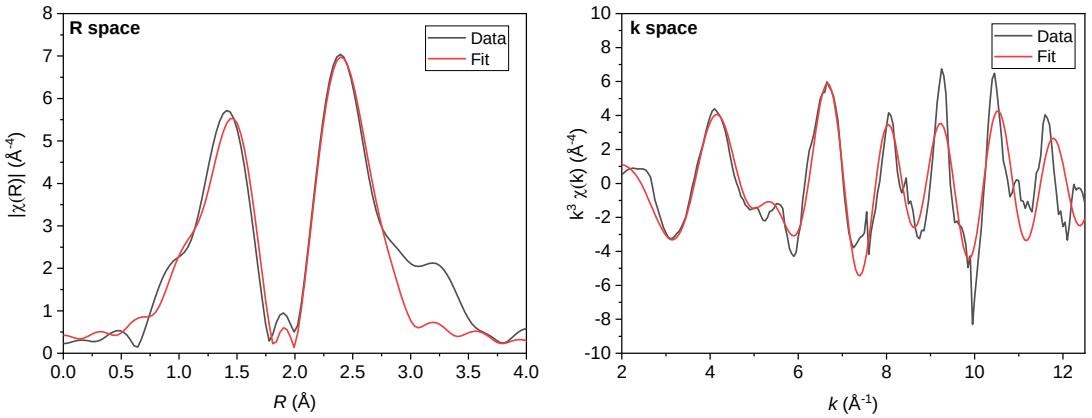


Figure 6. 10 k^3 weighted Fourier transform EXAFS data fits and k^3 weighted χ data of Co@KMnO-Cl at the Co K-edge.

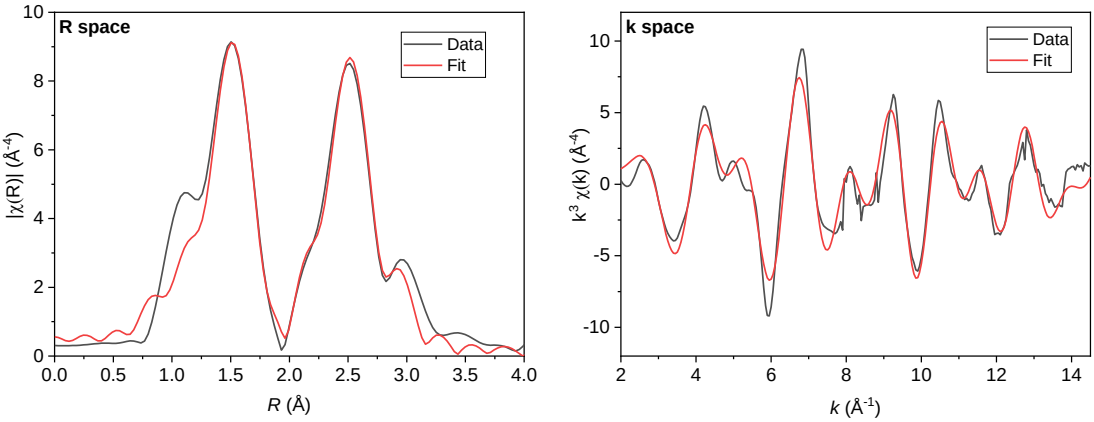


Figure 6. 11 k^3 weighted Fourier transform EXAFS data fits and k^3 weighted χ data of Co@KMnO-Cl at Mn K-edge.

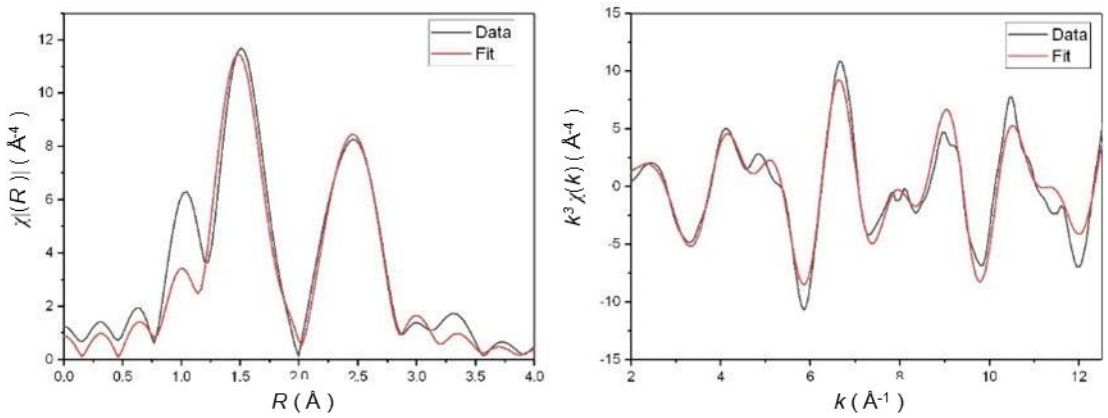


Figure 6. 12 k^3 weighted Fourier transform EXAFS data fits and k^3 weighted χ data of KMO at Mn K-edge.

Table 6. 2 EXAFS distances and fitting parameters for the Co@KMO-Cl catalyst. Fitting parameters: $S_0^2 = 0.8$ calculated using a Co foil standard; fit range $2.7 < k < 11.3$, $1.0 < R < 3.0$. $\Delta E_0 = -3.1 \pm 1.7$ eV; $R_{factor} = 0.016$

Scattering	CN	R / Å	σ^2 x 10^3 / Å^2
Co–O	4.7 ± 0.9	1.91 ± 0.02	9.7 ± 3.4
Co–Co/Mn	2.3 ± 0.7	2.82 ± 0.02	3.2 ± 2.5

Table 6. 3 EXAFS distances and fitting parameters for the Co@KMnO-Cl catalyst. Fitting parameters: $S_0^2 = 0.8$ calculated using a Mn foil standard; fit range $3.0 < k < 13.8$, $1.2 < R < 3.5$. $\Delta E_0 = 0.2 \pm 1.0$ eV; $R_{factor} = 0.011$

Scattering	CN	R / Å	σ^2 x 10^3 / Å^2
Mn–O	3.3 ± 0.3	1.90 ± 0.01	2.7 ± 1.0
Mn–Mn/Co	6.8 ± 1.3	2.91 ± 0.01	9.8 ± 2.3
Mn–Mn/Co	1.7 ± 1.1	3.15 ± 0.03	4.2 ± 3.6

Table 6. 4 EXAFS distances and fitting parameters for the KMO catalyst. Fitting parameters: $S_0^2 = 0.8$ calculated using a Mn foil standard; fit range $3.0 < k < 12.2$, $1.2 < R < 3.2$. $\Delta E_0 = -2.3 \pm 1.7$ eV; $R_{factor} = 0.010$

Scattering	CN	R / Å	σ^2 x 10^3 / $Å^2$
Mn–O	3.8 ± 0.5	1.90 ± 0.01	1.3 ± 1.1
Mn–Mn	6.4 ± 2.3	2.91 ± 0.03	7.5 ± 3.1
Mn–Mn	2.4 ± 1.6	3.13 ± 0.08	7.5 ± 3.1

6.3.2 Effect of the anions on morphology and electronic structure of Co@KMOs

We extended the investigation to the preparation of Co@KMO to explore the effects of the anions, examining both $(NO_3)^-$ and $(SO_4)^{2-}$, denoted as Co@KMO-NO and Co@KMO-SO. The SEM and TEM images of Co@KMO-NO and Co@KMO-SO show similar morphologies to Co@KMO-Cl with the main feature as the formation of densely packed ultrathin Co-OH nanoflakes on the surface of the KMO nanoparticles (**Figure 6.13**). The EDS in **Figure 6.13g-h**, XRF spectra in **Figure 6.14** and XPS in **Figure 6.15** confirmed the incorporation of Co into the KMO particles. Interestingly, the signals associated to S or N elements on the Co@KMO-NO and Co@KMO-SO were absent in both the XRF and EDS**,** in contrast to the observation of a considerable contribution of Cl in the spectra of Co@KMO-Cl. Since the sensitivity of non-metal ions on XPS is better than the XRF/EDS techniques, fairly weak N and S signals were detected in **Figure 6.16f**, which contrast to the sharp peak of Cl. The XRF, EDS and XPS deliver consistent results, although slight difference due to the measuring resolution.

The presence or absence of the anions in the catalyst was further evaluated by ToF-SIMS 3D reconstruction (**Figure 6.17A**). As can be seen in the ToF-SIMS depth profiles (**Figure 6.17B**), the Co-O is the dominant etched species in the three catalysts. With regards to the Co-anion species, the spectra indicate coordination of the Co-Cl and Co-NO_3 in the corresponding catalysts. However, the correlation of Co to SO_4^{2-} species is very poor. On the other hand, the signal of the SO_4 is significant when detected as $MnSO_4$. These results suggest a stronger interaction of Cl^- and NO_3^- with Co, while the SO_4^{2-} is interacting more strongly with Mn rather than with Co. It should

be noted that the sensitivity of XPS/ToF SIMS is higher than the sensitivity of XRF and EDS. Therefore, XPS/ToF SIMS provide more accurate information of anions Cl, N, S than the XRF and EDS.

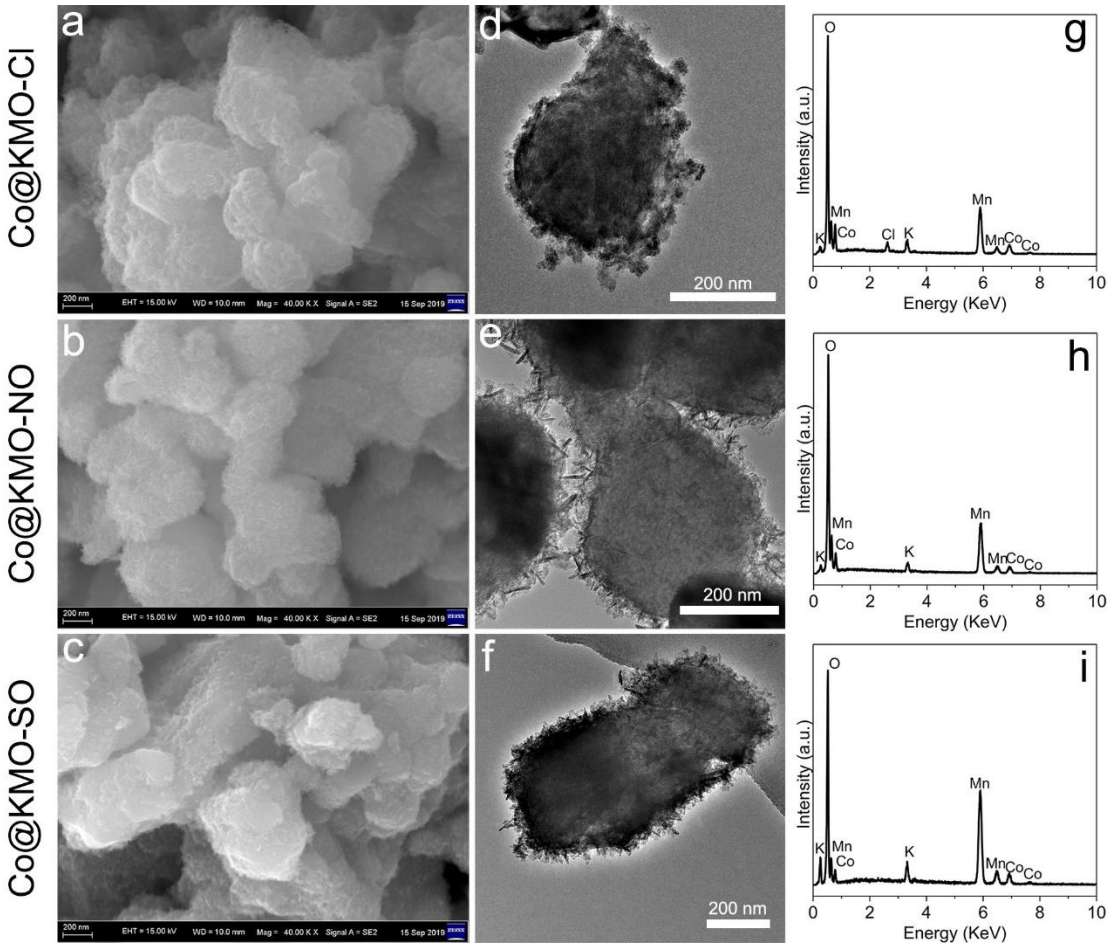
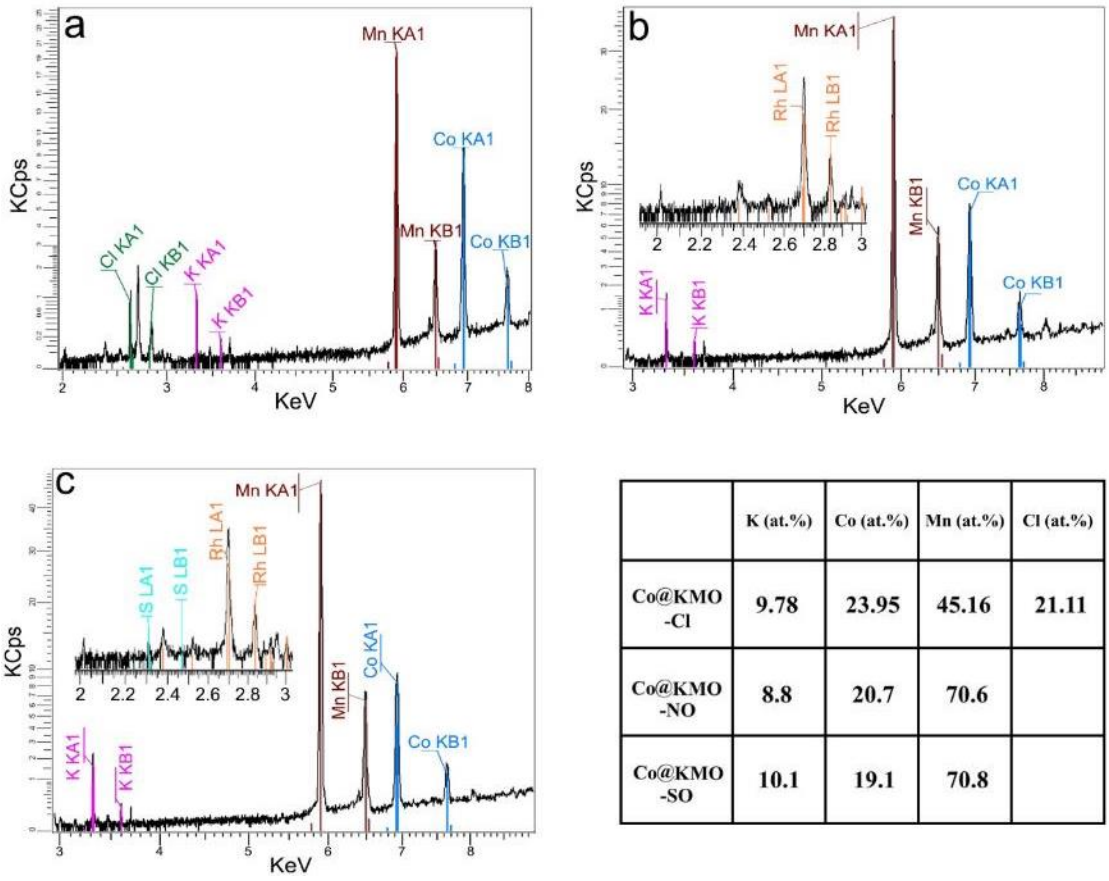


Figure 6. 13 (a-c) SEM, (d-f) TEM and (g-i) EDS spectra of Co@KMO-Cl, Co@KMO-NO and Co@KMO-SO as indicated left of the figure.



	K (at.%)	Co (at.%)	Mn (at.%)	Cl (at.%)
Co@KMO -Cl	9.78	23.95	45.16	21.11
Co@KMO -NO	8.8	20.7	70.6	
Co@KMO -SO	10.1	19.1	70.8	

Figure 6. 14 XRF spectra of (a) Co@KMO-Cl, (b) Co@ KMO-NO and (c) Co@ KMO-SO, with corresponding elemental atomic fractions summarized in table.

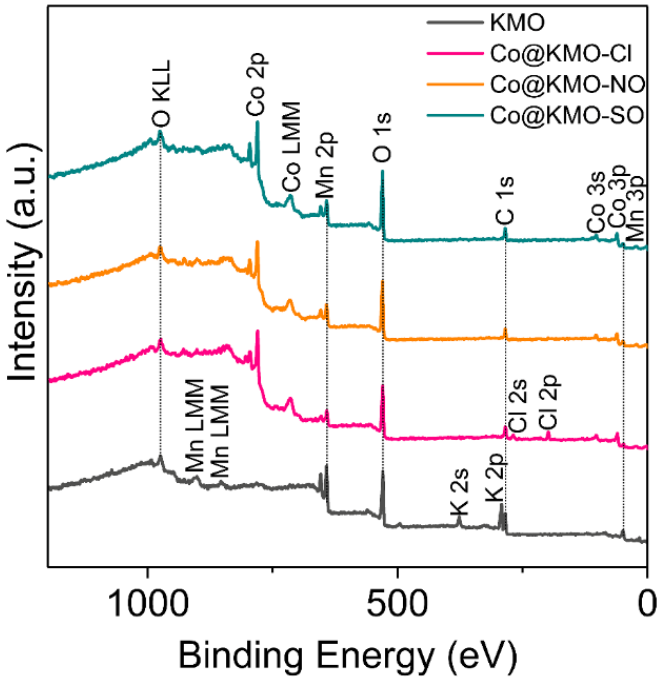


Figure 6. 15 XPS spectra of KMO before/after reaction with different Co salts.

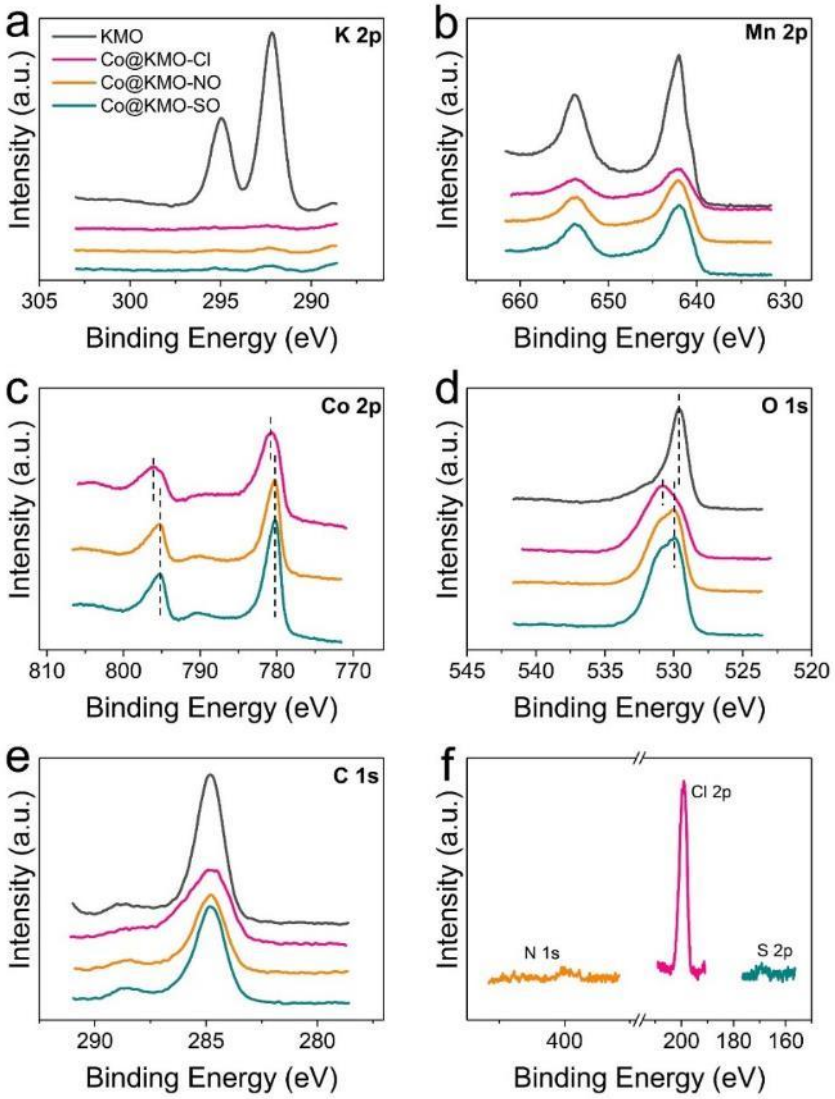


Figure 6. 16 High resolution XPS of pristine KMO and the relative Co reacted samples, (a) K 2p, (b) Mn 2p, (c) Co 2p, (d) O1s, (e) C 1s, (f) Cl 2p of Co@KMO-Cl, N1s of Co@KMO-NO, S 2p of Co@KMO-SO. KMO, Co@KMO-Cl, Co@KMO-NO, Co@KMO-SO.

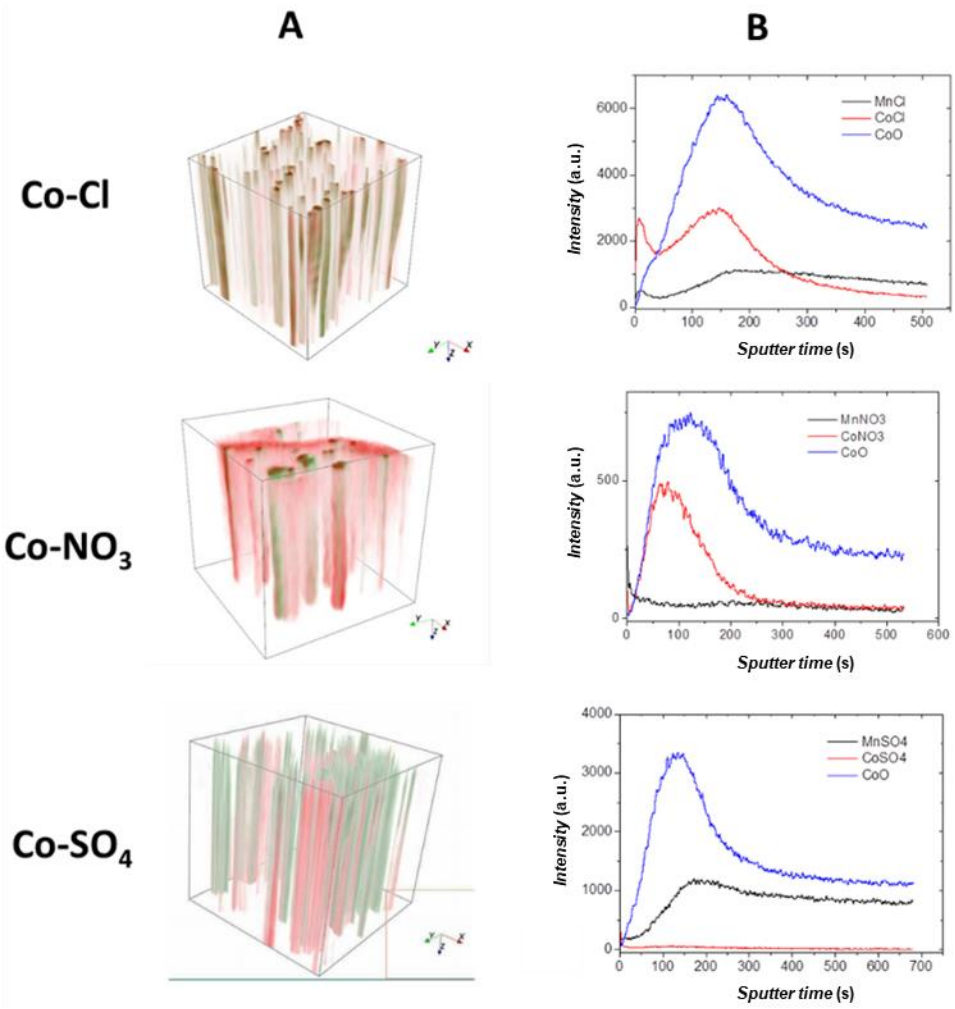


Figure 6. 17 (A) ToF-SIMS positive ions 3D data reconstruction on the Co@KMO-Cl, Co@KMO-NO and Co@KMO-SO catalysts supported on glassy carbon. ToF-SIMS data were acquired using collimated, burst, alignment mode.[45, 46] The 3D overlay images are reconstructed with the Co^+ fragments (m/z= 59) in green and the anion (Cl, NO_3 and SO_4) fragments in red respectively. Each system was acquired with a different field-of-view (FoV); 50×50 μm^2 for the Co@KMO-Cl and Co@KMO-SO systems and 20×20 μm^2 for the Co@KMO-NO system. (B) ToF-SIMS negative ions depth profiles using the spectrometry mode (high-current bunched mode) on the Co@KMO-Cl, Co@KMO-NO and Co@KMO-SO catalysts. Information about the acquisition and sputtering is given in the experimental section.

Figure 6.15-16 show the survey and fine-scan XPS spectra of Co modified samples. For the Co 2p spectra, previous reports have shown that the separation of the peaks (Δ) associated to Co $2p_{3/2}$ and $2p_{1/2}$ can provide useful information of the electronic structure of the material. It has been suggested that for high spin Co^{2+} the separation between the two peaks is 16.0 eV and for low spin Co^{3+} is 15.0 eV.[47, 48] The separation of the peaks for Co@KMO-Cl is 15.3 eV, whereas this separation for Co@KMO-NO and Co@KMO-SO is 15.0 eV. The oxidation state of Co on Co@KMO-Cl suggests that it has a lower oxidation state in comparison with the other two samples. The oxidation of Co on Co@KMO-Cl is in accordance with the XAS analysis. Detailed deconvoluted spectra of the Co 2p with fits of $2p_{3/2.}$ are presented in **Figure 6.18a**. The changed electronic structure can be attributed to the Cl incorporation, since the Mn shows identical chemical state for all Co modified samples (**Figure 6.19**). Partial Cl bonding with Co changes the electron density, leading the Co easily bonding with OH (as shown in the following O 1s spectra analysis). This result provides solid support to the formation of O…Co…Cl bonding.

The detailed XPS spectra of the O 1s convolution and fitting curves for the unmodified and Co-modified materials are presented in **Figure 6.18b**. The band assigned to the lattice-O component (oxygen-metal interaction) shifted positively from 529.4 eV on KMO to 529.9 eV for all the Co-modified samples due to the new contribution of O-Co or the mixed interaction of O-Mn/O-Co. The branch at around 531.1 eV can be assigned to an OH contribution,[49] and this component increased markedly in all Co-modified samples while the lattice-O branch simultaneously decreased. It is important to notice that the highest gain was observed on the Co@KMO-Cl compared to Co@KMO-NO and Co@KMO-NO. This strongly suggests that the presence of Cl favours the adsorption of OH, which is the active phase towards the OER. The small convoluted peak at ~532.5 eV can be assigned to adventitious carbon contaminations.[50] **Figure 6.19** displays the multiplet fitting curves of Mn $2p_{3/2}$ of KMO and Co@KMOs.

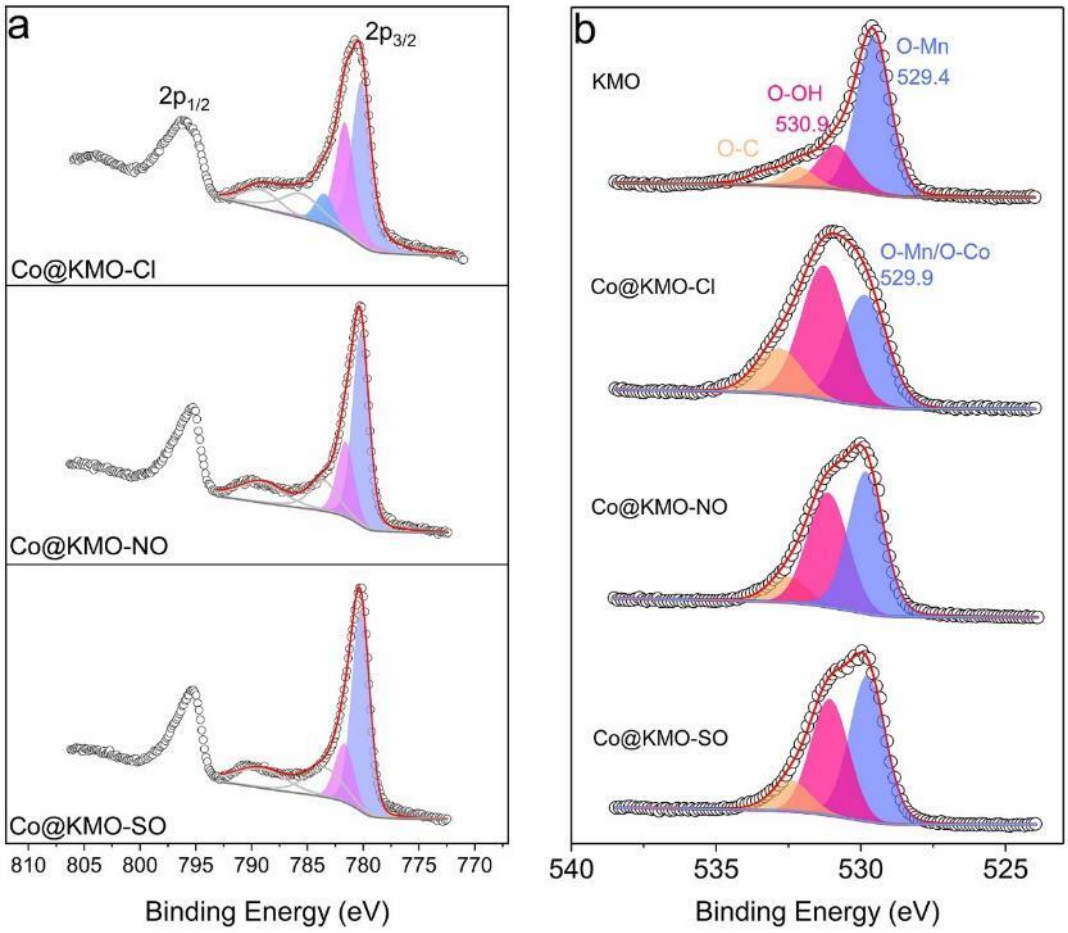


Figure 6. 18 High resolution XPS spectra of different Co-modified KMOs: (a) Co 2p, (b) O 1s.

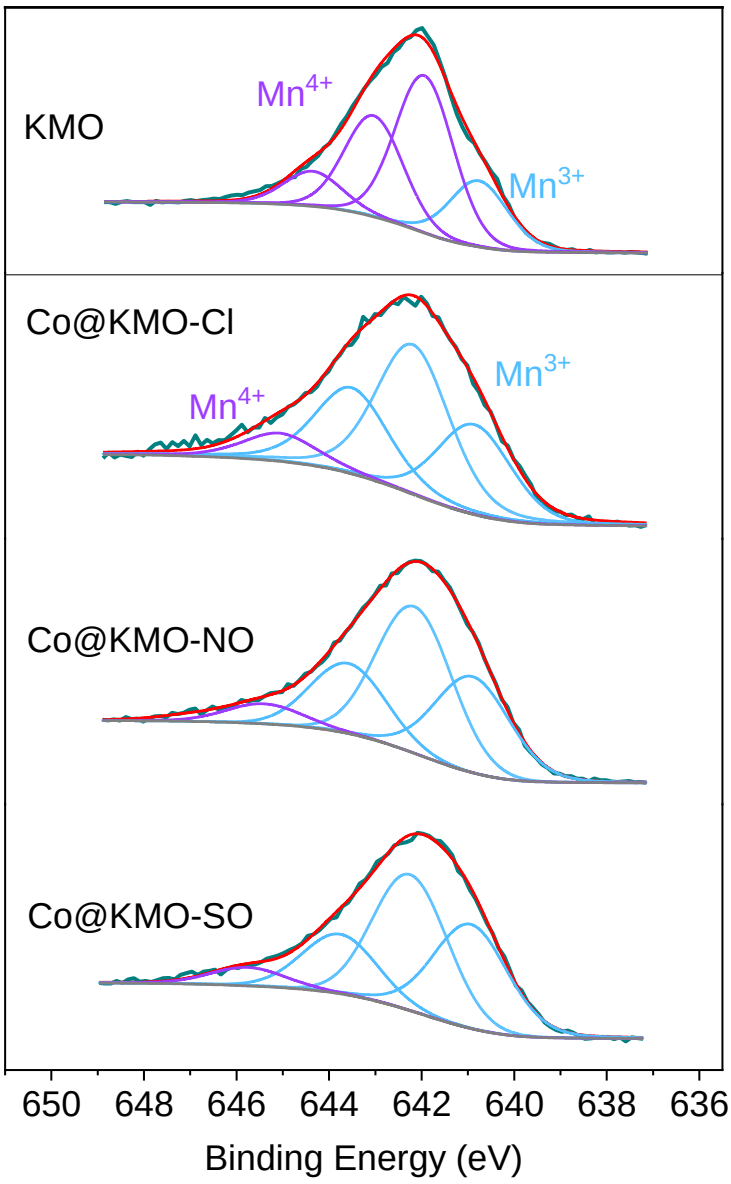


Figure 6. 19 High resolution Mn $2p_{3/2}$ spectra of KMO, Co@KMO-Cl, Co@KMO-NO, and Co@KMO-SO. correspond to the original data, correspond to the convoluted curves of Mn^{+3}, correspond to the convoluted curves of Mn^{+4} and correspond to the fit.

To systematically study the surface redox reaction taking place on KMO, Co@KMO-Cl samples were prepared in varying $CoCl_2$ concentrations. **Figure 6.20-21** shows the SEM, TEM images of KMO modified with different $CoCl_2$ concentration (0.5 M, 0.25 M, 0.05 M and 0.01 M). It is clearly observed that the density of Co-OH nanoflakes on the surface is proportional to the $CoCl_2$ concentration. Thus, the electrochemically

available surface area (ECSA) as a function of the concentration of chloride for the samples Co@KMO-$Cl_{0.5}$ and Co@KMO-$Cl_{0.01}$ were evaluated by measuring of the double layer capacitance as described in the experimental section. As shown in **Figure 6.22**, the sample synthesized using a concentration of 0.5 M shows larger ECSA of 6.3-fold higher than that of 0.01 M.

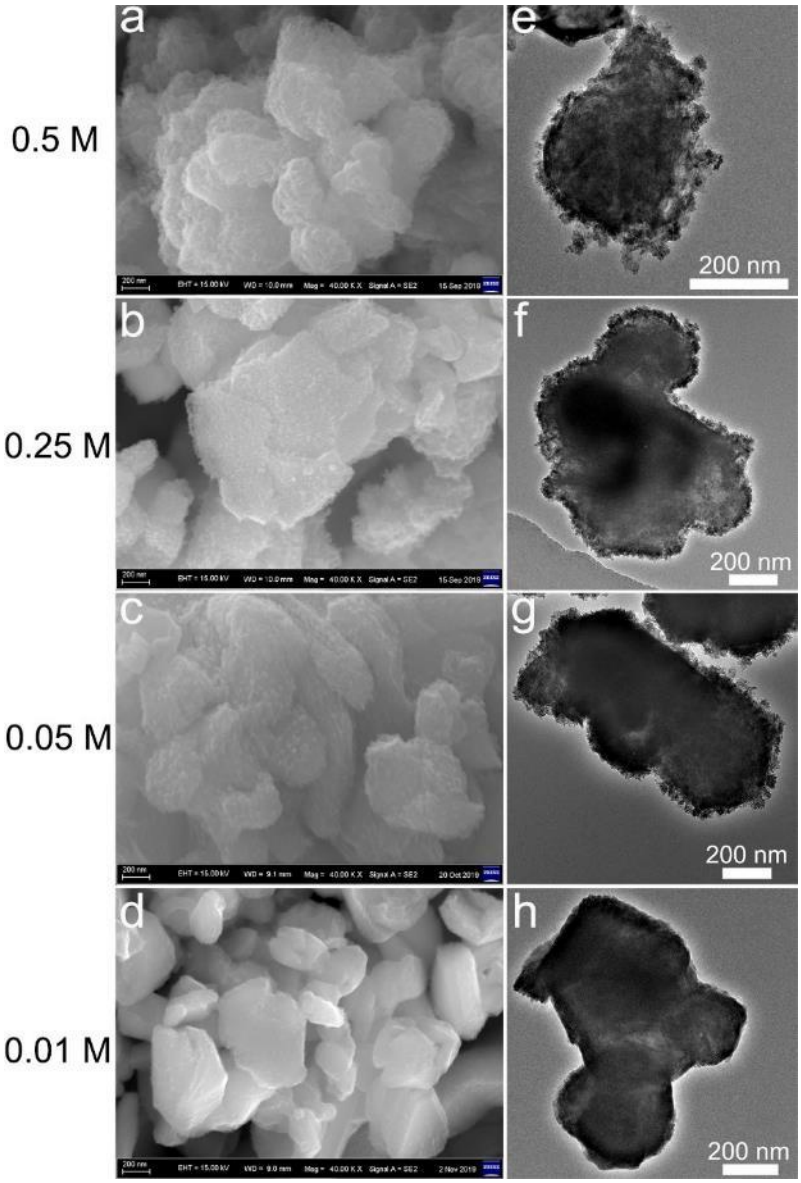


Figure 6. 20 SEM (a-d) and TEM (e-h) images of Co@KMO-Cl prepared by different concentrations of $CoCl_2$ as indicated in the figure.

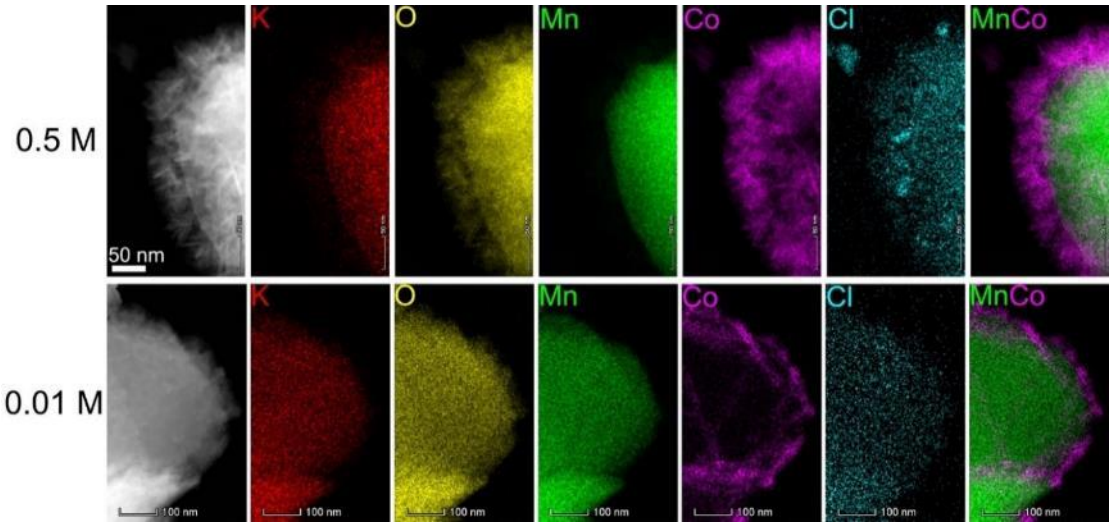


Figure 6. 21 STEM-EDS mappings of Co@KMO-$Cl_{0.5}$ and Co@KMO-$Cl_{0.01}$.

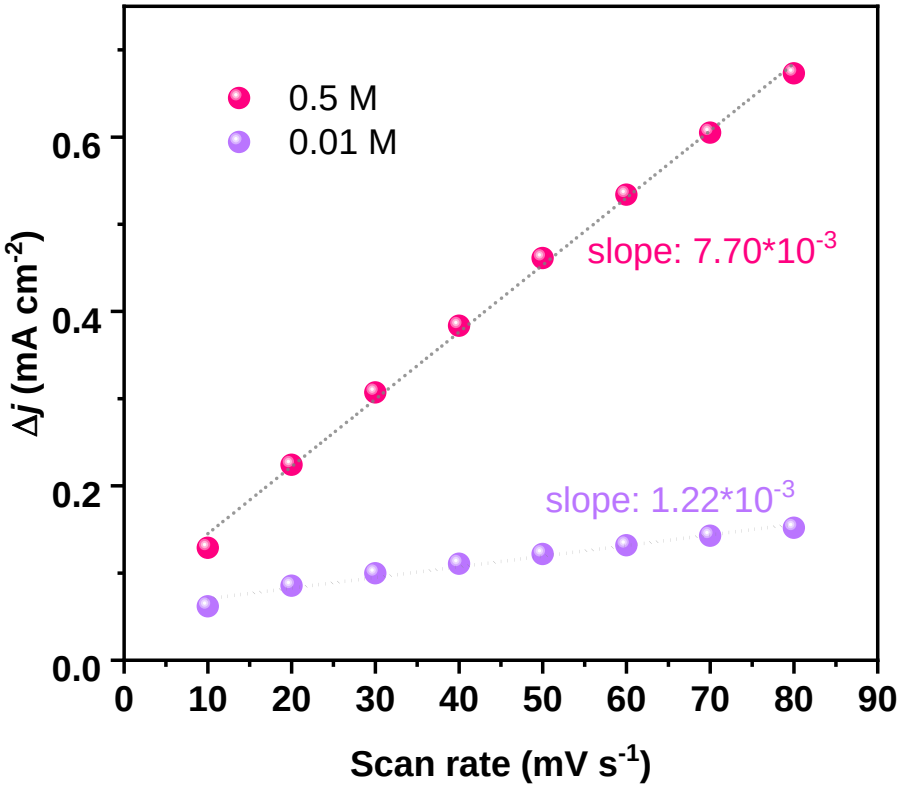


Figure 6. 22 Difference of the anodic and cathodic current densities (Δj) at 1.15 V vs RHE as a function of the scan rate.

The electronic structure of Co@KMO-$Cl_{0.5}$ and Co@KMO-$Cl_{0.01}$ were also investigated by XPS. As can be seen in **Figure 6.23-25**, a significantly weaker Cl signal

was detected in Co@KMO-$Cl_{0.01}$. Correspondingly, the binding energies of Co 2p and O 1s were negatively shifted for Co@KMO-$Cl_{0.01}$ as compared to Co@KMO-$Cl_{0.5}$. Deconvoluted curves in **Figure 6.24** confirms that the valence of Co slightly increased. At the same time the OH component in O 1s was clearly decreased. Unchanged Mn 2p spectra depicted that the Cl ligand has negligible effect on the Mn, which in turn suggested the bonding with Co. XPS elements analysis in **Figure 6.25** shows that the ratio of Co/Cl was 0.24 in Co@KMO-$Cl_{0.5}$, while this value in Co@KMO-$Cl_{0.01}$ decreased to 0.07. Incorporation of Cl led to a promoted interaction between Co and O, as the content of Cl decreased, this effect was found to be weakened. Hence, the tailoring effect of Cl on electronic structure was confirmed.

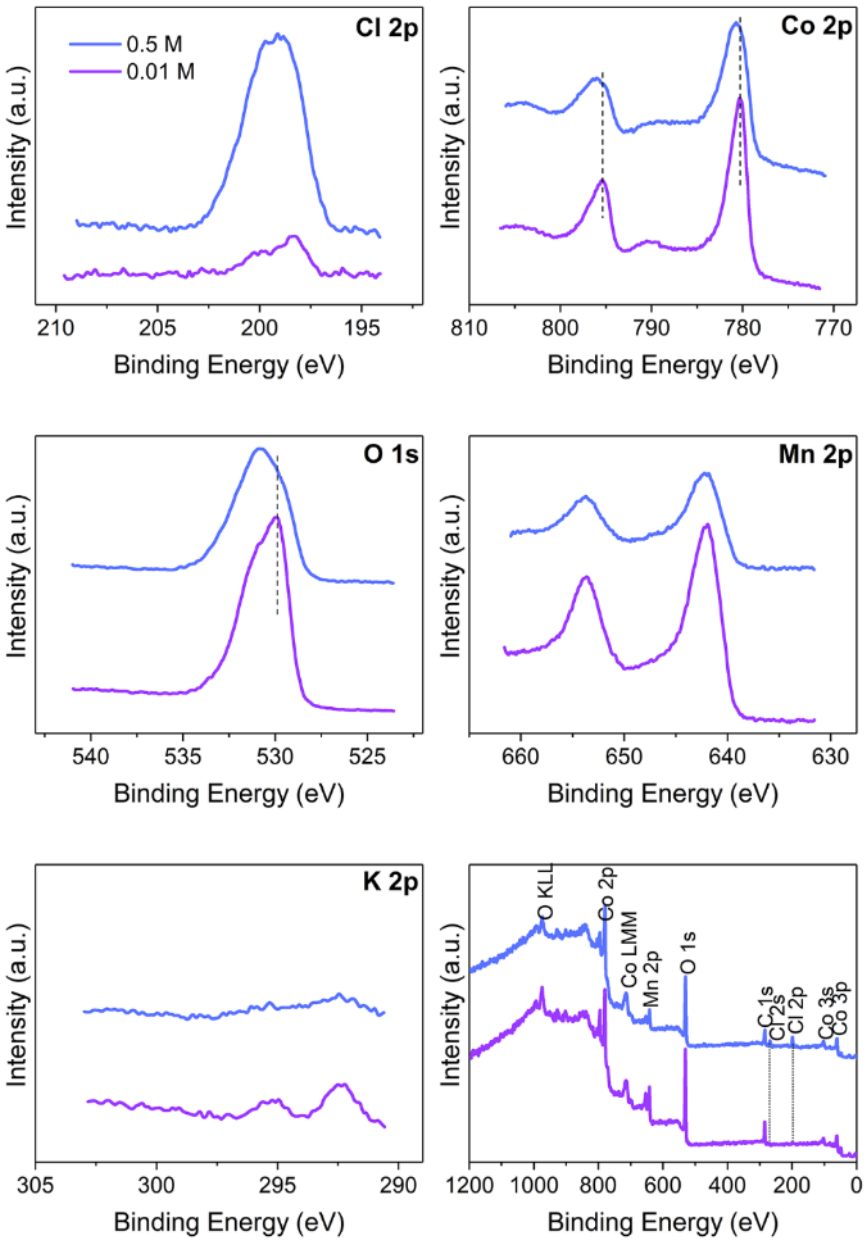


Figure 6. 23 Survey and high resolution XP-spectra of Co@KMO-$Cl_{0.5}$ and Co@KMO-$Cl_{0.01}$.

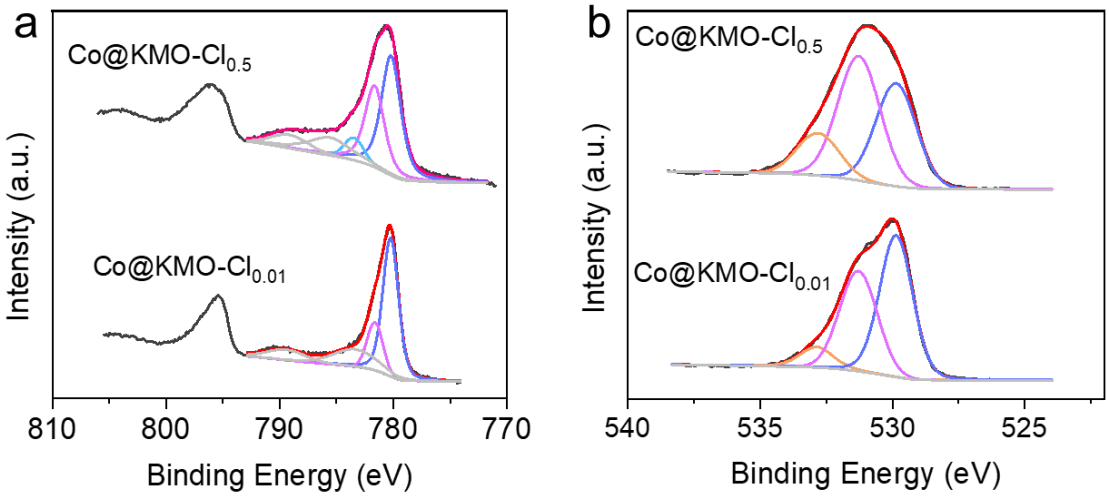


Figure 6. 24 (a) Co $2p_{3/2}$ and (b) O 1s fit results of Co@KMO-$Cl_{0.5}$ and Co@KMO-$Cl_{0.01}$.

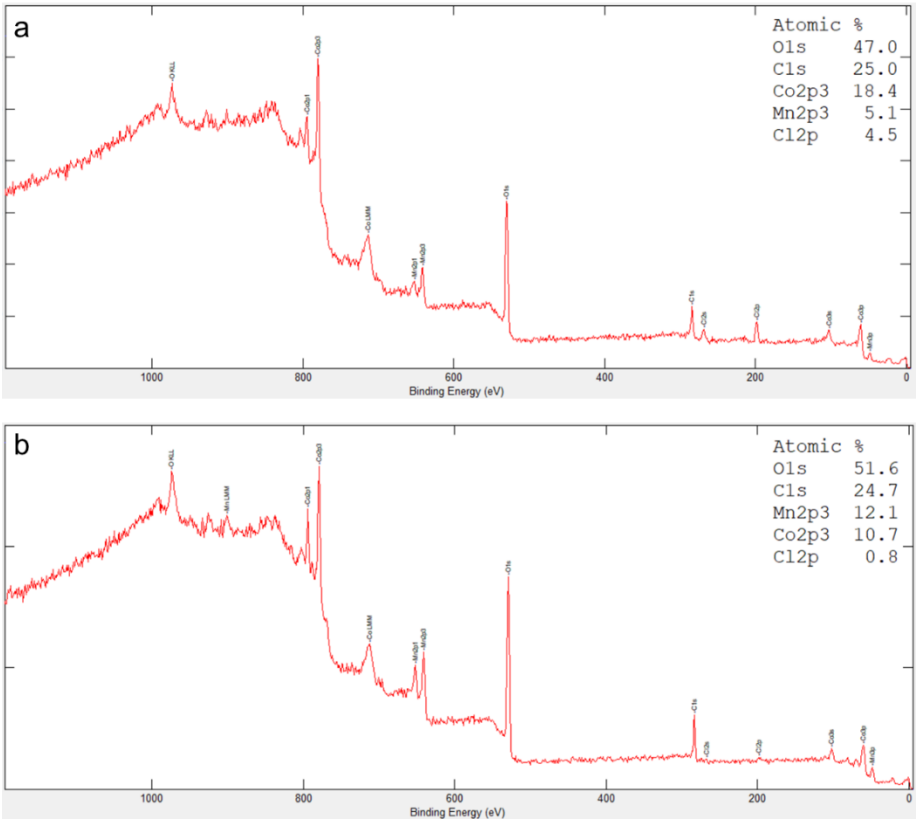


Figure 6. 25 XPS spectra and elements ratio of (a) Co@KMO-$Cl_{0.5}$ and (b) Co@KMO-$Cl_{0.01}$.

6.3.3 Assessment of the oxygen evolution reaction on Co@KMOs

The electrocatalytic performance and durability of Co@KMOs were evaluated in Ar-saturated 1 M NaOH solution using a rotating disk electrode (RDE). **Figure 6.26a-c** shows the comparison of the iR-corrected voltammetric profiles for all the Co@KMOs catalysts. The current density is reported as mA cm^{-2}, where the area is the geometric area of the electrode. All the Co@KMO catalysts are highly active towards the OER in contrast to the pristine KMO that does not show any catalytic activity as demonstrated in previous works.[27] Amongst all the catalysts prepared, Co@KMO-Cl exhibited the highest catalytic activity (η_{onset} = 170 mV, η_{10} = 245 mV). Co@KMO-NO displayed the second best performance (η_{onset} = 220 mV, η_{10} = 338 mV) and Co@KMO-SO the lowest catalytic activity (η_{onset} = 230 mV, η_{10} = 377 mV).

A close look at the potential window between 0.9 and 1.5 V vs RHE, **(Figure 6.26b)** shows a large increase in the double layer capacity of the Co@KMO voltammograms. This increase is largest for the Co@KMO-Cl sample, which might be indicative of differences in the surface area. Common practice in the literature is the utilization of the double layer capacity to determine the electrochemical surface area of metal oxide catalysts, however this electrochemical double-layer capacitance-based method involves empiric assumptions, which are certainly inaccurate.[51, 52] A more tangible method of comparison of electrocatalyst is the normalization per mass of the active center, which in the case of this work is the mass of cobalt. In order to be able to provide a result that enables us to compare the catalytic activity of our catalyst with other reports in the literature we provide the catalytic activity using both methods: *i)* normalization per ECSA and *ii)* normalization per mass of Co. The determination of the ECSA based on the double layer capacitance (C_{dl}) is described in the experimental section,[13] and the results presented in **Figure 6.27**. The largest increase in C_{dl} and thus, ECSA, was found for the Co@KMO-Cl compared to that for Co@KMO-NO and Co@KMO-SO. Such an increase of the ECSA can be associated with the different material morphologies described above.

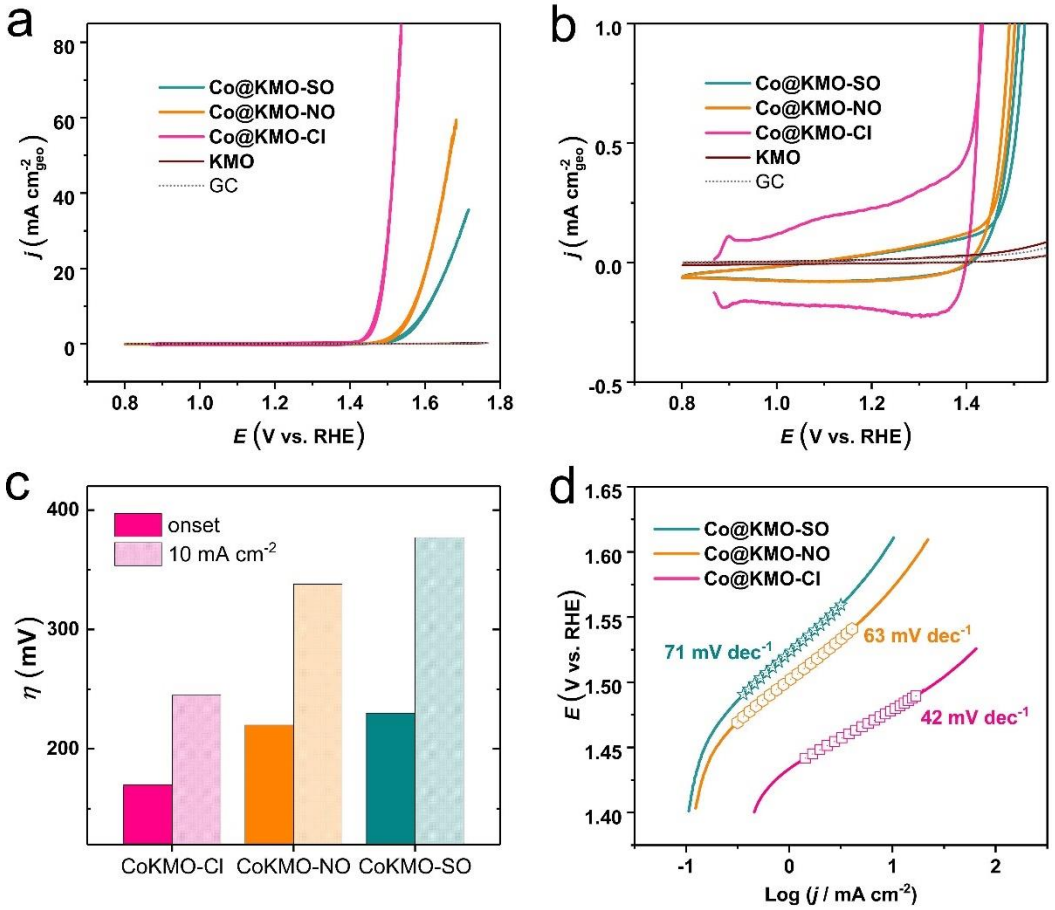


Figure 6. 26 (a) Stable cyclic voltammograms of Co salts reacted Co@KMO at pH=14 after 10 consecutive scans in NaOH electrolyte, with a scan rate of 20 mV s^{-1}. The profile of the glassy carbon (GC) support is included for comparison. All the curves are iR-corrected. (b) Enlarged region showing the double layer region of various Co@KMO. (c) The onset overpotential (η_{onset}) and overpotential at j = 10 mA cm^{-2} (η_{10}) obtained from (a). (d) Tafel slopes for the OER on the Co@KMO catalyst prepared with different anions.

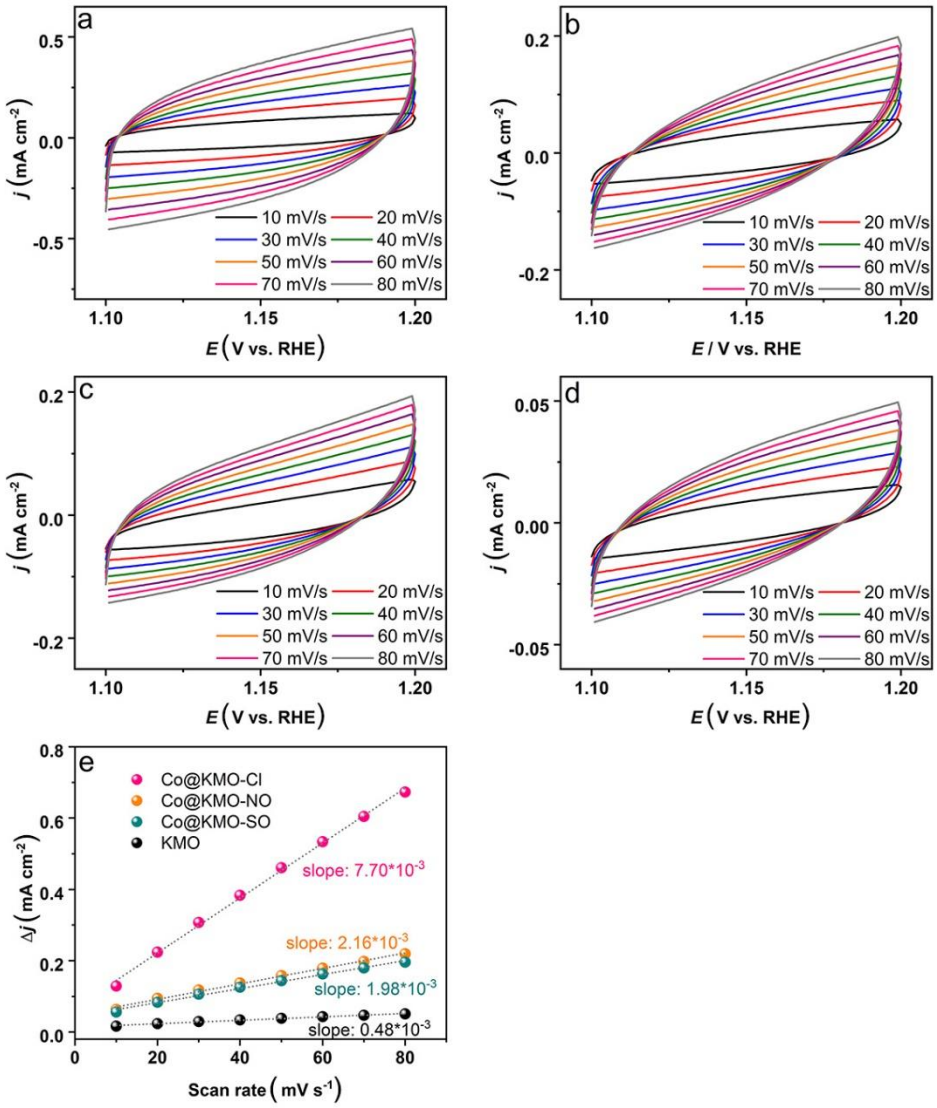


Figure 6. 27 Cyclic voltammetry in the double-layer capacitive potential window a at different scan rates (a) Co@KMO-Cl, (b) Co@KMO-NO, (c) Co@KMO-Cl, (d) KMO. (e) difference of the anodic and cathodic current densities (Δj) at 1.15 V vs RHE taken from (a-d) as a function of the scan rates.

The mass activity normalized by Co loading and the ECSA-normalized curves of Co@KMOs are shown in **Figure 6.28**. As can be seen, the catalytic activity of the Co@KMO-Cl is larger than that of the Co@KMO-NO and Co@KMO-SO independent of the normalization method. Considering that our primary figure of benchmarking the catalyst against those in the literature is the overpotential required to achieve a current

density ECSA at 10 mA cm^{-2}, the catalytic activity of the Co@KMO-Cl is comparable or better than the non-precious metals state-of-art catalysts for the OER in alkaline media (**Table 6.5**).

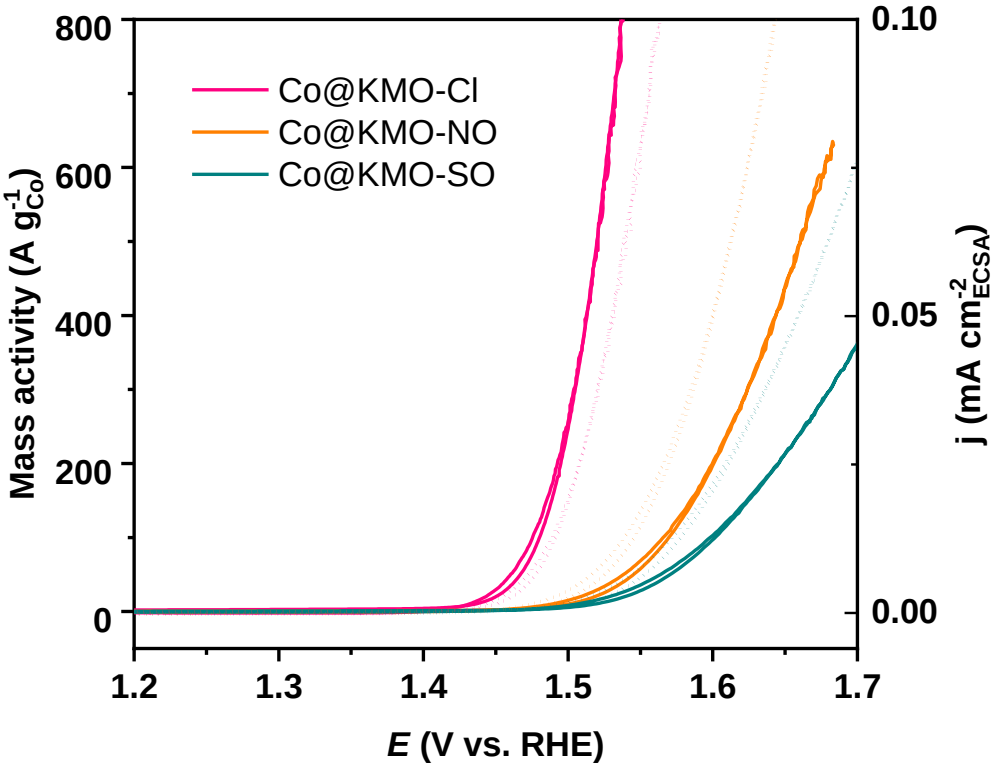


Figure 6. 28 Mass activity normalized by loaded Co mass of Co@KMOs (solid line); ECSA-normalized curves of Co@KMOs (dot line) measured in 1M NaOH electrolyte.

Table 6. 5 Comparative values of state-of-the-art catalyst for the oxygen evolution reaction in alkaline media.

Material	Electrolyte	η (10 mA/cm^2)	Comment	Ref.
Co@KMO-Cl	1 M NaOH	245 mV	GCE (5 mm), Loading: 0.2 mg cm^{-2}	This work
IrO_2	1 M KOH	300 mV	GCE (5 mm)	53
IrO_2/MoO_3	0.1 M NaOH	350 mV	Ti plate, Loading: 0.2 mg cm^{-2}	54
$RuTe_2$ porous nanorods	1 M KOH	285 mV	GCE (5 mm), Loading: 0.2 mg cm^{-2}	55
$Co_2Mo_3O_8$@NC-800	1 M KOH	331 mV	GCE (3 mm), Loading: 0.14 mg cm^{-2}	56
Fe doped Co_3O_4 hierarchical NPs	1 M KOH	262 mV	GCE (5 mm), Loading: 0.25 mg cm^{-2}	57
CoO/Co_3O_4	1 M KOH	260 mV	Ti foil or CFP Loading: 0.5 mg	58
CoFe oxide heterostructure	1 M KOH	302 mV	GCE (4 mm), Loading: 0.3 mg cm^{-2}	59
ER-Co_3O_4 nanowires	1 M KOH	344 mV	GCE	60
Co_3O_4/CeO_2 hybrid nanostructure	1 M KOH	270 mV	GCE (5 mm), Loading: 0.2 mg cm^{-2}	61
Ru_{SAC}@CoFe LDH	1 M KOH	198 mV	CFP, (1 cm^2) Loading: 1 mg cm^{-2}	62

Note: GCE: glassy carbon electrode, CFP: carbon fiber paper

In order to get more insight regarding the kinetics of the reaction and the rate-determining step (RDS), the Tafel slopes were extracted for all the samples (**Figure 6.26d)**. The smallest Tafel slope (faster kinetics) was found for the Co@KMO-Cl (42 mV dec^{-1}); while the values of Co@KMO-NO and Co@KMO-SO are 63 and 71 mV

dec^{-1}, respectively. The proposed proton-coupled electron-transfer mechanism (water nucleophilic attack) for the OER in alkaline media on Co catalyst is as follows:[63, 64]

$$Co^* + OH^- \rightarrow Co^*OH + e^- \quad [6.4]$$

$$Co^*OH + OH^- \rightarrow Co^*O + H_2O + e^- \quad [6.5]$$

$$Co^*O + OH^- \rightarrow Co^*OOH + e^- \quad [6.6]$$

$$Co^*OOH + OH^- \rightarrow Co^* + O_2 + H_2O + e^- \quad [6.7]$$

(*) correspond to adsorbed species, for example *OH, *O and *OOH. Based on the values of the Tafel slope, we propose the RDS of the OER for the Cl-containing sample is the second electron transfer step (Eq. 6.5, a theoretical value of 40 mV dec^{-1}). On the other hand, Tafel slopes of 60 mV dec^{-1} observed on the Co@KMO-NO and Co@KMO-SO samples, suggest a change of the reaction mechanism. Thus, Eq. 6.5 can be written as nonconcerted proton-electron transfer steps [65, 66]:

$$Co^*OH + OH^- \rightarrow Co^{*}O^- + H_2O + \quad [6.8]$$

$$Co^{*}O^- \rightarrow Co^*O + e^- \quad [6.9]$$

the RDS is associated with the deprotonation step of Co*OH to $Co^{*}O^-$, which occurs prior to the second electron transfer. As shown in **Figure 6.18** and **Figure 6.24**, the electronic structure of Co@KMO-Cl was tailored by the presence of Cl. The positively shifted Co 2p binding energy and the enhancement of OH adsorption on Co@KMO-Cl suggest a favorable interaction of the OH^- reactant with the active sites, which moved the RDS to second electron transfer step. This effect on Co@KMO-Cl can be also associated with the negatively shifted OER onset potential, where the adsorption step has finished and subsequent electron-proton step is initialized.[66, 67] Furthermore, a possible explanation for the higher catalytic activity of the chloride containing samples can be linked to the presence of a higher density of defects on the surface of the catalyst as a result of the etching of cobalt hydroxides by chloride ions.[68]

Figure 6.29 shows the voltammograms and Tafel plots of the OER on the Co@KMO-Cl prepared with different concentration of $CoCl_2$ precursor. When normalized by the geometrical area, the catalytic activity of the OER increases as the concentration of $CoCl_2$ used in the preparation of Co@KMO-Cl increases from 0.01 M $CoCl_2$ to 0.5 M $CoCl_2$. Thus, we assume that the activity is directly controlled by the Co-OH species generated on the surface due to the increase in concentration of the $CoCl_2$ precursor. To confirm this assumption, the loading of Co on the catalyst as a function of the concentration of the precursors was determined by XRF and the mass activity (normalized by the Co loading) is shown on **Figure 6.29a**. It is evident that higher Co loading resulted in higher mass activity, following the same trend observed for geometrical activity. A higher catalytic activity was observed on the Co@KMO-$Cl_{0.5}$, which only requires an overpotential of 230 mV to reach 50 mA g_{Co}^{-1}.

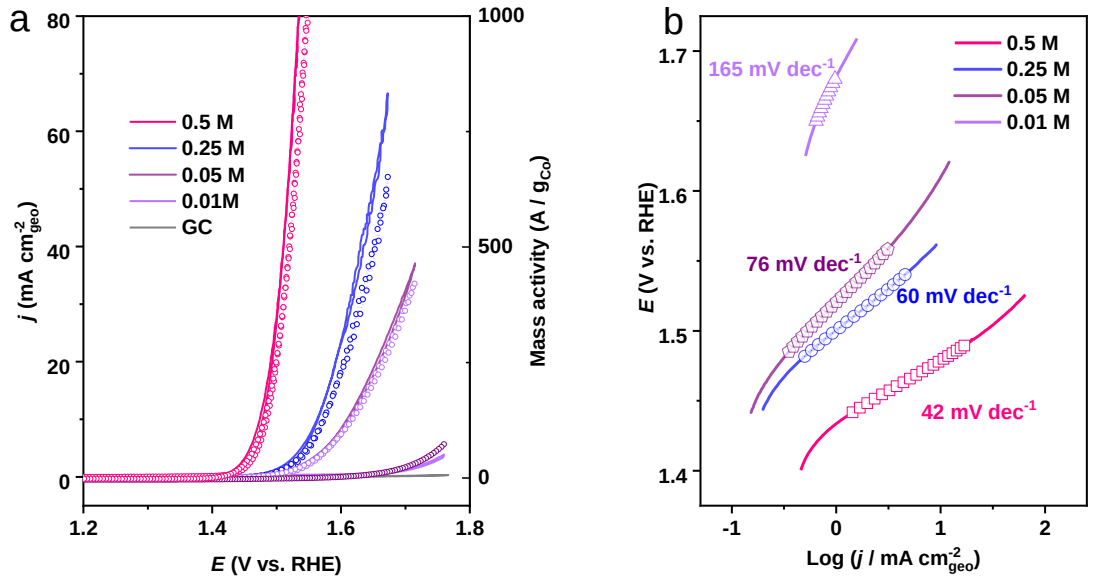


Figure 6. 29 (a) Stable cyclic voltammograms in 1 M NaOH solution of Co@KMO-Cl samples synthesized with different concentrations of $CoCl_2$ as indicated in different color, solid lines (left Y axis): geometrical activity; (◦) symbols (right Y axis): mass activity. The stable voltammogram was recorded after 10 consecutive scans. The voltammogram of the glassy carbon (GC) support is included for comparison. All the curves are iR-corrected. Scan rate υ= 20 mV s^{-1}. (b) corresponding Tafel plots in the potential range between 1.4 and 1.7 V vs RHE.

6.3.4 Long term stability of Co@KMOs during the oxygen evolution reaction

The long-term stability also plays a pivotal role in the evaluation of an electrocatalyst, especially for commercial applications. **Figure 6.30a** shows the electrolysis in a 1 M NaOH solution at 1.48 V vs. RHE for 22 h using the Co@KMO-$Cl_{0.5}$ as electrocatalyst. The chronoamperometric curve shows a stable signal of $j \approx 10$ mA cm^{-2} during the total duration of the experiment. HR-TEM and cyclic voltammetry of the catalyst before and after the electrolysis were recorded in order to determine any changes or degradation of the catalyst over time. HR-TEM image of Co@KMO-$Cl_{0.5}$ after 22 h electrolysis shows transformation of the edge of the Co-OH nanoflakes from a more crystalline structure to a more amorphous one (**Figure 6.30b, c**). Such changes during OER process have been previously reported and have been associated with oxidation state evolution of active sites and its coordinations.[69-71] Even though, structural changes were observed on the electron microscopy, the cyclic voltammograms of the Co@KMO-Cl before and after the electrolysis show negligible differences (**Figure 6.31**). No additional signals were found in the Raman spectra on Co@KMO-Cl after a long-term stability test, while slight change in peak intensity at 578 cm^{-1} clearly demonstrated the surface reconstruction, as observed in TEM image. In order to confirm whether the changes of the morphology of the catalyst occurred at the start of the reaction or during the whole chronoamperometry, high resolution SEM images where obtained after 10 cycles between 0.8 and 1.5 V (**Figure 6.32**). It was observed that the structure of the catalyst changed at very early stages of the reaction. Thus, after the formation of this reconstructed morphology, the catalyst is stable not only in terms of catalyst activity but also the morphology of the matrix. Despite of the local surface reconstruction, the identical phase structure (**Figure 6.33**) and homogenous element distribution visualized by SEM-EDS (**Figure 6.34**) confirm the observed stability.

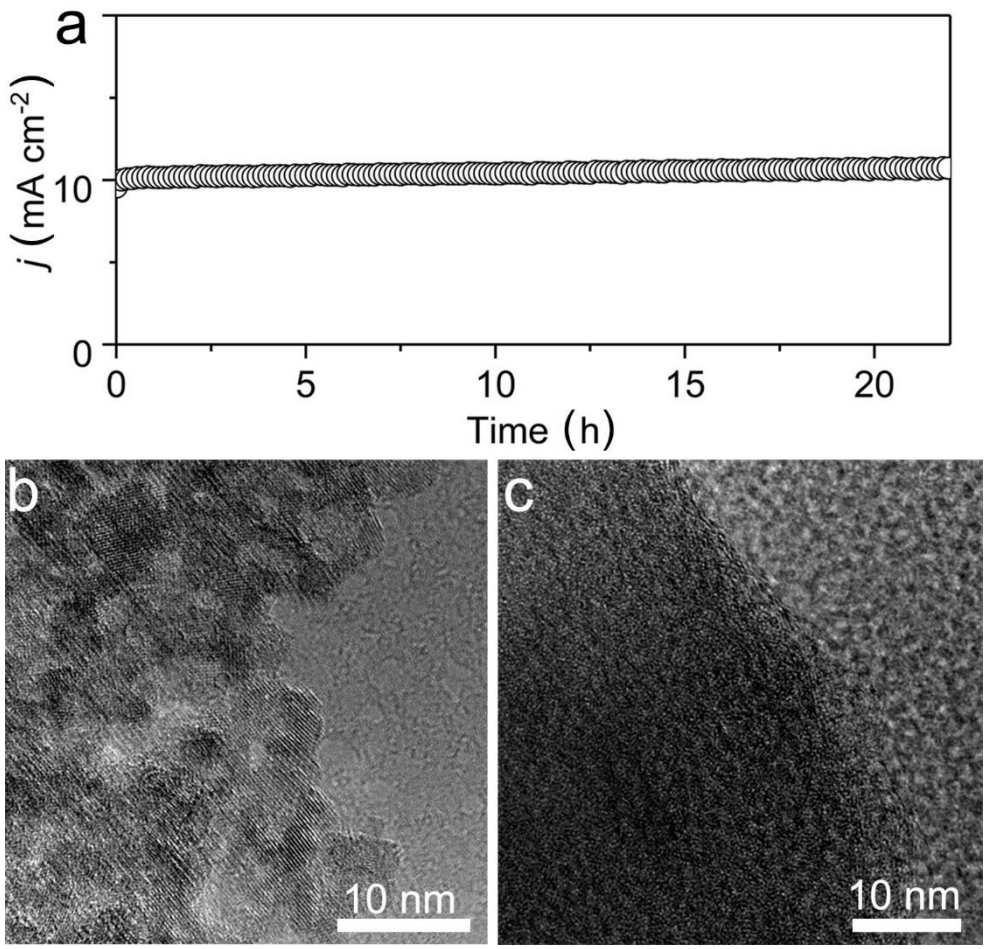


Figure 6. 30 (a) 24 h chronoamperometry profile of Co@KMO-$Cl_{0.5}$ at 1.48 V vs. RHE in 1 M NaOH solution. HR-TEM images of Co@KMO-Cl (b) before, and (c) after electrolysis.

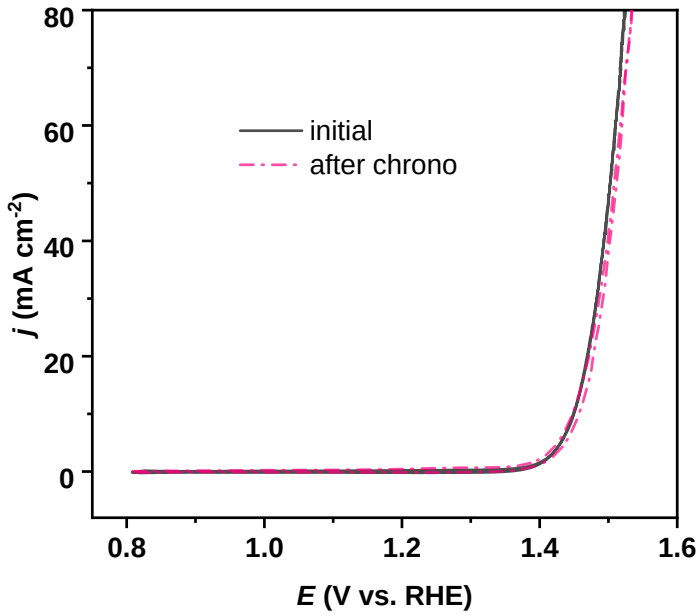


Figure 6. 31 Cyclic voltammograms of Co@KMO-Cl before and after long term durability test.

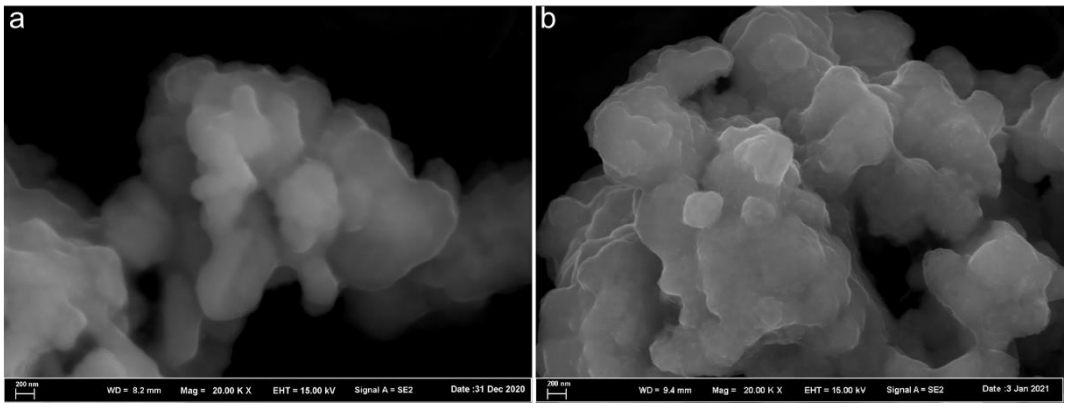


Figure 6. 32 SEM images of Co@KMO-Cl after 10 cycles of OER.

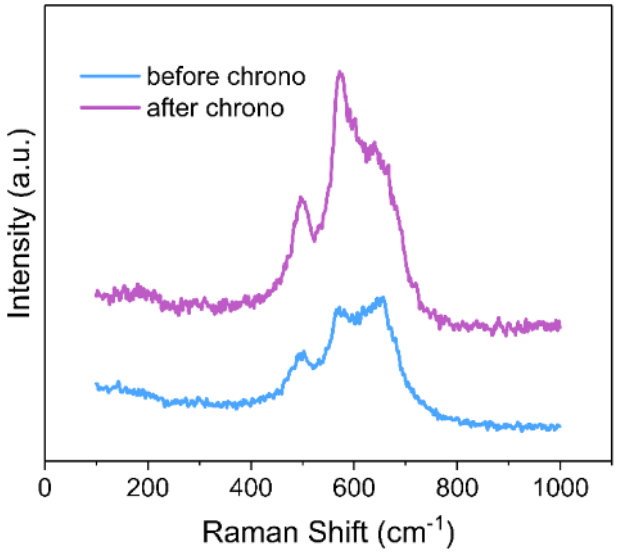


Figure 6. 33 Raman spectra of Co@KMO-Cl before/after chronoamperometry.

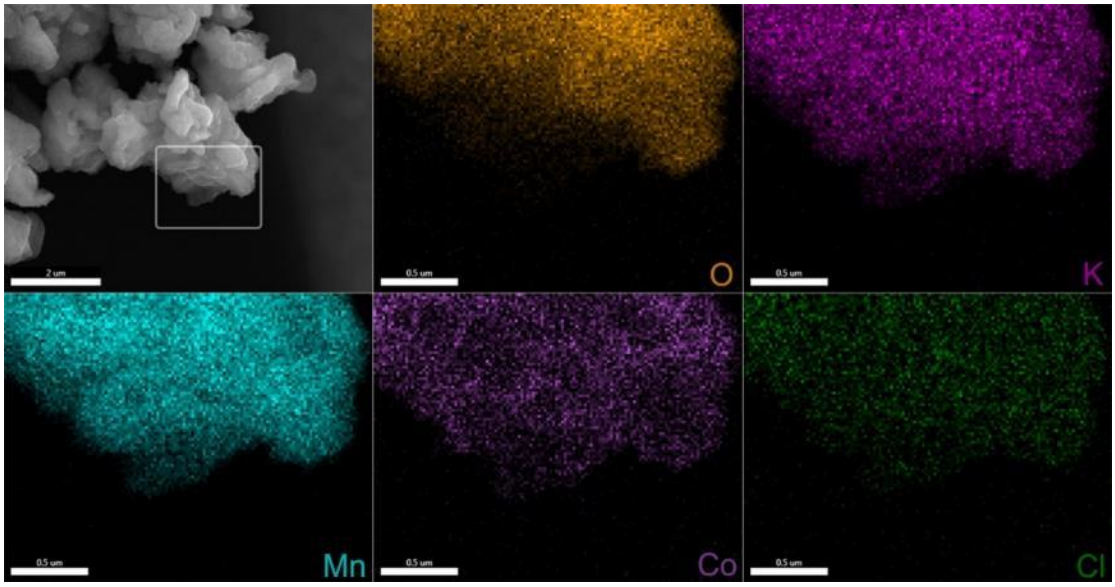


Figure 6. 34 SEM-EDS mapping of Co@KMO-Cl after chronoamperometry at 1.48 V vs. RHE in 1 M NaOH.

6.4 Conclusions

In this work, we demonstrated that surface galvanic formation of Co-OH on Birnessite is a clean, green route for the design of highly efficient catalysts for OER. This simple method provides a route for the synthesis of ultrathin and high surface area Co-OH nanosheets with 3-4 nm thickness supported on KMO. The simple and clean synthesis method involves the surface redox reaction of hydrated Co^{2+} and crystalline Mn^{4+} at ambient temperature, without use of additional surfactants or capping materials. Thus, the resulting catalyst can be implemented directly as catalyst without extra cleaning or high-temperature steps.

XAS and XPS analysis confirmed the changes in the oxidation state of the bulk and surface species Co^{+2} → $Co^{+2.75}$ and $Mn^{+3.9}$ → $Mn^{+3.1}$. The effect of the anions of Co precursors, such as $CoCl_2$, $Co(NO_3)_2$ and $CoSO_4$ was evaluated. It was found that the use of different anions in the preparation of the catalyst results in changes to the coordination chemistry and electronic structure of the catalyst. These changes influenced the activity of the catalyst with Co@KMO-Cl being identified as the most active for OER compared to Co@KMO-NO and Co@KMO-SO catalysts. The presence of Cl was found to favor the formation of Co-OH. Further, the kinetic analysis suggests that such an increase in the catalytic activity on Co@KMO-Cl is due to the change of the RDS from the OH adsorption step to the coupled electron-deprotonation step. The Co@KMO-Cl showed improved catalytic activity in comparison with non-precious metal state-of-the-art catalyst for the OER in alkaline media with an overvoltage of only 245 mV to achieve 10 mA cm^{-2}_{geo} (**Table 6.5**). Long-term stability tests demonstrated that the Co@KMO-Cl has an excellent stability by showing steady current density during the OER for at least 20 h.

References

1. Z. W. Seh, J. Kibsgaard, C. F. Dickens, I. Chorkendorff, J. K. Nørskov and T. F. Jaramillo, *Science*, 2017, **355**.
2. D. A. Kuznetsov, B. Han, Y. Yu, R. R. Rao, J. Hwang, Y. Román-Leshkov and Y. Shao-Horn, *Joule*, 2018, **2**, 225-244.
3. C. Spoeri, J. T. H. Kwan, A. Bonakdarpour, D. P. Wilkinson and P. Strasser, *Angewandte Chemie International Edition*, 2017, **56**, 5994-6021.
4. J. H. Montoya, L. C. Seitz, P. Chakthranont, A. Vojvodic, T. F. Jaramillo and J. K. Nørskov, *Nature Materials*, 2017, **16**, 70-81.
5. M. T. Koper, *Topics in Catalysis*, 2015, **58**, 1153-1158.
6. L. C. Seitz, C. F. Dickens, K. Nishio, Y. Hikita, J. Montoya, A. Doyle, C. Kirk, A. Vojvodic, H. Y. Hwang and J. K. Norskov, *Science*, 2016, **353**, 1011-1014.
7. P. C. Vesborg and T. F. Jaramillo, *Rsc Advances*, 2012, **2**, 7933-7947.
8. B. M. Hunter, H. B. Gray and A. M. Müller, *Chemical Reviews*, 2016, **116**, 14120-14136.
9. J. O. M. Bockris, *The Journal of Chemical Physics*, 1956, **24**, 817-827.
10. A. C. C. Tseung and S. Jasem, *Electrochimica Acta*, 1977, **22**, 31-34.
11. J. O. M. Bockris and T. Otagawa, *the journal of physical chemistry*, 1983, **87**, 2960-2971.
12. S. I. Córdoba, R. E. Carbonio, M. L. Teijelo and V. A. Macagno, *Electrochimica Acta*, 1987, **32**, 749-755.
13. C. C. L. McCrory, S. Jung, J. C. Peters and T. F. Jaramillo, *Journal of the American Chemical Society*, 2013, **135**, 16977-16987.
14. W. T. Hong, M. Risch, K. A. Stoerzinger, A. Grimaud, J. Suntivich and Y. Shao-Horn, *Energy & Environmental Science*, 2015, **8**, 1404-1427.
15. F. Song and X. Hu, *Journal of the American Chemical Society*, 2014, **136**, 16481-16484.
16. F. Song, M. M. Busch, B. Lassalle-Kaiser, C.-S. Hsu, E. Petkucheva, M. Bensimon, H. M. Chen, C. Corminboeuf and X. Hu, *ACS Central Science*, 2019, **5**, 558-568.
17. J. Zhang, J. Liu, L. Xi, Y. Yu, N. Chen, S. Sun, W. Wang, K. M. Lange and B. Zhang, *Journal of the American Chemical Society*, 2018, **140**, 3876-3879.
18. G. Chen, Y. Zhu, H. M. Chen, Z. Hu, S.-F. Hung, N. Ma, J. Dai, H.-J. Lin, C.-T. Chen, W. Zhou and Z. Shao, *Advanced Materials*, 2019, **31**, 1900883.
19. M. W. Louie and A. T. Bell, *Journal of the American Chemical Society*, 2013, **135**, 12329-12337.
20. O. Diaz-Morales, I. Ledezma-Yanez, M. T. Koper and F. Calle-Vallejo, *ACS Catalysis*, 2015, **5**, 5380-5387.
21. M. J. Lawrence, V. Celorrio, X. Shi, Q. Wang, A. Yanson, N. J. E. Adkins, M. Gu, J. Rodríguez-López and P. Rodriguez, *ACS Applied Energy Materials*, 2018, **1**, 5233-5244.
22. J. Guan, Z. Duan, F. Zhang, S. D. Kelly, R. Si, M. Dupuis, Q. Huang, J. Q. Chen, C. Tang and C. Li, *Nature Catalysis*, 2018, **1**, 870.
23. L. S. Balistrieri and J. W. Murray, *Geochimica et Cosmochimica Acta*, 1986, **50**, 2235-2243.
24. A. Manceau, E. Silvester, C. Bartoli, B. Lanson and V. A. Drits, *American mineralogist*, 1997, **82**, 1150-1175.
25. A. C. Thenuwara, E. B. Cerkez, S. L. Shumlas, N. H. Attanayake, I. G. McKendry, L. Frazer, E. Borguet, Q. Kang, R. C. Remsing, M. L. Klein, M. J. Zdilla and D. R. Strongin, *Angewandte Chemie International Edition*, 2016, **55**, 10381-10385.

26. A. C. Thenuwara, S. L. Shumlas, N. H. Attanayake, Y. V. Aulin, I. G. McKendry, Q. Qiao, Y. Zhu, E. Borguet, M. J. Zdilla and D. R. Strongin, *ACS Catalysis*, 2016, **6**, 7739-7743.
27. Y. Pu, M. J. Lawrence, V. Celorrio, Q. Wang, M. Gu, Z. Sun, L. A. Jácome, A. E. Russell, L. Huang and P. Rodriguez, *Journal of Materials Chemistry A*, 2020, **8**, 13340-13350.
28. A. J. Dent, G. Cibin, S. Ramos, A. D. Smith, S. M. Scott, L. Varandas, M. R. Pearson, N. A. Krumpa, C. P. Jones and P. E. Robbins, *Journal of Physics: Conference Series*, 2009, **190**, 012039.
29. B. Ravel and M. Newville, *Journal of synchrotron radiation*, 2005, **12**, 537-541.
30. M. Newville, *Journal of synchrotron radiation*, 2001, **8**, 96-100.
31. S. Diaz-Moreno, M. Amboage, M. Basham, R. Boada, N. E. Bricknell, G. Cibin, T. M. Cobb, J. Filik, A. Freeman and K. Geraki, *Journal of synchrotron radiation*, 2018, **25**, 998-1009.
32. S. Hayama, G. Duller, J. P. Sutter, M. Amboage, R. Boada, A. Freeman, L. Keenan, B. Nutter, L. Cahill and P. Leicester, *Journal of synchrotron radiation*, 2018, **25**, 1556-1564.
33. M. B. Stevens, L. J. Enman, A. S. Batchellor, M. R. Cosby, A. E. Vise, C. D. M. Trang and S. W. Boettcher, *Chemistry of Materials*, 2017, **29**, 120-140.
34. C. Julien, M. Massot, R. Baddour-Hadjean, S. Franger, S. Bach and J. Pereira-Ramos, *Solid State Ionics*, 2003, **159**, 345-356.
35. C. M. Julien, M. Massot and C. Poinsignon, *Spectrochimica Acta Part A: Molecular and Biomolecular Spectroscopy*, 2004, **60**, 689-700.
36. H. An, Z. Chen, J. Yang, Z. Feng, X. Wang, F. Fan and C. Li, *Journal of catalysis*, 2018, **367**, 53-61.
37. T. Pauporté, L. Mendoza, M. Cassir, M. C. Bernard and J. Chivot, *Journal of The Electrochemical Society*, 2005, **152**, C49.
38. J. Yang, H. Liu, W. N. Martens and R. L. Frost, *The Journal of Physical Chemistry C*, 2010, **114**, 111-119.
39. M. C. Militello and S. J. Simko, *Surface Science Spectra*, 1994, **3**, 402-409.
40. H. Jiang, Q. He, X. Li, X. Su, Y. Zhang, S. Chen, S. Zhang, G. Zhang, J. Jiang, Y. Luo, P. M. Ajayan and L. Song, *Advanced Materials*, 2019, **31**, 1805127.
41. J. Suntivich, K. J. May, H. A. Gasteiger, J. B. Goodenough and Y. Shao-Horn, *Science*, 2011, **334**, 1383-1385.
42. E. Ahmad, G. Mallia, D. Kramer, V. Tileli, A. Kucernak and N. Harrison, *Physical review letters*, 2012, **108**, 259701.
43. A. Ignatov, S. Khalid, R. Sujoy and N. Ali, *Journal of synchrotron radiation*, 2001, **8**, 898-900.
44. J. Chaboy, *Journal of synchrotron radiation*, 2009, **16**, 533-544.
45. G. Holzlechner, M. Kubicek, H. Hutter and J. Fleig, *Journal of Analytical Atomic Spectrometry*, 2013, **28**, 1080-1089.
46. M. Kubicek, G. Holzlechner, A. K. Opitz, S. Larisegger, H. Hutter and J. Fleig, *Applied surface science*, 2014, **289**, 407-416.
47. P. W. Menezes, A. Indra, A. Bergmann, P. Chernev, C. Walter, H. Dau, P. Strasser and M. Driess, *Journal of Materials Chemistry A*, 2016, **4**, 10014-10022.
48. M. Oku and K. Hirokawa, *Journal of Electron Spectroscopy and Related Phenomena*, 1976, **8**, 475-481.
49. Z.-F. Huang, J. Song, Y. Du, S. Xi, S. Dou, J. M. V. Nsanzimana, C. Wang, Z. J. Xu and X. Wang, *Nature Energy*, 2019, **4**, 329-338.
50. J. Stoch and J. Gablankowska-Kukucz, *Surface and Interface Analysis*, 1991, **17**, 165-167.

51. T. Bligaard, R. M. Bullock, C. T. Campbell, J. G. Chen, B. C. Gates, R. J. Gorte, C. W. Jones, W. D. Jones, J. R. Kitchin and S. L. Scott, *ACS Catalysis*, 2016, **6**, 2590-2602.
52. J. G. Chen, C. W. Jones, S. Linic and V. R. Stamenkovic, *ACS Catalysis*, 2017, **7**, 6392-6393.
53. G. Li, L. Anderson, Y. Chen, M. Pan and P.-Y. Abel Chuang, *Sustainable Energy & Fuels*, 2018, **2**, 237-251.
54. M. Tariq, W. Q. Zaman, W. Sun, Z. Zhou, Y. Wu, L.-m. Cao and J. Yang, *ACS Sustainable Chemistry & Engineering*, 2018, **6**, 4854-4862.
55. J. Wang, L. Han, B. Huang, Q. Shao, H. L. Xin and X. Huang, *Nature communications*, 2019, **10**, 5692.
56. T. Ouyang, X.-T. Wang, X.-Q. Mai, A.-N. Chen, Z.-Y. Tang and Z.-Q. Liu, *Angewandte Chemie International Edition*, 2020, **59**, 11948-11957.
57. S. L. Zhang, B. Y. Guan, X. F. Lu, S. Xi, Y. Du and X. W. Lou, *Advanced Materials*, 2020, **32**, 2002235.
58. D. He, X. Song, W. Li, C. Tang, J. Liu, Z. Ke, C. Jiang and X. Xiao, *Angewandte Chemie International Edition*, 2020, **59**, 6929-6935.
59. Y. Huang, R. Yang, G. Anandhababu, J. Xie, J. Lv, X. Zhao, X. Wang, M. Wu, Q. Li and Y. Wang, *ACS Energy Letters*, 2018, **3**, 1854-1860.
60. S. Liu, H. Cheng, K. Xu, H. Ding, J. Zhou, B. Liu, W. Chu, C. Wu and Y. Xie, *ACS Energy Letters*, 2019, **4**, 423-429.
61. Y. Liu, C. Ma, Q. Zhang, W. Wang, P. Pan, L. Gu, D. Xu, J. Bao and Z. Dai, *Advanced Materials*, 2019, **31**, 1900062.
62. P. Li, M. Wang, X. Duan, L. Zheng, X. Cheng, Y. Zhang, Y. Kuang, Y. Li, Q. Ma, Z. Feng, W. Liu and X. Sun, *Nature communications*, 2019, **10**, 1711.
63. H. Dau, C. Limberg, T. Reier, M. Risch, S. Roggan and P. Strasser, *ChemCatChem*, 2010, **2**, 724-761.
64. J. Hessels, R. J. Detz, M. T. M. Koper and J. N. H. Reek, *Chemistry – A European Journal*, 2017, **23**, 16413-16418.
65. M. S. Burke, M. G. Kast, L. Trotochaud, A. M. Smith and S. W. Boettcher, *Journal of the American Chemical Society*, 2015, **137**, 3638-3648.
66. Y. Surendranath, M. W. Kanan and D. G. Nocera, *Journal of the American Chemical Society*, 2010, **132**, 16501-16509.
67. B. S. Yeo and A. T. Bell, *Journal of the American Chemical Society*, 2011, **133**, 5587-5593.
68. P. F. Liu, S. Yang, L. R. Zheng, B. Zhang and H. G. Yang, *Journal of Materials Chemistry A*, 2016, **4**, 9578-9584.
69. N. Ortiz Peña, D. Ihiawakrim, M. Han, B. Lassalle-Kaiser, S. Carenco, C. Sanchez, C. Laberty-Robert, D. Portehault and O. Ersen, *ACS Nano*, 2019, **13**, 11372-11381.
70. A. Grimaud, K. J. May, C. E. Carlton, Y.-L. Lee, M. Risch, W. T. Hong, J. Zhou and Y. Shao-Horn, *Nature communications*, 2013, **4**, 2439.
71. Z. Chen, L. Cai, X. Yang, C. Kronawitter, L. Guo, S. Shen and B. E. Koel, *ACS Catalysis*, 2018, **8**, 1238-1247.

Chapter 7 Conclusions and future work

7.1 Conclusions

Under the global demand of developing highly efficient electrocatalysts with low cost to realize industrial scale production of hydrogen fuel, this thesis aims to fabricate supported catalysts for water electrolysis based on layered metal oxide family. Cost-effective layered manganese oxide and titanate oxide materials have been developed as support to accommodate small loading of Ni, Co and Pt active species. Ultrahigh atomic efficiency has been achieved due to the highly dispersed active atoms, cluster and phase. Excellent mass activity of our electrocatalysts indicate the great potential of these materials to be employed in practical applications. In addition, the correlation between coordination/electronic structure and HER/OER catalysis was elucidated through systematically physical characterization and electrochemical study. This understanding provides effective guideline for new catalyst design.

Since the properties of metal oxide supports themselves have a strong effect on the HER/OER active species deposited, the phase transformation from layered structured lepidocrocite TiO_2 (L-TiO_2) nanosheets to its polymorphs anatase/rutile TiO_2 (R- TiO_2 and A- TiO_2) was studied firstly (***Chapter 4***). Phase transition of the L-TiO_2 nanosheets as a function of temperature and pH reveals that the temperature determines the final phase-structure of the TiO_2 nanoparticles while the pH mostly influences the morphology and particle size. By fixing the reaction temperature of 180 °C, dominant A-TiO_2 was obtained at all range of pHs. Whereas A-TiO_2 particles in acid solution (pH=3) exhibit granular shape amorphous structure, while in alkaline solution pH=9 the nanoparticles are shuttle-like with highly exposed (101) lattice plane. The synthesized A-TiO_2 with different electronic structure exhibit different responses to the UV-Vis light. On the basis of this feature, Pt decorated TiO_2 with modified electronic structure were synthesized through a photochemical reduction reaction. UV-Vis spectra and XPS clearly confirm the charge transfer from Ti to Pt on Pt@TiO_2-pH9 which resulted from stronger absorption towards UV-Vis light irradiation. Pt species on Pt@TiO_2-pH9 with reduced oxidation state exhibited better electrochemical HER

performance than the Pt@TiO_2-pH3 counterpart. Moreover, in terms of mass activity and long-term stability, photochemical deposited Pt@TiO_2-pH9-N300 with ultralow Pt loading (~1 wt%) exhibits a current density of 3954 A g_{Pt}^{-1} at an overpotential of 30 mV, which is 17-folds larger than that of commercial Pt/C.

As the counter reaction of HER, OER on the anode commonly requires higher overpotential because of the sluggish kinetics from four electron transfer steps. Ni intercalated catalysts based on layered manganese oxide and layered titania oxide were synthesized and investigated (***Chapter 5***). Combination of XRD and XAS/XES reveals the intercalation of Ni^{2+} taken place at Mn^{3+} sites, via reduction of Mn^{3+} to Mn^{2+}. The amount of Ni intercalated in each of the samples is proportional to the concentrations of Mn^{3+}, where 8 wt% Ni was detected in Ni-KMO and 16 wt% in Ni-HMO. With EXAFS analysis, different coordination environments of Ni species were confirmed in Ni-KMO and Ni-HMO, where Ni-K/H_2O in Ni-KMO was replaced by Ni-H_2O in Ni-HMO. The alignment of H_2O molecules in interlayer gallery therefore altered. Changed coordination structure leads to different electrochemical redox feature of Ni^{2+}/Ni^{3+} transition, which further give rise to different OER activities. Electrochemical study shows that the geometrical activity of Ni-KMO (η_{10} = 240 mV, Tafel slope = 60 mV dec^{-1}) in 1 M NaOH electrolyte is much smaller than that of Ni-HMO (η_{10} = 300 mV, Tafel slope = 113 mV dec^{-1}). It can be concluded that instead of positive relation between Ni content and OER activity, the coordination structure plays a more essential role in determining catalytic activity. The optimal Ni loading intercalation with optimal alignment of H_2O molecules can boost higher activity. In terms of mass activity, Ni-KMO and Ni-HTO show excellent mass activity of 602 A g_{Ni}^{-1} and 710 A g_{Ni}^{-1} at overpotential of 240 mV, respectively. Ni-HTO shows a 6-fold increase in catalytic activity per mass of Ni in comparison with the state-of-the-art Ni-based nanocatalysts.

Chapter 6 further extended the interaction of active species of cobalt with layered manganese oxide. Different to intercalation mechanism of Ni, redox reaction

mechanism was demonstrated in Co-KMO system due to more labile chemical property of high spin hydrated $[Co(H_2O)_6]^{2+}$ than the low spin $[Ni(H_2O)_6]^{2+}$. HRTEM and HAADF-STEM show that ultrathin Co-OH nanosheets with poor crystallinity *in-situ* formed at the KMO surface. Such core-shell structure significantly alters the surface roughness and increase the ECSA by 16-folds. XAS and XPS analysis confirmed the changes in the oxidation state of the bulk and surface species Co^{+2} → $Co^{+2.75}$ and $Mn^{+3.9}$ → $Mn^{+3.1}$. By means of XES analysis, the change of each Mn species ($Mn^{2+}/Mn^{3+}/Mn^{4+}$) in Co@KMO and KMO were determined that the reaction mechanism was proposed: $\delta Co^{2+}{}_{(liq.)} + Mn^{4+}{}_{(cryst.)} \rightarrow \delta Co^{3+}{}_{(cryst.)} + Mn^{(4-\delta)+}{}_{(cryst.)}$ ($0 < \delta < 1$). This reaction can be extended to varying type of Co precursors, such as $CoCl_2$, $Co(NO_3)_2$ and $CoSO_4$. It was found that the use of different anions in the preparation of the catalyst results in changes to the coordination chemistry and electronic structure of the catalyst. These changes can be associated to OER activity. The presence of Cl was found to favour the formation of Co-OH, which increase the ECSA and change of the RDS from the OH adsorption step to the coupled electron-deprotonation step instead. Obtained Co@KMO-Cl showed excellent catalytic activity in comparison with non-precious metal state-of-the-art catalyst for the OER in alkaline media with an overvoltage of only 245 mV to achieve 10 mA cm^{-2}_{geo}. This work provides a clean, surfactant free and large scalable strategy for electrocatalyst design.

7.2 Further work

In this thesis, highly efficient catalysts based on layered metal oxides (titania and manganese) for water splitting and their electrochemical properties are presented. Through the photochemical reduction, ion exchange and surface redox reaction, active species can be readily incorporated and have a strong interaction with the oxide support. Owing to the interaction, charge transfer between active species and support, coordination structure difference originated from spacing confinement and ligand effect have been elucidated and correlated to the electrochemical behavior. However, some issues still need attention and further work to get deeper insight.

All the physical characterizations in this thesis are *ex-situ* that can not provide real-time dependent information during the electrochemical process. For example, the valence state and coordination environment of Pt species on Pt@TiO_2 samples in the catalytic HER process is not clear. *In-situ* XANES characterization is a powerful technique to monitor chemical state change under a fixed applied potential. In *Chapter* 5, we infer a crystal structure transition of $Ni(OH)_2$ → NiOOH inserted in Mn-O layers. *In-situ* EXAFS technique can reveal the coordination structure change during the electrochemical process that provides direct evidence of structure change.

The developed catalysts for HER and OER in this thesis were evaluated in different pH solutions. Pt@TiO_2 catalyzed HER in acidic medium while Ni-KMO and Co@KMO samples promoted OER in alkaline medium. Further work needs to be done to design bifunctional catalyst which has the capability to drive the HER/OER at the same condition. In that way, membrane-electrode-assembly made by synthesized catalysts can be operated at single cell for practical application.

In addition, layered metal oxides with a wide range of elements pool, such as Ti, V, Mn, Co, W, Mo, *et al.*, have great potential to be the support or nanoreactor. For example, recent work on widened interlayer gap of layered MoO_3 have been applied in lithium

ion battery.[1] Through lithiation/delithiation, O defects and water molecules have been introduced into MoO_3. It can be supposed that the modified MoO_3 can be an ideal support for foreign atoms anchoring/deposition thus to fabricate specific catalysts, *i.e.* hydrogen evolution reaction. Rodriguez's group previously reported that Cu intercalated titania oxide can catalyze the photoanodic oxygen evolution.[2] In future work, by means of ion exchange protocol to intercalated Cu into layered oxides, different valence state Cu species and specific coordination environment can be engineered. Deep insight into the correlation of valence/coordination structure and catalytic reaction needs to be explored.

References

1. M. Yu, H. Shao, G. Wang, F. Yang, C. Liang, P. Rozier, C.-Z. Wang, X. Lu, P. Simon and X. Feng, *Nature communications*, 2020, **11**, 1348.

2. M. J. Lawrence, V. Celorrio, X. Shi, Q. Wang, A. Yanson, N. J. E. Adkins, M. Gu, J. Rodríguez-López and P. Rodriguez, *ACS Applied Energy Materials*, 2018, **1**, 5233-5244.